THE UNIVERSITY OF QUEENSLAND

AUSTRALIA

Simulating the collective behaviour of a monolayer of epithelial cells using a cellular Potts model

Adrian R. Noppé

BSc (Hons)

A thesis submitted for the degree of Doctor of Philosophy at

The University of Queensland in 2018

School of Mathematics and Physics

Abstract

We use a two and three-dimensional cellular Potts model (CPM) to represent the behaviour of an epithelial cell layer and describe its dynamics in response to a microscopic wound and a single modified cell. The energy function of the CPM describes mechanical properties of the cells and it was found that the interaction between contractile tension on cell membranes and the adhesion interactions between cells and substrate surfaces play an important role in the cell morphology, the closure of a wound and extrusion of a cell in the monolayer. Our results suggest that, depending on the balance between cell-cell adhesion and junctional tension, mechanics of the monolayer can either correspond to a hard or a soft regime that determines cell morphology and polygonal organisation in the monolayer.

The presence of a wound in a hard regime, where junctional tension is significant, or soft regime, where cell-cell adhesion dominates, can determine whether a wound will close or not. Theoretical approximations and simulations allowed us to determine the thresholds in the values of cell-cell adhesion and initial wound size that allow the system to lead to wound closure. Additional mechanisms, such as adhesion between the substrate and cells and apical perimeter contraction can shift where the threshold between the hard and soft regimes occurs. Overall, our results suggest that changes in the balance between contraction and adhesion around the site of injury determine whether or not non-monotonous wound closure occurs.

The extrusion of a single cell is only present if that cell adhesion and contractile tension is modified to differ from that of its neighbours and the interaction of the neighbouring cells' cell-cell adhesion and contraction lead to remove the cell from the monolayer and close of the void left by the modified cell. Theoretical approximations and simulations give a clearer picture of the interaction between different mechanisms and the condition of which the cell needs to be extruded.

Declaration by author

This thesis is composed of my original work, and contains no material previously published or written by another person except where due reference has been made in the text. I have clearly stated the contribution by others to jointly-authored works that I have included in my thesis.

I have clearly stated the contribution of others to my thesis as a whole, including statistical assistance, survey design, data analysis, significant technical procedures, professional editorial advice, and any other original research work used or reported in my thesis. The content of my thesis is the result of work I have carried out since the commencement of my research higher degree candidature and does not include a substantial part of work that has been submitted to qualify for the award of any other degree or diploma in any university or other tertiary institution. I have clearly stated which parts of my thesis, if any, have been submitted to qualify for another award.

I acknowledge that an electronic copy of my thesis must be lodged with the University Library and, subject to the policy and procedures of The University of Queensland, the thesis be made available for research and study in accordance with the Copyright Act 1968 unless a period of embargo has been approved by the Dean of the Graduate School.

I acknowledge that copyright of all material contained in my thesis resides with the copyright holder(s) of that material. Where appropriate I have obtained copyright permission from the copyright holder to reproduce material in this thesis.

Publications during candidature

Primary author:

Noppe, A., Roberts, A., Yap, A., Gomez, G., and Neufeld, Z. (2015). Modelling wound closure in an epithelial cell sheet using the cellular Potts model. *Integrative Biology*, *7*(10), 1253-1264. doi:10.1039/c5ib00053j

Contributing author:

Coburn, L., Lopez, H., Caldwell, B., Moussa, E., Yap, C., Priya, R., Noppe, A., Roberts, A.P., Lobaskin, V., Yap, A.S., Neufeld, Z., and Gomez, G.A. (2016). Contact inhibition of locomotion and mechanical cross-talk between cell-cell and cell-substrate adhesion determine the pattern of junctional tension in epithelial cell aggregates. *Mol Biol Cell*., *27*(22), 3436-3448. doi:10.1091/mbc.E16-04-0226

Publications included in this thesis

Noppe, A., Roberts, A., Yap, A., Gomez, G., and Neufeld, Z. (2015). Modelling wound closure in an epithelial cell sheet using the cellular Potts model. *Integrative Biology*, *7*(10), 1253-1264. doi:10.1039/c5ib00053j – incorporated as Chapter 2 with additional content and parts of the introduction are incorporated in the literature review in Chapter 1.

Contributor	Statement of contribution
A. Noppe (Candidate)	Wrote simulation code (100%) Results analysis (80%) Wrote the paper (80%)
A. Roberts	Wrote and edited paper (5%)
A. Yap	Wrote and edited paper (5%)
G. Gomez	Wrote and edited paper (5%) Biology experiments (100%)
Z. Neufeld	Wrote and edited paper (5%)

Contributions by others to the thesis

"No contributions by others."

Statement of parts of the thesis submitted to qualify for the award of another degree

None.

Acknowledgements

Firstly, I would like to thank my primary supervisor, Zoltan Neufeld, and secondary supervisor, Tony Roberts, for their help and guidance throughout my PhD. Besides my supervisors, I wish to acknowledge Alpha Yap and Guillermo Gomez, from the Institute for Molecular Bioscience (IMB) at the University of Queensland, for their contribution to the paper Chapter 2 is based upon and discussions regarding the biological behaviour of epithelial cells. Finally, I would also like to thank my family for their support throughout the years of my study.

Keywords

cellular Potts model, CPM, epithelial cells, wound healing, cell extrusion, cell cluster

Australian and New Zealand Standard Research Classifications (ANZSRC)

ANZSRC code: 010202 Biological Mathematics 90%

ANZSRC code: 010299 Applied Mathematics not elsewhere classified 10%

Fields of Research (FoR) Classification

FoR code: 0102 Applied Mathematics 100%

Table of Contents

Chapter 1: Introduction and Literature Review

1.1 INTRODUCTION

Epithelial cells connect with one another using adhesive molecules to form protective layers (epitheliums, see Figure 1.1) that line the inside of the body of metazoic organisms. The failure of these epitheliums can lead to complications. During the development of an organism the failure of the epithelia can lead to problems in organ development; and the failure of the epithelia in a mature organism can lead to the development of epithelial carcinoma, severe asthma and other cancers (Chanez, 2005). As a protective layer, the epithelium can be damaged by the removal, death or transformation of cells. To maintain its protective function the epithelium is able to close up wounds (Abreu-Blanco, Verboon, Liu, Watts, & Parkhurst, 2012) and extrude dead, dying or transformed cells (Eisenhoffer et al., 2012) to maintain homeostasis in the monolayer.

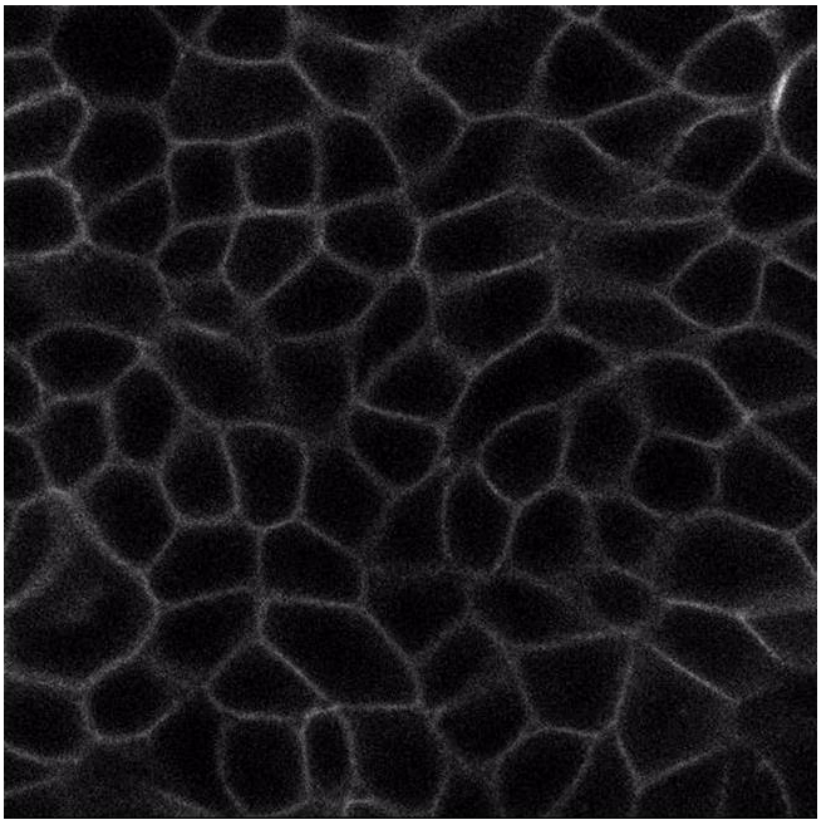

Figure 1.1. An example of an epithelium, where the fluorescent white in the image shows the curvature of the cells, provided by Institute for Molecular Bioscience (IMB) at the University of Queensland.

The aim of this thesis is to model the collective behaviour of epithelial cells in response to a microscopic wound (micro-wound), the extrusion of a single modified cell and the morphology of a cell cluster using a two and three-dimensional cellular Potts model (CPM). The CPM (Glazier & Graner, 1993; Graner & Glazier, 1992), also referred to as the Graner and Glazier Model or extended large Q-Potts Model, is a lattice-based cellular automata mathematical model used to simulate and investigate cell behaviour. Additional models that investigate cell behaviour include; vertex models (Fletcher, Osborne, Maini, & Gavaghan, 2013) and agent-based models (Landman & Fernando, 2011). These models that represent individual cells in a system will be referred to as discrete models. Models that represent the population densities of cells will be referred to as continuous models. Reaction diffusion equations, such as those implementing the Fisher-Kolmogorov Equation (Fisher, 1937), are examples of continuous models that are alternatives to the discrete models.

The use of the CPM to study cells includes a focus on their morphology, motility and behaviours to stimuli. Investigating wounds with the CPM has mostly focused on macro-wounds (hundreds of cells removed) and there is little to no literature describing the CPM to investigate micro-wounds (one to several cells removed). Further, the author could not identify any studies using the CPM to investigate the behaviour of the cells with the extrusion of a single modified cell. This thesis explores the behaviour of the simulated epithelium monolayer for a two-dimensional CPM (Chapter 2) and three-dimensional CPM (Chapter 4) when a single cell is removed, and the extrusion of a modified cell using a three-dimensional CPM (Chapter 4).

The CPM is a model that minimises a global energy function which in turn produces cell-like behaviours. We use this minimisation component to approximate the “configuration” of cells at the minimum energy with three cell aggregate cases: micro-wounds (Chapter 2 and 4), cell clusters (Chapter 3) and a single cell extrusion (Chapter 4).

1.2 EPITHELIAL CELLS

Epithelial cells have been investigated for their morphology, cell proliferation, migration, transformed cells, contribution to embryonic development , wound healing, cell extrusions and the homeostasis of the epithelium (Abreu-Blanco et al., 2012; Arwert, Hoste, & Watt, 2012; Eisenhoffer & Rosenblatt, 2013; Gu & Rosenblatt, 2012; Gu et al., 2015; Hogan et al., 2009; P. Martin & Lewis, 1992; Monier et al., 2015; Naszai, Carroll, & Cordero, 2015; Osterfield, Du, Schupbach, Wieschaus, & Shvartsman, 2013; Pang, Daniels, & Buck, 1978; Schleich, Abdulla, Summers, & Houyel, 2013).

The epithelium can consist of one or several layers of cells depending on its location in the body. The shape of the epithelial cells also depends on the location of the epithelium and can be classified as; squamous epithelial cells (flat cells), which cover surfaces such as blood vessels; cuboidal epithelial cells (as the name suggests cube-like or rounded shapes), which cover organs such as kidneys and glands; and columnar epithelial cells, which are found in areas such as the inside of the nose, intestines and taste buds. Packed layers of similar cell shapes can have either a single layer where the cells reach the basal lamina or be layered. In some parts the epithelium can be pseudostratified, which commonly occurs with columnar cells.

The epithelial cells form the epithelium with tight junctions using various proteins and molecules to provide cell adhesion between neighbouring cells. Epithelial cadherin (E-cadherin) is a transmembrane protein that mediates homophilic cell-cell adhesion to form cohesive cell-cell junctions and creates the adhesion between the cells (X. Liang, Gomez, & Yap, 2015; Niessen, Leckband, & Yap, 2011; van Roy & Berx, 2008). Lateral surfaces of epithelial cells have E-cadherin molecules distributed as clusters throughout the lateral surfaces where epithelial cells come into contact with one another (S. K. Wu, Budnar, Yap, & Gomez, 2014; S. K. Wu, Gomez, et al., 2014; Y. Wu, Kanchanawong, & Zaidel-Bar, 2015), see Figure 1.2. E-cadherin clusters also show distinct patterns of organisation within cell-cell contacts in simple polarised epithelia. In the apical region of contacts, E-cadherin clusters concentrate in a relatively immobile ring-like structure to form the adherens junctions, known as zonula adherens (ZA), see Figure 1.2. In contrast, within the lateral junctions located basal to the ZA, E-cadherin clusters undergo dynamic movements in the plane of the plasma membrane. These differences in cadherin motion reflect differences in the dynamic behaviour of the junctional actomyosin cytoskeleton (Moore et al., 2014; S. K. Wu, Gomez, et al., 2014).

The cytoskeleton is a network of protein filaments that form the structural frame of the cells commonly responsible for the movement of cells. In particular, the actomyosin cytoskeleton refers

to the collection of actin and myosin protein in the cells. Actin is a structural protein found in many cells with two particular forms; the globule form (G-actin) and filaments (F-actin). The actin interacts with myosin when contraction between the F-actin and the G-actin occurs. Myosin itself is known as a motor protein using the nucleotide ATP (adenosine 5-triphosplate) as a chemical energy source to interact with F-actin to generate mechanical energy and movement. There are a number of myosin varying in their size and activities; however, they are all classified as motor proteins (Edelblum & Turner, 2015; Lowe & Anderson, 2015).

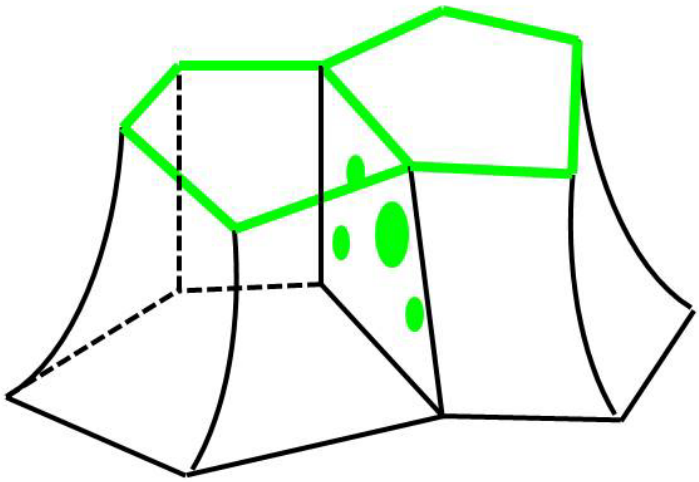

Figure 1.2. An illustration of E-cadherin (green) clusters on the lateral surfaces of the connected cells and ring-like formations on the apical region of the cells.

At cell junctions, cadherins mechanically couple the contractile cytoskeletons of neighbouring cells together, leading to the generation of junctional tension (Maître & Heisenberg, 2013). This is reflected in the concentration of actomyosin at both the ZA and lateral cell-cell junctions. However, the cortical cytoskeleton at the ZA is able to generate strong, sustained contractile forces, whereas stress-induced turnover of cortical actin leads to the dissipation of contractile stress at the lateral junctions (S. K. Wu, Gomez, et al., 2014). As a consequence, junctional tension at the ZA (hereafter referred to as line tension) is greater than that at the lateral junctions. Junctional tension has been demonstrated experimentally in a variety of systems, from Drosophila (fruit fly) and Zebrafish embryos to cultured cells (Fernandez-Gonzalez, Simoes Sde, Roper, Eaton, & Zallen, 2009; Hutson et al., 2003; A. C. Martin, Gelbart, Fernandez-Gonzalez, Kaschube, & Wieschaus, 2010; Ratheesh et al., 2012).

Changes in the line tension of the epithelium affects the morphology of the cells and the epithelial layer. One example is the growth of the tubular eggshell appendages of the epithelial cell layer covering Drosophila melanogaster (common fruit fly) egg. These forces occur with the

collection of myosin and Bazooka protein (Baz), and are hypothesised to have a role in generating the forces in the apical sheet of the epithelium (Osterfield et al., 2013).

The motility and migration of the epithelial cells is important for the movement of a single cell in the system and the interaction between both transformed and normal cells. Individual cells within aggregates of cells move randomly in the absence of chemical or adhesion gradients (Kabla, 2012; Mombach & Glazier, 1996).

There are a few experiments that can be used to investigate the motility of epithelial cells. One is the movement of epithelial cells up columns of varying sizes. Vedula et al. (2012) investigated epithelial cell migration and movement using the proliferation and growth of cells. It was found that cell migration through wide channels ($100\mu m$ or larger) produce large swirling motions and in narrower channels the cells migration is more directional with the contraction and relaxation of the cells to generate motility.

A second experiment that can be used to investigate the motility of cells utilises scratch assays. This experiment is closely related to macro-wound healing behaviour. A scratch assay experiment (see Figure 1.3) takes an epithelia monolayer and removes a large number of cells from the epithelia with a “scratch” (Motegi et al., 2003). This leaves two edges to investigate the leading edge of the epithelia as it moves to fill the empty space left by the scratch (C. C. Liang, Park, & Guan, 2007).

The cell behaviour is influenced by the adhesion and tensions within and on the cell junctions. Having discussed the structure of the epithelium and cells we now describe the two behaviours that maintain the integrity of the epithelium; wound healing and cell extrusion.

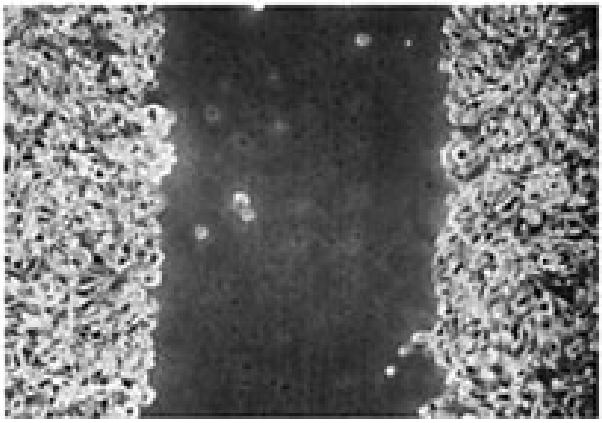

Figure 1.3. An example of a macroscopic wound scratch assay with an empty space in the centre and cell on either side. Adapted from "Role of the CD47–SHPS-1 system in regulation of cell migration," by S. Motegi, H. Okazawa, H. Ohnishi, R. Sato, Y. Kaneko, H. Kobayashi, K. Tomizawa, T. Ito, N. Honma, H. Bühring, O. Ishikawa, T. Matozaki, 2003, *The EMBO Journal, 22*(11), p. 2637. Copyright 2003 by John Wiley and Sons. Reprinted with permission.

1.2.1 Wound healing

Epithelia must preserve their barrier integrity despite a range of challenges, including cell death, injury, infection and cell division (Gomez, McLachlan, & Yap, 2011). In all these instances, cadherin junctions must reorganise without compromising tissue integrity. One noteworthy example here is the case of wound healing, which can be separated into microscopic wounds (see Figure 1.4a), where a small numbers of cells are damaged (e.g. one to several cells), or macroscopic wounds, where a much larger number of cells are damaged resulting in tissue injury (Sonnemann & Bement, 2011). We will only briefly discuss the large tissue injuries in relation to the mathematical modelling since this thesis is concerned with micro-injuries (micro-wounds).

Complications with epithelia wound healing can lead to complications in the body. Iizuka and Konno (2011) review the biology of wound healing in the intestines, given that some inflammatory bowel diseases may result from problems with the barrier function of epithelial cells (Laukoetter, Bruewer, & Nusrat, 2006; Sturm & Dignass, 2008). The healing of microscopic wounds may involve multiple mechanisms (Bement, Forscher, & Mooseker, 1993; Brock, Midwinter, Lewis, & Martin, 1996; P. Martin & Lewis, 1992; Radice, 1980; Sonnemann & Bement, 2011). One mechanism is the migration of cells from the edge of the wound into the injury space, a process that involves lamellipodial cell motility, which is the movement of the cells based on protrusions from the cell basal boundaries. A second mechanism entails the contraction of cells underlying the wound, which occurs when epithelia overlay other tissues, such as the epithelial tissue of the Drosophila (fruit fly) embryo. Thirdly, the cells at the margins of wounds can form an actomyosin ring (purse-string) that encloses the wound. Contraction of the purse-string then pulls neighbouring cells into the wound to drive wound closure (Abreu-Blanco et al., 2012; Antunes, Pereira, Cordeiro, Almeida, & Jacinto, 2013). The relative importance and coordination of these mechanisms differ depending on the system examined.

Microscopic wounds must be repaired for tissue integrity to be maintained. Experiments examining these wounds in the epithelia create the injury by killing cells using laser ablation on a small cluster of cells within the epithelium. Time-lapse imaging has revealed that the area of microscopic wounds typically changes in a non-monotonic fashion, first opening and then closing (healing) over a period of 10 minutes to 1 hour, shown in Figure 1.4b from Abreu-Blanco et al. (2012).

Unlike the scratch assay (see Figure 1.3), larger scale experiments examine wound healing with the removal of tissue from animals. While the experiments may vary, the experiments generally include surgically injuring a live animal, such as a rabbit's ear, and observing the healing

of the wound over the next few days (Chien & Wilhelmi, 2012; Van Den Brenk, 1956). These studies on much larger wounds, more in line with tissue wounding, are mathematically modelled with continuous models. For example, Sherratt and Murray (1990) used reaction diffusion equations to compare and fit the experimental results of Van Den Brenk (1956).

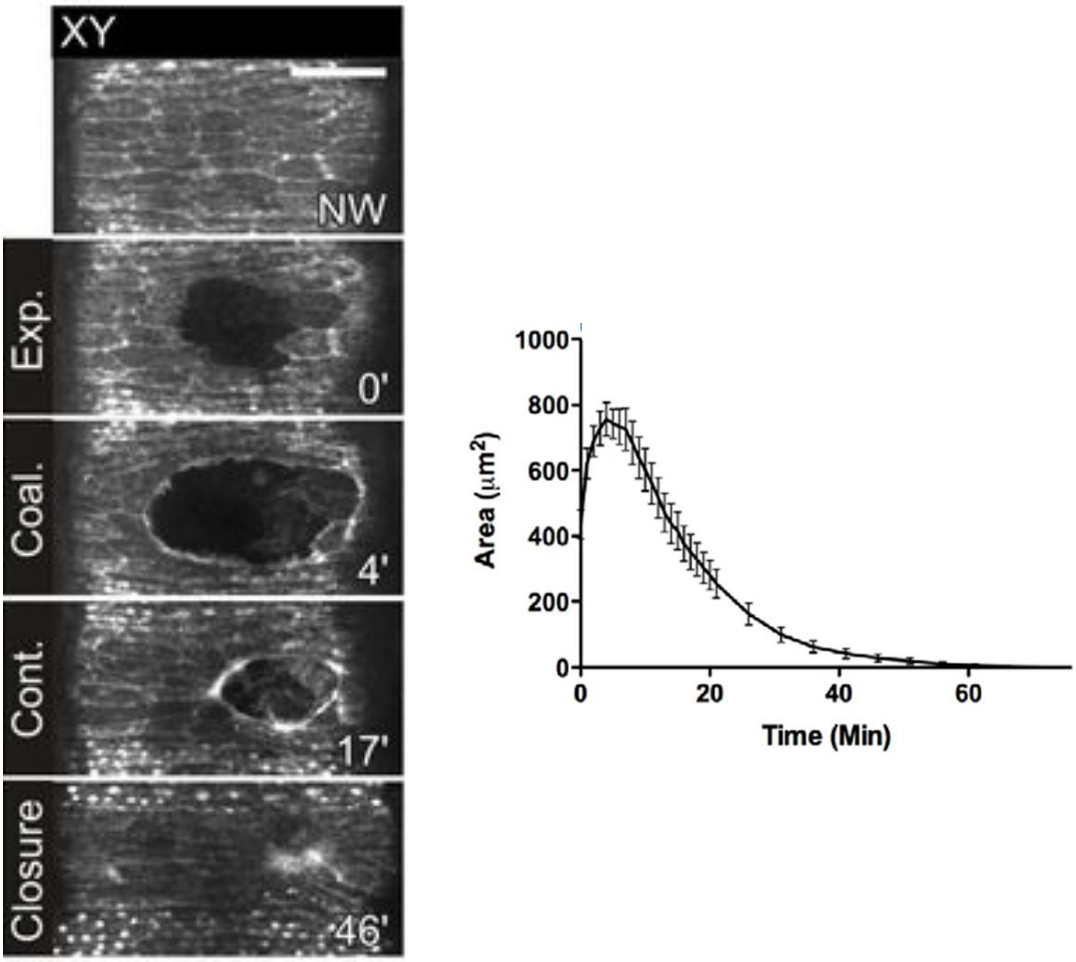

(a) (b)

Figure 1.4. a) An example of a microscopic wound healing in an epithelium from and b) a plot of a surface area of a wound against time, from Abreu-Blanco et al. (2012), showing an initial expansion and eventual closure of the wound. Adapted from "Drosophila embryos close epithelial wounds using a combination of cellular protrusions and an actomyosin purse string," by M. T. Abreu-Blanco, J. M. Verboon, R. Liu, J. J. Watts and S. M. Parkhurst, 2012, *Journal of Cell Science*, *125*(24), p 2. Copyright 2012 by The Company of Biologists Ltd. Reprinted with permission.

1.2.2 Cell extrusion from epithelial layers

In addition to wound healing, cell extrusion is another cellular mechanism that helps to maintain the integrity of the protective epithelial layer, see Figure 1.5a. Epithelial cells have a high turnover rate (Blanpain, Horsley, & Fuchs, 2007; Hooper, 1956; Pellettieri & Sanchez Alvarado, 2007), allowing the protective layer to replace extruded cells in the system to keep the barrier operational. The extruded cells could be old, dead or dying cells, or be extruded by the natural process of apoptosis to maintain the homeostasis of the system (Andrade & Rosenblatt, 2011; Denning, Hatch, & Horvitz, 2012; Eisenhoffer et al., 2012; Marinari et al., 2012; Meghana et al., 2011; Muliyil, Krishnakumar, & Narasimha, 2011; Rosenblatt, Raff, & Cramer, 2001). A diagram of the extrusion of a dying and live cell due to damage or overcrowding from Eisenhoffer and Rosenblatt (2013) is in Figure 1.5a. Disruption of the extrusion process can lead to a void forming in the epithelia which is a failure of the protection function of the epithelial barrier (Marshall, Lloyd, Delalande, Nathke, & Rosenblatt, 2011; Slattum, McGee, & Rosenblatt, 2009).

Apoptosis is one of the ways in which the epithelia naturally turn-over cells in the system. Apoptosis is a process in which the cells are extruded from the epithelium. However, cells extruded by apoptosis are not necessarily dead cells but can be alive when extruded (Eisenhoffer et al., 2012; Marinari et al., 2012) and later die (Frisch & Francis, 1994; Reddig & Juliano, 2005; Taddei, Giannoni, Fiaschi, & Chiarugi, 2012).

Cells can extrude both apically or basally (Hogan et al., 2009), and basal extrusion is referred to as delamination. Cells in vertebrates are typically extruded apically, while in Drosophila (fruit fly) the cells extrude basally (Marinari et al., 2012; Muliyil et al., 2011). Signalling pathways and molecular alterations can determine if a cell is extruded apically or basally (Slattum et al., 2009).

It was found that overcrowding in an epithelial layer can increase the amount of live cell extrusion (Eisenhoffer et al., 2012). Overcrowding is one mechanism that can influence the process of apoptosis; particularly the rate of the cell extrusion seems to be influenced by the pressure in the system or the number of cells in the system. Figure 1.5b from Marinari et al. (2012) shows the increase in the number of extruded cells over time for different pressure in the system due to overcrowding.

An alternative to overcrowding causing the extrusion of cells from an epithelium is the formation of an actin and myosin IIA ring. This ring is formed around a cell by its neighbouring cells and the contraction of this ring ejects the cell from the epithelium (Slattum et al., 2009).

Typically, a cell, which is about to die, signals its neighbours by using sphingosine-1 phosphate (S1P) (Gu, Forostyan, Sabbadini, & Rosenblatt, 2011).

Wang et al. (2011) suggest that intestinal epithelial shedding does not depend on the formation of the actomyosin ring in the live neighbourhood of cells. Apical cell deformations depend largely on the internal forces of the cells rather than the external cell forces generated by extension of neighbouring cells. An in vitro actomyosin ring is formed for extrusion, but in in vivo the cells are extruded much faster and leave a transient gap that eventually closes.

The author could not identify any studies using the CPM to investigate the extrusion of cells, in particular the extrusion of only a single cell. However, there are studies that concentrate on the invasion of cells into cell clusters or a monolayer.

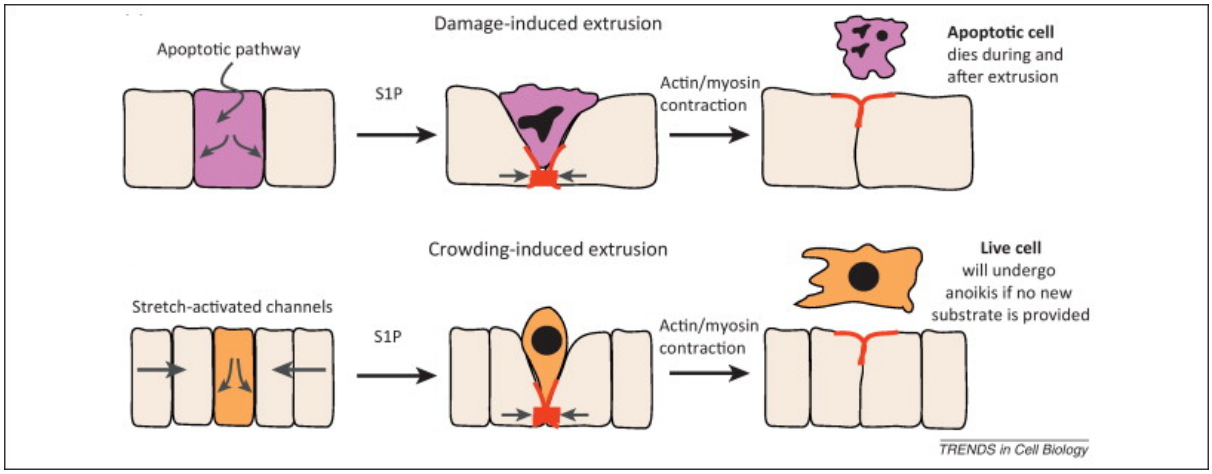

(a)

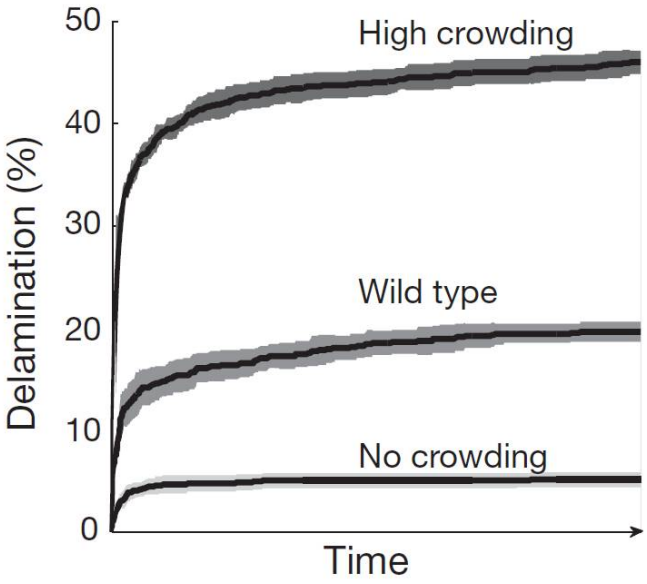

(b)

Figure 1.5. a) An illustration from Eisenhoffer and Rosenblatt (2013) of the extrusion of a live and apoptotic cell from the epithelium from the natural apoptosis process. Reprinted from "Bringing balance by force: live cell extrusion controls epithelial cell numbers," by G. T. Eisenhoffer, J. Rosenblatt, 2013, *Trends in Cell Biology, 23*(4), p. 187. Copyright 2013 by Elsevier. Reprinted with permission. b) Plot from Marinari et al. (2012) showing that overcrowding in the epithelium leads to an increase in the number of extruded cells (delamination). Reprinted from "Live-cell delamination counterbalances epithelial growth to limit tissue overcrowding," by E. Marinari, A. Mehonic, S. Curran, J. Gale, T. Duke, B. Baum, 2012, *Nature, 484*(7395), p. 544. Copyright 2012 by Springer Nature. Reprinted with permission.

1.3 MATHEMATICAL MODELS OF CELLS

Mathematical models are able to describe cell biology at various scales, for example the macro-scale of tissue where cells are un-identifiable, to the micro-scale of the inner workings of a single cell. In-between these two scales is the multicellular level, describing collections of cells identifiable from each other, which can number from one to a few thousand cells. The multicellular level can be simulated with different mathematical models. The cellular Potts model (CPM) represents the cells as a collection of pixels and applies an energy function to represent different system mechanisms, see Figure 1.6a. The vertex model is similar to the CPM but represents the cells as vertices and edges, to which equations of motion can be applied, see Figure 1.6b. Agent based models represent the cells as individual agents in a system with rules applied to their random motion (random walkers), see Figure 1.6c. Alternatively, diffusion equations and other continuous models commonly represent the population of cells rather than individually identifiable cells described by the models above. Other models may be a variation or combination of the models mentioned.

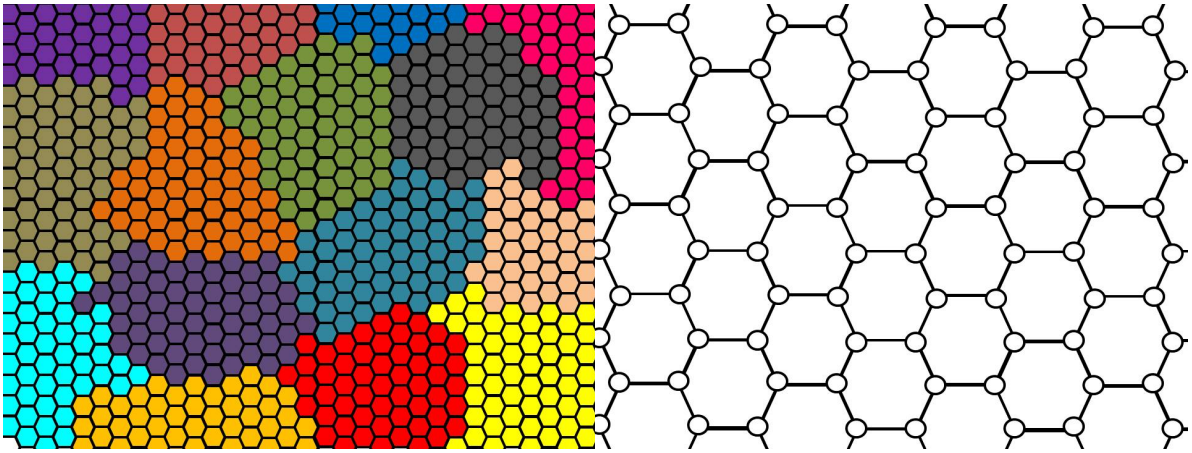

(a) (b)

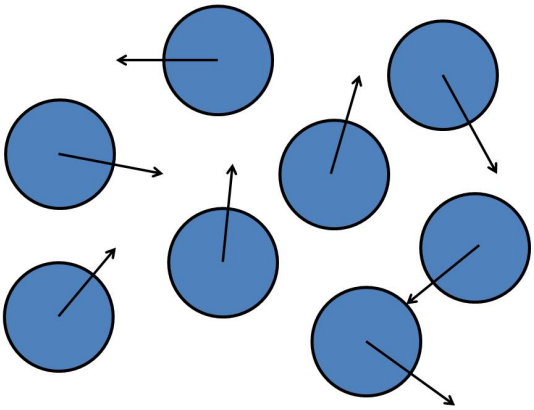

(c)

Figure 1.6. Visual representation of cells for three discrete models: a) cellular Potts model, b) vertex model and c) agent based (random walkers).

1.3.1 Cellular Potts model

The CPM is a lattice-based cellular automata using label changing pixels developed in 1992 by Grainer and Glazier (Graner & Glazier, 1992). The model was extended from the Potts model, developed by Potts (Domb & Potts, 1951), which is also an extension of the Ising model of magnetisation, developed by Ising in 1925 (Ising, 1925). The CPM represents the cells as groups of similarly labelled pixels on a set lattice and minimises a Hamiltonian function,

$$H = \sum_{(\sigma(i),\sigma(j))\ \text{neighbours}} J\left(1 - \delta\big(\sigma(i), \sigma(j)\big)\right) + \sum_{\alpha} \lambda\big(A_\alpha - A_p\big)^2,$$

otherwise referred to as an energy function. The energy function above contains two main mechanical representative components: a surface area interaction which refers to the Kronecker delta counting term which specifies an energy value, J, on the boundary of the pixels at position i and j with labels, σ; and an area constraint with an energy value λ for each cell, α, for the square difference between the cell area, A_α, and preferred area, A_p. The CPM was first used as a cell sorting model of two different cell types and the structures they would create (Graner & Glazier, 1992).

The CPM applies a Metropolis algorithm (Metropolis, Rosenbluth, Rosenbluth, Teller, & Teller, 1953) to find a minimum energy configuration. The Metropolis algorithm was developed in 1953 as a sampling method to investigate equations of state for substances consisting of interacting individual molecules (Metropolis et al., 1953). The algorithm is implemented by selecting a lattice site (pixel) and changing its label to one of its neighbours labels. If the change in energy function is negative the change is kept, and if the change is positive the change is kept with a probability of $e^{-\Delta H/T}$ where T represents a noise parameter and is commonly referred to as "temperature" in the CPM. This is repeated for all the lattice sites and once completed is commonly referred to as a Monte Carlo step (MCS). In order to simulate the behaviour of the cells many MCS (or iterations) are implemented to achieve a cell configuration with a minimum energy.

The temperature parameter in the model adds noise into the system to adjust the model by enabling the movement of the cells, where low noise may direct the system to a cell configuration at a local minimum energy, while higher temperature values (high noise) can help the system reach a cell configuration at a global minimum energy. The temperature can be separated into three temperature ranges which change the cell formations. The temperature range 0 to Tn1 still has cells connected to one another, at Tn1 to Tn2 cells begin separating from one another and at larger than Tn2 the cells pixels begin to separate from one another (Glazier & Graner, 1993; Graner & Glazier,

1992). Although some models are able to identify the temperatures appropriate for the model, the temperature is dependent on the model and the energy components used in each model. The “speed” of the system can also be influenced by the temperature, as the system may reach equilibrium with fewer MCS at higher temperatures (Glazier & Graner, 1993; Graner & Glazier, 1992). The simulated cells can break down at very large temperatures and noise values due to the cell pixels separating from each other (Marée, Grieneisen, & Hogeweg, 2007; Schleich et al., 2013; Summers, Abdulla, & Schleich, 2014).

The CPM is commonly set up as a sequential iteration to avoid inconsistent updates which may occur with parallelising. Parallelising the code involves separating the lattice into domains and each domain is updated simultaneously. Problems occur when two pixels (lattice sites) that are in contact, but in separate domains, attempt to change. While this problem may decrease the accuracy and MCS (iterations), it does not affect the final equilibrium solution achieved at the end of the simulation (Chen, Glazier, Izaguirre, & Alber, 2007; Tapia & D'Souza, 2011).

The programming of the model is largely dependent on the proficiency and quality of the equipment. Chen et al. (2007) report that parallelising allows the model to handle 107 cells. Tapia and D'Souza (2011) reported the model being able to handle 256^3 lattice sites and 106 cells with 25 node clusters when using consumer-grade computer graphics cards. It has been suggested that this parallelisation of the model will be included in the open source code CompuCell3D.

CompuCell3D (Swat et al., 2012) is a program, and code, available online to provide a common, up-to-date, code for similar cell studies by using a single source code in two and three-dimensions. However, the usefulness of the code depends on the research and study for which the model is used (Swat et al., 2012). The program and code allow the application of a volume constraint, line tension/adhesion, and contraction on the cell perimeter and surface areas and also includes a variety of chemotaxis fields. The CompuCell3D code is also available to model cell morphology, cell sorting, tumour growth, the vascular system, and cell invasion into a monolayer (Shirinifard et al., 2009).

Another collection of source code is the CHASTE (Cancer, Heart and Soft Tissue Environment) code (Mirams et al., 2013; Pitt-Francis et al., 2009) which is similar to the CompuCell3D, but focuses on including a wider range of models, including agent-based, vertex models and variations of these models.

Given the CPM represents cells as groups of pixels it can be used to investigate the morphology of the cells, such as the morphology of embryo development (Merks & Glazier, 2005), tumour growth (Shirinifard et al., 2009), and vascular systems (Shirinifard et al., 2009). Any study

using the CPM allows the morphology of the cells and the effect on the cell shape from different mechanisms to be investigated. While the cell shape can be affected by mechanical components of the system, certain artefacts can arise in the models that use specific pixels (Marée et al., 2007). Typically, square or hexagonal pixel shapes are chosen to tessellate the area. For example, part of Marée et al. (2007) use the CPM to study cell shapes and artefacts resulting from the pixel shapes. In certain systems the cells can form hexagons with hexagonal pixels, whereas square pixels can form rectangular cells.

In addition to studying the cell morphology, Marée et al. (2007) also used the CPM to study cell motility and movement with applied chemotaxis. Chemotaxis is commonly referred to as the extra external influence added to the simulated cells in the CPM using chemical and force fields. This influence is commonly added using diffusion or partial differential equations acting on the centre of mass of the simulated cells. These fields can either be fixed in the system or influenced by the movement of the cells.

Chemotaxis is not the only mechanism to influence the cell motility. Alternatively, the motility can be included as an internal mechanism of the cell, such as including it as an additional term in the energy function. Kabla (2012) uses a two-dimensional CPM that focuses on the interaction between two “species” of cells and their motility. While maintaining the traditional energy function components of an area constraint and cell-cell surface junctional interactions, a motility mechanism was added to the function to influence the cell’s movement based on its movement history. The paper investigates the movement of the cells collectively, the influence of leading cells on the other cells in the monolayer and their influence on the invasion of cells in clusters of similar cell species.

While the CPM is commonly used in two dimensions there are studies that require the model to be in three dimensions. Shirinifard et al. (2009) apply a three-dimensional CPM using a basic energy function of volume and surface area energy to simulate tumour growth and angiogenesis. The paper examines how tumour growth can affect blood vessel growth and deformation and the morphology of the tumour growing in such an environment. The study applied additional mechanisms such as chemical fields, chemotaxis, and the proliferation of cells for the tumour growth.

While various authors suggest the CPM can simulate wound healing, common practice has been to investigate the closure of much larger wounds (Scianna, 2015) which can be compared with the scratch assay experiments mentioned previously. These wounds would be considered to be

macro-wounds on the cellular level; however, there is little to no literature on using the CPM to investigate the smaller micro-wounds of one to several cells in size, as examined in this thesis.

1.3.2 Vertex model

The vertex model has some similarities to the CPM. Cells are defined with vertices and edges, rather than pixels, and the system either applies a Hamiltonian energy function with simulated annealing similar to the CPM, or applies equations of motion and other mechanics. While the Hamiltonian energy function may be similar to the CPM, there are additional complications that the model needs to address. For example, vertices of the cells can interact to "combine" with one another, cells can come into situations where arrangement of two interacting vertices need a larger swap than is generated with the annealing, cells can disappear, or the edges of an individual cell can cross each other.

The complications that can arise from the movement of the vertices are addressed with three main vertex operators or swaps that occur in order for the vertex model to form and break bonds (Fletcher et al., 2013; Honda & Eguchi, 1980; Nagai & Honda, 2001). There can be slight differences and variations to these operators depending on the variables in the vertex model. A T1 swap (or edge rearrangement) occurs when two vertices are located within a minimum distance, d_{min}, from each other. The vertices are rearranged as shown in Figure 1.7a, from Fletcher et al. (2013), and placed at a separating distance, d_{sep}, from one another. The separation distance is calculated by a coefficient, k, multiplied with the minimum distance where k is referred to as the separation ratio. This swap can also occur on the boundary of the monolayer shown in Figure 1.7a. A T2 swap (or element removal) occurs when an enclosed area (usually triangular in shape) falls below a minimum area, A_{min}. All vertices then combine and the area disappears. If the area represented a cell, the cell is removed from the simulation (see Figure 1.7b from Fletcher et al. (2013)). If the two vertices are only identified with one cell, then they combine into one single vertex if the distance between the vertices is less than d_{min} (see Figure 1.7b from Fletcher et al. (2013)). A T3 swap (or element intersection) occurs when free moving boundaries in a void interact with a different edge. This is particularly important when modelling wound closure so that the monolayer can reconnect with itself. Fletcher et al. (2013) refer to four different cases where this T3 swap could happen and expresses them in Figure 1.7c. Each time there is an interaction, the vertices must be at least distance, d_{min}, away from any other vertices. If there is no space on the cell edge, then all vertices are moved so that they are distance, d_{sep}, from each other.

To avoid self-intersecting cells (a cell's edges crossing), Fletcher et al. (2013) introduced a new kind of rearrangement, node switching. Node switching (or internal element intersection)

occurs when a cell's vertices arrangement causes the cell edges to intersect with one another. If this occurs Fletcher et al. (2013) suggest that there is only a resolution if the intersection does not cause the cell to split into two cells (see Figure 1.7d). However, this situation will only happen for some force laws where cells can become concave (Fletcher et al., 2013).

The vertex model commonly has straight edges between the vertices; however, Ishimoto and Morishita (2014) have included cell curvature using the assumption that there are fast and slow dynamics in the system. The curvature expressed in Ishimoto and Morishita (2014) identifies the edges of the cell to minimise tension in both cells that the edge belongs to. The model also assumes that the curvature edges are controlled by fast dynamics and the vertices by slow dynamics. Adding this curvature allows the T2 swap rearrangement to change, since the curvature allows the system to have a cell with a minimum of two vertices, whereas the cell would not be considered without this curvature. Slow dynamics involve the movement of the vertices in accordance with an energy function and fast dynamics involve the minimisation of the energy to apply the curvature of the edges given the "pressure" between the cells. The vertices move first and the curved edges of the cells are applied after.

Working in three spatial dimensions, and representing the cells as a three-dimensional object, adds extra computational costs to the use of the vertex model (Fletcher et al., 2013), and together with the vertex rearrangements, T1, T2 and T3, the result is that only a smaller number of cells can be simulated in the system.

Traditionally, the vertex model can be used in three dimensions by allowing the cells to contain the volume with vertices, edges and surfaces areas interacting with other cells. An alternative way to implement the vertex model is to include a two-dimensional sheet of epithelial cells which can move in three dimensions. Du, Osterfield, and Shvartsman (2014) use a two-dimensional vertex model representing a sheet of epithelial cells in a three-dimensional environment. The paper investigates three-dimensional structures that can arise from the forces and mechanical properties of cells. These mechanical properties include cell area, membrane elasticity and line tension, which could also be referred to as adhesion between the cells, and a final term describing the bending of the sheet (membranes), also used in Seung and Nelson (1988).

The application of the vertex model to study the biology of cells is similar to the CPM. Wyczalkowski, Chen, Filas, Varner, and Taber (2012) provide an overview of a wide variety of biological cell topics with a focus on morphogenesis and the mathematical models that can be used to investigate them, such as the vertex model and mechanical mechanism models. In many ways the cell representations of the two models are similar. Much like the CPM, the vertex models' cell

shape representation allows it to be used to investigate the morphology of the simulated cells. However, unlike the CPM, the cell edges are represented with straight lines or surfaces and so the cell morphology falls into a classification of polygonal structures. Weliky and Oster (1990) investigate the rearrangement (morphology) of cells with an early iteration of the vertex model that uses a mechanical basis, namely the elastic tension in the cell membranes and the pressure in the cells. Farhadifar, Roper, Aigouy, Eaton, and Julicher (2007) on the other hand use a vertex model to investigate the morphology of a sheet using an energy function with an area constraint, perimeter contraction, proliferation and line tension or adhesion. The study investigates the polygonal shape of the cells influenced by the different mechanisms and the comparison to the shapes of actual epithelial cells.

Y. Li, Naveed, Kachalo, Xu, and Liang (2011) use a model based on the vertex model to investigate topology changes and distortions in sheets of cells, but focus on the mechanical forces of pressure and tension with the addition of proliferation. The study found that the mechanical forces exert a larger influence than local proliferations on the behaviour of the cells.

As mentioned previously, Nagai and Honda (2009) investigate micro-wounds using a vertex model with the implementation of equations of motion. The energy equation includes three main components: an area constraint for the cells, an interaction between cell junctions, and a negative linear wound area constraint. However, the use of a negative wound area term in the study facilitated the system closing the wound.

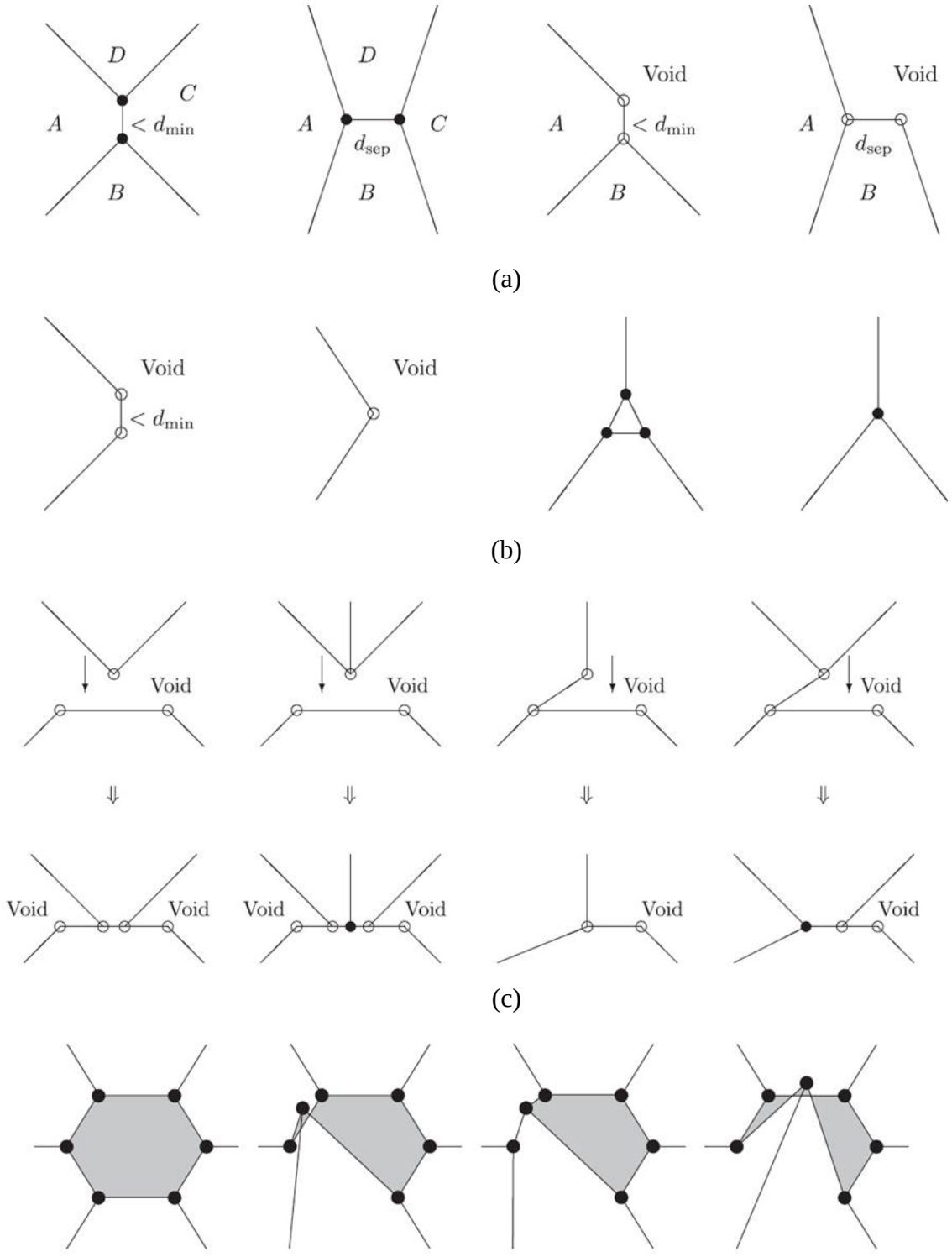

Figure 1.7. An example of the transitions of the vertices for the a) T1 (edge rearrangement), b) T2 (element removal), c) T3 (element intersection) and d) swaps to prevent self-intersecting cell edges. Reprinted from "Implementing vertex dynamics models of cell populations in biology within a consistent computational framework," by A. G. Fletcher, J. M. Osborne, P. K. Maini, D. J. Gavaghan, 2013, *Progress in Biophysics & Molecular Biology, 113*(2), p. 306-308. Copyright 2013 by Elsevier. Reprinted with permission.

1.3.3 Agent-based models

Instead of identifying cell boundaries and shapes using the CPM and vertex models they can be described by the location of their centres and classified as single entities. These models are often referred to as agent-based models or otherwise as random walker models. The agent-based models apply rules and probabilities to the agent's movements and random walks to replicate different mechanisms and properties of the cells. Random walker models can be expressed in any number of dimensions and as an on-lattice or off-lattice system; however, cells are restricted to three spatial dimensions.

A basic random walk has an agent on a one-dimensional lattice at site i. The agent is given a probability to move from site i to either site $i + 1$ or $i - 1$ with equal probability of 0.5, the agent completes its move and the process starts again. Modelling a collection of cells would require more agents in the system and considering interactions between them. The exclusion process is a simple mechanism that prevents cells from occupying the same lattice site (Chowdhury, Schadschneider, & Nishinari, 2005). A cell's movement from site i to site j is rejected if site j already contains an agent. This type of exclusion assumes only the agent has no knowledge that another agent already occupies the site. Alternatively, the agent can ignore that particular movement and adjust its probabilities to select a different movement (Landman & Fernando, 2011).

The exclusion process is only one of the rules that can be applied to the agents. Other rules can include the interacting connectivity between cells, such as the formation, breaking and maintaining of connections between agents (Deroulers, Aubert, Badoual, & Grammaticos, 2009; Fernando, Landman, & Simpson, 2010) as well as the movement based on population density surrounding the agents (Simpson, Landman, Hughes, & Fernando, 2010).

Many variations of a random walk can be implemented by adding boundaries, obstacles or defining specific rules that the random walker must follow (Rudnick & Gaspari, 2010). An example of this is where agents do not have to follow the same rules as each other, and can be split into different "species" with different probabilities of movement. Simpson, Landman, and Hughes (2009) and Landman and Fernando (2011) look at two different "species" of agents and their interaction when diffusion occurs in different configurations.

The random walker models provide one component able to be linked to continuous diffusion equations. A diffusion equation can be derived from the random walker probabilities using standard conservation arguments (Liggett, 1999). Providing the diffusion coefficient, from a linear or nonlinear diffusion, is positive, the quantitative connection between the discrete random walkers and continuous diffusion equations are similar (Fernando et al., 2010). This means that the

probabilistic rules that are applied to discrete agents can also be investigated in the diffusion equations that describe the populations of the cells.

1.3.4 Diffusion and other models

While there are variations to the discrete models discussed above, there are alternative models such as continuous diffusion models and hybrid models that combine different components of models to explain a natural phenomenon. Continuous diffusion models treat the populations of the cells as a density rather than as the individual cells in the discrete models, and the cell interaction is treated or assumed in the model as a diffusion coefficient or other such mechanisms.

The Fisher-Kolmogorov equation (Fisher, 1937; Murray, 2002) is a reaction diffusion equation model that has been used to study a variety of biological mechanisms and behaviours, such as wound healing (Sherratt & Murray, 1990) and tissue repair (Cai, Landman, & Hughes, 2007). However, this equation has been included as part of modelling macro-wound healing rather than the focus of this thesis which is micro-wound healing. A simple one dimension representation of the equation is written as

$$\frac{\partial u}{\partial t} = D\frac{\partial^2 u}{\partial x^2} + ku(1-u),$$

where the variables and parameters represent the population density of cells, u, at a position, x, at time, t, with a cell diffusion coefficient, D, and cell proliferation rate, k. The equation is separated into two components, namely the diffusion term (containing the random motility of the cells) and the limiting proliferation growth term. Initially the model was used to represent the diffusion (spatial spread) of an advantageous gene through a cell population (Fisher, 1937). The propagation wave solutions to the Fisher-Kolmogorov equation and variants are quantitatively comparable to the propagation of the epithelial cells (or epithelium edges) into empty spaces, such as wounds (Maini, McElwain, & Leavesley, 2004; Sherratt & Murray, 1990).

An application of the reaction diffusion model is presented in Sherratt and Murray (1990). In the study, wound healing is investigated where one case of the model is a linear Fickian diffusion with comparative equations to the Fisher-Kolmogorov equation above. While the study explains the model and its properties, the model is only compared to wound data from Van Den Brenk (1956). However, further studies using the diffusion model investigate the differences between embryo and adult wound healing, focusing on an actin cable closing the wound and the regulation of cell division, the effect of other auto-regulation of mitosis and the effect of wound shape on the results of the model (Sherratt, Martin, Murray, & Lewis, 1992; Sherratt & Murray, 1992).

On a population-scale the Fisher-Kolmogorov equation, model or other variations of the model, capture parts of the epithelium behaviour such as the shape and speed of a traveling wave of the epithelium closing edge of a wound assay. However, discrete models, such as random walkers, can also model these behaviours as well as other mechanics such as contact inhibition of cells with their neighbours (Cai et al., 2007). While one of the more important differences between the discrete and continuous equation is time, it is possible to extract population-scale continuum equations from the discrete models. One example of this is random walker derivation to a linear and nonlinear diffusion equation using transition probabilities (Cai et al., 2007; Liggett, 1999). The nonlinear diffusion equations derived from the contact rules, transition probabilities, of the random walker process can be nontrivial (Liggett, 1999). Another example is the CPM itself using transition probabilities of the cells changing from one state to another which can be equivalent to the Keller Segel model (Alber et al., 2007). However, these modifications are dependent on the various rules set for the cells' motions and properties and can be nontrivial.

These reaction diffusion models are not limited to the physical representation of cell populations but can also be implemented to represent the effects of other component concentrations of the epithelial cells. An example is the application to the intracellular dynamics of Mitogen Activated Protein Kinase (MAPK) which Posta and Chou (2010) represent with four concentrations: Epithelial Growth Factor, Epithelial Growth Factor Receptor, Reactive Oxygen Species, and protease. The model investigates the intracellular signalling of wound healing, specifically the activations of MAPK during the process.

As an alternative to the continuous reaction diffusion equation models, the hybrid models incorporate the discrete representation of cells and other continuous model mechanics. Cumming, McElwain, and Upton (2010) present a general hybrid model framework that investigates macro-wound healing and scarring based on the work of Dallon, Sherratt, Maini, and Ferguson (2000); Dallon, Sherratt, and Maini (1999, 2001) and McDougall, Dallon, Sherratt, and Maini (2006). Cells are represented as individual agents, similar to the random walker models. The cell movement and behaviour is based on their interaction with fibrin and collagen represented with a density for their concentration and a tensor for their orientation. The concentrations change with the influence of cells, other concentrations and other properties such as tPA concentration, TGF-Beta concentration, macrophages and fibroblasts. In addition to simulating the closure of a wound, the model also represents the scarring of the wound, associated with the orientation and invasion of collagen into the wound.

Generating reaction diffusion equations can depend on what properties of the cell are of interest. Armstrong, Painter, and Sherratt (2006) developed a continuous model using adhesive

forces to replicate cell sorting behaviours for a single cell and multiple cell populations as an alternate to the discrete models such as the CPM. They classify the pattern formation of two interacting populations in four cases depending on the strengths of the adhesion. These cases include the mixing of both populations, engulfment of one population with another, partial engulfment, and complete cell sorting. This model has been used to investigate cellular invasion in cancer and tumour development (Painter, Armstrong, & Sherratt, 2010). The ideas in Armstrong et al. (2006) were expanded on by Gerisch and Chaplain (2008) who also use a continuous model, although it is based on Anderson, Chaplain, L. Newman, Steele, and Thompson (2000).

As an alternative to representing the cells as continuous populations, or as the discrete models discussed above, the epithelium and cells can be considered to be elastic material. There are models and hybrid models developed around this concept. Abate et al. (2012) use vertex geometry to represent the cells and elasticity components rather than a Hamiltonian equation, to investigate a two-dimensional layer on different topologies. Tabatabai, Eby, and Singh (2011) present a mathematical model that focuses on differential equations and the size of the macro-wounds, rather than the morphology or shape of the wound and neighbouring cells. Shraiman (2005) investigates tissue growth and models the cells with a continuous approximation of the elastic strain energy of the cells.

1.4 SUMMARY

While wound healing has been investigated with diffusion models for the larger cell population scale systems, it has rarely been applied to study the behaviour of smaller-scale wounds of around one to several cells. Although the vertex model from Nagai and Honda (2009) investigates a micro-wound, this applies mechanisms within the wound itself to close the wound rather than the interaction between the cells in the epithelium. Instead, we use the CPM as an alternative approach to the vertex model and apply an energy function containing the preferred cell area, perimeter contraction and the adhesion between the cells to examine how a monolayer of simulated cells will behave with a micro-wound in both two and three dimensions.

The protective property of an epithelium not only closes wounds but also extrudes cells from its layers. The extrusion of cells has previously been investigated using continuous models measuring populations rather than the discrete models (Scianna, 2015); however, there are few studies that focus on the extrusion of a single cell.

This thesis models the collective behaviour of epithelial cells using our own code developed for a two and three-dimensional cellular Potts model (CPM) rather than the available CompuCell3D and CHASTE source code. By using our own code we are able to examine the model in detail and introduce and manage additional mechanisms and measures that are not available in the published code. However, the difference between our code and the CompuCell3D and CHASTE source code is not the aim of the thesis. The two and three-dimensional CPMs are used to investigate the effect of the interaction between the adhesion and contraction of the cells on the behaviour of the epithelia during the closure of micro-wounds and the extrusion of a single cell. While there are components of biological cells, such as actin and myosin, that impact cell behaviour, there is a lack of biological data to directly compare to the CPMs. The models in this thesis are intended to motivate and allow further investigation into the mechanisms occurring in cell behaviour.

Chapter 2: Simulating Epithelial Wound Healing and Cell Islands Using a Two-Dimensional Cellular Potts Model

2.1 INTRODUCTION

The closure of a wound is fundamental function of the epithelial cells. To achieve wound closure the junctions of the cells are governed by proteins, such as actin, myosin and cadherins. These proteins lead to the generation of adhesion between cells and contraction of the junctions. The types of mechanisms used to close a wound include the migration of cells from the edge of the wound into the injury space, a process that involves lamellipodial cell motility. A second mechanism involves the contraction of cells underlying the wound, which occurs when epithelia overlay other tissues, such as the amnioserosa of the Drosophila embryo. Thirdly, the cells at the margins of wounds can form an actomyosin ring (purse-string) that encloses the wound. Contraction of the purse-string then pulls neighbouring cells into the wound to drive wound closure (Abreu-Blanco et al., 2012; Antunes et al., 2013). The relative importance and coordination of these mechanisms differs depending on the model system tested and its developmental context.

The cellular Potts model (CPM) developed by Glazier and Graner (1993) and Graner and Glazier (1992) and its off-lattice alternative, the vertex model (Fletcher, Osterfield, Baker, & Shvartsman, 2014; Nagai & Honda, 2001, 2009), are computational algorithms designed to represent cell organisation at small scales (from a few to hundreds of cells). They are particularly suited to study the dynamics of such systems in the presence of microscopic wounds. However, a potentially significant difference between the two models lies in their representation of cell edges. The CPM allows for arbitrary edges, whereas, by definition, the vertex model utilizes straight cell edges, or in certain variants curved boundaries with constant curvature (Ishimoto & Morishita, 2014). We use the CPM to investigate microscopic wound repair and the interactions of adhesion and contraction that influence the repair process. Minimisation of the energy of the CPM using Metropolis Sampling leads to two different regimes, and the boundary between these regimes depends on the relative contribution of adhesion and line tension to the energy function of the system. When applied to microscopic wounds, the interaction between contractile junctional tension and adhesion between the cells plays an important role in determining whether a site of damage will monotonically increase and stay open or whether it will close and heal. Moreover, our theoretical analysis predicts that in the hard regime, there is a critical wound size above which the wound will

not close. Thus, our data suggest that changing the balance between contraction and adhesion at the cell-cell junctions is required for non-monotonic wound closure to occur.

This chapter is an altered version of the Noppe, Roberts, Yap, Gomez, and Neufeld (2015) paper which models a micro-wound with a two-dimensional CPM and provides a geometrical approximation model to help understand some of the mechanisms influencing epithelial behaviour.

2.2 TWO-DIMENSIONAL CELLULAR POTTS MODEL

We model the epithelial cell layer and micro-wounds in two dimensions using the CPM. The CPM represents the apical region of cells, the sites where the zonulae adherent are located, as collections of pixels on a lattice (Kabla, 2012; Szabo et al., 2010). Depending on which cell they belong to, each pixel is assigned a cell index j (represented by different colours in Figure 2.1). The modelled cells evolve in time by randomly selecting a pixel, from a list without replacement, at the boundary between two cells and measuring the change in an "energy" function E that would result if the pixel were reassigned to a neighbouring cell. If the energy decreases, $E \leq 0$, the index change is always allowed, whereas if the energy increases, $E > 0$, the site index change is allowed with the probability $exp(-\Delta E/T)$, where T is a temperature like parameter that controls the "noise" in the system. Each and every pixel is given the opportunity of an index change and this represents one Monte Carlo Step (MCS), which we refer to as a single iteration in the CPM. Changing the cell index of the pixels at the boundaries between neighbouring cells allows the cell boundaries to change.

The pixels in the CPM ideally need to tessellate and contain an equal number of connecting edges. The two-dimensional CPM adopted in this thesis uses hexagonal shaped pixels (triangular lattice). Other two-dimensional pixel shapes could include the square pixels (square lattice), or the triangular pixels. Each of the pixel and lattice configurations can be found in Appendix A. Other tessellated configurations could be used; however, non-uniform shapes in the model would require identifying and classifying each edge of the pixels in the model. In addition, the choice of the pixel shape can lead to artefacts being created in the system. An example of an artefact is identifying a cell with a collection of pixels with a minimum perimeter (membrane length). A square lattice would form rectangular cells (preferably a square), the triangular pixels would form a triangular shape and hexagonal pixels would form a hexagonal shape. Another consideration when selecting pixel shapes is the connection between pixels. Square and triangular pixels have corners which are only in contact with the corners, but not edges, of other pixels. Square pixels are commonly said to be only have contact with other pixel edges. When using these pixels shapes a decision needs to be made about whether the corners of the pixels will be a form of contact. However, the hexagonal pixels do not require this classification because the pixels only connect with edges.

An algorithm of the two-dimensional CPM is presented in Appendix B as additional material to explain the CPM algorithm described in this section.

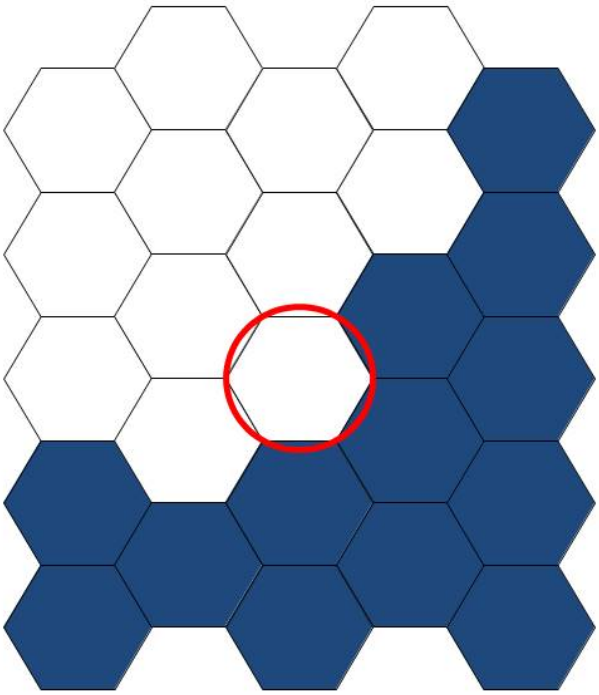

Figure 2.1. Representation of cells as groups of pixels on a hexagonal lattice where pixels change their labels to one of their neighbours. The hexagons of a given colour represent pixels belonging to the same cell.

To prevent the biologically unrealistic situation where a simulated cell may separate into multiple disconnected groups of pixels an additional constraint is added to the model to restrict pixel changes, specifically every cell is represented by a single connected pixel configuration. We refer to this as the "connection condition" in the model. Figure 2.2a is a diagram of a single pixel with its six neighbours; each pixel (site) is labelled with a number to identify it. Each of these pixels can be labelled with a cell label. Figure 2.2b is the simple initial example of a configuration of different labelled pixels, with labels A and B and blank pixels which can be labelled A or B or have a different cell label.

Two neighbouring pixels are connected if they have the same cell label, for example pixels 5 and 0 with label A in Figure 2.2b. Two neighbouring pixels are not connected if they have different labels, for example pixels 0 and 1 in Figure 2.2b. Non-neighbouring pixels do not share and edge, for example the pixels labelled B in Figure 2.2b. These two non-neighbouring pixels can be connected if there is an uninterrupted series of same labelled pixels connecting sites 1 and 3. For example, if site 2 has a label B then site 1 and 3 in Figure 2.2b are connected. Each cell is made up

of a single connected group of same label pixels, for example, pixels labelled A in Figure 2.2b can be defined as cell A. We use an initial configuration that satisfies the connection condition and apply an algorithm to the local pixel changes instead of checking the connection condition for every cell and pixel in the model.

The changed pixel label and its neighbouring pixels are checked to identify if a cell has split as a result of the change. If two pixels have the same label and are connected by a same label path, then the change is accepted. If two pixels do not have a path connected with the neighbours they may still be connected by a longer path around the neighbouring pixels, see Figure 2.2c. However, if the pixel label changes to a label of non-neighbouring pixels then this change is cancelled, for example in Figure 2.2d these are the pixels with the label B. If the label pixel site 0 in Figure 2.2c changes from label A to label B in Figure 2.2d, the change is not accepted. This change splits cell A into two groups because in Figure 2.2c cell B must be connected by some path around the other pixels but when site 0 changes to label B the cell B now surrounds one of the groups of cell A with no possibility for there to be a path connecting the separate pixel groups of cell A. So the change of site 0's label is cancelled.

The case of a different cell labelled pixel in Figure 2.2e, label C at site 2, is possible but unlikely in this model. All the cells try to maintain the same area and shape. So cell B must encase cell C or A to connect site 1 and 3. We can ignore this case and treat it as similar to the previous case. If site 0 was to change to label B, then the change is cancelled.

To simplify these cases, and identify them in the simulation code, we use the condition that if there are two similar labelled pixels (sites), and they are not connected by a path through the neighbours, for example in Figure 2.2b paths through sites 16543 or 123 for the pixels labelled B, then the change is cancelled.

The dynamics of the model are driven by minimising a phenomenological energy determined by the cell configuration. We use the same form of the energy function that has been previously used in models of cell-cell interactions (Farhadifar et al., 2007). In particular, the vertex model (Farhadifar et al., 2007) is based on a simplified representation of cells as polygons, and their shape is determined by tracking the movement of cell vertices. The total energy of a system of N-cells is defined in terms of the area A_j and perimeter L_j of jth cell through the sum,

$$E(A_j, L_j) = \frac{k}{2}\sum_{j}^{N}(A_j - A_p)^2 + \frac{\Gamma}{2}\sum_{j}^{N} {L_j}^2 - \frac{S}{2}\sum_{j}^{N} L_j. \qquad (2.1)$$

The first term represents an energy cost for deviating from a preferred area A_p, i.e. the cells resist expansion or compression. The second term models the contractile line tension due to the apical actin ring around the perimeter of the cells, while the last term represents cell-cell adhesion, attributed to the presence of adhesion molecules like E-cadherin, and is proportional to the perimeter of the cells. The parameters k, Γ and S determine the relative magnitude of the different contributions to the energy.

Note that the adhesion term is assumed to be negative, i.e. the cells preferentially expand their boundaries shared with neighbouring cells. However, this expansion competes with the contractile tension that dominates when the perimeter becomes elongated. For the pixel-based CPM the adhesion interaction term is commonly expressed using the double sum,

$$\sum_{i,j}^{N}\left(1-\delta_{\sigma(i),\sigma(j)}\right),$$

where σ are the site labels and the Kronecker delta term prevents counting contributions to the energy from pixels that belong to the same cell. This term counts the number of pixels on the edges of the cells and we use this to compute the perimeter L_j.

In order to eliminate "internal pressure" in the system we assume that the preferred cell area, A_p, coincides with the total area of the simulation domain divided by the number of cells, $A_p = A_T/N$, so that the cell layer is not compressed or stretched.

The initial cell configurations of all simulations in this chapter without a wound were generated by creating a configuration of 44 approximately 5×5 square pixel cells on a 160×160 pixel grid. This configuration was run with the parameters $k = 2$, the S and Γ ratio $\beta = 1$ and $T = 10$. These simulations generated cell configurations similar to Figure 2.3b. Simulations used these configurations and included required parameter values for k, S, Γ and T to obtain the observed results.

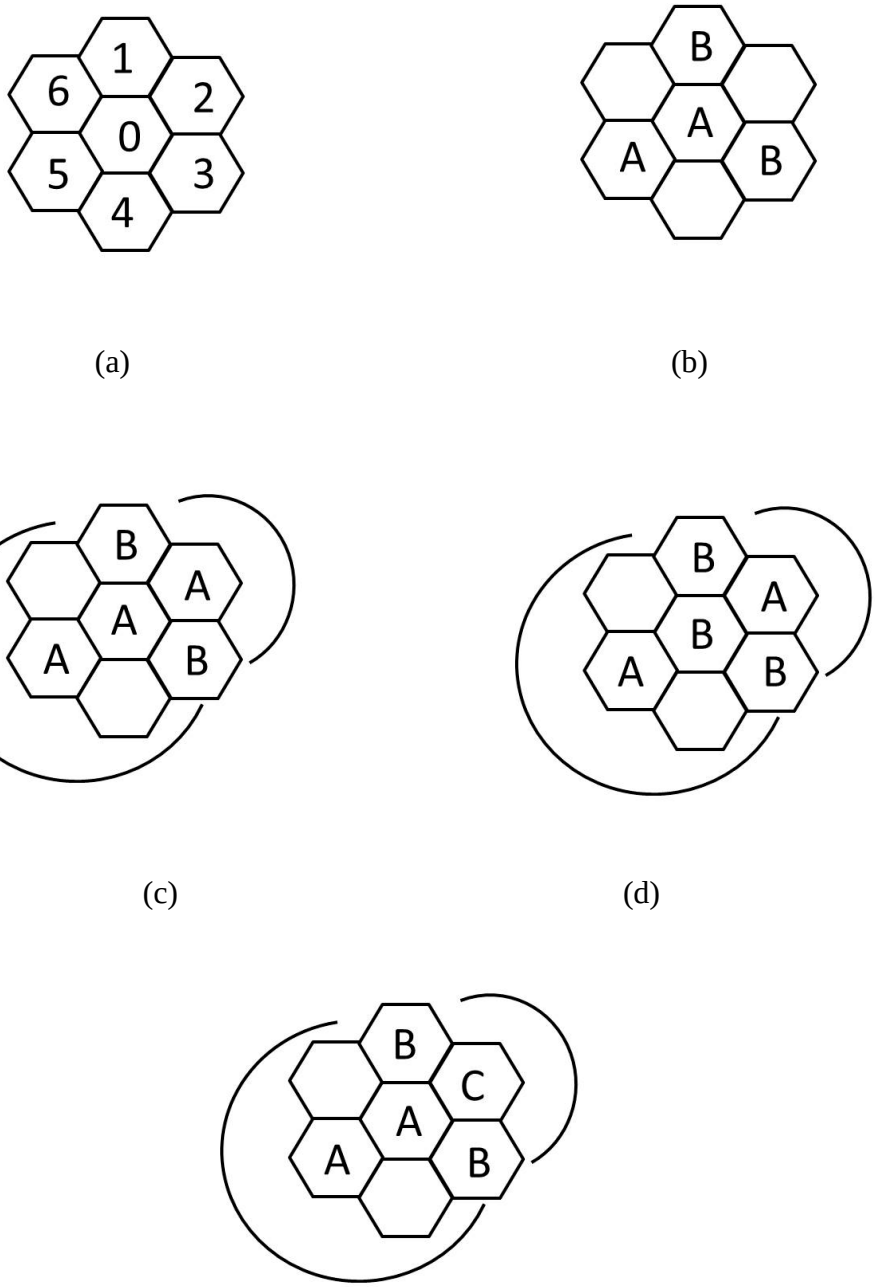

Figure 2.2. Diagrams of a single pixel with six neighbouring pixels surrounding it. a) Labels of the pixels (sites) with numbers from 0 to 6. b) The simple case of a configuration of two cells with label A and B. The case can change depending on the label of the empty pixel (sites). c-d) Shows a case of an initial pixel configuration in (c) and a change of configuration to (d) which would encase part of the cell A no matter how cell B is connected. This change is not allowed. e) Is a case which should not occur because cell B would have to encase cell A or C depending on how the pixel 1 and 3 are connected.

2.2.1 Hard and soft cell regimes

First, we consider the steady state condition of a confluent monolayer of cells. We performed numerical simulations of the CPM and characterised the morphology and dynamic behaviour of cells in the stationary state. We found that the cell shape is determined primarily by the interaction between contraction (the second term in the energy formula) and adhesion (third term in the energy function). For high contractility values, cells exhibit straight contacts and polygonal shapes with a typical vertex number of 6. In contrast, when the adhesion term dominates, cells lose their regular pattern of organisation and cell contacts become more irregular and wavy. Examples of the model showing the two regimes are given in Figure 2.3. It has been shown that when contractility is inhibited, either by direct perturbation of the actin cytoskeleton (Caldwell et al., 2014; Kovacs et al., 2011) or by disrupting the signalling pathways that regulate actomyosin (Gomez et al., 2015; Otani, Ichii, Aono, & Takeichi, 2006), cells exhibit these properties of junctional organisation, showing a good concordance with the results of our CPM model.

The above-mentioned behaviour is similar to that of the vertex model with the same energy function that was described in Farhadifar et al. (2007). Differences between the two models arise; however, due to the different representation of the cell boundaries in the two models. The CPM allows for non-polygonal boundaries leading to the formation of irregular cell protrusions in the soft regime.

To better study the role of the various model parameters and the transition between the hard (high contractility) and soft (low contractility) regimes of junctional organisation it is useful to theoretically analyse the model. The effect of competition between contractility (shortening) and adhesion (elongating) on the cell perimeter is best seen by combining the quadratic and linear terms of the cell perimeter and completing the square of Function 2.1 to give:

$$E(A_j, L_j) = \frac{k}{2}\sum_{j}^{N}\left(A_j - A_p\right)^2 + \frac{\Gamma}{2}\sum_{j}^{N}\left(L_j - L_p\right)^2 - \frac{\Gamma N}{2}{L_p}^2, \tag{2.2}$$

where

$$L_p = \frac{S}{2\Gamma}.$$

The constant term, $\Gamma N {L_p}^2/2$, can be neglected as it does not influence the behaviour of the system. This form of the energy function shows that, in addition to the preferred cell area, A_p, the cells also have a preferred cell perimeter, L_p, whose value is not prescribed, but arises from the competition between cell-cell adhesion and contractile line tension.

Depending on the geometry of the cells, the average/preferred cell area may correspond to different values of the cell perimeter length. Although the energy function stipulates a preferred perimeter, it has an upper and lower bound for a fixed cell area comprised of finite pixels. The upper bound corresponds to a long cell of single pixel width and is less relevant for cell modelling. More interesting is the lower bound, defined by the shortest boundary that can enclose a cell of given area. In a single cell problem this would be the circumference of a circle, in a regular tiling the Honeycomb conjecture (proven by Hales (2001) states that the minimum perimeter is given by that of a hexagon. The number of pixels along the perimeter of a hexagonal cell made up of hexagonal pixels (Figure 2.4) is

$$L_n = 12n - 6,$$

where n is the number of pixel layers making up the cell, and the area of the hexagonal cell is

$$A_n = 3n^2 - 3n + 1.$$

We use this to calculate an approximation for the minimal perimeter,

$$L_{min} = 2\sqrt{12A_p - 3}.$$

The model is highly dependent on whether the preferred cell perimeter, L_p, is larger or smaller than L_{min} leading to a hard and a soft regime with qualitatively different behaviour.

In the hard regime, the cells cannot reach their preferred perimeter, L_p, since $L_p \leq L_{min}$. So their perimeter is close to the minimum perimeter. In this case the energy minimum corresponds to the hexagonal tiling and contraction along the perimeters dominates, creating a tight configuration with mechanical tension maintained along the cell interfaces. Numerical simulations, with a relatively small temperature parameter, are consistent with a quasi-hexagonal tiling with fluctuations arising from defects along cell boundaries (Figure 2.3a).

In the alternative case, where $L_p > L_{min}$, we have a soft regime. Cell boundaries are loose and become wavier. The energy minimum is highly degenerate, i.e. there are infinitely many possible spatial configurations that satisfy both the area and perimeter constraints. The consequence of this degeneracy is that the junctions are very irregular (non-linear) in shape and mobile, even at low temperatures (Figure 2.3c, d).

This interpretation is confirmed by computing the average cell perimeter attained by the cells (Figure 2.5a, b). In the hard regime this is approximately equal to L_{min}, whereas in the soft

regime the average cell perimeter is approximately L_p. Of note, the temperature in the system also plays a role in determining the cell shape in the model. In the hard regime increasing the temperature causes the cells to change from regular hexagons to more irregular cell shapes (Figure 2.3b).

Finally, we analysed the dynamics of cell-cell boundaries in the hard and soft regimes (Figure 2.5c). We found that the number of pixel changes per iteration is approximately constant in the hard regime. In contrast, as the simulations move to the soft regime the number of pixel changes increases with L_p, implying that cell boundaries in the soft regime are more dynamic than in the hard regime. S. K. Wu, Gomez, et al., (2014) experimentally found that contractile tension at the ZA is greater than that at the lateral junctions. A prediction of our model analysis is that these differences in tension will lead to differences in the dynamics of these regions. To test this, our collaborators at the IMB at UQ performed live cell imaging of cell-cell junctions at the apical and lateral junctions of cells. They found that, in qualitative agreement with the simulations, cell-cell boundaries at the lateral junctions are more curved and dynamic than those at the corresponding apical junctions (Figure 2.6). This further suggests that the balance between adhesion and contractility not only determines the amount of tension at the cell-cell junctions but also influences the plasticity of the cell-cell interface.

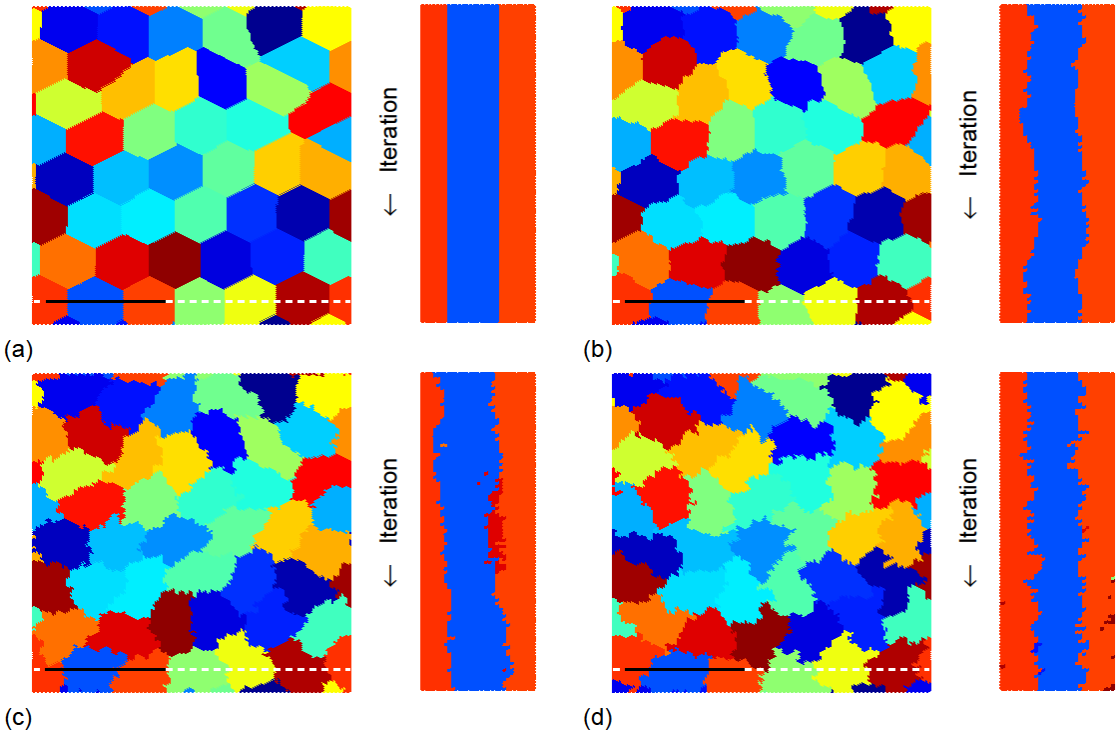

Figure 2.3. Distribution of the cells in the different regimes and kymographs showing the time evolution of cell junctions (at the location indicated by the black line): a) represents a very hard system of cells creating quasi-polygonal shapes close to a hexagon, $S = 1500$ and $\Gamma = 6$ ($\beta = 0.7480$) at $T = 10$; b) the cells are still in a hard regime, but with a higher temperature $S = 1500$ and $\Gamma = 6$ ($\beta = 0.7480$) at $T = 500$; c) example of cells in the soft regime, $S = 3000$ and $\Gamma = 6$ ($\beta = 1.4961$) at low temperature $T = 10$; d) soft regime at higher temperature, $S = 3000$ and $\Gamma = 6$ ($\beta = 1.4961$) at $T = 500$. All simulations use parameters $k = 2$ and $N = 44$ on a 160×160 hexagonal pixel grid.

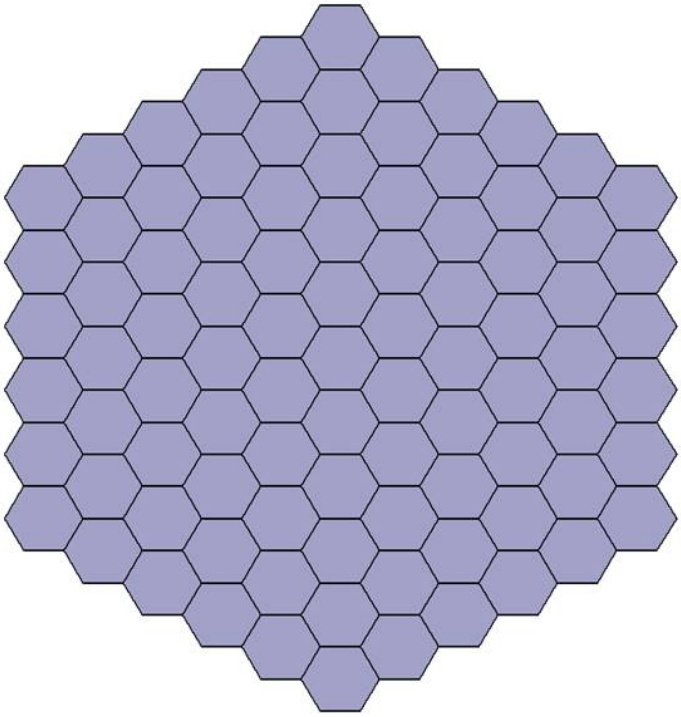

Figure 2.4. Representation of a hexagonal cell created with $n = 6$ hexagonal pixel layers.

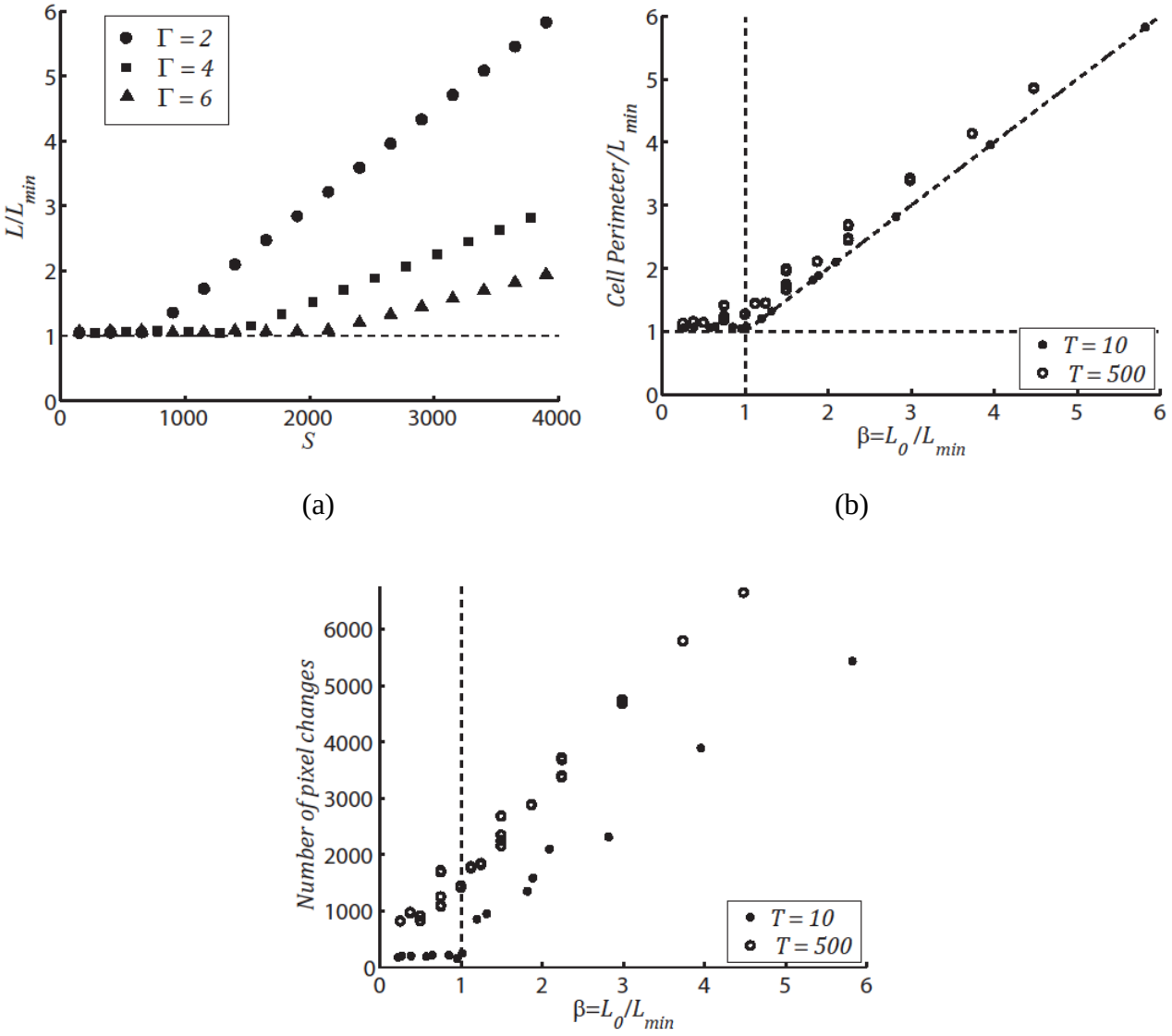

Figure 2.5. Representation of the change from the hard to soft regime; a) average perimeter of the cells as a function of the adhesion coefficient S. The symbols represent simulations for different values of the line tension parameter Γ (Γ = 2, circles Γ = 4 squares, and Γ = 6 triangles). b) Rescaling the adhesion coefficient on the horizontal axis ($L_p = S/2\Gamma$) shows the comparison between cell perimeters and the preferred perimeter L_p. The perimeter is approximately constant in the hard regime ($L_p/L_{min} < 1$) but increases linearly in the soft regime ($L_p/L_{min} > 1$). c) Shows the number of pixel changes that occur in a single iteration. In the hard regime the cells have a fairly constant number of changes but that increases when the cells move into the soft regime. The other parameters are $k = 2$ and $N = 44$ on a 160×160 hexagonal pixel grid.

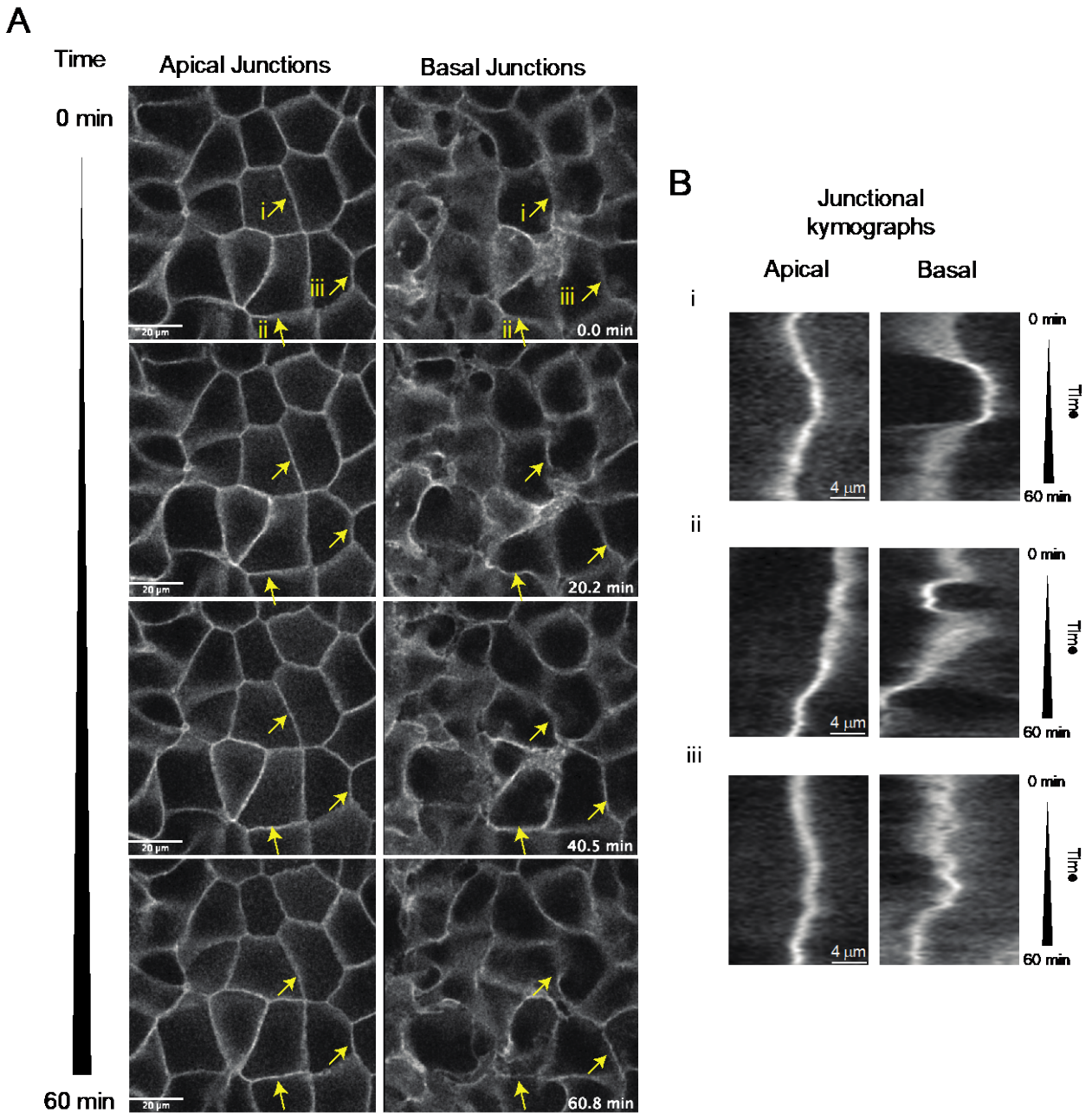

Figure 2.6. Morphology of apical (ZA) and lateral cell-cell contacts within confluent epithelial cells. a) Cells expressing a plasma membrane targeted fluorescent reporter were imaged by confocal live cell microscopy. Images taken at various times during the movie are shown (times indicated in far right of each panel). Left and right panels correspond to different Z positions, one located to the top of the cells (apical junctions, left) and the other 4mm below in the basal direction (basal junctions, right). Scale bar= $20\mu m$. b) Kymographs showing the time evolution of the apical and basal cell junctions indicated by the arrows on the left panel. This figure was provided by the contributors from the Institute for Molecular Bioscience (IMB) at the University of Queensland.

2.3 WOUND IN THE SYSTEM

2.3.1 Simulations and results

Now we consider the dynamic behaviour of the system in response to a small injury or wound, so that M adjacent cells are eliminated. In the model we remove the terms corresponding to the injured cells from the energy equation. Removal of these cells also affects the adhesion along the interface between the normal cells and the injury site. Accordingly, the adhesion term is now composed of two parts, one where a cell is connected to other neighbouring cells and the other where the cell is adjacent to a cell that is being removed and where there is no adhesion contribution to the energy. Thus, after completing the square in the energy Function (2.1) and grouping the terms corresponding to the cell boundaries along the injury, we obtain a new adhesion term that is proportional to the injury perimeter L_w,

$$E(A_j, L_j, L_w) = \frac{k}{2}\sum_{j}^{N-M}\left(A_j - A_p\right)^2 + \frac{\Gamma}{2}\sum_{j}^{N-M}\left(L_j - L_p\right)^2 + SL_w - \frac{\Gamma(N-M)}{2}{L_p}^2. \qquad (2.3)$$

Note, however, that compared to the Function (2.2) there is a new positive adhesion term, which arises as a consequence of the wound, represents an empty space within the sheet, denoting the absence of adhesion along its perimeter.

If, after removing cells, the wound perimeter reaches zero, it implies that the system has evolved to a state where the wound closes completely. Reducing L_w has competing energy costs involving the extension of cell area on the cells surrounding the wound and, in the hard regime, also requires an increase in their cell perimeter.

Thus, we performed numerical simulations where first we let the system reach equilibrium before the wound was created. The simulations for different parameters show that the area of the injury can expand from its original value then reach a fluctuating steady state, or decrease to a smaller area and eventually close completely. These cases can be seen in Figure 2.7. In all cases the change is monotonic in time. In general the equilibrium wound size is determined by the competition between adhesion and apical contractile (line) tension. When the perimeter contraction coefficient Γ is kept constant the equilibrium wound size decreases as the adhesion coefficient is increased. Moreover, the wound closes spontaneously when the adhesion coefficient is larger than a certain threshold. This threshold in the adhesion parameter decreases when the contraction coefficient is reduced. Qualitatively, spontaneous wound closure occurs with weak perimeter contraction and/or strong adhesion, i.e. when the system is approaching the soft regime, a result that has been also suggested during the extrusion of dying cells (Kuipers et al., 2014).

Although the wound closure in the model is primarily determined by adhesion and contraction we found that the temperature parameter T can also have some effect on the results of the simulations. When the temperature is too low the wound may not open or close to the equilibrium wound size that would be reached with higher values of T. This is because the system is unable to move easily between different states to reach the optimal configuration. This means that the noise amplitude must be taken into consideration, as it has to be large enough to change the system configuration but small enough to maintain realistic cell shapes over cellular time scales.

The initial cell configurations of all simulations in this chapter with a wound were generated by creating a configuration of 44 approximately 5×5 square pixel cells on a 160×160 pixel grid. These simulations generated cell configurations similar to Figure 2.3b. Simulations used these configurations and included required parameter values for k, S, Γ and T. Once an energy equilibrium was reached, the simulation would remove a cell from the system and continue the simulation to obtain the observed results.

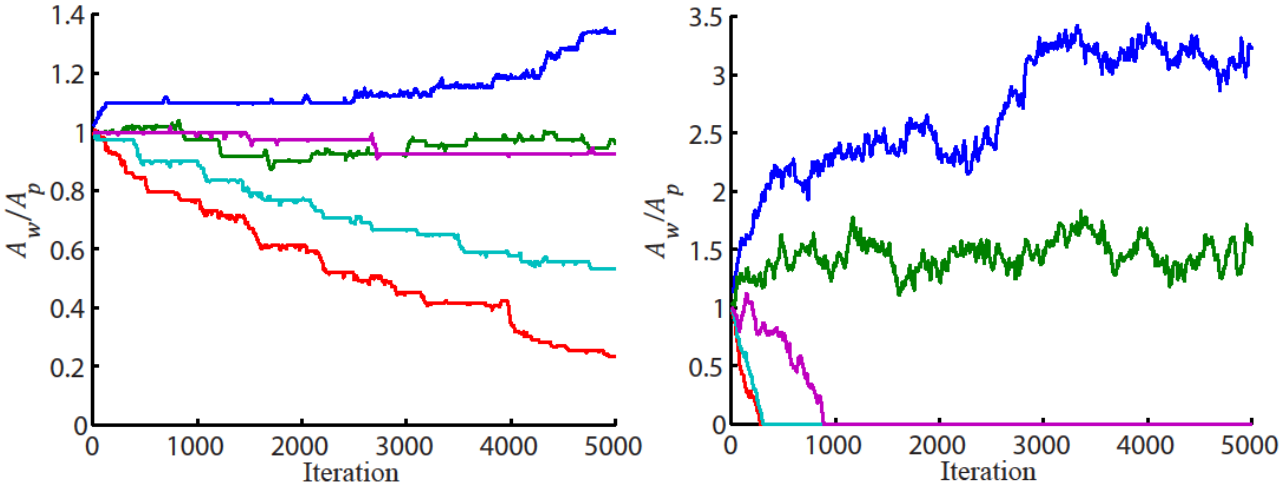

(a) (b)

Figure 2.7. Injury size vs "time" (iteration) showing how the initial injury may expand or collapse given different parameter values for two different temperatures a) $T = 100$ and b) $T = 500$. Each line represents a different combination of Γ and S, blue $\Gamma = 6$ and $S = 700$ ($\beta = 0.3491$), green $\Gamma = 4$ and $S = 700$ ($\beta = 0.5236$), magenta $\Gamma = 4$ and $S = 900$ ($\beta = 0.6732$), cyan $\Gamma = 6$ and $S = 1500$ ($\beta = 0.7480$) and red $\Gamma = 5$ and $S = 1500$ ($\beta = 0.8976$). All simulations have other parameters set as $k = 2$ and $N = 44$ on a 160×160 hexagonal pixel grid.

2.4 GEOMETRIC REPRESENTATION OF CELLS FOR THEORETICAL ANALYSIS

In order to better understand the mechanisms that determine the closure threshold and the dependence of equilibrium wound area on the parameters of the model, we make several simplifying assumptions to rewrite the energy of the system as a function of a single variable, the wound perimeter, and then determine the energy minima corresponding to the equilibrium state. First, we assume that the area and perimeter of the cells are all identical: $A_j = A_c$ and $L_j = L_c$ for $j = 1, \dots, N$, so the energy becomes

$$E(A_c, L_c, L_w) = \frac{k(\mathrm{N}-\mathrm{M})}{2}\left(A_c - A_p\right)^2 + \frac{\Gamma(\mathrm{N}-\mathrm{M})}{2}\left(L_c - L_p\right)^2 + SL_w - \frac{\Gamma(N-M)}{2}{L_p}^2. \quad (2.4)$$

Conservation of area links the wound area to the cell area, A_c, and total area, $A_T = NA_p$, through the relation

$$A_c + (N-M)A_c = A_T.$$

To proceed, we need to estimate the relationship between the area of the cells and their perimeter. This relationship depends on the shape of the cells but in general can be written in the form ${A_c = gL_c}^2$. For example, for a true hexagonal shape $g = 1/\left(4\sqrt{3}\right)$, or for a circle $g = 1/4\pi$. For the hexagonal cell made of n hexagonal pixel layers,

$$g^* = \frac{3n^3 - 3n + 1}{(12n-6)^2} = \frac{1}{48} + \frac{1}{4(12n-6)^2},$$

so for $n >> 1$, $g^* \approx 1/48$.

For simplicity we assume that the shape parameter of the wound and cells are approximately the same, so ${A_w = gL_w}^2$. Using the area conservation

$$A_c = \frac{1}{N-M}\left(NA_p - A_w\right),$$

the relationship between the linear dimensions of the wound and cells can be written as

$$L_c = \sqrt{\frac{NA_p}{g(N-M)} - \frac{{L_w}^2}{N-M}}.$$

Essentially this states that a reduction in the wound perimeter leads to a reduction in the wound area, the excess area is then equally shared among the live cells so that their perimeter grows (and vice

versa for an increase in the wound perimeter). This allows us to eliminate the live cell perimeter from the energy and write it as a function of the wound perimeter alone,

$$E(L_w) = \frac{k}{2(N-M)}\left(MA_p - gL_w{}^2\right)^2 + \frac{\Gamma A_p}{2g}\left(\sqrt{\frac{NA_p}{g} - L_w{}^2} - L_p\sqrt{N-M}\right)^2 + \frac{S}{2}L_w.$$

By using a length scale unit, the cell perimeter corresponding to the preferred area, A_p, we introduce the non-dimensional variable $l_w = L_w\sqrt{g/A_p}$, and the non-dimensional control parameter $\beta = L_p\sqrt{g/A_p} = S\sqrt{g}/\left(2\Gamma\sqrt{A_p}\right)$, and the energy function becomes

$$E^*(l_w) = \frac{2E}{S}\sqrt{\frac{g}{N-M}} = \frac{\phi M^2}{N-M}\left(1 - \frac{l_w{}^2}{M}\right)^2 + \frac{1}{2\beta}\left(\sqrt{N - l_w{}^2} - \beta\sqrt{N-M}\right)^2 + l_w,$$

where $\phi = kg^{1/2}A_p{}^{3/2}/S$. The equilibrium states of the system are represented by the minima of the energy function. We find that there are two cases. In the first case there are two minima: one corresponding to positive values of the wound perimeter, l_w, and the other one to negative (unphysical) values. In the other case there is only one energy minimum for negative values of l_w. Figure 2.8 shows the two cases.

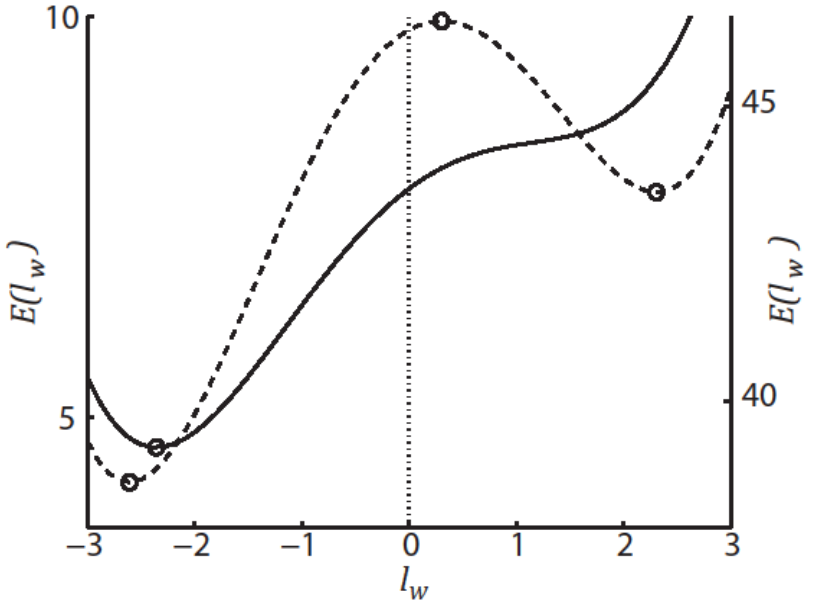

Figure 2.8. Plot of the energy function $E(l_w)$ with parameters $S = 700$ and $\Gamma = 8$ ($\beta = 0.2618$) (dashed line, right axis) and $S = 1500$ and $\Gamma = 8$ ($\beta = 0.5610$) (solid line, left axis). Other parameters are $k = 2$, $N = 44$, $M = 1$ and $g = 1/48$.

In the first case (identified by the dashed line in Figure 2.8) the two minima are separated by a local maximum. If the initial wound size, l_w, is larger than the local maximum the wound will

open to the local minimum. Alternatively, if the value of the initial wound size is lower than the maximum, then the wound will close to $l_w = 0$. In the second case, no positive equilibrium solutions exist so the wound will always close from any initial size. The transition from case 1 to case 2 occurs when the control parameter β is increased, i.e. the balance between adhesion versus apical line tension is modified in the favour of adhesion. In this case the energy minimum attains the same value as the maximum and disappears, leaving no equilibrium state with positive l_w, which indicates that the wound dimension decreases to zero. Physically the cells are driven by adhesion to "zip up" the wound, as the contractile resistance is insufficient to exert a countervailing force,

$$\frac{dE^*(l_w)}{dl_w} = \frac{4\phi M {l_w}^3}{N-M} - \left(\frac{4\phi M}{N-M} + \frac{1}{\beta}\right) l_w + \frac{l_w\sqrt{1-\frac{M}{N}}}{\sqrt{1-\frac{{l_w}^2}{N}}} + 1 = 0.$$

A slightly simplified form of the equation for the energy derivative function can be obtained by using the assumption that $N >> 1$ and, using Taylor expansion (in $1/N$), we obtain the equation

$$\frac{dE^*(l_w)}{dl_w} = -\left(\frac{4\phi}{N-M} + \frac{1}{\beta N}\right) {l_w}^3 + \left(\frac{4\phi M}{N-M} + \frac{1}{\beta} - 1\right) l_w - 1 = 0.$$

Thus, the equilibrium wound size corresponds to the positive root of a cubic equation of the form

$$-a{l_w}^3 + bl_w - 1 = 0,$$

where $a > 0$ for any parameter combination. So, if $b < 0$ no positive roots exist, i.e. the wound will always close. We let $\varepsilon = 4M/(N-M)$, which is a small positive number for $N >> M$. Thus, a sufficient condition for wound closure is

$$\frac{L_{min}}{L_p} < 1 - \varepsilon = 1 - \frac{4k{g^{1/2}}{A_p}^{2/3}M}{S(N-M)}.$$

This suggests that the wound in the simulations with cells in the soft regime, $L_{min}/L_p < 1$, will always close if N is sufficiently large.

Using the above expression for the energy as a function of wound size we can determine numerically the positive roots of the energy derivative function: $dE^*(l_w)/dl_w = 0$. Comparing these with results from the full numerical simulations of the CPM (Figure 2.9), we obtain a reasonable approximation of the equilibrium wound size and of the transition to possible wound closure when the parameters S and Γ are varied. For example, for the particular case of $\Gamma = 2$, $S = 200$ and an initial wound $l_w = 1$, the system corresponds to a hard regime in which the wound

will open and reach an equilibrium value of around ~ 1.2 (blue solid line). However, if the initial wound size is lower than $l_w = \sim 0.2$ (blue dashed line), then the wound will start to collapse and eventually close. Thus, whether or not the wound size l_w is larger or smaller than the location of the energy maximum, which corresponds to an unstable wound solution, will determine whether or not the wound will close or open. In addition, if we keep constant all the parameters but increase the adhesion coefficient S, the local maximum corresponding to l_w disappears, implying that the wound will close independently of its initial size.

We then used this theoretical approach to the equilibrium wound size and closure threshold to investigate the dependence on the number of cells, N. Varying the control parameter $\beta = L_p/L_{min}$, which changes the relative strength of adhesion versus contraction, we found that the threshold for spontaneous wound closure from any initial size (i.e. when the open equilibrium wound state disappears) shifts towards higher adhesion values as N is increased (Figure 2.10a) and approaches the boundary between the hard and soft regime, $\beta = 1$, for large N. The equilibrium wound size also increases with the number of cells as $l_w \sim \sqrt{N}$ (Figure 2.10b). This is because in the hard regime the cells contract their perimeter when a wound is created, which is then balanced by the increase of wound perimeter. Since the contractile tension term in the energy function is proportional to the number of cells, the equilibrium is reached for a larger wound size as the cell number increases. However, in real tissues, it is likely that the number of cells affected by the mechanical perturbation due to injury is limited to a finite neighbourhood of the wound (e.g. due to adhesion to underlying tissue), which was not taken into account in our theoretical analysis.

In addition to relaxing the tension in the tissue, by increased adhesion or reduced perimeter contraction, other mechanisms can also contribute to the process of wound closure. An example of this is the formation of a supra-cellular purse string that contracts the perimeter of the wound (Vedula et al., 2015). This mechanism can be easily included in the energy function as an extra term similar to the cell perimeter contraction term,

$$\Gamma^* / 2{L_w}^2,$$

with a contraction strength of Γ^*. We can then use our theoretical approximation to determine the equilibrium wound size from the positive root of the energy derivative function. As expected, increasing the strength of the purse string, Γ^*, the wound closure threshold shifts further into the hard regime meaning that wound closure could be favourable even for a system in the hard regime (Figure 2.11).

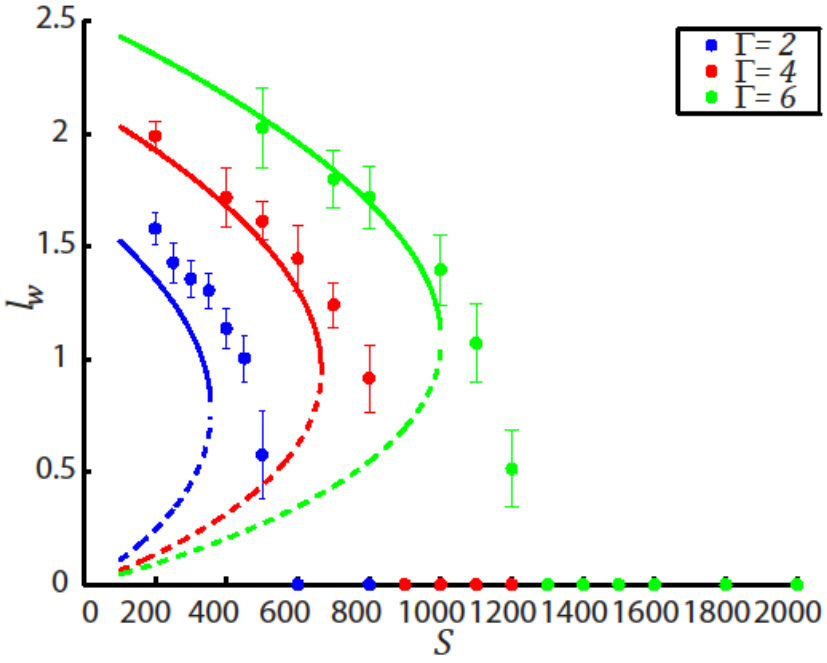

Figure 2.9. Comparison of the theoretical approximation of equilibrium with the direct numerical results from the CPM simulations; showing the normalised wound area as a function of the adhesion coefficient S for different values of the line tension parameter Γ. The solid line represents the local energy minimum and the dashed line is the local energy maximum. Other parameters are $k = 2$ and $N = 44$ on a 160×160grid of hexagonal pixels with one cell removed, $M = 1$.

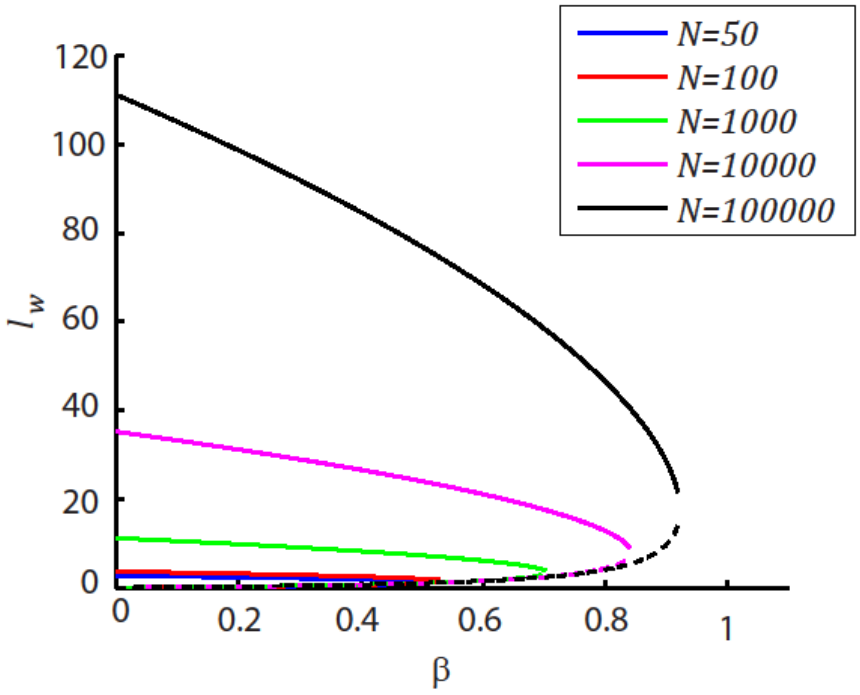

(a)

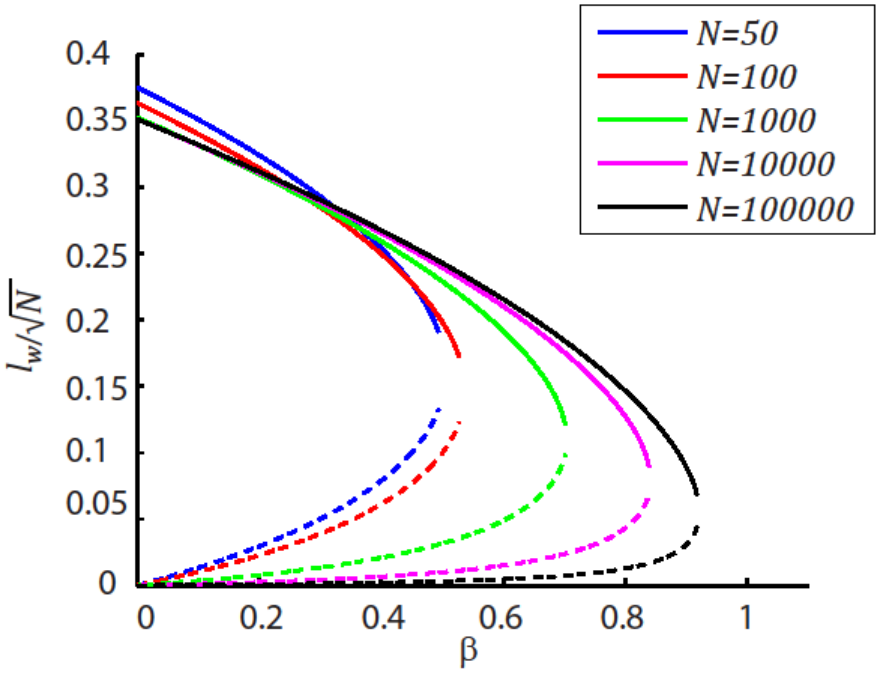

(b)

Figure 2.10. Equilibrium wound size obtained from the theoretical approximation: a) stable equilibrium wound size (solid line) and unstable equilibrium wound size (dashed line) against $\beta = L_p/L_{min}$. The parameters are $\Gamma = 6$, $k = 2$, $A_p = 582$ with one cell removed, $M = 1$, for different number of cells in the system $N = (50,100,1000,10000,100000)$; b) same as a) but the wound size, vertical axis, is rescaled as $l_w/\sqrt{N}$.

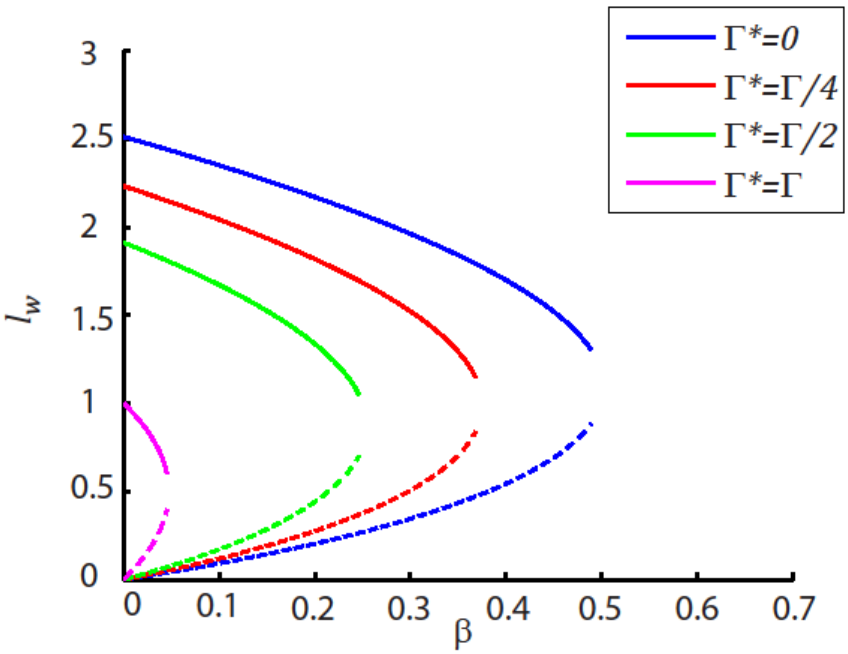

Figure 2.11. Equilibrium wound size calculated from the theoretical approximation, with the addition of the contractile purse string around the wound. Stable equilibrium wound size (solid line) and unstable equilibrium wound size (dashed line) against $\beta = L_p/L_{min}$. The parameters are $\Gamma = 6$, $k = 2$, $A_p = 582$ and $N = 44$ with one cell removed, $M = 1$, for different strengths of the contraction of the wound perimeter $\Gamma^* = (0, \Gamma/4, \Gamma/2, \Gamma)$.

2.4 DISCUSSION

We have used the CPM to describe an epithelium including simple mechanical representations of adhesion, contraction and pressure in the cells (Graner & Glazier, 1992; Kabla, 2012; Szabo et al., 2010). Using these components, we find the cells occur in two regimes, either a hard regime where cell shape is governed by the contractile line tension, or in a soft regime, where the cell shape is determined by adhesion. This is similar to what has been described using a vertex model (Farhadifar et al., 2007). However, by implementing a CPM model we were able to obtain a more accurate representation of cell shapes when compared with the vertex model, particularly of the cell shapes that correspond to a soft regime. Additionally, our CPM model also allowed us to more precisely characterize the dynamics of cell boundaries, yielding simulations that are in agreement with previous experimental observations. In particular, we found that for steady state conditions apical junctions of cells exhibit properties that are well characterised by a hard regime in the model. The results demonstrate an advantage of the CPM approach compared to the use of vertex models.

Using our cell representation with an added microscopic wound, we observe that the wound can increase (open) or decrease (close) its area depending on the relative balance between adhesion and line tension. Experimental data indicate that performing a micro-wound by laser irradiation leads to a rapid relaxation of the perimeter of the injured area (Antunes et al., 2013; Fernandez-Gonzalez & Zallen, 2013) followed by the reorganisation of the junction around the injury.

Combined with our theoretical analysis, these observations imply that for a wound to close it is necessary for the properties of the cells to change to favour the remodelling of the junctional organisation around the wound. Evidence in the literature suggests that the response of cells to the wounding process is complex and may involve different complementary and overlapping mechanisms that involve biochemical or mechanical signals (Abreu-Blanco et al., 2012; Anon et al., 2012; Antunes et al., 2013; Brugues et al., 2014; Fernandez-Gonzalez & Zallen, 2013; Tamada, Perez, Nelson, & Sheetz, 2007). For example, it has been described that calcium waves around the wound site are able to propagate waves of myosin activation (contractility) that alter the morphology of the cells surrounding the wound, ultimately leading to the formation of a contractile purse string (Antunes et al., 2013). On the other hand, it has been shown that myosin II is required for cadherin accumulation at the ZA (Shewan et al., 2005; Smutny et al., 2010), which suggests that myosin can influence cell-cell adhesion as well as contributing to line tension in junctions. Another factor that may influence wound closure is lamellipodial motility, which allows cells bordering a wound to migrate into, and thereby close the wound (Abreu-Blanco et al., 2012; Anon et al., 2012).

Cadherin adhesion is also required for the development of higher and polarized traction forces within epithelial sheets (Mertz et al., 2013; Weber, Bjerke, & DeSimone, 2012). However, whether lamellipodial migration is coordinated or influenced by changes in cell-cell adhesion during wound healing is yet to be determined. Potentially, the complex interplay between these mechanisms may alter the properties of the cells surrounding a wound to ultimately favour the wound closure process.

Our theoretical analysis allowed us to estimate the equilibrium wound size using some assumptions. We found that when adhesion is weaker than a critical value (or equivalently apical tension is above a certain threshold) an open wound represents the equilibrium state. However, the basin of attraction of the equilibrium state is limited by a minimum wound size (corresponding to the energy maximum) and wounds below this threshold close spontaneously. This can have several biological implications, particularly for microscopic defects in the monolayer on the scale of single cells. An interesting example occurs when individual cells undergo apoptosis within confluent epithelia. Under these conditions, the apoptotic cell contracts and reduces its apical area to eventually be extruded from the monolayer. Contraction of the dying cell (Brugues et al., 2014; Kuipers et al., 2014; Monier et al., 2015) alters the shapes of its neighbouring cells, as the neighbours are pulled by the dying cell through cadherin-based cell-cell adhesion (Grieve & Rabouille, 2014; Lubkov & Bar-Sagi, 2014). Thus, the active contraction of the dying cell could be required to reduce its apical area below a minimal threshold, allowing neighbouring cells to spontaneously heal the monolayer at the same time dying cells are being extruded.

Similarly, the threshold in the wound size may have some relation to the purse string mechanism of wound closure in small wounds, where an actomyosin contractile ring is formed in the cells that border the wound (Abreu-Blanco et al., 2012; Antunes et al., 2013; Fernandez-Gonzalez & Zallen, 2013). In this case the purse string contracts, thus reducing the wound size below the threshold that would allow it to close spontaneously even if an open wound equilibrium solution exists. However, for larger wounds, it is anticipated that higher forces could be required for this process to occur, which indeed can be facilitated if surrounding cells actively participate in the healing process as has been suggested recently (Kuipers et al., 2014).

Our results thus indicate that for the above-mentioned cases, either a change in contractility that helps to reduce the area size of the wound or an increase in adhesion (or reduction in tension) will favour spontaneous wound closure regardless of the initial size of the wound. Moreover, as cells at steady state behave like those in a hard regime, our modelling data also propose that for wounds which are larger than a few cells, changes in the balance between contraction and adhesion is required for non-monotonous wound closure to occur. In particular, the properties of apical

junctions of cells needs to be modified in order to facilitate the remodelling required for efficient wound closure.

Chapter 3: Simulating Cell Islands with the CPM

3.1 INTRODUCTION

In this chapter we use the two-dimensional CPM, introduced in Chapter 2, to investigate the changes in the size and morphology of a simple cluster of connected cells we refer to as cell islands. These cell clusters are not a common occurrence in nature; however, they can be used in biological experiments to investigate the properties of cells, such as the tension in cell junctions (Coburn et al., 2016), cancer growth (Aceto et al., 2014), and as an alternate to the free edge of an epithelial sheet.

Cell island systems have been a component in CPM studies beginning with the investigations of cell sorting. The boundaries of cells with high energy contributions decrease in length allowing those cells with smaller contributions of energy to increase their boundary lengths, organising the cells in the cluster to change from high energy configurations to lower energy. The differences in the energy between the boundaries of the cells result in the organisation of the cells in the cluster into structures representative of biological cells (Glazier & Graner, 1993; Graner & Glazier, 1992). The properties of cell clusters can also be applied to the growth of certain cells, such as tumours. The growth of a cluster is affected by the stiffness parameter, i.e. more cells are contained in a cluster if there is less compressibility (greater stiffness). However, the cell organisation and morphology of the cluster can be greatly affected by the introduction of motility to the system (J. F. Li & Lowengrub, 2014). Differences in adhesion on the boundaries between the cells can lead to the deformation of the cluster. Parameters, such as adhesion, are dependent on the orientation differences between cells, for example, cell clusters can become elongated where cells align in orientation (Zajac, Jones, & Glazier, 2003).

The geometry of the cell island is similar to that of the cell monolayer with a microscopic wound, see Chapter 2. In cell clusters the cells are surrounded by a free edge instead of the free edge surrounded by cells as in the case of the wound.

In this chapter we simulate a single cell and cell islands with two or more cells with the two-dimesional CPM with three mechanisims: an area constraint, a perimeter contraction, and adhesion between cells. The cell area and perimeter values, which influence the cell and cell island size and geometry, achieve an energy equilibrium that can be approximated by minimising the energy function. We compare the simulations and optimisation solutions of a simplified energy function with the application of various assumptions and constraints. The similarities and differences

between the simulations and optimisation solutions of the cells and cell island sizes and shapes from the CPM enegy function are discussed, together with their causes.

3.2 CPM SIMULATION OF A CELL ISLAND

A cell island aggregate, see Figure 3.1, can occur as an artefact of the micro-wound case in Chapter 2. The artefact occurs in the simulation when the wound becomes larger than the size of the periodic boundaries of the system. In such a case the free edge of the wound "wraps" itself around the cells, compressing them to smaller proportions than their preferred area and perimeter. This change transforms the simulated micro-wound into the simulation of a cell island.

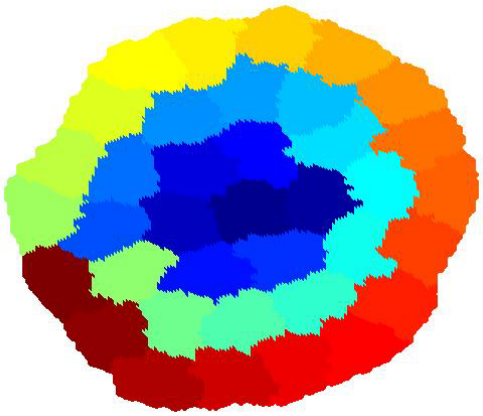

Figure 3.1. An example of a CPM simulation of a cell island with 37 cells.

The same energy function and mechanisms from the CPM simulations in Chapter 2 are applied to the cell island simulations. The CPM energy function for the cell island aggregate is the same as the energy function of the micro-wound, Function (2.3), except the variables are specific to the cell island case. This means the energy function for the cell island is written as

$$E = \frac{k}{2}\sum_{j}^{N}\left(A_j - A_p\right)^2 + \frac{\Gamma}{2}\sum_{j}^{N}\left(L_j - L_p\right)^2 + \frac{S}{2}L_I + Constant, \qquad (3.1)$$

where $L_p = S/2\Gamma$ is the preferred cell perimeter, L_I is the perimeter of the cell island and the third term arises due to the absence of adhesion around the boundary of the island. Even though the physical representation of the cell island system is different to that for the wound, the mechanisms of the area constraint, perimeter contraction, adhesion, and the application of the CPM does not change from Chapter 2.

The initial cell configurations of all simulations in this chapter for three dimensions were generated by creating a configuration of 25 $10 \times 10 \times 5$ pixel square prism cells in a sheet located in a $50 \times 50 \times 10$ pixel system and a $50 \times 50 \times 5$ empty region above the cell sheet. These configurations were run with the parameters $k = 100$, the S and Γ ratio $\beta = 1$ and $T = 2000$ until

an energy equilibrium was reached. These simulations generated cell configurations with cross sections of the cells similar to Figure 4.3b. Once an energy equilibrium was reached the modified cell parameter values were adjusted and the simulation continued to run, obtaining the observed results.

3.3 APPLICATION OF THE MODEL TO A SINGLE ISOLATED CELL

Before investigating cell islands, we consider a single cell case. Implementing the model with a single cell will include only two of the three mechanisms from the energy function, namely the area constraint and the perimeter contraction. The interaction between the two mechanisms in the single cell size and shape can be observed.

In the simulations a single cell's size and shape is determined by the interaction between the perimeter contraction parameter, Γ, area constraint parameter, k, and the preferred area, A_p. We understand that parameter k maintains the cell area close to the preferred area and parameter Γ attempts to reduce the cell's perimeter to zero. This means that increasing k will make it more difficult for the cell area to differ from the preferred area and increasing Γ will decrease the cells perimeter and size.

The equilibrium state of the single cell can be characterised by the cell area and perimeter. The simulation results are compared to an optimisation solution resulting from the optimisation problem described below.

We assume all cells have a shape categorised by the cell area and perimeter. The cell perimeter squared cannot fall below a particular area, i.e. $A \leq gL^2$. The value of g is the ratio of area and perimeter squared, A/L^2, of a defined shape, referred to as the minimum shape in Chapter 2, and occurs when $A = gL^2$. In an unrestrictive lattice the minimum shape is represented by a circle; however, in a restrictive lattice the cell is instead represented by a polygon. Due to the selection of hexagonal pixels the polygon is a "hexagon", see Figure 2.4, to replicate the simulations, and the ratio is given as $g = 1/48$.

Only the interaction between the cell area constraint and cell perimeter contraction is expressed in the energy function for a single cell,

$$E(A, L) = \frac{k}{2}\left(A - A_p\right)^2 + \frac{\Gamma}{2}L^2. \qquad (3.2)$$

Additionally, simple conditions are applied, namely that the cell area and perimeter are non-negative and the inequality discussed previously between the cell area and perimeter, i.e. $A \leq gL^2$.

An optimisation problem can be expressed with the energy Function (3.2) and conditions giving the Lagrangian function

$$\begin{aligned} E^*(A, L, \lambda_1, \lambda_2, \lambda_3) = \frac{k}{2}\left(A - A_p\right)^2 + \frac{\Gamma}{2}L^2 \\ +\lambda_1(A - gL^2) + \lambda_2(-A) + \lambda_3(-L), \end{aligned} \qquad (3.3)$$

with the use of Karush-Kuhn-Tucker (KKT) conditions (Lange, 2004). The KKT conditions are a generalisation of the equality conditions used with Lagrangian multipliers to incorporate the

inequalities of the problem. The Lagrangian Function (3.3) with these conditions results in the simultaneous equations

$$\frac{\partial E^*(A,L,\lambda_1,\lambda_2,\lambda_3)}{\partial A} = k\big(A - A_p\big) + \lambda_1 - \lambda_2 = 0,$$

$$\frac{\partial E^*(A,L,\lambda_1,\lambda_2,\lambda_3)}{\partial L} = \Gamma L - 2\lambda_1 g L - \lambda_3 = 0,$$

$$\lambda_1(A - gL^2) = 0,$$

$$\lambda_2(-A) = 0$$

and

$$\lambda_3(-L) = 0.$$

The results of these simulations equations need to satisfy the inequalities of

$$\lambda_1 \geq 0, \lambda_2 \geq 0, \lambda_3 \geq 0, (A - gL^2) \leq 0, -A \leq 0 \text{ and } -L \leq 0.$$

In this problem there are eight different cases including $(\lambda_1 = 0, \lambda_2 = 0, \lambda_3 = 0)$, $(\lambda_1 > 0, \lambda_2 = 0, \lambda_3 = 0)$, $(\lambda_1 = 0, \lambda_2 \geq 0, \lambda_3 = 0)$, $(\lambda_1 = 0, \lambda_2 = 0, \lambda_3 \geq 0)$, $(\lambda_1 \geq 0, \lambda_2 \geq 0, \lambda_3 = 0)$, $(\lambda_1 = 0, \lambda_2 \geq 0, \lambda_3 \geq 0)$, $(\lambda_1 \geq 0, \lambda_2 = 0, \lambda_3 \geq 0)$ and $(\lambda_1 \geq 0, \lambda_2 \geq 0, \lambda_3 \geq 0)$. The only solution that satisfies the equations and inequalities is from the case $(\lambda_1 \geq 0, \lambda_2 = 0, \lambda_3 = 0)$ and gives the solution of the cell area,

$$A_1 = A_p - \frac{\Gamma}{2gk}, \tag{3.4}$$

and the solution of the cell perimeter,

$$L_1 = \sqrt{\frac{A}{g}} = \sqrt{\frac{A_p}{g} - \frac{\Gamma}{2g^2k}}. \tag{3.5}$$

These solutions show that the area of a single cell, A_1, and perimeter of a single cell, L_1, decrease with the perimeter contraction parameter Γ, see Figure 3.2a and 3.2c, respectively, and increase with the area constraint k, see Figures 3.2b and 3.2d, respectively. The cell can disappear when the area and perimeter equal zero for both the simulation and optimisation solutions, shown in Figure 3.3, when $A_p \leq \Gamma/(2gk)$.

The simulation results and the mathematical optimisation solutions above are qualitatively similar. However, a few differences between them are a result of the restrictions of the discretised lattice structure of the simulations. The main differences are observed in Figure 3.2c and 3.2d, showing the cell perimeter against the parameters k and Γ, respectively. They show differences between the simulations and optimisation solution occur at comparatively small values of the contraction parameter of those values tested, such as $\Gamma = 1$. With "low" values of contraction the deviation of the cell's perimeter requires less energy, and therefore the noise in the system distorts the cell's shape more readily than a cell with a larger contraction parameter. This trend is also

replicated in the ratio $g = A/L^2$ against k and Γ, shown in Figure 3.2e and 3.2f, respectively. The equilibrium results of the cell simulations and $g = 1/48$, representing the "hexagonal" shape of the cell on the lattice (shown on the figure as a black line), display a large difference between them for "small" values of the contraction, such as $\Gamma = 1$. The values of g from the simulation are smaller than $1/48$, representing distorted shapes. These differences are similar to the differences in the perimeters because the ratio is calculated with the perimeter, $g = A/L^2$.

Furthermore, there is a difference between the simulation and the optimisation solution cell area, observed in Figure 3.3a, which is caused by the lattice and smaller preferred area. For simulations with an area constraint parameter $k = 3$ and perimeter contraction parameter greater than 5, the simulation cell area results are greater than the optimisation solutions. The optimisation solutions tend towards zero while the simulation cell area increases as Γ increases. As the cell becomes smaller in the simulations there are situations where the decrease in the cell perimeter requires the cell to initially increase its perimeter. This means the cell can become fixed at a larger perimeter with larger perimeter contraction coefficient values and no longer decreases its perimeter to achieve the calculated equilibrium. This artefact can be eliminated by increasing the amount of noise, or for larger preferred area values as shown in Figure 3.2. However, the artefact of the cell perimeter, discussed above, is still observable in both situations.

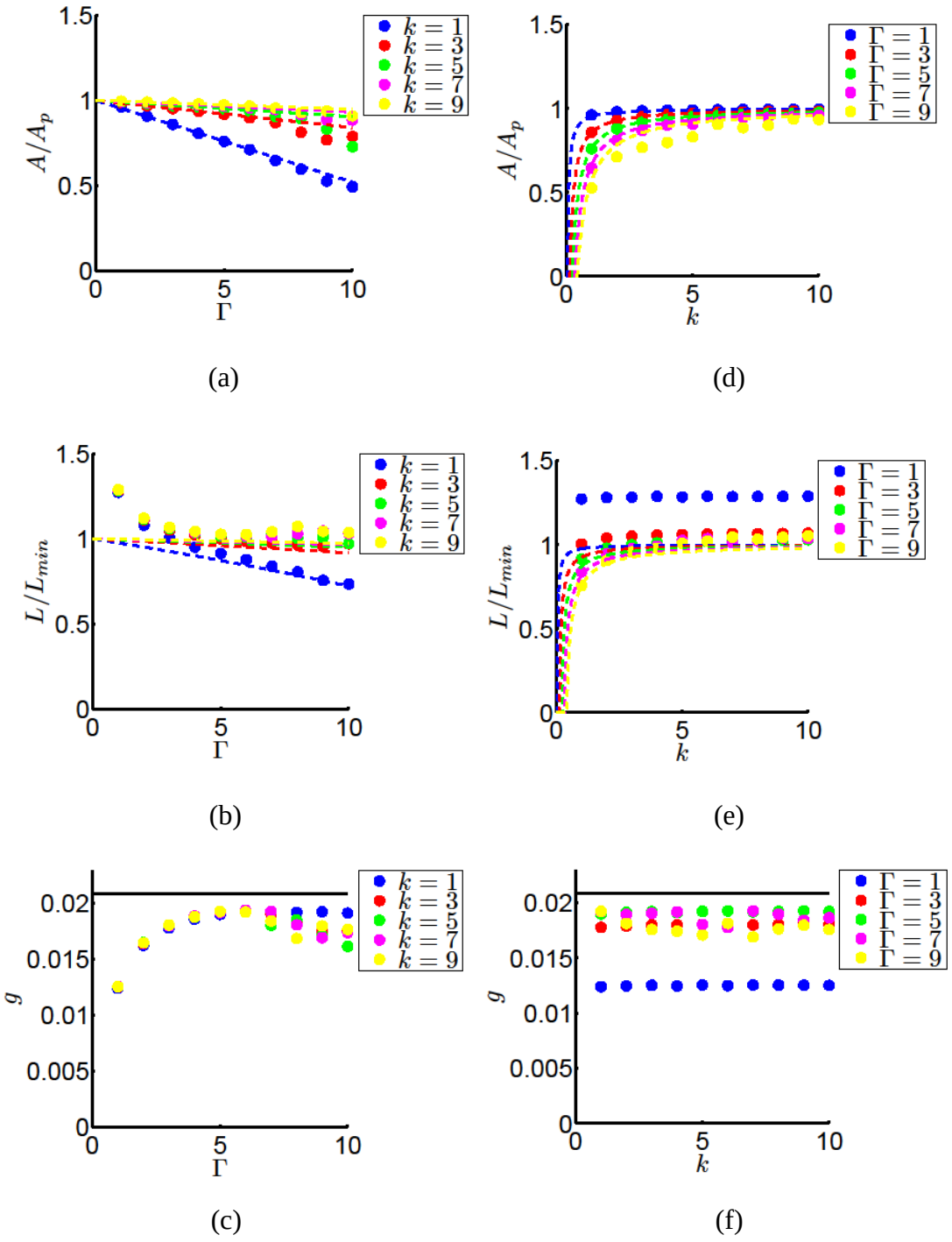

Figure 3.2. Plots, with the preferred area $A_p = 500$, for a single cell simulated on a hexagonal pixel grid with the CPM showing the (a) mean cell area with the geometric solution from Equation (3.5), (b) mean cell perimeter with the geometric solution from Equation (3.4) and (c) ratio $g = A/L^2$ against the perimeter contraction, Γ, for different area constraint parameters, k; and the (d) mean cell area with the geometric solution from Equation (3.5), (e) mean cell perimeter with the geometric solution from Equation (3.4) and (f) ratio $g = A/L^2$ against the area constraint parameter, k, with different perimeter contractions, Γ. Each point is averaged over the last 50 of 1000 iterations and the simulations have a temperature of $T = 100$.

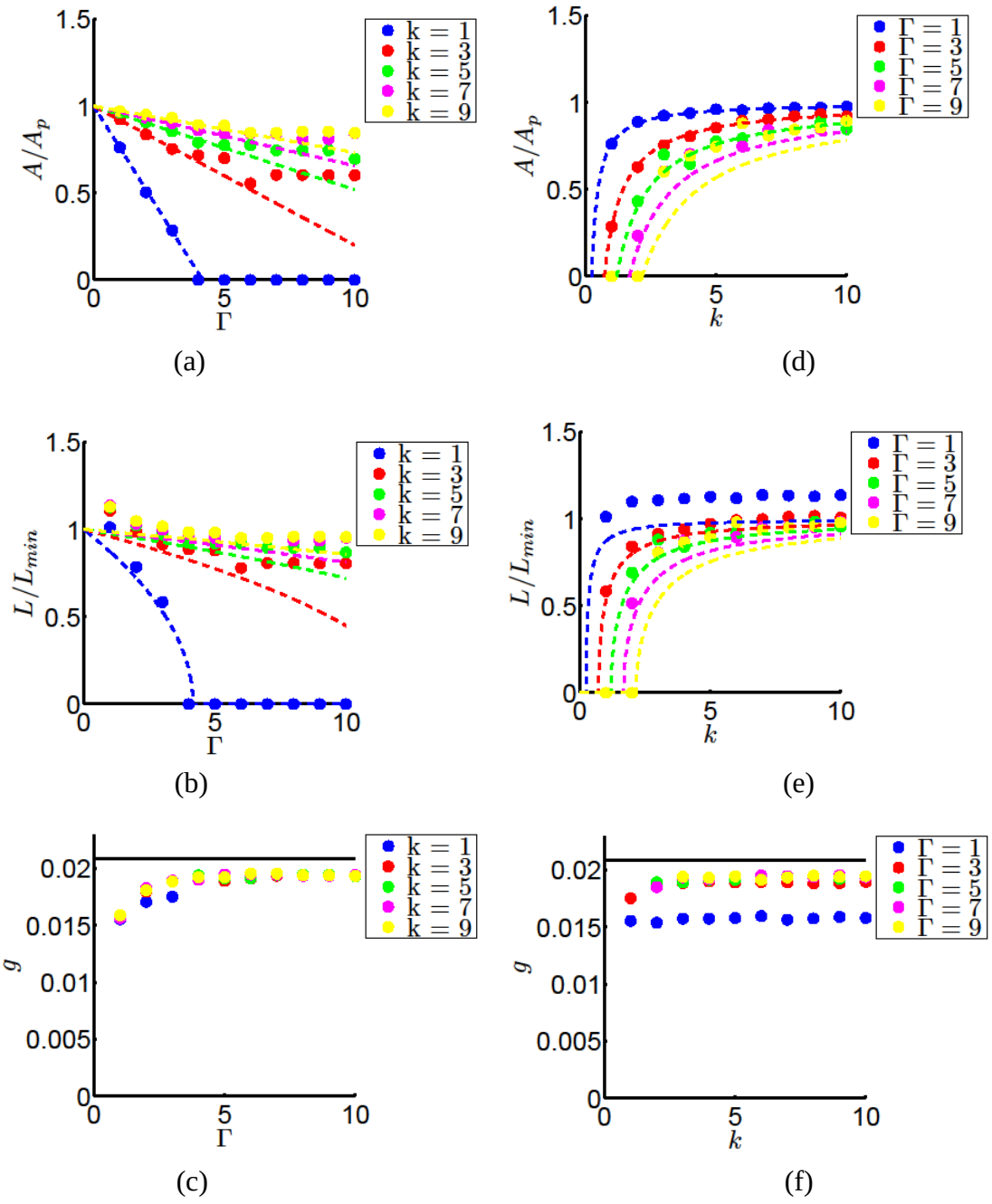

Figure 3.3. Plots, with the preferred area $A_p = 100$, for a single cell simulated on a hexagonal pixel grid with the CPM showing the (a) mean cell area with the geometric solution from Equation (3.5), (b) mean cell perimeter with the geometric solution from Equation (3.4) and (c) ratio $g = A/L^2$ against the perimeter contraction, Γ, for different area constraint parameters, k; and the (d) mean cell area with the geometric solution from Equation (3.5), (e) mean cell perimeter with the geometric solution from Equation (3.4) and (f) ratio $g = A/L^2$ against the area constraint parameter, k, with different perimeter contractions, Γ. Each point is averaged over the last 50 of 1000 iterations and the simulations have a temperature of $T = 100$.

3.4 IMPLEMENTATION OF THE CPM FOR TWO OR MORE CELLS

Previously we discussed the effect on the morphology and size of a single cell from the CPM with only the area constraint and perimeter contraction mechanisms. However, cell islands cannot exist with only these two mechanisms in the model, given that the cells would not be attached to each other they would separate from one another at any time due to cell movement or change in the cell size. The adhesion mechanism is required to attach the cells together to form the cell island case.

The introduction of adhesion with multiple cells influences both the size and shape of the cells and the cell island shape itself. This is understandable because the combination of the adhesion and perimeter contraction in the energy Function (3.1) now produces the preferred perimeter $L_p = S/2\Gamma$ for the cells. The preferred perimeter in this cell island case is the total perimeter of a cell and not the partial perimeter of the interconnected junctions between cells. The preferred perimeter leads to the formation of the hard and soft regimes discussed in Chapter 2.

3.4.1 Geometric optimisation problem for a cell island

As with the single cell we can approximate the cell area and perimeter and, in addition, the cell island area and perimeter using the energy function. For an island with two or more cells we assume all cells have the same shape, area and perimeter, and all cells are connected to each other in the cluster. The area of the cell island is then the sum of N cells' areas, $A_I = NA$.

Unlike the single cell, the cell island includes adhesion between the cell boundaries that is included in the energy function and as such we obtain the energy function,

$$E(A, L, L_I) = \frac{Nk}{2}\left(A - A_p\right)^2 + \frac{N\Gamma}{2}\left(L - L_p\right)^2 + \frac{S}{2}L_I + Constant, \qquad (3.6)$$

which is similar to energy Function (2.4) of the wound except instead of the wound perimeter there is the perimeter of the cell island. Additionally, there are the simple constraints that the cell area, cell perimeter, cell island area and the cell island perimeter are non-negative. The inequality between the cell area and perimeter, $A \leq gL^2$, discussed in the single cell case also holds and we will assume that this inequality is similar to the cell island area and cell island perimeter $A_I \leq g{L_I}^2$.

An optimisation problem can be expressed with the energy Function (3.6) and conditions giving the Lagrangian function

$$\begin{aligned} E^*(A, L, \lambda_1, \lambda_2, \lambda_3, \lambda_4, \lambda_5) = {} & \frac{Nk}{2}\left(A - A_p\right)^2 + \frac{N\Gamma}{2}\left(L - L_p\right)^2 + \frac{S}{2}L_I + \lambda_1(A - gL^2) \\ & + \lambda_2\left(NA - g{L_I}^2\right) + \lambda_3(-A) + \lambda_4(-L) + \lambda_5(-L_I) + Constant. \end{aligned} \qquad (3.7)$$

The Lagrangian Function (3.7) with the use of KKT conditions results in the simultaneous equations

$$\frac{\partial E^*(A,L,\lambda_1,\lambda_2,\lambda_3,\lambda_4,\lambda_5)}{\partial A} = k\left(A - A_p\right) + \lambda_1 - \lambda_2 = 0,$$

$$\frac{\partial E^*(A,L,\lambda_1,\lambda_2,\lambda_3,\lambda_4,\lambda_5)}{\partial L} = \Gamma L - 2\lambda_1 gL - \lambda_3 = 0,$$

$$\frac{\partial E^*(A,L,\lambda_1,\lambda_2,\lambda_3,\lambda_4,\lambda_5)}{\partial L} = \Gamma L - 2\lambda_1 gL - \lambda_3 = 0,$$

$$\lambda_1(A - gL^2) = 0,$$

$$\lambda_2\left(NA - g{L_I}^2\right) = 0,$$

$$\lambda_3(-A) = 0,$$

$$\lambda_4(-L) = 0$$

and

$$\lambda_5(-L_I) = 0.$$

The results of these simultaneous equations need to satisfy the inequalities of

$$\lambda_1 \geq 0, \lambda_2 \geq 0, \lambda_3 \geq 0, \lambda_4 \geq 0, \lambda_5 \geq 0,$$

$$(A - gL^2) \leq 0, \left(NA - g{L_I}^2\right) \leq 0, -A \leq 0, -L \leq 0 \text{ and } -L_I \leq 0.$$

In this problem there are 32 different cases depending on whether $\lambda_i > 0$ or $\lambda_i = 0$ for $= 1, 2, 3, 4,$ or 5. There are only two cases that produce solutions that satisfy the equations and inequalities. The first case, ($\lambda_1 \geq 0$, $\lambda_2 \geq 0$, $\lambda_3 = 0$, $\lambda_4 = 0$, $\lambda_5 = 0$), results in $L > L_p$, $A = gL^2$, $NA = g{L_I}^2$ and the cubic equation

$$A^{\frac{3}{2}} + A_1 A^{\frac{1}{2}} + \left(\frac{S}{4k\sqrt{gN}} - \frac{S}{4k\sqrt{g}}\right) = 0.$$

The second case, ($\lambda_1 = 0$, $\lambda_2 \geq 0$, $\lambda_3 = 0$, $\lambda_4 = 0$, $\lambda_5 = 0$), results in $L = L_p$, $NA = g{L_I}^2$ and the cubic equation

$$A^{\frac{3}{2}} - A_p A^{\frac{1}{2}} + \frac{S}{4k\sqrt{gN}} = 0.$$

These equations show the results are divided between two cell regimes: the hard regime when $L > L_p$, and the soft regime when $L = L_p$. These regimes can be identified with the ratio $\beta = L_p/L_{min} < 1$ for the hard regime, and $\beta \geq 1$ for the soft regime. The length measurement, L_{min}, is calculated from the preferred area specified in Equation (2.5), see Chapter 2. The solutions of these cubic equations give the cell perimeter as

$$L = \begin{cases} \frac{\sqrt{A}}{\sqrt{g}} & \beta < 1 \\ L_p & \beta \geq 1 \end{cases}, \qquad (3.8)$$

cell island perimeter as

$$L_I = \frac{\sqrt{NA}}{\sqrt{g}}, \tag{3.9}$$

and cell area as

$$A = \begin{cases} \left(\sqrt[3]{\frac{1}{2}A_1 + \sqrt[2]{\frac{1}{2}A_1{}^2 + \frac{1}{27}\left(\frac{S}{4k\sqrt{g}} - \frac{S}{4k\sqrt{Ng}}\right)^3}} + \sqrt[3]{\frac{1}{2}A_1 - \sqrt[2]{\frac{1}{2}A_1{}^2 + \frac{1}{27}\left(\frac{S}{4k\sqrt{g}} - \frac{S}{4k\sqrt{Ng}}\right)^3}} \right)^2 & \beta < 1 \\ \left(\sqrt[3]{\frac{-1}{2}A_p + \sqrt[2]{\frac{1}{2}A_p{}^2 - \frac{1}{27}\left(\frac{S}{4k\sqrt{Ng}}\right)^3}} + \sqrt[3]{\frac{-1}{2}A_p - \sqrt[2]{\frac{1}{2}A_p{}^2 - \frac{1}{27}\left(\frac{S}{4k\sqrt{Ng}}\right)^3}} \right)^2 & \beta \geq 1 \end{cases}. \tag{3.10}$$

Note that the cell area and perimeter solutions for the cell island are the same as for the single cell system when there is no adhesion in the system, $S = 0$.

3.4.2 Simulation of a cell island with two cells

Initially we observe the effect of adding cell-cell adhesion on a single boundary between the two cells, see Figure 3.4. There is a clear difference in the morphology of the cells between the hard and soft regimes at the extremes. While some of the observations of the hard and soft regimes of cells are similar to those discussed in Chapter 2, there are also differences observed in the cell island perimeter and changes observed in the cell size.

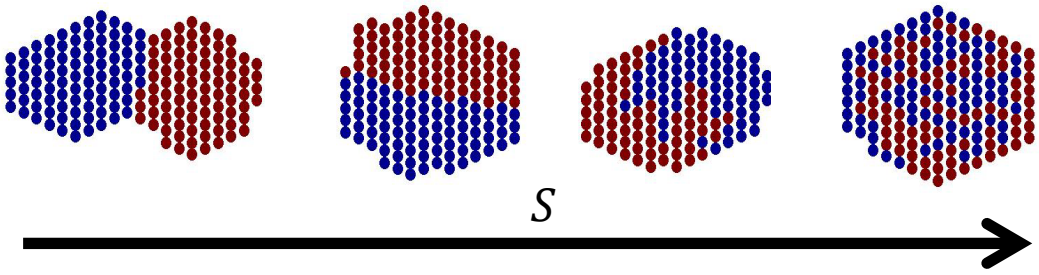

Figure 3.4. Plot of two cells with increasing adhesion from $S = 100, 200, 300, 400, 500$ and 1000. Other parameters are $k = 2$, $\Gamma = 2$ and $A_p = 100$ on a hexagonal pixel grid.

When $\beta < 1$, a hard cell regime occurs. In a hard cell regime cells are stiff polygonal shapes and in the case of hexagonal cell pixels the cells themselves form hexagonal shapes. In the very hard regime in Figure 3.4, when $S = 100$ the pair of cells are stiff with a hexagonal shape and a small connected edge between them. A much larger perimeter is seen on the free edge boundary. This is opposite to the concept of the cell island boundary having a minimum perimeter and affects the comparison between the simulation and the geometric solutions below. When increasing the value of adhesion and creating softer regimes, the interconnected cell boundary grows while still maintaining a polygonal shape. However, the two-cell island forms a hexagonal shape rather than two distinct hexagons.

When $\beta \geq 1$, a soft regime occurs and the cell boundaries are more malleable, forming a more diverse collection of shapes. In softer regimes the boundary between the cells deforms, and the shapes of the cells are no longer polygonal. Larger adhesion values lead to the interconnected cell boundary deforming so that the total cell perimeter can achieve the larger preferred perimeter while using the minimum amount of cell edges connected to empty space, forming a hexagonal cell island. The deformations of the cells in the very soft regime, Figure 3.4 with $S = 1000$, form tendril features inside the islands, the same tendril features seen in Chapter 2.

With no adhesion, $S = 0$, between the cells, the cells would form hexagonal shapes and the system would be the same as above with only the area constraint and perimeter contraction. This system is the same as the single cell case.

The solutions of the cell perimeter, cell island perimeter and cell area in Equation (3.8), (3.9) and (3.10), respectively, are split into two expressions depending on the cell regime. AS in Chapter 2 the cell systems can be distinguished between the hard and soft regimes by the cell perimeter (Figure 3.5a). If a cell is in the hard regime the cell perimeter does not achieve the preferred cell perimeter. Instead the perimeter is larger than L_p and is approximately L_{min} (Figure 3.5a). In a complete epithelial sheet the perimeter would be expected to be L_{min}. However, cells in the island case are able to shrink and as such the cells can be smaller than L_{min}, which is suggested in predictions of the cell perimeter solution, Equation (3.8) shown in Figure 3.5a when $\beta < 1$. The difference in perimeter depends on how strong the area constraint parameter is. In the soft regime the preferred cell perimeter is reached.

While Figure 3.5a shows the mean perimeter of a two-cell island system for simulations with different parameters, Figure 3.5b shows the plot of the mean cell area. In the hard regime the simulation reveals that the cells' areas are smaller than the preferred area; however, the "softer" the regime the smaller the difference between the cell area and A_p. This is expected, because when the influence of the difference in perimeter is lowered in the energy, the cell perimeter becomes closer to the preferred perimeter, and the change in area becomes dominant. However, the cell never

reaches the preferred area, instead when in the soft regime the cell area is reduced further and the softer the system the smaller the cell area becomes.

Qualitatively there are similarities in the behaviour and patterns between the equilibrium of the simulations and the geometric solutions to the geometric optimisation problem in Figure 3.5a, b, and e. However, this is not the case with the plot of the cell island perimeter in Figure 3.5d. The island perimeters in the simulations are larger than the geometric solutions in the hard regime by a factor of 1.2. Although, in the soft regime it appears that the simulation and geometric solutions begin to converge. This difference occurs because of the assumptions placed on both the cells and island and their shapes. As shown in Figure 3.4, when the two-cell island is in the hard regime the border of the island has an irregular edge, in this case two hexagon cells with a connected edge. Whereas in the soft regime, the two cells create a single hexagon to minimise the energy contribution of the cell island boundary, and as a result the cell island has a "smoother" edge. These edges are formed with the interaction between the cell boundaries and cell island boundary and change depending on the value of the regime parameter, β.

Figure 3.5c shows the progression of the shape ratio, g, of the cells and Figure 3.5f shows the shape ratio of the island, g_I. We observe that in the hard regime the cell shape ratio is close to the value $1/48$, representing "hexagons", and decreases in softer regimes. This is a numerical representation of the system changing from "hexagonal" shapes in the hard regime, to shapes with a more malleable boundary with tendrils in the soft regime. However, for harder systems the island shape ratio begins smaller than $g = A/L^2$, the "hexagonal" ratio, and for softer systems the value is closer to the "hexagonal" ratio.

Ideally the difference between the simulations and the geometric solutions could be rectified by expressing g_I as a function of the parameter β or adhesion, S. However, this would require the simulation results beforehand to estimate the correction, although an approximated value can be added if needed.

Understandably, in Figure 3.5, the larger the contraction the smaller the cell will attempt to become. However, the parameter k can counter this cell behaviour as seen in Figure 3.5a which shows that the system "forces" the cell to follow the predicted approximations more closely given that it tries to keep the cell at the preferred area from which the predictions are taken.

Other artefacts in the simulations can occur for a "small" value of the preferred area. In Figure 3.6 the simulations and geometric solutions are similar to Figure 3.5. The cell perimeter follows a similar pattern as seen before. However, in Figure 3.6b, when adhesion is large, $\beta > 2$, the plot shows the difference increasing between the simulations and analytic solution, and the simulations show the cell area is larger than predicted. This effect is similar to the one shown in Figure 3.3 and occurs when the preferred cell perimeter is much larger than the preferred area,

given the number of pixels. At some value, in Figure 3.6b this is $\beta > 2$, the perimeter of the system has a greater influence than the area in the energy equation. Given the area of the cells increase, the cell island area also increases, seen in Figure 3.6e, and hence the cell perimeter also increases, seen in Figure 3.6c, instead of following the geometry model behaviour. The energy cost of increasing the area is smaller than the energy change when increasing the cell perimeter to reach the preferred perimeter. All these differences can be attributed to the cells themselves which are intertwined tendril shapes, seen in Figure 3.4. The simulated cell's size will increase to reach the preferred perimeter due to the restrictions of the lattice.

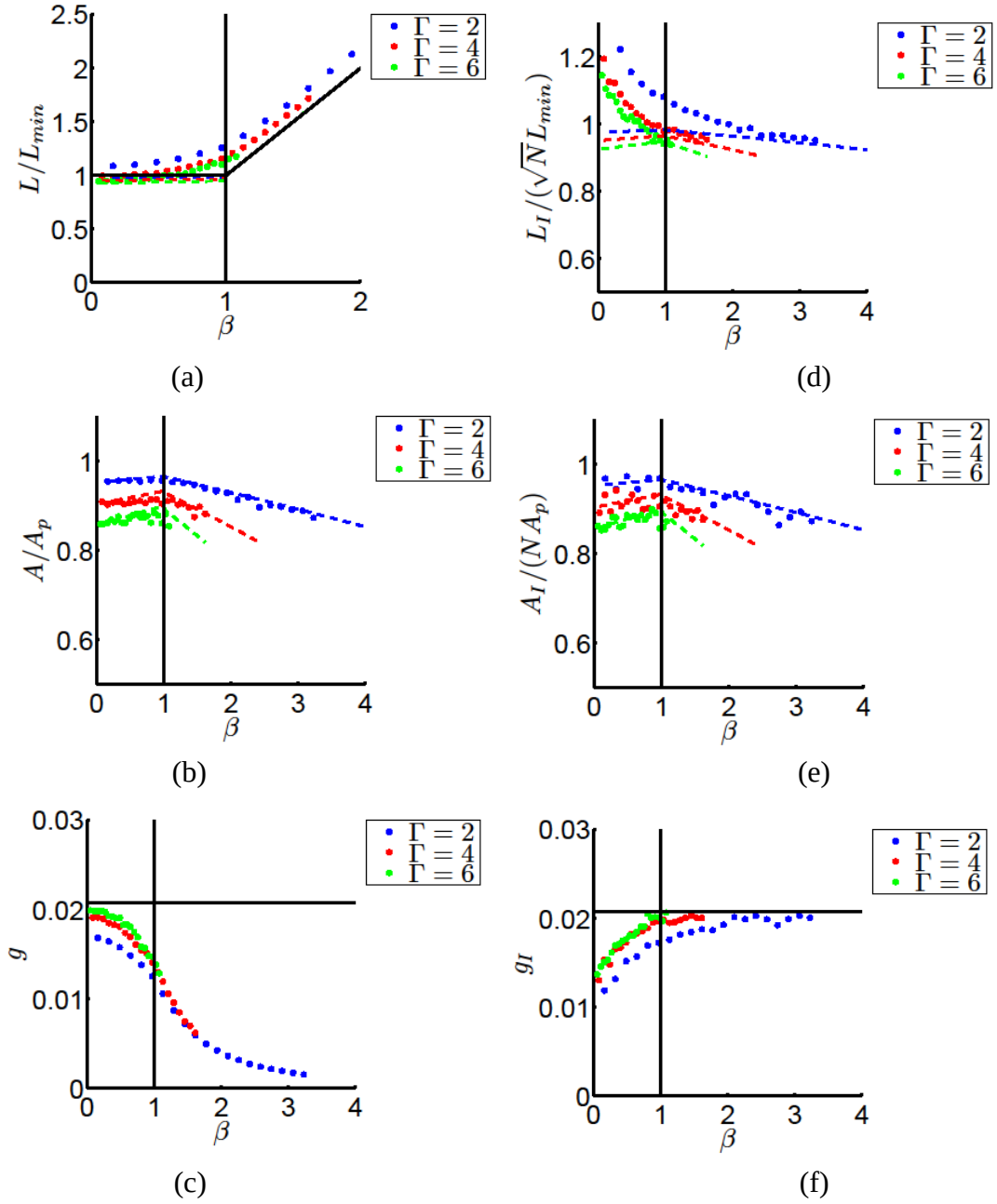

Figure 3.5. Plots, with the preferred area $A_p = 500$, for two-cell island simulated on a hexagonal pixel grid with the CPM showing the (a) mean cell perimeter with the geometric solutions from Equation (3.8), (b) mean cell area with the geometric solutions from Equation (3.10) and (c) ratio $g = A/L^2$ against parameter β, for different perimeter contractions, Γ; and the (d) mean cell island perimeter with the geometric solutions from Equation (3.9), (e) mean cell island area with the sum of the geometric solutions of cell area and (f) ratio $g_I = A_I/{L_I}^2$ against parameter β, for different perimeter contractions, Γ. Each measurement of the cell is averaged over the two cells for the last 50 of 1000 iterations and the island measurements are averaged over the last 50 of 1000 iterations. The simulations have a temperature of $T = 200$ and area constraint parameter, $k = 2$.

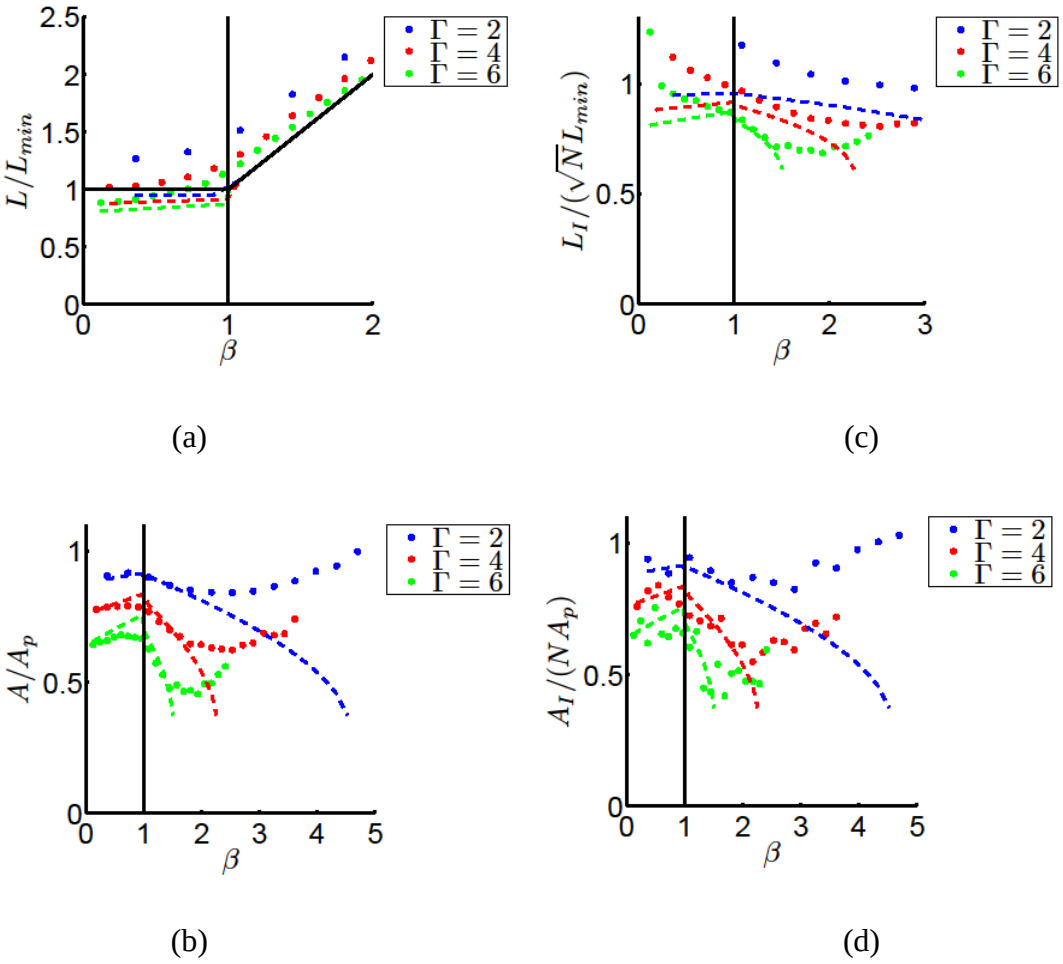

Figure 3.6. Plots, with the preferred area $A_p = 100$, for two cell-island simulated on a hexagonal pixel grid with the CPM showing the (a) mean cell perimeter with the geometric solutions from Equation (3.8) and (b) mean cell area with the geometric solutions from Equation (3.10) against parameter β, for different perimeter contractions, Γ; and the (c) mean cell island perimeter with the geometric solutions from Equation (3.9) and (d) mean cell island area with the sum of the geometric solutions of cell area from Equation (3.10) against parameter β, for different perimeter contractions, Γ. Each measurement of the cell is averaged over the two cells for the last 50 of 1000 iterations and the island measurements are averaged over the last 50 of 1000 iterations. The simulations have a temperature of $T = 200$ and area constraint parameter, $k = 2$.

3.4.3 Simulation of cell islands with more than two cells

Islands with more than two cells follow the same characteristics as the two-cell island case; however, the structure of the island and the organisation of the cells are different. In the hard regime, $\beta < 1$, see Figure 3.7a, the cell boundaries are rigid and as such the cell island boundaries are also rigid. In the soft regime, $\beta \geq 1$, see Figures 3.7b and 3.7c, the cell boundaries are malleable, even forming tendrils in Figure 3.7c, and as a result the cell island boundary is much more regular.

Aspects of the cell island morphology are best exhibited with a larger number of cells. Not only can the boundaries of a cell island be rigid in a hard regime, but the formation and optimal equilibrium configurations of the cell island can be difficult to achieve depending on the initial placement of the cells. Without an increase in fluctuation, from increased "noise", on the cells' boundaries, the cells become fixed and their configuration may not achieve the expected form. Softer, more malleable cells change their shape to geometrically pack themselves to achieve a minimum perimeter of the island, forming a "hexagonal" shape seen in Figure 3.7b. This is particularly evident on the edge of the island. In the soft regime we observe that there are physical differences between the outer layer of cells in contact with the empty space, see Figure 3.7b, compared to the cells surrounded by other cells. The outer layer of cells form "wedges" to fit the circular shape of the island, and the cell island is not restricted by this, forming any shape the parameters will allow.

A change in the number of cells in the simulations or geometric solutions has no significant effect on the average cell and cell island perimeter, in Figures 3.8a and 3.8d, respectively. Figure 3.8a plots the average cell perimeter against β, and shows that the number of cells in the island does not affect the cell perimeter, as the value of the cell perimeter is similar for different numbers of cells in an island. Also, Figure 3.8d plots the average cell island perimeter divided by the square root of the number of cells in the islands against β, and, as with the average cell perimeters, the value of the rescaled cell island perimeters are similar for different numbers of cells in the islands. However, the difference between the simulation values and the geometric solutions seen in Figure 3.5d is also seen in Figure 3.8d.

There is a small difference in the cell and cell island areas as β increases between the different numbers of cells in the cell islands, in Figures 3.8b and 3.8e. Figure 3.8b plots the average area of the cells in the cell islands and Figure 3.8e plots the rescaled value of the cell island area divided by the number of cells in the cell islands. The average area of the cells in the cell islands and the rescaled value of the cell island areas are equivalent. These figures suggest that systems with a smaller number of cells in the cell islands will have smaller cell areas than systems with cell islands containing a larger number of cells, especially for larger values of β (i.e. soft cell regimes). This is most likely due to the cell island perimeter tending to a minimum contracting the boundary

of the cell island. We note that in Figures 3.8b and 3.8e there is a larger difference between the simulation and geometric solution values of the cell area when $\beta \geq 4$. This artefact is similar to the divergence between the simulation and geometric solution values in Figures 3.6b and 3.6d, which were caused by the perimeter mechanisms influencing the cells more than the area constraint mechanism for a "small" preferred area, $A_p = 100$. The divergence occurs here but at a larger value of β for a larger preferred area, $A_p = 500$. This suggests that the artefact occurs for any value of A_p in the simulation of the cell island, but the value of β the artefact occurs at depends on the value of A_p.

Given that the cell perimeters are similar and the differences in the cell areas is small for different numbers of cells in cell islands, the shape ratio of cells, g, plotted in Figure 3.8c against β, is similar for cells in cell islands containing different numbers of cells. Figure 3.8f plots the shape ratio of the cell islands, g_I, against β for cell islands containing different numbers of cells and shows that they are similar for any island size. The behaviour of both of these shape ratios is the same as the behaviour of the shape ratios of the islands with two cells in Section 3.4.2.

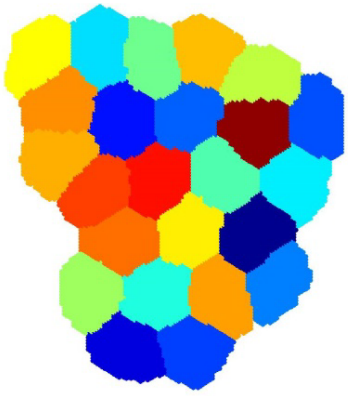

(a) $S = 1000$

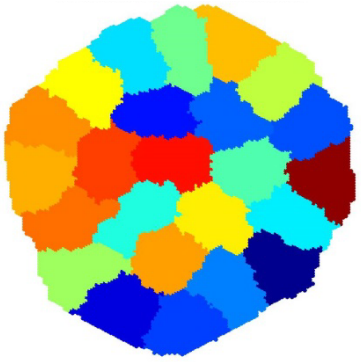

(b) $S = 2000$

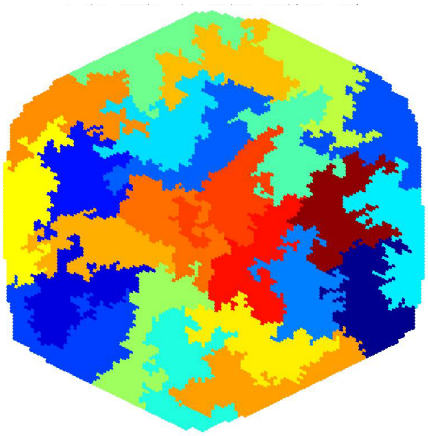

(c) $S = 5000$

Figure 3.7. Example of cell islands a) in the hard regime ($\Gamma = 6$, $S = 1000$, $\beta < 1$) b) the soft regime ($\Gamma = 6$, $S = 2000$, $\beta > 1$), and c) very soft regime ($\Gamma = 6$, $S = 5000$, $\beta > 1$). Each simulation has the parameters $k = 2$ and $T = 500$.

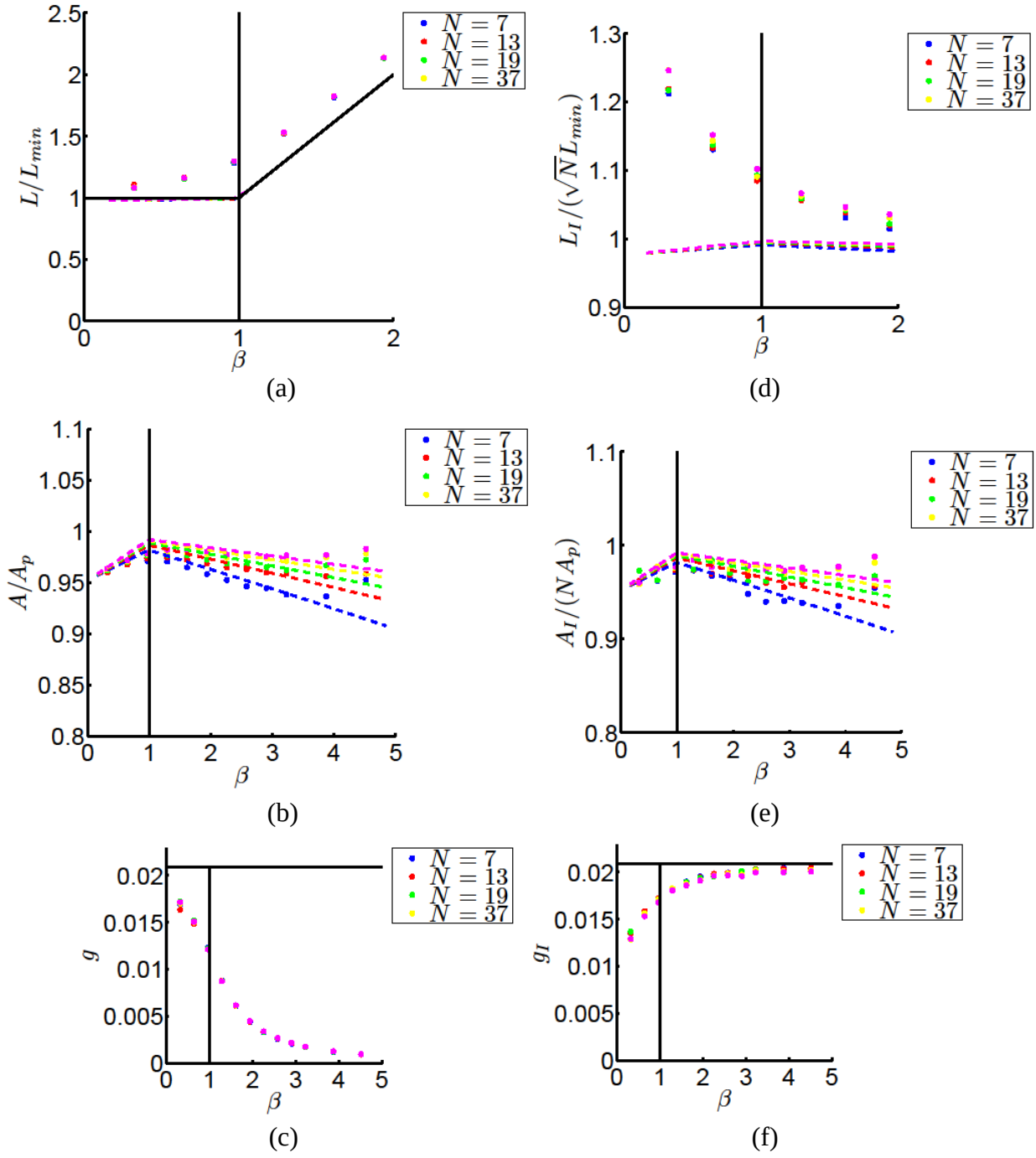

Figure 3.8. Plots, with the preferred area $A_p = 500$, for cell islands simulated on a hexagonal pixel grid with the CPM showing the (a) mean cell perimeter with the geometric solutions from Equation (3.8), (b) mean cell area with the geometric solutions from Equation (3.10) and (c) ratio $g = A/L^2$ against parameter β, for different number of cells in the cell islands, N; and the (d) mean cell island perimeter with the geometric solutions from Equation (3.9), (e) mean cell island area with the sum of the geometric solutions of cell area and (f) ratio $g_I = A_I/{L_I}^2$ against parameter β, for different number of cells in the cell islands, N. Each measurement of the cell is averaged over the cells for the last 50 of 1000 iterations and the island measurements are averaged over the last 50 of 1000 iterations. The simulations have a temperature of $T = 200$ and area constraint parameter, $k = 2$.

3.5 DISCUSSION

The cell and cell island size are strongly influenced by the interacting mechanisms of the cell area constraint and perimeter contraction, and the cell and cell island shapes are influenced by the interacting mechanisms of the cell perimeter contraction and adhesion.

In Chapter 2 a geometric representation was developed from the simulated system; however, in this case we consider an optimisation approximation of the energy function. These geometric solutions are comparable to the simulation results, with a few differences.

The cell island can still be separated into a hard and soft regime as described for the epithelial layer in Chapter 2; however, with the addition of "empty space" cells can become smaller and hence the perimeters can become smaller than the calculated minimum perimeter, L_{min}. This behaviour is the same as the wound case in Chapter 2. Although there can be a decrease of the cell perimeter, the perimeter is still larger than the preferred perimeter, L_p, and the cells follow the same behaviour, with stiff polygon shapes in the hard regime and malleable cell perimeters in the soft regime.

The different shapes of cells in the hard and soft regimes affect the perimeter of the free edge of the cell island and that of epithelial cell aggregates. The hard systems create stiff cells with a small number of fluctuations compared to the soft systems. This results in a cell island boundary with irregular edges created by the tiling of the cells. In addition, the cells have difficulty attaining the preferred perimeter due to the small number of fluctuations. These outcomes can be countered by increasing the noise of the system. Comparatively, softer systems create smoother boundaries due to the malleable nature of the cell boundaries. This difference between cells and the system edges in the simulation of the hard and soft regimes is the reason for the difference in results between the simulations and the geometric solutions, since the optimisation assumes specific cell and cell island shapes.

An unexpected result from the investigation of the cell island case is the behaviour of the cell island in a soft regime. Both the simulations and geometric solutions show the cell island will become smaller in softer regimes. However, it was found that the cells themselves follow this pattern as well. In addition, the cell area never reaches the preferred area of A_p, and the larger the contraction or the number of cells, the larger the decrease of the relative area. This result is due to only one mechanism acting on the perimeter of island, namely the perimeter contraction mechanism.

Chapter 4: The Three-Dimensional CPM and Single Cell Extrusion from an Epithelium

4.1 INTRODUCTION

In this chapter we investigate the extrusion of a modified cell, defined as a cell with different parameter values to its neighbours, from an epithelium using a three-dimensional CPM. The three-dimensional CPM is an extended version of the two-dimensional CPM from Chapter 2. The addition of the third dimension, height, allows the extruded cell in the simulations to interact with all its surrounding neighbours in the epithelium and provides space for the cell to extrude into, which a two-dimensional model does not.

Epithelial cells have a high turnover rate that is essential for the upkeep of the protective epithelial layer (Blanpain et al., 2007; Hooper, 1956; Pellettieri & Sanchez Alvarado, 2007). This turnover or replenishment requires dead or dying cells to be extruded from the layer. Biological experiments show that certain factors, such as overcrowding in the system, can affect the rate of cell extrusion (Marinari et al., 2012). In addition, an actomyosin ring can form around the cell neighbours to extrude a cell by squeezing it out of the epithelium (Slattum et al., 2009). While pressure due to overcrowding can cause cells to extrude, this chapter focuses on the reorganisation of cells, the main use of the CPM, to extrude a modified cell out of the epithelium.

Much like the two-dimensional CPM in Chapters 2 and 3 a geometric model of the cells can be implemented in three dimensions. These geometric models do not have to be derived from the CPMs but apply similar mechanisms of adhesion and contraction as energy components. Hannezo, Prost, and Joanny (2014) present a geometric model which describes epithelial cells and epithelium in three dimensions. These geometric models can be altered to generate additional information about the model and cells. As such the model presented in Hannezo et al. (2014) is examined and conditions are applied to generate information about the homeostasis state of the epithelium, focusing on the changes of the number of cells relative to the adhesion and contraction mechanism in the model. The extrusion of cells from the epithelium can be associated to the changes in the capacity of the epithelium to achieve homeostasis.

The extrusion of a single modified cell can be thought as an alternate form of the two-dimensional micro-wound healing case in Chapter 2. In the micro-wound case a cell is removed

from the system and the neighbouring cells need to fill the opening; whereas in the case of the extrusion of a cell, a cell is still located in the position that would otherwise be an opening.

When the two-dimensional CPM represents the epithelium as a horizontal cross-section, or a top down view, of the cells and cell layer it does not include a space for the modified cell to move into if extruded. For the two-dimensional CPM to account for the lack of space changes need to be made to the modified cell's mechanisms, such as the area constraint from Function (2.1). Ultimately this problem becomes a wound closure problem similar to that in Chapter 2 but with the addition of a modified cell occupying the wound.

Alternatively, when the two-dimensional CPM represents the epithelium as a vertical cross-section, space is available for the extrusion of a modified cell. However, the representation of the two-dimensional CPM restricts the number of neighbours interacting with the selected cell to two rather than the potential six in the horizontal representation. Again, the parameters of a selected cell would need to change; however, the area constraint can remain and only the mechanisms affecting the junctions and boundaries of the cell would need to change, specifically the contact of the cell boundaries.

Unlike the two-dimensional CPM, the three-dimensional CPM includes space for the modified cell to move into if extruded and allows the selected cell to interact with all possible neighbours in the epithelium. Given the extrusion of a modified cell is an alternative to the micro-wound case, this chapter investigates a micro-wound scenario as well as the extrusion of a modified cell. In particular, we will focus on the CPM simulations with the interactions between the adhesion and contraction mechanisms that lead to the closure of a micro-wound and the extrusion of a single modified cell.

4.2 THE THREE-DIMENSIONAL CPM

A three-dimensional CPM emulates cells as a collection of connected voxels (three-dimensional pixels). The voxels tessellate the area and are ideally the same shape, for example cubes; hexagonal prisms shown in Figure 4.1a with the respective lattice in Figure 4.1b; and rhombic dodecahedrons shown in Figure 4.1c and respective lattice in Figure 4.1d. Each shape has a different number of surfaces connected to the neighbouring voxels: the cube has six connections; the hexagonal prism has eight and the rhombic dodecahedron has ten. Similarly to the pixel shape of two-dimensional models, the voxels can also be connected by their edges and corners to other voxels and the implementation of the models must consider whether these connections should influence the mechanisms. Artefacts in the shape of the cells can arise depending on the three-dimensional lattice structure. Ideally the dodecahedron can be used to remove the influence of corners; however, for this chapter we have selected hexagonal prism pixels, consistent with the two-dimensional model, to expand the model and mechanisms from Chapter 2.

The representation of the cell interaction mechanisms of the three-dimensional model is incorporated differently to that of the two-dimensional model. While the two-dimensional models incorporate the area and perimeter of the cells and their pixels, the three-dimensional model uses the volume and surface area, respectively. The energy Function (2.1) can be generalised for the 3D model as

$$E = \frac{k}{2}\sum_{j}^{N}\left(V_j - V_p\right)^2 + \frac{\Gamma}{2}\sum_{j}^{N} {A_j}^2 - \frac{S}{2}\sum_{i,j}\left(1 - \delta_{i,j}\right).$$

The first term represents volume constraint (analogous to the area constraint in the two-dimensional model) with the cell volume, V_j, the preferred volume, V_p, and a strength parameter k. The second term represents a cell surface area contraction with the total cell surface area, A_j, and a strength parameter Γ. The third and final term represents the adhesion with $\delta_{i,j}$ identifying the surface area connection between pixels (voxels) i and j and the strength parameter S.

The metropolis algorithm of the model does not change from the two-dimensional CPM. The cells and their boundaries evolve over time by randomly selecting a voxel on the boundary of the cells and measuring the change in the "energy" function, ΔE, that would result if the voxel were reassigned to a neighbouring cell label. If the energy decreases, $\Delta E < 0$, the index j will change, whereas if the energy increases, $\Delta E > 0$, the change is allowed with the probability $exp(-\Delta E/T)$, where T is a temperature-like parameter that controls the "noise" in the system. Each and every

pixel has the opportunity for an index change and this represents the Monte Carlo Step (MCS), which we refer to as a single iteration in the CPM.

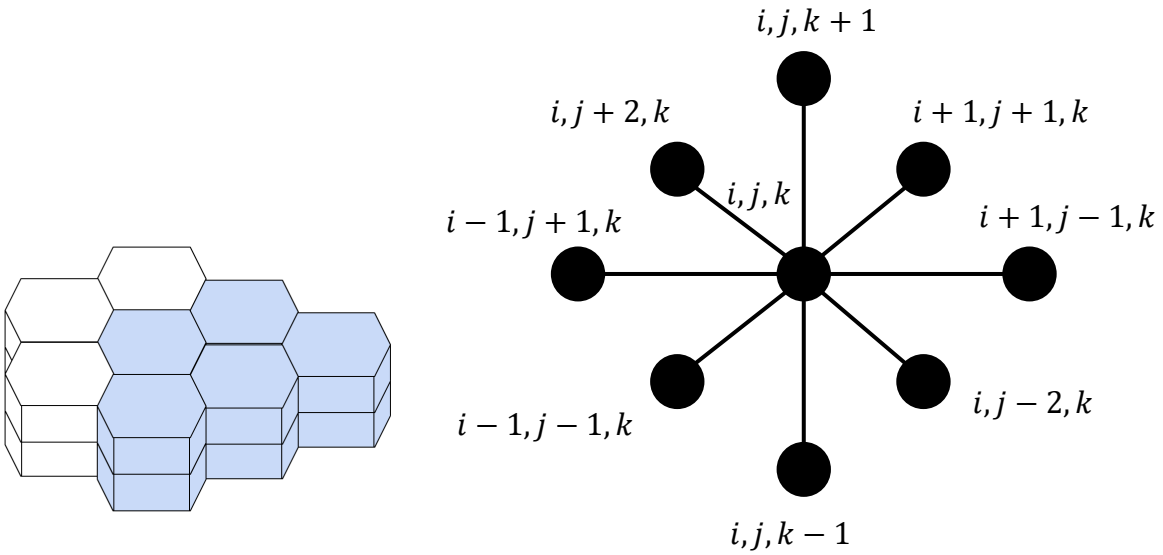

(a) (b)

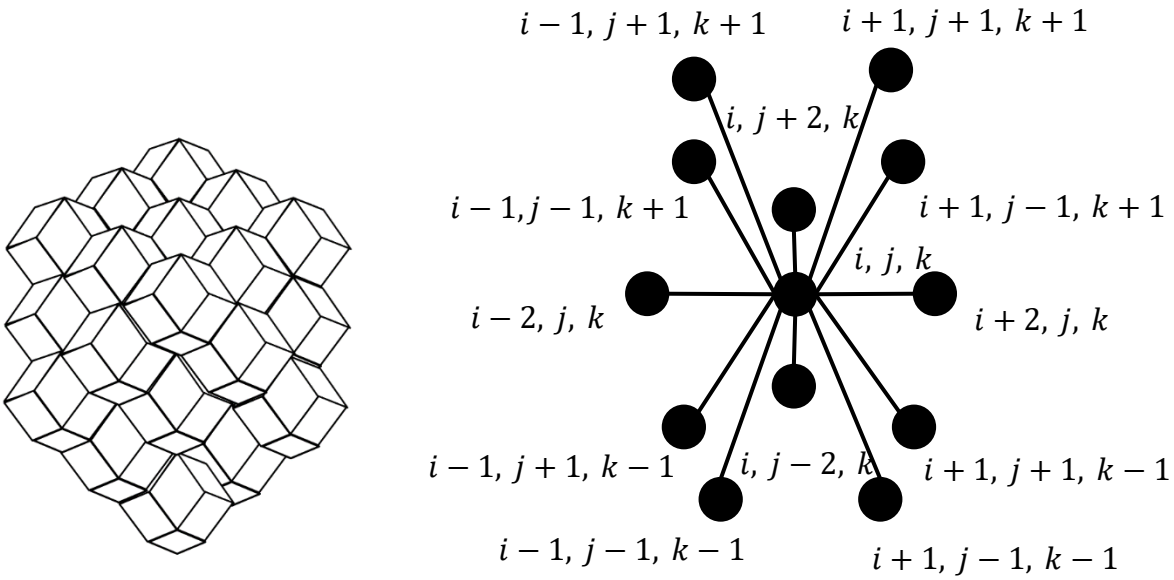

(c) (d)

Figure 4.1. a) Three-dimensional hexagonal prism pixels configuration, and b) the corresponding lattice. c) Three-dimensional dodecahedron pixels configuration, and d) the corresponding lattice.

Unlike the two-dimensional CPM in Chapter 2, a connection condition is not included in the three-dimensional model. The “paths” of connected voxels, with the same label, no longer split or encase other cells since there is an extra spatial dimension. By excluding a connection condition, voxels of a cell can separate from the main group and can result in cells breaking apart or “disintegrating” in a very soft or noisy system. We will avoid these parameter regimes in this chapter when investigating the three-dimensional model.

The epithelial layer is modelled and simulated in three dimensions using the CPM as a collection of pixels in a three-dimensional lattice. For simplicity the “hexagonal prism” voxels, shown in Figure 4.1a, were chosen. The hexagonal prism pixels can extend the mechanisms and results from Chapter 2 into three dimensions.

The energy of the system with N-cells is expressed in the function

$$E = \frac{k}{2}\sum_{j}^{N}\left(V_j - V_p\right)^2 + \frac{\Gamma}{2}\sum_{j}^{N}{A_j}^2 - \frac{S}{2}\sum_{j}^{N}A_{j,c-c} - \frac{\alpha}{2}\sum_{j}^{N}A_{j,c-b} + \frac{\Gamma_t}{2}\sum_{j}^{N}{L_{j,t}}^2, \qquad (4.1)$$

with summation terms related to the jth cell volume, V_j, total surface area, A_j, surface area in contact with other cells, $A_{j,c-c}$, surface area in contact with the substrate, $A_{j,c-b}$, and the apical (top) perimeter of the cells, $L_{j,t}$ (see Figure 4.2).

The first term in Function (4.1) represents an energy cost for deviating from a preferred volume, V_p, i.e., the cells resist expansion or compression. The second term represents the cortical contraction around the membrane of the cells. The third term represents the cell-cell adhesion, attributed to the presence of adhesion molecules, such as E-cadherin, and is proportional to the surface area in contact with the cells. The fourth term represents the adhesive connection of the cells to the substrate, with a strength parameter α, and the final term is the apical ring contraction proportional to the perimeter of the top of the cells, with a strength parameter of Γ_t.

The apical perimeter contraction term requires an average height for each cell. The average height for a cell is calculated by averaging all the cell pixel heights where their top surface is connected to an empty pixel. The apical perimeter of the cell is the perimeter on the layer closest to the average height.

Note that the cell-cell and cell-substrate adhesion terms are assumed to be negative, i.e., the cells preferentially expand their boundaries shared with neighbouring cells or substrate. However, these adhesion terms compete with the contractile surface tension that dominates when the perimeter becomes elongated.

Unlike the energy Function (2.1) in the two-dimensional CPM the three dimensional CPM cannot be expressed in a similar way as Function (2.2) given the differences parameters and related surface areas. Even when completed there is not information that can be observed from the resulting function.

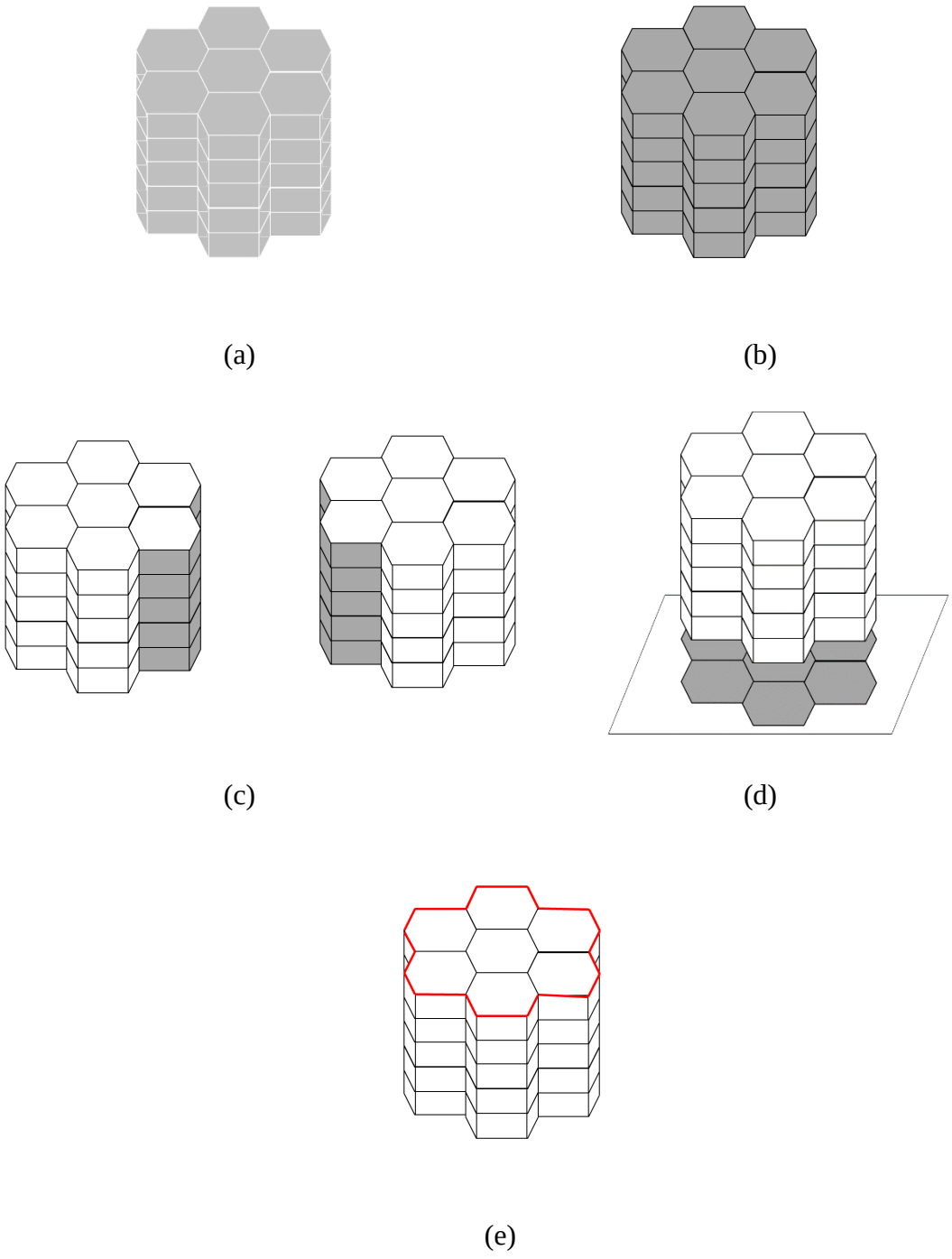

Figure 4.2. Representations of components that contribute to the energy described in the three-dimensional CPM: a) the volume, V_j, b) the total surface area, A_j, c) the surface area in contact with a neighbouring cell, $A_{j,c-c}$, d) the surface area in contact with the substrate, $A_{j,c-b}$, and e) the apical perimeter contraction of the cell, $L_{j,t}$.

4.3 THE HARD AND SOFT REGIME IN THE THREE-DIMENSIONAL CPM

The two-dimensional CPM (Noppe et al., 2015) and vertex model (Farhadifar et al., 2007) use three components in the energy function, namely: the area constraint (similar to the volume), perimeter contraction (similar to surface area), and adhesion between cells. This competition between contraction and adhesion results in the cell behaviour falling into two regimes: the “hard” regime and “soft” regime. The cells exist in either the hard regime, where cells are stiff and boundaries do not fluctuate frequently which creates fixed cell shapes (see Figure 4.3a), or the soft regime, where cells develop elongated boundaries (see Figure 4.3b).

The connection between cells operates differently in three dimensions. The cell-cell adhesion and total surface area contraction are the main contributors for determining the cell regime and in three dimensions we will use the same classification. However, the apical perimeter contraction and the cell substrate adhesion are mechanisms that could also influence the cell regime. The three-dimensional cell regimes are identified with a similar parameter to that in two dimensions, $\beta = \Gamma/(2SA_{min})$, where A_{min} is the minimum surface area for a cell given the preferred volume, the height, h, and shape dependent on the lattice structure. Hexagonal prism pixels create a “hexagonal” prism shaped cell, see Figure 4.2, to find the minimum surface area,

$$A_{min} = 2h\sqrt{\frac{12V_p}{h} - 3} + \frac{2V_p}{h},$$

where the area is expressed in two terms. The first term represents the lateral surface area and the second term represents the top and bottom surface area.

If $\beta < 1$ the system is in the hard regime and the cell’s surface area is close to the minimum cell surface area of A_{min}. For a temperature (noise) of $T = 2000$ in Figure 4.4a the cells achieve this minimum area; however, for a higher temperature of $T = 20000$ the cells overcome the volume constraint and can reduce in volume and hence can reduce in surface area below A_{min}. The shrinking of the cell is comparable to the observations of the cell islands in Chapter 3 where there are empty pixels surrounding the islands in the simulations. The volume constraints can also be overcome by other mechanisms, such as contraction, and strong fluctuations.

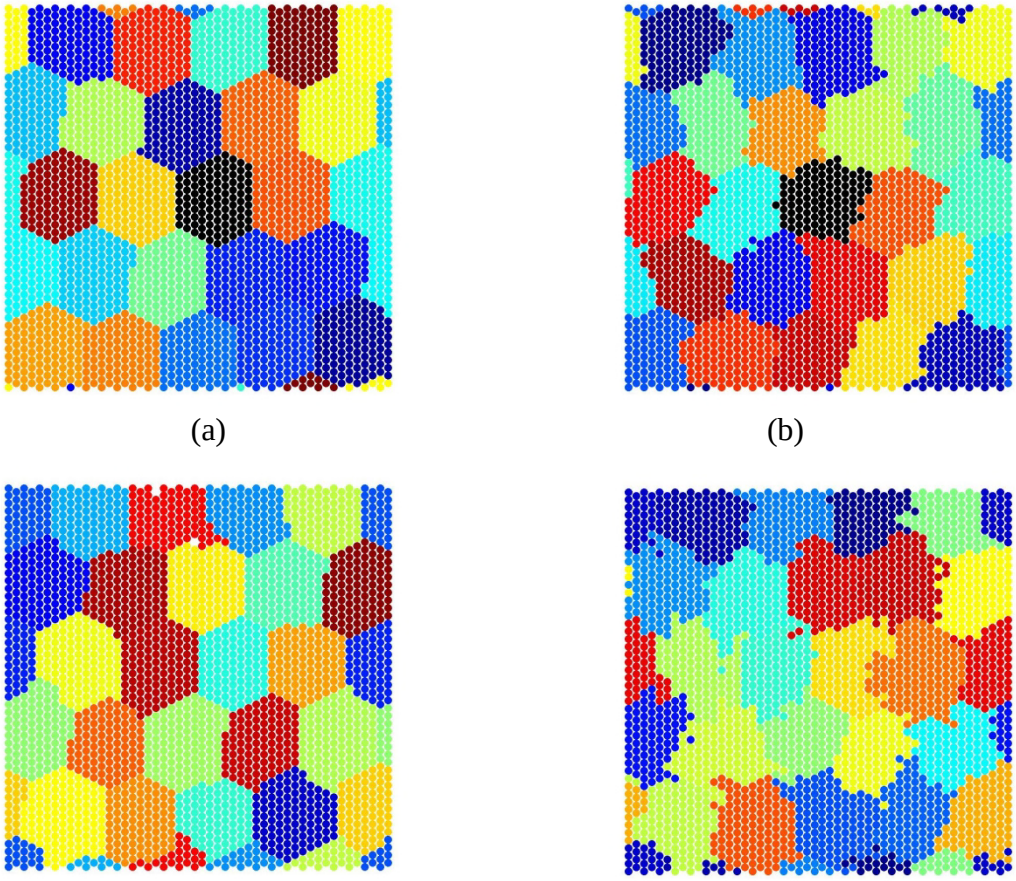

(a) (b)

(c) (d)

Figure 4.3. Distributions of simulated three-dimensional cells in different regimes viewed in horizontal cross-section. a) Represents a hard regime of cells creating quasi-polygonal shapes (approximating a hexagon) on the apical pixel layer, $S = 20000$ and $\Gamma = 50$ ($\beta = 0.3663$). This distribution is similar on each pixel layer of the monolayer. b) Represents a soft regime of cells on the apical pixel layer, $S = 65000$ and $\Gamma = 50$ ($\beta = 1.1905$). This distribution is similar on each pixel layer of the monolayer. c-d) Represent the apical and basal pixel layer, respectively, of a soft cell regime, $S = 65000$ and $\Gamma = 50$ ($\beta = 1.1905$), with the addition of an apical perimeter contraction of $\Gamma_t = 300$. All simulations use parameters $k = 100$, $\alpha = 2S$, $V_p = 500$ with $N = 25$ cells on a $50 \times 50 \times 10$ hexagonal layered pixel grid.

The cells are represented in three dimensions with distinctly different pixel layers on the top and the bottom of the cell monolayer. Figure 4.4b shows a plot of the ratio of the average apical, L_t, and basal, L_b, cell perimeters calculated for the top and bottom pixel layers of the cells. Similarly to Figure 4.4a, low noise in the system allows the cells in the hard regime to achieve the "minimum perimeter", expressed as

$$L_{min} = 2\sqrt{\frac{12V_p}{h} - 3},$$

and for a higher temperature, $T = 20000$, the cell perimeters deviate slightly from this "minimum perimeter". However, in a very hard system fewer basal layer cell perimeters drop below L_{min}, except in one case where the top perimeter, L_t, is zero, suggesting that the cells have shrunk in height.

If $\beta > 1$ the system is in the soft regime and the cells are able to achieve the preferred cell surface area, A_p, and the preferred cell volume, V_p, with different cell configurations. This is observed in Figure 4.4a, where at a low temperature, $T = 2000$, the cells follow the preferred cell surface area closely, and for a higher temperature, $T = 20000$, the system still follows the trend; however, with a slightly larger surface area. The difference of the simulated cell volume between the two temperatures is due to the amount of fluctuations. A low temperature has a small amount of fluctuations which means that the area is close to the value of A_p and a high temperature has more fluctuations increasing the surface area and will have a value larger than A_p.

Given the cells are represented in three dimensions we can observe differences in the apical and basal pixel layers of the cells. Figure 4.4b is a plot of the ratio of the average apical, L_t, and basal, L_b, cell perimeter. As the system becomes "softer", β increases, and the apical perimeter becomes smaller than the basal perimeter. This difference occurs because the apical surface of the cells are in contact with empty space, with only the surface area contraction applied, whereas the basal surface area is in contact with the substrate with both contraction and substrate adhesion applied. The addition of a cell-substrate adhesion constraint allows for greater flexibility in the junctions connecting the boundaries of the cells. However, by removing the basal adhesion from the system in Figure 4.4c there is no change in the behaviour of the cell perimeter from Figure 4.4b. This suggests that the only other difference between the apical and basal layers is that the basal layer is connected to a boundary rather than empty space above the apical pixel layer.

Although the substrate adhesion does not affect the regime of the cells, other mechanisms can, such as an apical perimeter contraction. Applying the apical perimeter contraction term to the cells in the system provides another property differentiating the apical and basal layers. Figure 4.4d shows the apical and basal layer perimeters with the addition of an apical perimeter contraction of $\Gamma_t = 300$. In the hard regime some of the apical layer perimeters are close to zero, while the basal layer is closer to the "minimum perimeter", showing that the cells have shrunk, or are attempting to shrink, in height. In the soft regime there is a clear difference in the apical and basal layer perimeters, where the apical perimeter remains at approximately L_{min} and the basal layer increases,

following the trend of the preferred cell perimeter. This is shown in Figure 4.3c and 4.3d; the apical pixel layer of the cells with the apical perimeter contraction appears to have the stiff polygonal shapes similar to the hard regime (see Figure 4.3c), and the basal pixel layer the cells have malleable boundaries which is characteristic of the soft regime (see Figure 4.3d). The difference in the apical and basal layers of the epithelial cells is also evident in biological experiments, such as in Figure 2.6, which shows a tight quasi-polygonal packing on the top while dynamically moving cell protrusions forming on the substrate.

The apical contraction can separate the connection of the cells on the apical layer if the surface contraction term, Γ_t , is too strong (see Figure 4.5). While the exact value at which this would occur is unknown, we choose to add this mechanism at varying strengths until the separation of cells occurs. The cell-substrate adhesion attaches the cell to the substrate and will provide the cells with greater coverage of surface area on the substrate when there is an adjacent empty space for the cells to move into.

The initial cell configurations of all simulations in this chapter for three dimensions were generated by creating a configuration of 25 $10 \times 10 \times 5$ pixel square prism cells in a sheet located in a $50 \times 50 \times 10$ pixel system and a $50 \times 50 \times 5$ empty region above the cell sheet. These configurations were run with the parameters $k = 100$, the S and Γ ratio $\beta = 1$ and $T = 2000$ until an energy equilibrium was reached. These simulations generated cell configurations with cross sections of the cells similar to Figure 4.3b. The three dimensional simulations used these configurations and included required parameter values to obtain the observed results.

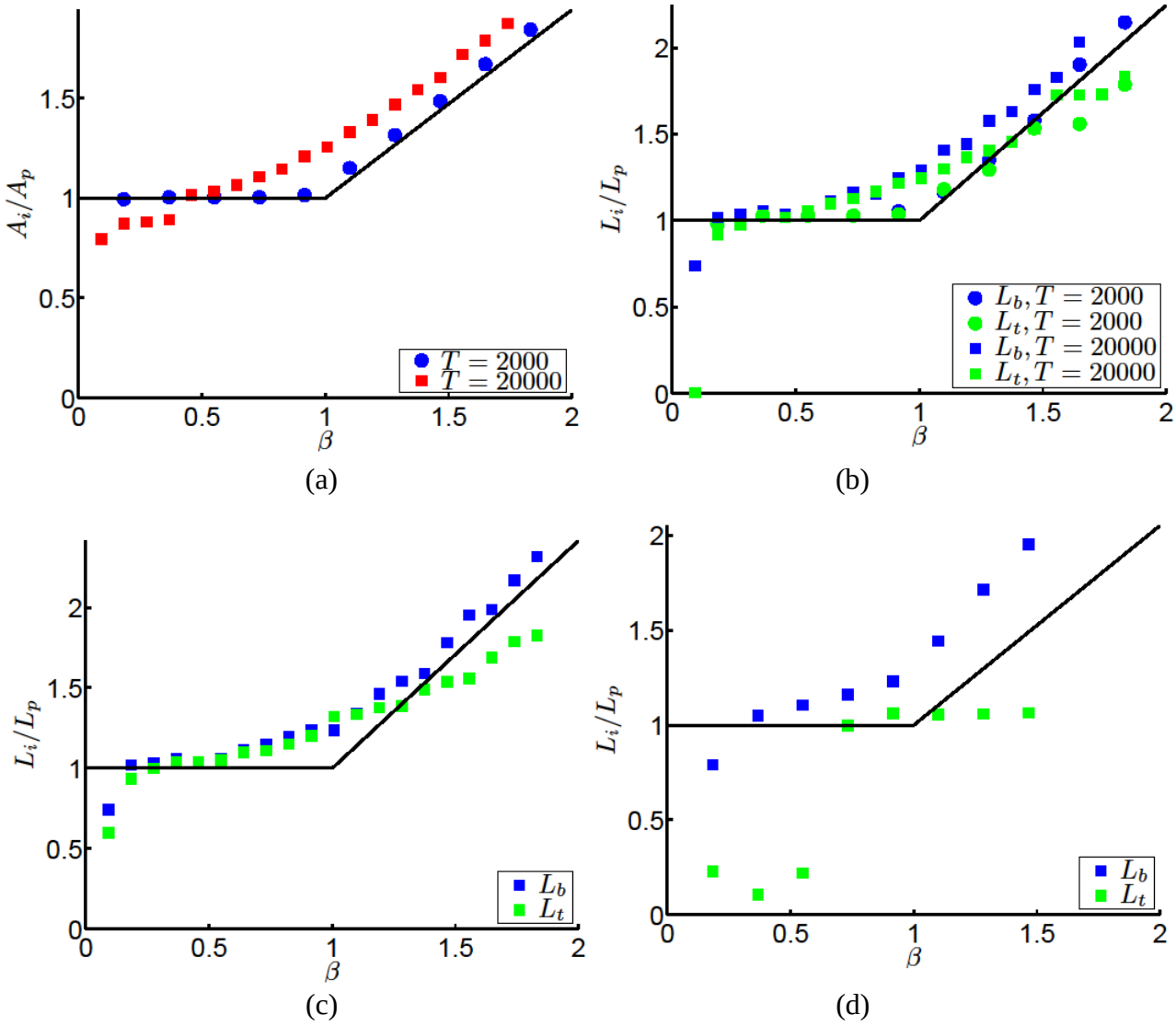

Figure 4.4. Plots of the differences between a hard and soft regime. a) Ratio of the average total cell surface area of all the cells at the final iteration of a single simulation with the minimum total surface area against β. Two temperatures are represented, $T = 2000$ (circles) and $T = 20000$ (squares). b) Ratio of the average apical (green) and basal (blue) pixel layer cell perimeter of all the cells at the final iteration of a single simulation with the minimum perimeter against β. Two temperatures are represented, $T = 2000$ (circles) and $T = 20000$ (squares). c) Ratio of the average apical (green) and basal (blue) pixel layer cell perimeter of all the cells at the final iteration of a single simulation with the minimum perimeter against β, with the removal of substrate adhesion, $\alpha = 0$. d) Ratio of the average apical (green) and basal (blue) pixel layer cell perimeter of all the cells at the final iteration of a single simulation with the minimum perimeter against β, with the addition of apical perimeter contraction, $\Gamma_t = 300$. All simulations have the parameters $k = 100$, $\Gamma = 50$, $\alpha = 2S$, $V_p = 500$ with $N = 25$ cells on a $50 \times 50 \times 10$ hexagonal layered pixel grid.

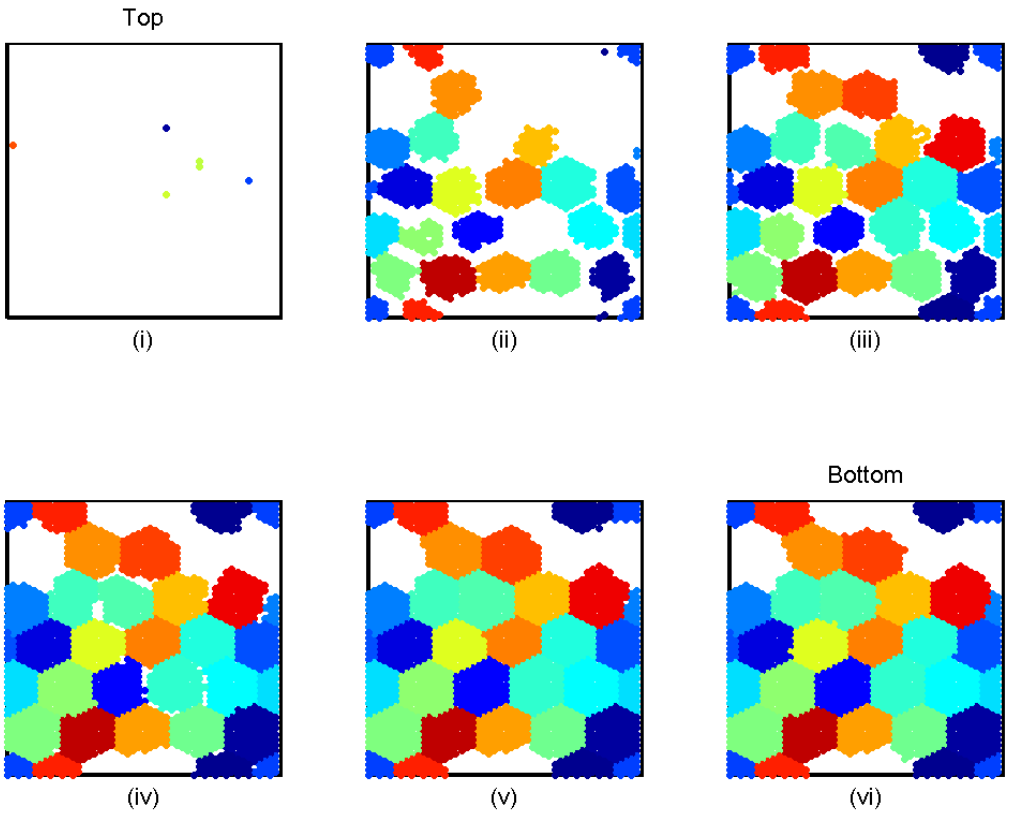

Figure 4.5. Example of a simulation with a large apical contraction which results in cells separating from each other. From left to right the figure shows pixel layers 6, 5, 4, 3, 2 and 1 of the simulations with the figures (i), (ii), (iii), (iv), (v) and (vi), respectively. Layer 5 is the top and layer 1 is the bottom of the monolayer. The parameters for this example are $k = 100$, $\Gamma = 50$, $S = 65000$ ($\beta = 1.1905$), $\alpha = 2S$, $T = 20000$ and $\Gamma_t = 800$ with $N = 25$ cells on a $50 \times 50 \times 10$ hexagonal layered pixel grid.

4.4 GEOMETRIC MODEL

Similarly to the two-dimensional models, the three-dimensional CPM can be simplified to a geometric representation model. These geometric models can be used to understand the behaviour of simulated cells in the CPM. Hannezo et al. (2014) presents one example of a geometric model using the geometric representation of cells in an epithelium with an energy function similar to those seen in the CPM and vertex models. Hannezo et al. (2014) expressed the energy for a single cell in an epithelium as

$$E = \frac{k}{V_o}(V - V_0)^2 + S_b A_{basal} - S_l A_{lat} + \Gamma_a P_{ap}. \quad (4.2)$$

The energy function of the geometric model contains: a volume constraint with the cell volume, V, a preferred volume, V_0, a strength parameter k; a perimeter contraction around the apical perimeter of the cell, P_{ap}, with the strength parameter Γ_a; an adhesion term between the cell and the substrate on the basal surface area, A_{basal}, with a parameter S_b; and an adhesion (or negative tension) on the lateral surface of the cells, A_{lat}, which is assumed to be in contact with the other cells, with the parameter S_l. The volume constraint is the same as the terms in the CPM. The lateral and surface area adhesion is the same as the cell-cell adhesion in the CPM and the basal surface area tension is the same as the substrate adhesion in the CPM. There is no surface area contraction term in the CPM and the model in Hannezo et al. (2014). Therefore, the apical perimeter contraction would instead be an additional mechanism. The main difference between the two energy functions is that there is no surface area contraction, which leads to extremes of the cell morphology.

Assuming that $k \to \infty$ then the volume of the cell will remain unchanged and $V = V_0$. Given this property and assuming the cell has the same shape with only varying height, h, and radius, r, they can be expressed as $h = 2V_0/(\sqrt{3}r^2)$ (Hannezo et al., 2014).

Energy Function (4.2) only produces two types of extreme cell shapes dependent on apical and basal adhesion (or tension). Large flat disk cell when $S_b < 0$ and $S_l > 0$ or very tall thin cell depending on $S_b > 0$ and $S_l < 0$. In order to avoid these extreme shapes and allow for the existence of an energy minimum at a finite value of r, Hannezo et al. (2014) added stabilising terms r^4 and $\frac{2}{r^2}$ which are expressed as the confinement energy of the cytoplasmic components. These terms are based on the confinement of a solution of non-adsorbing Gaussian polymers to a thickness h requiring an energy $\frac{A}{h^2}$ (Gennes, 1979) and $\frac{2A}{r^2}$ when the cell is tall. The coefficient A in the terms is dependent on the properties of the polymer (Hannezo et al., 2014). These stabilisation terms are

added because biological cells cannot be indefinitely compressed (Coulombe & Wong, 2004; Manning, Foty, Steinberg, & Schoetz, 2010) and the cell nucleus is a rigid object that is deformed when cells are confined (Versaevel, Grevesse, & Gabriele, 2012). While in this model cell volume is kept constant, without the stabilisation terms the cells have strong deformations creating highly anisotropic very flat or very thin elongated shapes.

In Hannezo et al. (2014) the unit length and unit energy are provided as $\frac{4^{1/6}}{3}V_0^{1/3}$ and $\frac{3^{1/3}}{4}\frac{A}{V_0^{2/3}}$. By rescaling the parameters $\frac{2^{1/3}}{3^{1/6}}\frac{S_b V_0^{4/3}}{A} \to S_b$, $\frac{2^{1/6}4^{5/6}S_l}{AV_0^{2/3}} \to S_l$ and $\frac{2^{5/3}3^{1/3}\Gamma_a}{A} \to \Gamma_a$ the energy for a single cell can be expressed as a function expressed with only the radius,

$$E(r) = S_b r^2 - \frac{S_l}{r} + \Gamma_a r + r^4 + \frac{2}{r^2}, \qquad (4.3)$$

and the energy for the epithelium is expressed as $E_{ep} = NE(r)$.

Hannezo et al. (2014) provided an alternate stabilising mechanism introducing components with terms in the energy equation which are similar to the CPM representation of cell surface area contraction. This mechanism applies active regulation of the tensions, and expands them to the first orders to achieve preferred basal and lateral surface areas, A_b^0 and A_{lat}^0, respectively:

$$S_b = S_b^0 + \delta_1(r^2 - A_b^0),$$

and

$$S_l = S_l^0 + \delta_2\left(\frac{V_0}{r} - A_{lat}^0\right).$$

It is noted that this results in the same terms as introduced in the other stabilising method. If we take the preferred areas to zero these stabilising terms produce the surface area contraction terms in the energy equations similar to the CPM. However, these surface area contractions are different to Function (4.1) since they split the surface area up into lateral and basal components whereas the CPM function uses the total surface area of the cell.

The cells in the model can have three typical morphologies derived from the parameter in Function (4.3): squamous (flat), cuboidal and columnar (Hannezo et al., 2014). If the basal surface tension is dominant ($S_b < 0$ and $|S_b| \gg 1$) the cells are squamous with $r \approx \sqrt{-S_b/2} \gg 1$, if the lateral cell-cell adhesion is dominant ($S_l > 0$ and $|S_l| \gg 1$) the cells are columnar with $r \approx 4/S_l \ll 1$, if the lateral cell-cell contraction is dominant ($S_l < 0$ and $|S_l| \gg 1$) the cells are squamous with a $r \approx (-S_l/4)^{1/5} \gg 1$ and if the apical perimeter is dominant ($\Gamma_a \gg 1$) the cells are also columnar with $r \approx 2/\sqrt{\Gamma_a} \ll 1$ (Hannezo et al., 2014).

4.4.1 Extrusion results from the geometric model equilibrium with a fixed area

While the purpose of the geometric model is not to represent the extrusion of cells from the epithelium but rather the morphology of the cells in an epithelium with their height and radii, we can modify the model to provide some information about the extrusion of cells. We do this by observing whether the number of cells corresponding to the energy minimum increases, or decreases, when parameters are varied. If we assume that the epithelium, with N cells, is contained in a fixed surface area, A_T, and the radii can be represented as the function of this area, $r = \sqrt{2A_T/3\sqrt{3}}\,(N)^{\frac{1}{2}}$, the energy can be expressed as a function of the number of cells in the epithelium,

$$E_{ep}(N) = \frac{2S_b A_T}{3\sqrt{3}} - S_l\sqrt{\frac{3\sqrt{3}}{2A_T}}N^{\frac{3}{2}} + \Gamma_a\sqrt{\frac{2A_T}{3\sqrt{3}}}N^{\frac{1}{2}} + \frac{4{A_T}^2}{27}N^{-1} + \frac{3\sqrt{3}}{A_T}N^2, \qquad (4.4)$$

and is plotted in Figure 4.6a. The equilibrium values corresponding to the energy minima are given by the root of the derivative of the energy function,

$$\frac{\partial\left(E_{ep}(N)\right)}{\partial N} = -\frac{3\sqrt[4]{27}\sqrt{A_T}}{2\sqrt{2}}S_l N^{\frac{1}{2}} + \frac{1}{2}\sqrt{\frac{2{A_T}^3}{3\sqrt{3}}}\Gamma_a N^{\frac{-1}{2}} - \frac{4{A_T}^2}{27}N^{-2} + \frac{6\sqrt{3}}{A_T}N, \qquad (4.5)$$

and is plotted in Figure 4.6b. Note that the cell adhesion to the substrate, S_b, is not in Function (4.5) because the fixed surface area, A_T, of the substrate will always be covered by cells. This means that the energy contribution of the substrate adhesion will remain the same regardless of the number of cells.

The roots of Function (4.5), the number of cells to give a minimum energy of Function (4.4), are plotted in Figure 4.6c and Figure 4.6d, with varying lateral cell adhesion, S_l, and apical perimeter contraction, Γ_a. Figure 4.6c plots the number of cells to provide the minimum energy in the system against the lateral cell adhesion. Even with the restricted area, the cells follow the same trend as the rest of the model with changing lateral adhesion. However, we observe the change in the number of cells in the monolayer rather than the change of the cell shape. When the lateral cell-cell adhesion is dominant ($S_l > 0$ and $|S_l| \gg 1$) the number of cells is large, indicating that a large number of narrow, columnar cells are generated to fit in the fixed area, see Figure 4.6c. This means that the monolayer provides more capacity for the cells, such as those generated from cell proliferation. However, when contraction of the lateral cell cortex is dominant ($S_l < 0$ and $|S_l| \gg 1$) there is a smaller number of cells, see Figure 4.6c, indicating that the cells are very wide. Considering that the volume is constant for the cells, the cells are therefore also thin flat cells. This

suggests that cells would be extruded from the monolayer when lateral contraction increases to achieve the smaller equilibrium number of cells.

The cell shape behaviour of a system with a varying number of cells and a fixed area is different to a system with a fixed number of cells with a varying area. Figure 4.6d plots the roots of the Equation (4.4), the number of cells that provides the minimum energy in the system, against the apical perimeter contraction. The figure shows that when the apical perimeter contraction is increased there are fewer cells in the system. As mentioned previously, a small number of cells indicate the cells are flat and wide. In Hannezo et al. (2014), increasing the apical perimeter contraction resulted in the cells having a columnar shape with a smaller radius. The reason for the difference between the results is due to the fixed area and the apical perimeter contraction energy components in our implementation of the model. Given that the apical perimeter contraction term is positive, increasing Γ_a would lead to decreasing cell perimeter (radius) which in turn decreases the energy contribution of the term for a single cell. In the monolayer, if the cells decrease their apical perimeters, which makes space for additional cells in the fixed area, the energy contribution of the apical perimeter contraction is also decreased; however, the additional cells would introduce additional energy, in particular the apical perimeter contraction energy. The increase of energy from the additional cells would be greater than the decrease of energy from the shrinking cells. So, no cells are added and some cells are removed to minimise the energy when the perimeter contraction parameter is increased in the fixed area system shown in Figure 4.6d.

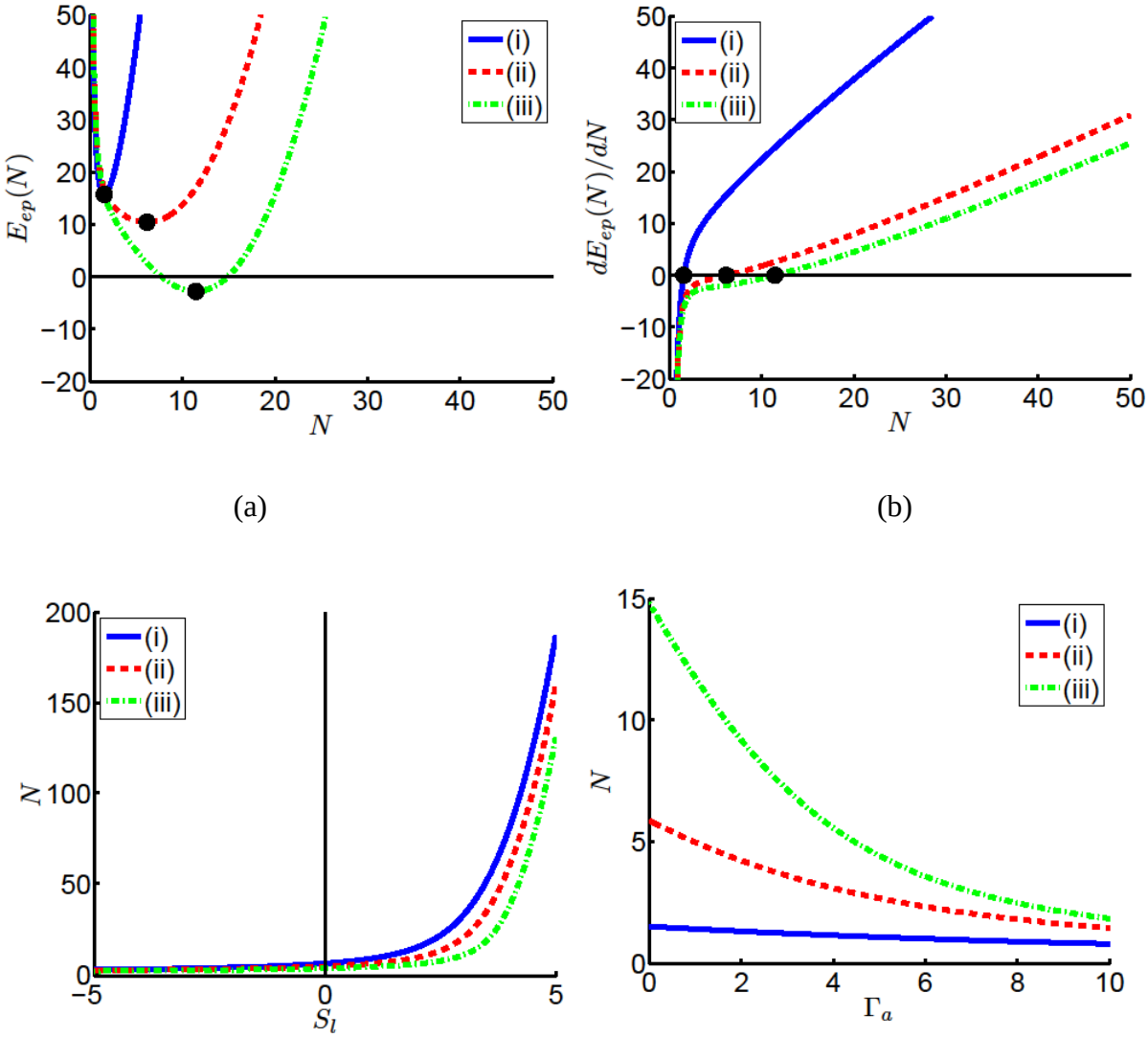

Figure 4.6. a) The plot of the energy function, Function (4.4), against the number of cells, N, with the roots represented by the red points with (i) $S_l = 1$ and $\Gamma_a = 1$, (ii) $S_l = 1$ and $\Gamma_a = 1$, and (iii) $S_l = 1$ and $\Gamma_a = 1$; b) The plot of the energy derivative, Function (4.5), against the number of cells, N, with the roots represented by the red points with (i) $S_l = 1$ and $\Gamma_a = 1$, (ii) $S_l = 1$ and $\Gamma_a = 1$, and (iii) $S_l = 1$ and $\Gamma_a = 1$; d) the plot of the roots (number of cells) of the derivative with (i) $\Gamma_a = 1$, (ii) $\Gamma_a = 1$ and (iii) $\Gamma_a = 1$; and c) the plot of the roots (number of cells) of the derivative with (i) $S_l = 1$, (ii) $S_l = 1$ and (iii) $S_l = 1$. The total area for all plots is $A_T = 10$.

4.5 MICRO-WOUND IN AN EPITHELIUM

The extrusion of a single cell is similar to the closure of a micro-wound where a cell occupies the void of the wound. A void is introduced into the system by replacing a cell in the monolayer with an empty space. The results from the two-dimensional CPM in Chapter 2 suggest that if cells are in a "hard" regime the void will stay open and if the cells are in a "softer" regime they can close the void. The transition value, β_c, represents the sudden change from an open to a closed system. The cell-cell adhesion and total surface area contraction are the main contributors for determining the cell regime and as a result the closure of the wound.

The initial cell configurations of all simulations in this chapter for three dimensions were generated by creating a configuration of 25 $10 \times 10 \times 5$ pixel square prism cells in a sheet located in a $50 \times 50 \times 10$ pixel system and a $50 \times 50 \times 5$ empty region above the cell sheet. These configurations were run with the parameters k=100, the S and Γ ratio $\beta = 1$ and $T = 2000$ until an energy equilibrium was reached. These simulations generated cell configurations with cross sections of the cells similar to Figure 4.3b. Once an energy equilibrium was reached, the simulation would remove a cell from the system and continue the simulation to obtain the observed results.

4.5.1 Numerical results for the three-dimensional CPM

In three dimensions we use the same classification as the two-dimensional model; however, the apical perimeter contraction and the cell substrate adhesion are mechanisms that not only influence the cell regime but also the closure of the wound. This leads to three different cases to consider: the case without substrate adhesion and apical contraction; the addition of the substrate adhesion; and the addition of apical contraction. All the terms are added to the energy Function 4.1.

With no substrate adhesion or apical contraction the cells are only influenced by the adhesion between the cells and the total perimeter contraction of the cells. However, this is not comparable to the two-dimensional CPM. In three dimensions the contraction not only affects the surface inside the wound and the surface area of connected cells, but also the apical surface area above the cells and the basal surface area connected to the substrate. The contraction effect on the apical and basal surface areas acts as an extra contraction "force" on the cells. While not a direct replication of this effect, in two dimensions it would be similar to adding a term $(\Gamma/2)\sum_j^N A_j$ to the system decreasing the preferred area, the opposite of adding the substrate adhesion to the cells. With no cell-substrate adhesion the cells are not attached to the substrate. The energy contribution of the cell surface area connected to the substrate is similar to the energy contribution of the cell's apical surface area connected with empty space above. The only difference between the apical and

basal surfaces of the epithelium is that one is in contact with a surface and the other is in contact with the empty space which can invade the monolayer. In Figure 4.7c the value of the wound's relative horizontal cross-sectional area for each pixel largely becomes indistinguishable. However, in the hard system the monolayer can shrink in height. The apical pixel layer of the monolayer shrinks from layer five to layer four. Moreover, the pixels without a cell label in the empty space fill layer five in the simulation leaving a ratio of the horizontal cross-section area of the wound at pixel layer five as $A_p/A_{min} = 25$.

The addition of the substrate adhesion connects the cells to the substrate and assists in closing the wound. To reduce the systems energy the substrate adhesion increases the amount of substrate surface covered by the cells and the only available uncovered substrate is located in the wound. The change in the basal layer of the cells connected to the substrate will increase in size and position, and in order to maintain a preferred shape the other layers of the cells will follow the same behaviour and in turn close the wound. Substrate adhesion is introduced in Figures 4.7a and 4.7b with the relative values of $\alpha = 2S$ and $\alpha = S$, respectively. These simulations show that the transition value, β_c, shifts toward the hard regime, meaning less soft cell regime is required to close the wound. Also, the addition of the substrate adhesion leads to a difference between the apical and basal layers of the epithelium. Figure 4.7a clearly shows a larger difference between the wound apical and basal areas (or all layers below the apical) than seen with weaker substrate adhesion (Figures 4.7b and 4.7c).

Adding the apical contraction to the system will change the regime of the cells on the apical pixel layer. The apical layer of the epithelium will increase the size of the wound compared to the other layers. As we consider the regime of the apical pixel layer to be harder, the closure of the wound will be hindered. Figure 4.7d shows the wound size of simulations with the addition of the apical contraction. Comparing these simulation results with Figure 4.7a we observe the trend and effects of changes of parameters stated above. The apical perimeter contraction shifts the transition, β_c, closer to the soft regime, hindering the closure of the wound, requiring the cells to be "softer" in order to close the wound. However, the apical contraction hinders the apical layer of the cells from closing the wound. The lower pixel layers are only influenced by the deformation of the apical layer of the cells. The value of Γ_t cannot be increased uncontrollably because this parameter can dominate the system and the adhesion between the cells lose influence in the system and separate the cells from each other. This is the same artefact as seen with a complete epithelium in Figure 4.5.

Chapter 2 specified a particular mechanism of perimeter contraction around a wound. In three dimensions this would be represented by the surface area of the wound or the perimeter of the

different layers of the wound. However, the identification of the surface area of the wound is difficult, as is the apical perimeter of the wound, given that the cells can change height. Rather, we introduce a perimeter contraction on the basal layer, $L_{ib,c-v}$, of the wound,

$$\frac{\Gamma_b}{2}\sum_{i}^{N} L_{ib,c-v}^2 ,$$

with a strength parameter, Γ_b. It must be mentioned that the cells can become detached from each other in the "harder" regime and any new voids created will contribute to the perimeter contraction term. However, this occurs at the extreme values of the hard regime and we are only concerned with the simulations near the transition point β_c. Figure 4.8 shows a plot of the simulations with the basal perimeter contraction on the substrate of the wound, comparable to the simulations in Figure 4.7a. The basal perimeter contraction has the opposite effect compared to the apical perimeter contraction of the cells. The basal perimeter contraction shifts the transition from open to closed for the lower layer of the wound into a "harder" cell regime, whereas the apical cell contraction increases the transition value of the apical layer of the wound hindering its closure.

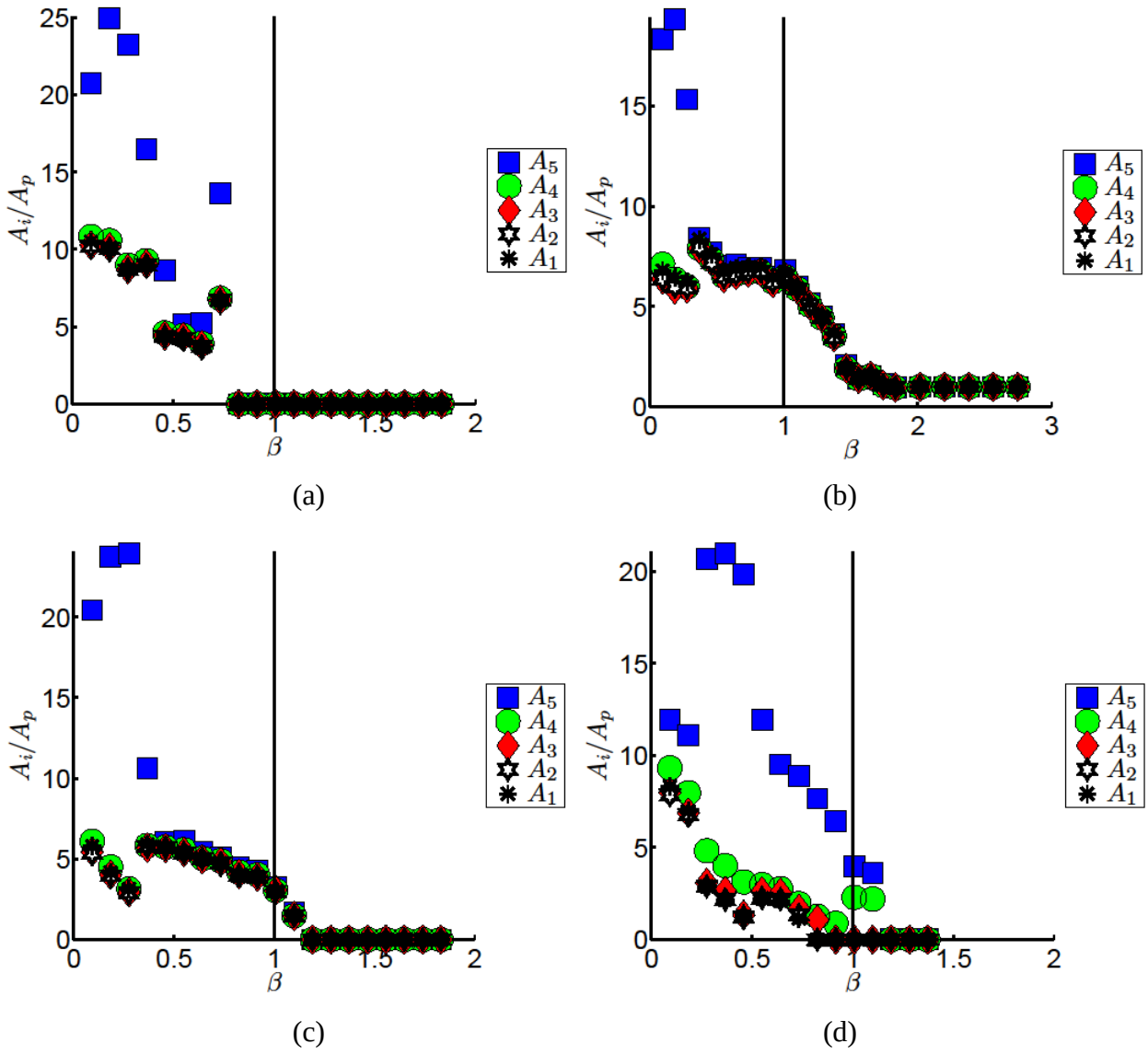

Figure 4.7. Plots of the equilibrium value of the average horizontal cross-section wound area over the last 100 iterations of a single CPM simulation of 2000 iterations against different cell regimes, β at five pixel layers: a) simulations with a substrate adhesion $\alpha = 2S$ and apical perimeter contraction of $\Gamma_t = 0$; b) a reduction in the substrate adhesion, $\alpha = S$, and apical perimeter contraction of $\Gamma_t = 0$; c) the removal of the substrate adhesion, $\alpha = 0$, and apical perimeter contraction of $\Gamma_t = 0$; and d) the inclusion of an apical perimeter contraction, $\Gamma_t = 300$, on the cells and substrate adhesion $\alpha = 2S$. Other parameters for the simulations include: $k = 100$, $\Gamma = 50$, $\alpha = 2S$, $V_p = 500$ with $N = 25$ cells on a $50 \times 50 \times 10$ hexagonal layered pixel grid.

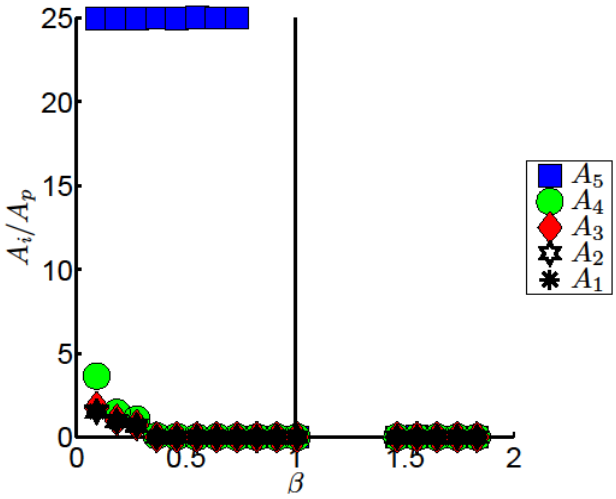

Figure 4.8. Plot of the equilibrium value of the average horizontal cross-section wound area over the last 100 iterations of a single CPM simulation of 2000 iterations against different cell regimes, β, at five pixel layers adding a basal perimeter contraction to the wound, $\Gamma_b = 300$. Parameters for the simulations include $k = 100$, $\Gamma = 50$, $\alpha = 2S$, $V_p = 500$ with $N = 25$ cells on a $50 \times 50 \times 10$ hexagonal layered pixel grid.

4.5.2 Cylindrical representation of cells and wound

To generate a geometric model for approximating the morphology of the equilibrium state of the cells and wound we use the same approximation method applied in Chapter 2. Cells are represented as geometrical shapes and the following assumptions are applied. All cells are assumed to be similar and have the same shape. Both the cell and wound shapes are initially assumed to be cylinders with variable radii R and R^*, respectively, and a fixed height, h, see Figure 4.9. Although the cells are able to shrink in the extreme simulated cases, i.e. a very hard regime, we wish to focus on the transition from an open to a closed wound configuration. The area is therefore assumed to be conserved for each pixel layer of the system.

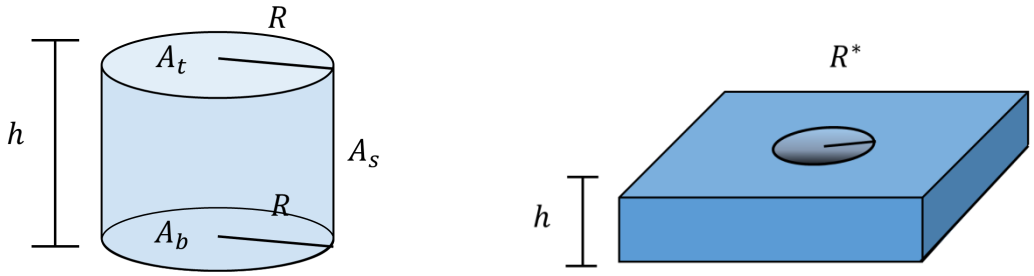

(a) (b)

Figure 4.9. a) Cylindrical representation of the cells with volume, V; height, h; and top, A_t, bottom, A_b, and lateral surface areas, A_s. b) The geometrical representation of a wound as a cylindrical hole in the monolayer with radius R^*.

Following on from the geometric representation of the two-dimensional model in Chapter 2 we express the energy function with a single variable. First, we assume that the surface area and volume of the cells are identical, i.e. the volume, V, total surface area, A, the apical surface area, A_t, and basal surface area, A_b, the lateral surface area, A_s, and the apical cell perimeter, L_t. In addition to the cell parameters, there are the values for the wound such as the surface area of the cells in connection with the wound, A_s^*, and the perimeter of the wound on the substrate, L_b^*. Each of these parameters are expressed with either the radii of the cells or the radii of the wound.

The cell and wound radii can be expressed by each other by assuming there is a conservation of horizontal area on the layers of the epithelial sheet linking the cells and wound,

$$A_T = (N-1)A_n + A_n^*,$$

where $n = t$ or b, and with a constant horizontal area of the system, $A_T = \left(NV_p\right)/(\pi h)$, which is the sum of the cells, A_n, and wound horizontal area, A_n^*. This allows the cell radius to be expressed with the wound radius,

$$R(R^*) = \sqrt{\frac{NV_p}{\pi h(N-1)} - \frac{R^{*2}}{N-1}},$$

allowing the function to be expressed with either the cell or wound radii variable.

The energy function can be expressed with a single variable, namely the radius of the cells,

$$E(R^*) = \frac{k(N-1)}{2}\left(V(R^*) - V_p\right)^2 + \frac{\Gamma N}{2}\left(A(R^*)\right)^2 - \frac{S(N-1)}{2}A_s(R^*) + \frac{S}{2}A_s^*(R^*) - \frac{\alpha(N-1)}{2}A_b(R^*) + \frac{\Gamma_t(N-1)}{2}L_t(R^*)^2 + \frac{\Gamma_b}{2}L_b^*(R^*)^2, \tag{4.6}$$

with the expressions for the volume of the cylinder as

$$V(R^*) = \pi h\left(\frac{NV_p}{\pi h(N-1)} - \frac{R^{*2}}{N-1}\right);$$

the total surface area as

$$A(R^*) = 2\pi h\sqrt{\frac{NV_p}{\pi h(N-1)} - \frac{R^{*2}}{N-1}} + 2\pi\left(\frac{NV_p}{\pi h(N-1)} - \frac{R^{*2}}{N-1}\right);$$

the lateral surface area of cells as

$$A_s(R^*) = 2\pi h\sqrt{\frac{NV_p}{\pi h(N-1)} - \frac{R^{*2}}{N-1}};$$

the lateral surface area of the wound as

$$A_s^*(R^*) = 2\pi h R^*;$$

the cell surface area in contact with the substrate as

$$A_b(R^*) = 2\pi R^{*2};$$

the perimeter of the wound at the substrate as

$$L_b^*(R^*) = 2\pi R^*;$$

and the apical perimeter of the cells as

$$L_t(R^*) = 2\pi\sqrt{\frac{NV_p}{\pi h(N-1)} - \frac{R^{*2}}{N-1}}.$$

Results of the micro-wound geometric model

The plot of energy Function (4.6) shows two distinct cases, seen in Figure 4.10. The function can either have a local minimum where the wound is open, $R^* > 0$, or a global minimum when the wound is closed, $R^* = 0$. We do not examine the non-physical values of $R^* < 0$, which we can observe in Figure 4.10, as having smaller energies than positive local minimum values.

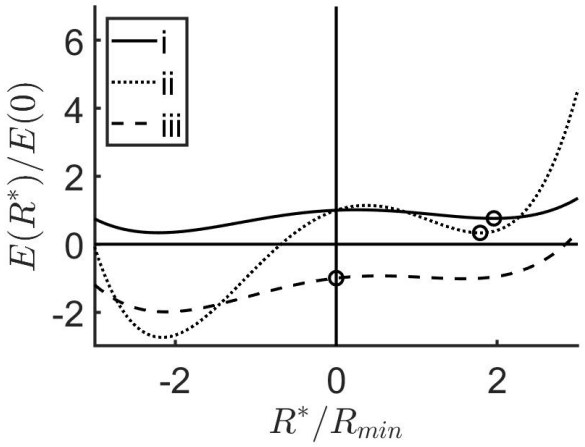

Figure 4.10. Plot of the energy function for hard and soft regimes showing the transition, similar to the two-dimensional case, where the local real minimum and maximum no longer occur so that the system will tend to close the wound. i) $= 30000$ $(\beta = 0.7952)$, ii) $S = 40000$ $(\beta = 1.0603)$ and iii) $S = 50000$ $(\beta = 1.3254)$. Other parameters include $k = 100$, $\Gamma = 50$, $\alpha = 2S$, $V_p = 500$ with $N = 25$ cells.

The trends of the minimum energy from Function (4.6) are similar to the two-dimensional wound case in Chapter 2. However, there are differences in the results due to the three-dimensional representation of the cells and the addition of the substrate adhesion and the apical contraction. It is important to note that the system has a local maximum, and if the wound size starts below this local maximum, the wound closes. However, the wound could also close in the simulation given the random fluctuations of the pixels occurring on the boundaries of the simulated cells. The plots in Figure 4.11 show the position of these local minima for varying cell regimes, β, indicating a transition value, β_c, between an open wound and a closed wound.

Substrate adhesion, α, has an effect on the transition point between an open and closed wound. The transition point shifts to a "softer" regime, meaning only much "softer" systems of cells can close the wound. In particular, with no adhesion the transition point in simulations is shifted into the "hard" regime in Figures 4.7b and 4.7c. Figure 4.11a plots the wound radius for the local minimum of energy for a system with substrate adhesion similar to the cell-cell adhesion, $\alpha = 2S$

(black) and decreased adhesion $\alpha = S$ (green) and $\alpha = 0$ (red). Similarly to the simulations, the transition point between the open and closed wound shifts to a "softer" regime.

The cylindrical representation of the cells and wound will not show the same behaviour at different "pixel" layers of the monolayer as the simulations. So, the addition of apical contraction will affect the lateral surface area of the cells directly. Figure 4.11b shows a plot of the radius of the local minima against β with added apical contraction for the geometric representation. The cylindrical geometry only provides one variable and cannot show the difference between the apical and basal layers. However, the plot does show that when the apical contraction increases the transition value shifts to a "softer" regime, similar to the simulations results.

The addition of the basal perimeter contraction of the wound in the geometrical representation is different to that in the simulations. This is similar to the application of the apical contraction that affects the lateral surface of the wound directly. Figure 4.11c on the other hand shows that adding the basal contraction at the perimeter of the wound shifts the transition point further into the "hard" regime, similar to the basal layers of the simulations, meaning that the system can more easily close the wound.

We can use the geometric energy function of the cells to derive an approximation for the open or closed transition value, β_c. Initially we find the zero of the derivative of the energy function with respect to the radius of the wound,

$$\begin{aligned} 0 = \frac{dE}{dR^*} = 4\left(\frac{\pi^2 h^2 k}{2(N-1)} + \frac{2\Gamma\pi^2}{N-1}\right)R^{*3} \\ + 2\left(\frac{-\pi h k N V_p}{N-1} + kV_p\pi h - 2\Gamma\pi^2 h^2 - \frac{4\pi\Gamma N V_p}{h(N-1)}\right)R^* \\ + \frac{\left(\frac{-4\pi\Gamma N V_p R^*}{N-1} + \frac{4\Gamma\pi^2 h R^{*3}}{N-1} + S\pi h R^* - \Gamma_t \pi R^*\right)}{\sqrt{\frac{NV_p}{\pi h(N-1)} - \frac{R^{*2}}{N-1}}} \\ - 8\Gamma\pi^2 h R^* \sqrt{\frac{NV_p}{\pi h(N-1)} - \frac{R^{*2}}{N-1}}, \end{aligned} \quad (4.7)$$

giving the value of the wound radius.

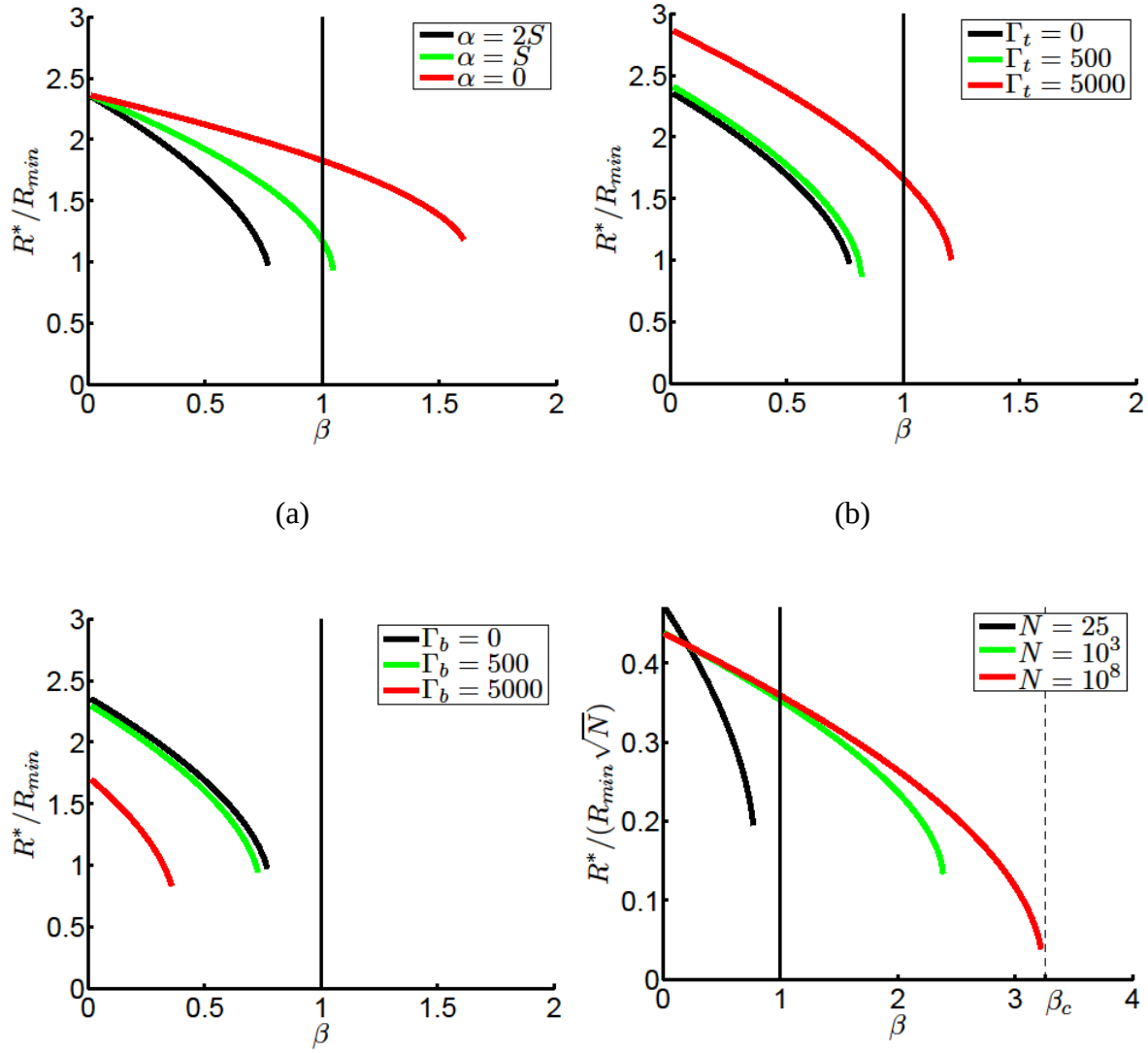

Figure 4.11. Plots of the root of Equation (4.6) where a) the substrate adhesion is varied with different values as a function of S, $\alpha = 2S$, (black) to $\alpha = S$ (green) and $\alpha = 0$ (red); b) includes an apical perimeter contraction representing $\Gamma_t = 0$ (black), $\Gamma_t = 500$ (green), and $\Gamma_t = 5000$ (red) with a substrate adhesion of $\alpha = 2S$; c) includes the addition of the basal perimeter contraction on the wound $\Gamma_b = 0$ (black) $\Gamma_b = 500$ (green), and $\Gamma_b = 5000$ (red) with a substrate adhesion of $\alpha = 2S$; and d) includes the addition of the basal perimeter contraction on the wound $N = 25$ (black) $N = 1000$ (green), and $N = 10^8$ (red) with substrate adhesion of $\alpha = 0$. Other parameters include $k = 100$, $\Gamma = 50$, $V_p = 500$ with $N = 25$ unless otherwise stated.

The values of the zeroes of the derivative in Equation (4.7) cannot be simply expressed algebraically. Therefore, we simplify the expression for an infinitely large system where $N \to \infty$ which results in

$$0 = \left(\frac{-8\Gamma\pi V_p}{h} - 12\Gamma\pi^2 h \sqrt{\frac{V_p}{\pi h}} - 4\Gamma\pi^2 h^2 + S\pi h \sqrt{\frac{\pi h}{V_p}} + \alpha\pi - 2\Gamma_t \pi \sqrt{\frac{\pi h}{V_p}} + 4\pi^2 \Gamma_b \right) R^* - S\pi h.$$

Small changes in the number of cells in the system do not change the results greatly except for increasing the wound size. However, for much larger changes in the number of cells the transition value will shift to a much softer regime. Figure 4.11d shows the positive local minimum value for similar systems of the red plot in Figure 4.11a with no substrate adhesion for $N = 25$, $N = 1000$ and $N = 10^8$ with increasing values of β_c.

The local minimum when applying the limit is

$$R^* = \frac{S\pi h}{\frac{8\Gamma V_p}{h} + 12\Gamma\pi^2 h \sqrt{\frac{V_p}{\pi h}} + 4\Gamma\pi^2 h^2 - S\pi h \sqrt{\frac{\pi h}{V_p}} - \alpha\pi + 4\pi^2 \Gamma_t - 4\pi^2 \Gamma_b},$$

where $\sqrt{V_p/(h\pi)} = R_{min}$. The system is closed if $R^* \leq 0$ and open if $R^* > 0$. For the system to be open the expression

$$\frac{8\Gamma V_p}{h} + 12\Gamma\pi^2 h \sqrt{\frac{V_p}{\pi h}} + 4\Gamma\pi^2 h^2 - S\pi h \sqrt{\frac{\pi h}{V_p}} - \alpha\pi + 4\pi^2 \Gamma_t - 4\pi^2 \Gamma_b > 0,$$

and the transition occurs when it switches to zero or a negative value. This equation is rearranged to find the value of β_c,

$$\beta_c = \frac{\frac{4V_p}{\pi h^2}\sqrt{\frac{V_p}{\pi h}} + 6\frac{V_p}{h} + 2\pi h\sqrt{\frac{V_p}{\pi h}}}{A_{min}} - \frac{\alpha}{2\Gamma h A_{min}}\sqrt{\frac{V_p}{\pi h}} + \frac{2\pi\Gamma_t}{\Gamma h A_{min}}\sqrt{\frac{V_p}{\pi h}} - \frac{2\pi\Gamma_b}{\Gamma h A_{min}}\sqrt{\frac{V_p}{\pi h}}, \quad (4.8)$$

where A_{min} is the total surface area of a cylinder with a radius R_{min} and height h. Assuming there is no adhesion or apical cell or basal wound perimeter contraction, shown in Figure 4.11d, the value of transition is $\beta_c = 3.2568$.

While this solution does not provide the transition values for systems for finite cell numbers in Figures 4.11a, 4.11b and 4.11c, the solution demonstrates the influence of different mechanisms on the transition values. The first term of the transition value, represented in Equation (4.8), consists of only the geometric components of the cells and does not include other mechanisms. Additional

mechanisms, represented in the second, third and fourth terms in Equation (4.8), can alter the transition value. Substrate adhesion, represented with the parameter α, will decrease the transition value to represent a softer cell regime. The apical perimeter contraction, represented with the parameter Γ_t, will increase the transition value to represent a harder cell regime. Finally, the basal wound perimeter contraction, represented with the parameter Γ_b, will decrease the transition value to represent a softer cell regime.

4.5.3 Truncated cone cell and wound representation

The cylindrical representation of the system only indicates whether the wound is open or closed and does not show the differences between the top and bottom of the layers. Instead, a truncated cone geometrical representation of the cells and wound, shown in Figure 4.12, can separate the layers and shows how the apical and basal layers behave. This means the cells and wound are represented by two variables, R_t and R_b, that measure the top and bottom radii of the cells, and R_t^* and R_b^*, measuring the top and bottom radii of the wound.

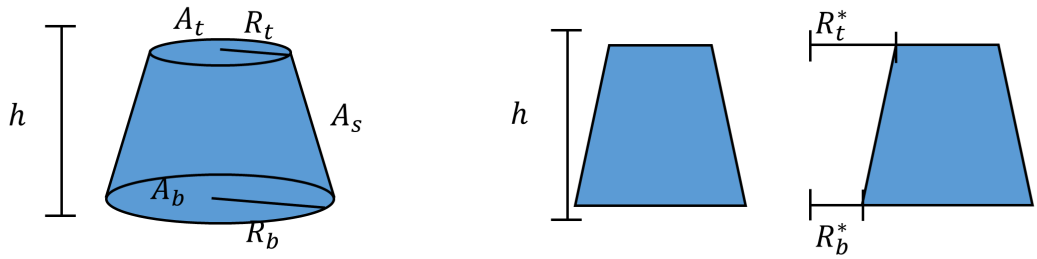

(a) (b)

Figure 4.12. a) The geometric representation of the cells as a truncated cone. b) The vertical segment of the geometric representation of the wound in the monolayer as a truncated cone.

Excluding the geometrical representations, all other assumptions for the truncated cone are the same as in the cylindrical case, namely the height is fixed at h, and the cells and wound are assumed to be connected to one another. The conservation of area on each layer links the cells and wound, meaning the energy function has an interchangeable pair of variables similar to the cylindrical geometry. The energy function is expressed with R_t^* and R_b^*,

$$E(R_t^*, R_b^*) = \frac{k(N-1)}{2}\left(V(R_t^*, R_b^*) - V_p\right)^2 + \frac{\Gamma N}{2}\left(A(R_t^*, R_b^*)\right)^2 - \frac{S(N-1)}{2}A_s(R_t^*, R_b^*) + \frac{S}{2}A_s^*(R_t^*, R_b^*) - \frac{\alpha(N-1)}{2}A_b(R_t^*, R_b^*) + \frac{\Gamma_t(N-1)}{2}L_t(R_t^*)^2 + \frac{\Gamma_b}{2}L_b^*(R_b^*)^2,$$

with the expressions for the volume of the truncated cone as

$$V(R_t^*, R_b^*) = \frac{1}{3}\pi h\left(R_t(R_t^*)^2 + R_b(R_b^*)^2 + R_t(R_t^*)R_b(R_b^*)\right); \quad (4.9)$$

the total surface area as

$$A(R_t^*, R_b^*) = \pi\big(R_t(R_t^*) + R_b(R_b^*)\big)\sqrt{\Big(R_t(R_t^*) - R_b(R_b^*)\Big)^2 + h^2} + \pi R_t(R_t^*)^2 + \pi R_b(R_b^*)^2; \quad (4.10)$$

the lateral surface area of cells as

$$A_s(R_t^*, R_b^*) = \pi\big(R_t(R_t^*) + R_b(R_b^*)\big)\sqrt{\Big(R_t(R_t^*) - R_b(R_b^*)\Big)^2 + h^2}; \quad (4.11)$$

the lateral surface area of the wound as

$$A_s^*(R_t^*, R_b^*) = \pi(R_t^* + R_b^*)\sqrt{(R_t^* - R_b^*)^2 + h^2}; \quad (4.12)$$

the cell surface area in contact with the substrate as

$$A_b(R_b^*) = 2\pi\left(\frac{NV_p}{\pi h(N-1)} - \frac{{R_b^*}^2}{N-1}\right)^2; \quad (4.13)$$

the perimeter of the wound at the substrate as

$$L_b^*(R_b^*) = 2\pi R_b^*; \quad (4.14)$$

and the apical perimeter of the cells as

$$L_t(R_t^*) = 2\pi\sqrt{\frac{NV_p}{\pi h(N-1)} - \frac{{R_t^*}^2}{N-1}}. \quad (4.15)$$

Results of the micro-wound geometric model

This representation of the cells can lead to three different equilibrium states for the wound rather than two from the cylindrical representation. The wound can remain open where $R_t^* > 0$ and $R_b^* > 0$; an equilibrium, at an energy minimum, is shown in plots of a hard system, $\beta = 0.2651$, in Figure 4.13a. The void of the wound can have the shape of an inverted cone where $R_t^* > 0$ and $R_b^* = 0$; an equilibrium, at an energy minimum, is shown in plots of a much "softer", but still hard, system, $\beta = 0.7952$, in Figure 4.13b. Finally, the wound can be closed where the minimum occurs at $R_t^* = 0$ and $R_b^* = 0$; this is shown in plots of a "soft" system, $\beta = 1.3254$, in Figure 4.13c.

A truncated cone geometrical representation of the cells allows for the separation of the apical and basal layer of the epithelium and as such the addition of the substrate adhesion and the apical contraction behaviours can be observed. The plots in Figure 4.14 show that the top and bottom radii of the wound can differ, similarly to simulated plots in Figure 4.7. Figure 4.14a shows that decreasing the substrate adhesion from $\alpha = 2S$ (black) to $\alpha = S$ (green) and $\alpha = 0$ (red) demonstrates a similar behaviour to that from the simulations. As the substrate adhesion decreases, the transition value moves to a "softer" regime and the apical and basal radii values move closer

together and are the same when $\alpha = 0$. Adding an apical contraction, from $\Gamma_t = 0$ (black) to $\Gamma_t = 500$ (green) and $\Gamma_t = 1000$ (red) in Figure 4.14b shows that the top radius of the wound deviates from the bottom radius and the transition value shifts to a "softer" regime. However, adding a basal contraction, from $\Gamma_b = 0$ (black) to $\Gamma_b = 500$ (green) and $\Gamma_b = 1000$ (red), on the wound perimeter in Figure 4.14c shifts the basal radius away from the top radius, and the transition value of the wound at the bottom layer moves further into the "hard" regime, meaning that the base of the wound can be closed more easily.

We also note that there is a discontinuity in the apical radii plots in Figure 4.14 which occurs when the basal radii drops to zero. The drop of the basal radii coincides with the disappearance of the two other critical points observed in Figure 4.13a on the basal radii axis.

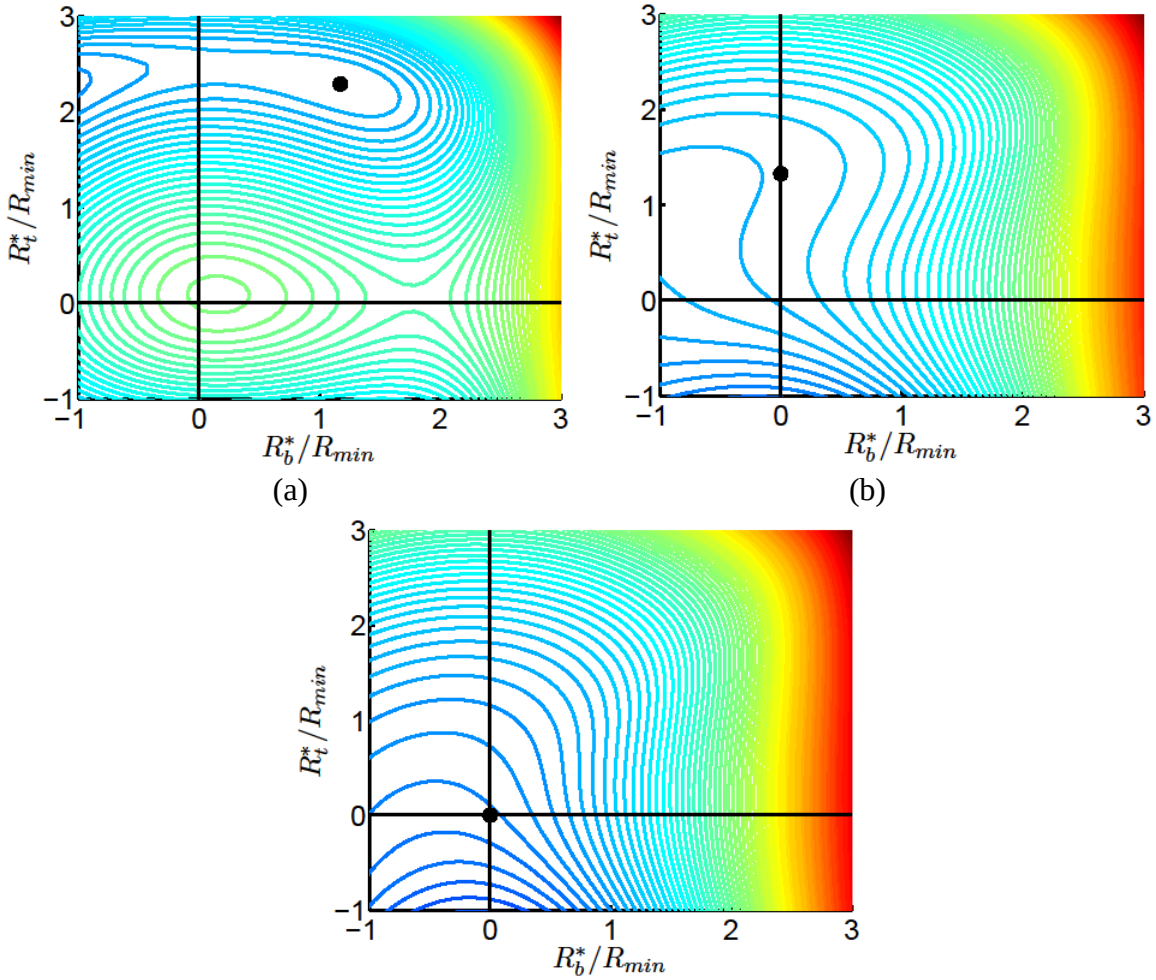

Figure 4.13. Contour plots for the energy function of the truncated cone geometric representation of cells and wound. A black point represents the local minimum energy. a) Open wound in a hard regime, $\Gamma = 50$ and $= 10000$ ($\beta = 0.2651$), b) a partially open wound in a softer regime, $\Gamma = 50$ and $S = 30000$ ($\beta = 0.7952$), and c) a closed wound in a soft regime, $\Gamma = 50$ and $S = 50000$ ($\beta = 1.3254$). Other parameters include $k = 100$, $\alpha = 2S$, $V_p = 500$ and with $N = 25$ cells.

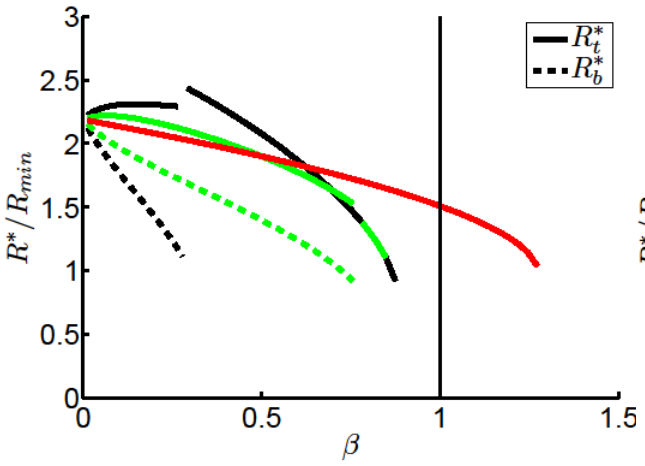

(a)

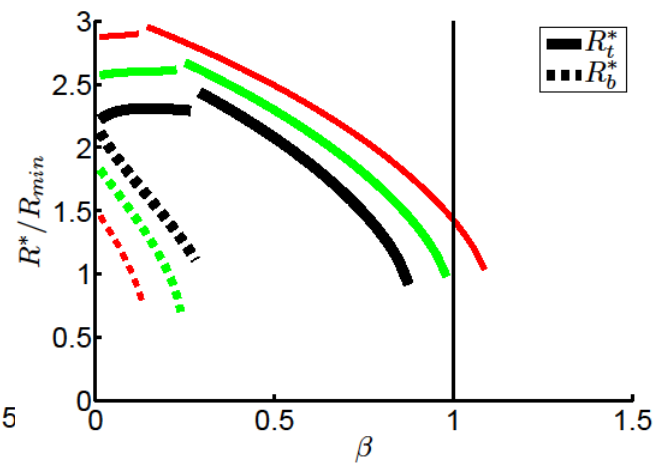

(b)

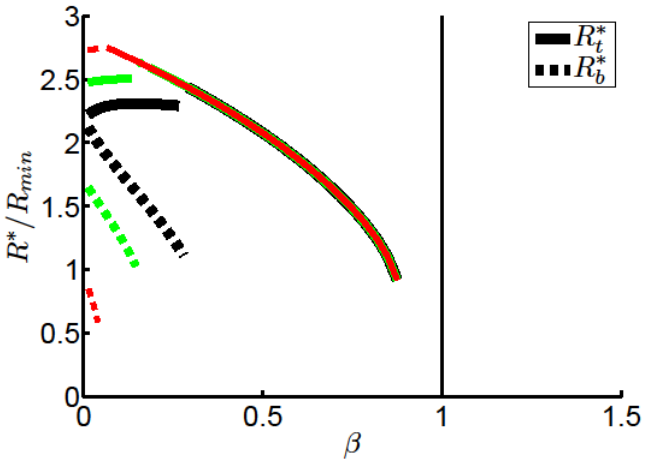

(c)

Figure 4.14. Plots of the local minima values of the horizontal cross section wound area for the apical (solid line) and basal (dashed line) layers of the energy function with a truncated cone geometric representation of cells and wound. a) Represents a reduction of the substrate adhesion $\alpha = 2S$ (black) to $\alpha = S$ (green) and $\alpha = 0$ (red). b) Includes an apical perimeter contraction representing $\Gamma_t = 0$ (black), $\Gamma_t = 500$ (green), and $\Gamma_t = 1000$ (red). c) With the addition of the basal perimeter contraction on the wound $\Gamma_b = 0$ (black), $\Gamma_b = 500$ (green), and $\Gamma_b = 1000$ (red). Other parameters include $k = 100$, $\Gamma = 50$, $\alpha = 2S$, $V_p = 500$ and with $N = 25$ cells.

4.6 MODELLING OF SINGLE CELL EXTRUSION

The extrusion of cells from a monolayer due to the pressure in the system or the increase of cell proliferation that leads to pressure to extrude cells has been discussed previously. In simulations this increased pressure would be attributed to increasing the preferred volume or increasing the number of cells in the simulations. However, we wish to examine the reorganisation of the cells to extrude only a single modified cell in the absence of any pressure in the system.

The initial cell configurations of all simulations in this chapter for three dimensions were generated by creating a configuration of 25 $10 \times 10 \times 5$ pixel square prism cells in a sheet located in a $50 \times 50 \times 10$ pixel system and a $50 \times 50 \times 5$ empty region above the cell sheet. These configurations were run with the parameters $k = 100$, the S and Γ ratio $\beta = 1$ and $T = 2000$ until an energy equilibrium was reached. These simulations generated cell configurations with cross sections of the cells similar to Figure 4.3b. Once an energy equilibrium was reached the modified cell parameter values were adjusted and the simulation continued to run, obtaining the observed results.

4.6.1 Numerical results for the three-dimensional CPM

A single cell in the epithelial layer can be identified as a modified cell, e.g. due to genetic mutation such as in cancer cells. The modified cell parameter strengths are varied from the non-modified neighbouring cells. However, the volume constraint, k, and the total surface area contraction, Γ, are kept constant. The cell-cell adhesion, cell-substrate adhesion and the apical perimeter contraction are represented by S, α and Γ_t for the non-modified cell and S^*, α^* and Γ_t^* for the modified cell.

An additional lateral (cell-cell) surface area contraction, with the parameter strength Γ^*,

$$\frac{\Gamma^*}{2}\left(A_{e,c-c}\right)^2,$$

and a basal perimeter contraction,

$$\frac{\Gamma_b}{2}\left(L_{e,b}\right)^2,$$

are added to the modified cell. These extra mechanisms are included in the energy Function (4.1) to create,

$$\mathrm{E} = \frac{k}{2}\sum_{j}^{N}\left(V_j - V_p\right)^2 + \frac{\Gamma}{2}\sum_{j}^{N}A_j^2 - \frac{\mathrm{S}}{2}\sum_{j}^{N}A_{j,c-c} - \frac{S^*}{2}A_{e,c-c} - \frac{\alpha}{2}\sum_{j}^{N}A_{j,c-b} - \frac{\alpha^*}{2}A_{e,c-b} + \frac{\Gamma_t}{2}\sum_{j}^{N}\left(L_{j,t}\right)^2 + \frac{\Gamma_t^*}{2}\left(L_{e,t}\right)^2 + \frac{\Gamma^*}{2}\left(A_{e,c-c}\right)^2 + \frac{\Gamma_b}{2}\left(L_{e,b}\right)^2. \quad (4.16)$$

The cell-substrate adhesion is removed from the modified cell, $\alpha^* = 0$, assuming that the extruding cell will have detached from the substrate.

Initially, the simple case is examined where the modified cell has only the volume constraint and the total surface area contraction. The volume constraint attempts to maintain a preferred volume for the cell and the total surface area contraction attempts to force the cell to attain a minimum surface area. These two mechanisms are the minimum required for the cell in the monolayer because without the volume constraint the surface area contraction will shrink the cell to a minimum surface area, A_{min}, and volume of zero. Without the surface area contraction the volume constraint will keep the cell at a particular volume, although the cell pixels may become separated from each other. The mechanisms complement each other and operate as opposing "forces".

If the modified cell is only subject to the volume constraint and surface area contraction, the modified cell's only contribution to the energy is the space it occupies in the epithelial layer. The modified cell can exit the layer in two ways. The time taken for the modified cell to leave the epithelial layer can be unpredictable. The modified cell itself can hinder the closing of the layer, or the modified cell can leave the layer at any point with no added assistance. The modified cell is either "pushed" out by the neighbouring cells thus "closing the wound", or it leaves the monolayer by itself allowing the neighbouring cells to close the wound that is left. Since the modified cell is not attached to its neighbours by adhesion and the energy contribution is the same whether the cell is connected to other cells or not, the system is the same as the wound case.

Adding cell-cell adhesion to the modified cell attaches it to its neighbouring cells in the epithelial layer. The modified cell adhesion, S^*, is represented as a ratio with the non-modified cell adhesion, S^*/S. Figure 4.15 illustrates the change in the adhesion ratio and the effect on the modified cell. When $S^*/S = 0$ the cell is not connected to any of its neighbouring cells in the monolayer and can leave at any time, as mentioned in the case above. Gradually increasing the adhesion, such that $0 < S^*/S \ll 1$, allows the modified cell to extrude while weakly attached to the neighbouring cells. The modified cell is less likely to extrude from the layer when increasing the ratio S^*/S , but with $S^*/S < 1$, see Figure 4.15. When the ratio is equal to one, the modified cell-cell adhesion is the same as that of the neighbouring cells and it does not extrude from the layer.

However, due to the lack of substrate adhesion in the modified cell, neighbouring cells with substrate adhesion are able to manoeuvre in-between the modified cell and the substrate. When $S^*/S > 1$, the neighbouring cells enclose the modified cell within the epithelial layer. A stronger modified cell-cell adhesion makes the modified cell "softer" than its neighbours since $\beta^* = S^*/2(\Gamma A_{min}) > \beta = S/2(\Gamma A_{min})$, and this creates the potential for the modified cell to break apart since there is no connection condition. This behaviour can only be rectified by increasing the cortical contraction of the modified cell. In contrast, the modified cell is "harder" than its neighbours when $S^*/S < 1$, since $\beta^* < \beta$.

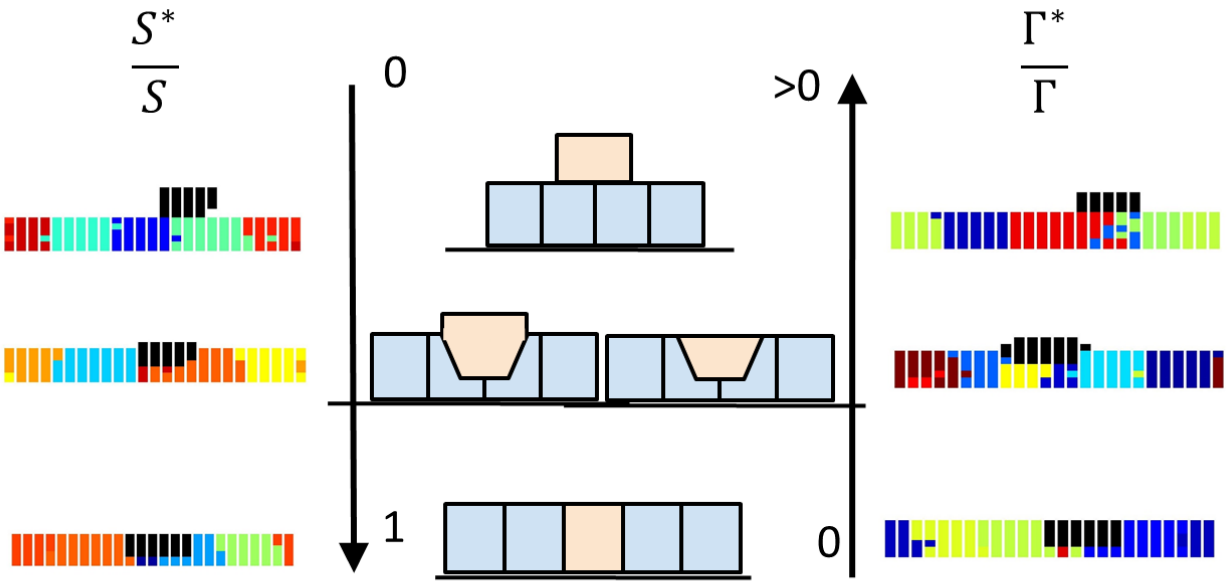

Figure 4.15. Examples of vertical cross-sections of simulations on the left and right of the figure of the effect of the mechanisms on the modified cell (black). The illustration in the figure generalises the effect on the modified cell (orange), of decreasing modified cell adhesion, S^*/S, and alternatively increasing the additional modified cell contraction, Γ^*/Γ.

An additional "lateral" contraction is added on the surface area of the modified cell connected to the neighbouring cells to assist the extrusion of the modified cell. The strength of the lateral contraction, Γ^*, is represented as a ratio of lateral contraction to the total surface area contraction, Γ^*/Γ. A ratio of $\Gamma^*/\Gamma = 0$ describes the case above with an adhesion ratio $S^*/S = 1$. Increasing the ratio Γ^*/Γ from zero results in a "hardening" of the modified cell on the surface area connected to neighbouring cells. A lack of adhesion between the modified cell and the substrate may allow neighbouring cells to manoeuvre themselves between the modified cell and the substrate. Further increasing the ratio Γ^*/Γ eventually results in the modified cell being partially extruded and,

eventually, completely extruded from the epithelial layer. These three “phases”, namely, minimal change, partial change, and total extrusion, illustrated in Figure 4.15, are similar to three of the four outcomes attained with adhesion changes, as described previously.

The modified cell can retract from its neighbouring cells faster than the neighbouring cells can close the empty space if the ratio Γ^*/Γ is large enough, resulting in the modified cell detaching from the neighbouring cells. However, the gradual encroachment and joining between the neighbouring cells can eventually result in the extrusion of the modified cell.

In combination, the modified cell-cell adhesion and the extra lateral contraction of the modified cell affects the strength of the parameters required to extrude the cell. The combinations of the two parameters are shown in the three phase diagrams in Figure 4.16. The phase diagrams in Figure 4.16 represent the condition of the modified cell for each a simulation where the modified cell is extruded (red) or not extruded (blue) from the monolayer. Other values in-between these outcomes represent a partial extrusion (green). The number of layers closed below the modified cell determines the state of the extrusion. For a five pixel-high monolayer there are several outcomes. Starting from the substrate: the “no change” case represents all pixel layers of the modified cell remaining; the “partial or non-extrusion” case represents the removal of different incremental pixel layers of the modified cell specifically the modified cell pixel layers 1 to 4; and finally the “modified cell extruded” from the monolayer represents the removal of all 5 layers of the modified cell. The extruded cell can be classified as being either “attached” or “detached” from the epithelial layer. Detachment occurs for very weak values of the modified cell-cell adhesion and high “lateral” contraction.

A modified cell can be extruded from the monolayer if the modified cell-cell adhesion is low, or if there is a sufficiently strong additional lateral contraction. The combination of both mechanisms can complement each other, i.e. a lower adhesion requires a smaller contraction to extrude the cell. Figure 4.16a plots the condition of the modified cell showing that with low modified cell adhesion and larger contraction the cell can extrude and if not the cell is only partially extruded.

The modified cell can only be extruded from the system if the neighbouring cells are able to close the resulting wound. A simulation with a regime that is unable to close a wound will be unable to extrude the cell. This is shown by the phase diagrams in Figure 4.16b, which drops the substrate adhesion, and Figure 4.17b, which shows systems that could close the wound in a soft regime cannot in a harder regime. This pattern is similar to the wound case. Alternatively, changing other parameters that hinder the system from closing the wound, such as halving the substrate

adhesion represented in Figure 4.16b, will also prevent the modified cell from extruding for any combination of modified cell-cell adhesion and additional lateral contraction values.

Adding an apical contraction to the cell perimeter adjusts the regimes between the apical and basal layer of the cells, with the apical layer behaving “harder” than the basal layer. The apical contraction perimeter of neighbouring cells can hinder the closure of a wound as seen in the previous Section 4.5 and largely only affects the apical layer of the cells. The transition between the open and closed wound can shift to a “softer” regime requiring “softer” cells to close the wound. The phase diagram in Figure 4.16c shows that the extrusion of the cell is also hindered with the addition of the apical perimeter contraction of $\Gamma_t = 300$ to simulations. Comparing the phase diagram in Figure 4.16a to the phase diagram in Figure 4.16c, with the added apical contraction, shows the modified cell only partially extrudes in Figure 4.16c, whereas it would extrude in Figure 4.16a without the apical perimeter contraction.

A strong apical perimeter contraction can force the cells to separate from each other. If the modified cell adhesion is small compared to the neighbouring cell adhesion, only the modified cell will detach from its neighbouring cells. However, the basal layer of the neighbouring cells can invade the space occupied by the modified cell. In such cases, it appears that the system can form “a bowl” (or void) which the modified cell can occupy. Running the simulations with strong apical contraction shows the system creates this “bowl” for the cell to sit in instead of extruding the cell. This “bowl” case occurs in systems shown in the phase diagrams in Figure 4.16c when there is low modified cell adhesion and large additional modified cell contraction. The “bowl” case is identified as a partial extrusion case. The weaker the apical perimeter contraction the less likely for the “bowl” case to exist. This can occur whether the apical perimeter contraction is applied to the modified cell or not.

The phase diagrams in Figure 4.16 show only one regime value $\beta = 1.1902$ for the monolayer. However, by changing the value of beta Figure 4.17a shows a system for a soft regime and Figure 4.17b for a hard regime. While there is little to no difference in Figure 4.17a compared to Figure 4.16a, a hard system shown in Figure 4.17b demonstrates that the modified cell does not extrude for a similar range of values for S^*/S and Γ^*/Γ. This suggests that the regime condition has an effect on the extrusion of the modified cell.

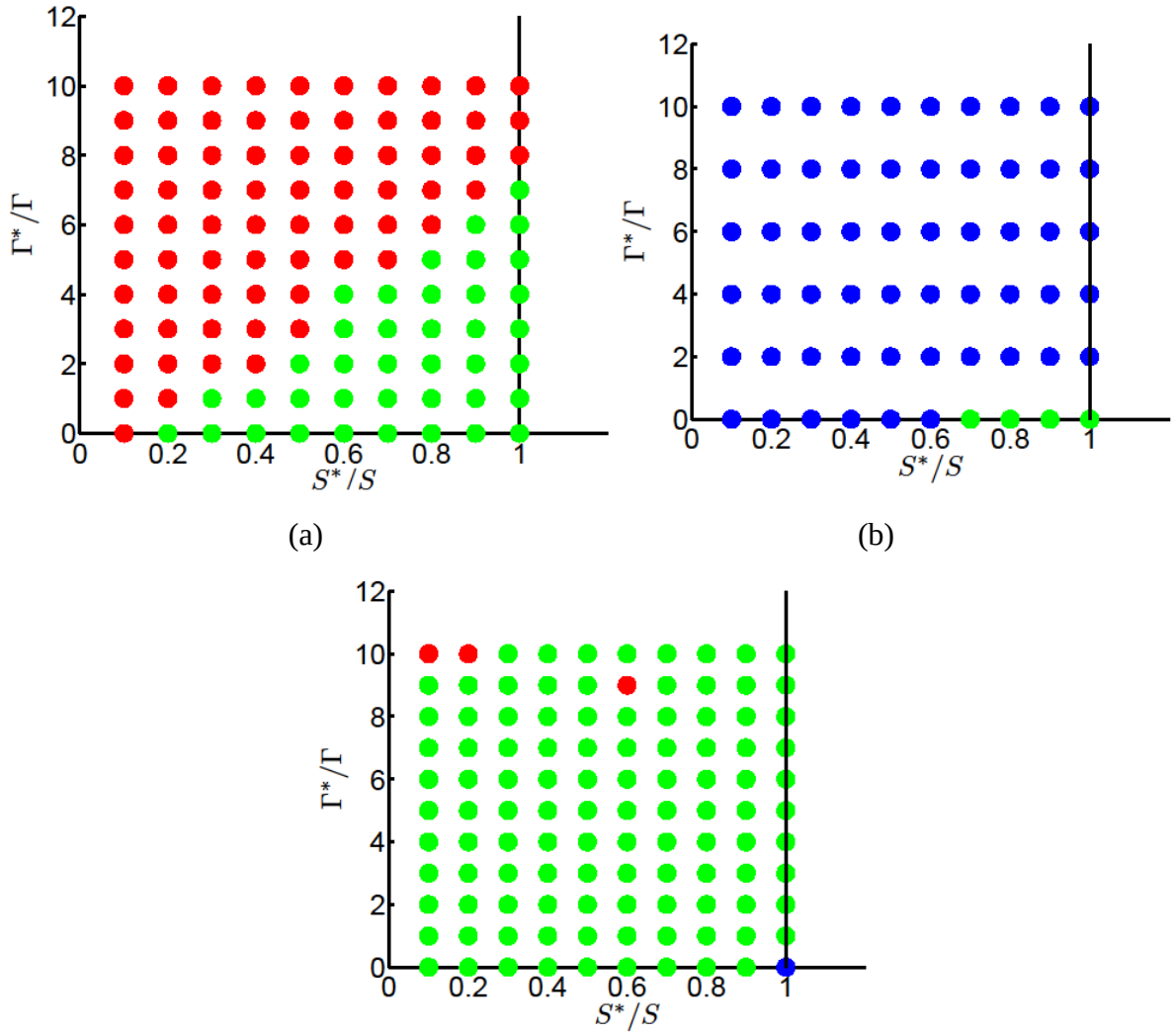

Figure 4.16. Phase diagrams comparing the modified cell adhesion ratio, S^*/S, and additional modified cell contraction ratio, Γ^*/Γ . Each marker represents a single simulation and a modified cell is identified as an extruded cell in the diagram with a red marker, partially extruded with a green marker, and not extruded with a blue marker. a) Represents the base case, b) represents a reduction in the substrate adhesion, $\alpha = S$, and c) includes an apical perimeter contraction, $\Gamma_t = 300$, for all the cells. The base case parameters include $k = 100$, $S = 65000$ ($\beta = 1.1905$), $\Gamma = 50$, $\alpha = 2S$, $V_p = 500$ and $h = 5$ with $N = 25$ cells on a $50 \times 50 \times 10$ hexagonal layered pixel grid.

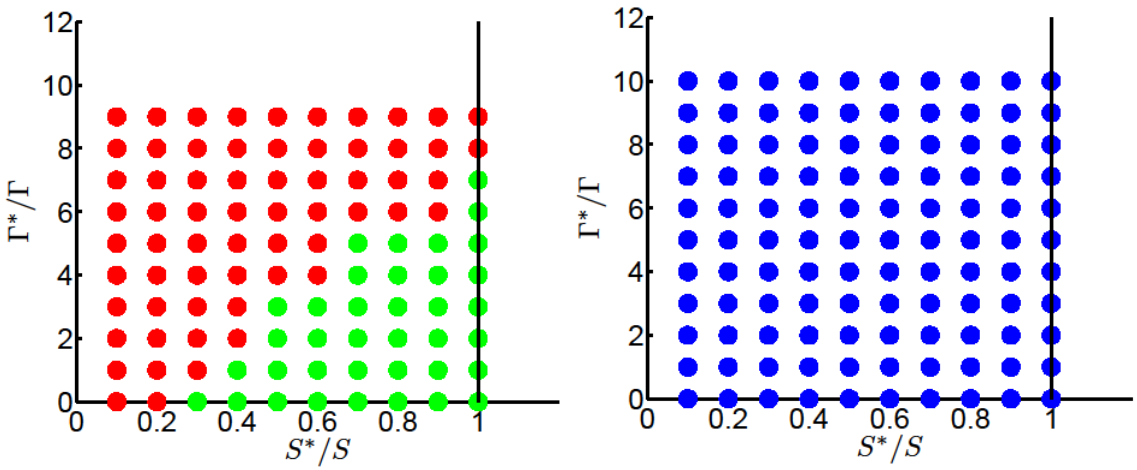

(a) (b)

Figure 4.17. Phase diagrams comparing the modified cell adhesion ratio, S^*/S, and additional modified cell contraction ratio, Γ^*/Γ. Each marker represents a single simulation and a modified cell is identified as an extruded cell in the diagram with a red marker, partially extruded with a green marker, and not extruded with a blue marker. a) Represents a soft system, $S = 90000$ and $\Gamma = 50$ ($\beta = 1.6484$), and b) represents a hard system, $S = 30000$ and $\Gamma = 50$ ($\beta = 0.5495$). Other parameters include $k = 100$, $\alpha = 2S$, $V_p = 500$ with $N = 25$ cells on a $50 \times 50 \times 10$ hexagonal layered pixel grid.

Similar to the wound case in the Section 4.5 we examine, in Figures 4.18 and 4.19, the horizontal cross-sectional area of the modified cell against different values of β. The extrusion of the modified cell in the hard and soft regimes is similar to the open and closed wound case. Rather than the showing the cross-sectional area of the wound from the five pixel layers of the monolayer in Figure 4.7, Figures 4.18 and 4.19 show the cross-sectional area of the modified cell in the same five pixel layers against different regimes, β, in the system. When the modified cell does not occupy a pixel layer of the monolayer the area, A_i,will be zero.

Figure 4.18a presents systems with parameters, $\Gamma^*/\Gamma = 0$, and $S^*/S = 1$. The cell does not extrude since the cross-sectional area of all the layers of the cells does not reduce to zero. However, the simulations in the soft regime show that the area of the bottom of the modified cell does reduce to zero, meaning the modified cell lifts off the substrate but no other changes occur. Note that the top apical layer in the hard regime also reduces to zero. This occurs because the modified cell has shrunk and does not necessarily mean that the cell has been enclosed in the monolayer by other cells. In either case the modified cell does not extrude. Figure 4.18b shows that by reducing the modified cell adhesion of the modified cell, represented by the ratio S^*/S, to 0.2, the cell can extrude in the soft regime. As the modified cell adhesion becomes weaker the extrusion of the

modified cell is comparable to the wound case, where soft cell regimes can extrude the modified cell and harder cell regimes cannot extrude a modified cell. The partial extrusion of the modified cell, where the modified cell has extruded from four of the five pixel layers of the monolayer, can also be seen in Figure 4.18c, with a modified cell adhesion of $S^*/S = 1$, which shows the effect of the additional lateral contraction, $\Gamma^*/\Gamma = 6$. The full extrusion of the modified cell was seen in the phase diagram in Figure 4.16a with stronger lateral contraction. Figures 4.18a, 4.18b and 4.18c show when the modified cell adhesion is decreased, seen between Figures 4.18a and 4.18b, or when the additional lateral contraction is added and increased, seen between Figures 4.18a and 4.18c, the extrusion of the modified cell is similar to the closure of a wound in Section 4.5. Softer cell regimes are able to extrude the modified cell and harder cell regimes cannot. This suggests that, in the simulations, the extrusion of the modified cell is closely related to the closure of the wound.

Additional parameters and changes, such as the addition of an apical perimeter contraction, the reduction of the substrate adhesion and the additional of the modified cell basal perimeter contraction, can also affect the extrusion of the modified cell and are shown in the plots in Figure 4.19. Figure 4.19a plots similar systems to those plotted in Figure 4.18b, except additional apical contraction, $\Gamma_t = 300$, is applied to the cells surrounding the modified cell. The simulations in the soft regime that were able to extrude a cell in Figure 4.18b now only partially extrude the modified cell in Figure 4.19a, where the modified cell only occupies the upper pixel layers and is removed from the lower pixel layers. Figure 4.19b also plots similar systems to those plotted in Figure 4.18b, except the substrate adhesion is $\alpha = S$. The systems that showed an extruded modified cell in Figure 4.18b are not able to extrude the modified cell in Figure 4.19b, as the modified cell still occupies all the pixel layers in the monolayer of cells. This is similar to the effect in the micro-wound simulations with a decreased substrate adhesion seen by comparing Figure 4.7a, 4.7b and 4.7c. Finally, Figure 4.19c plots simulations similar to Figure 4.18a, except basal perimeter contraction, $\Gamma_b = 300$, is added to the modified cell. Figure 4.18a showed that all simulations did not extrude the modified cell with the modified cell only being removed from basal pixel layer, A_1. However, with the addition of the basal perimeter contraction in Figure 4.19c the modified cell is shown to be partially removed in soft regime systems with the modified cell only occupying the apical pixel layer of the monolayer of cells. This is similar to the wound closure in Figure 4.8. The values of the wound cross-sectional area in Figure 4.8 suggest that the apical pixel layer was still open, $A_i/A_p = 25$, but this represents the monolayer of cells decreasing in height since the empty space of the empty space representing the wound covers the entire monolayer's horizontal cross-section area in the simulation, which means the wound did close. Whereas in Figure 4.19c the modified cell still occupies the apical pixel layer.

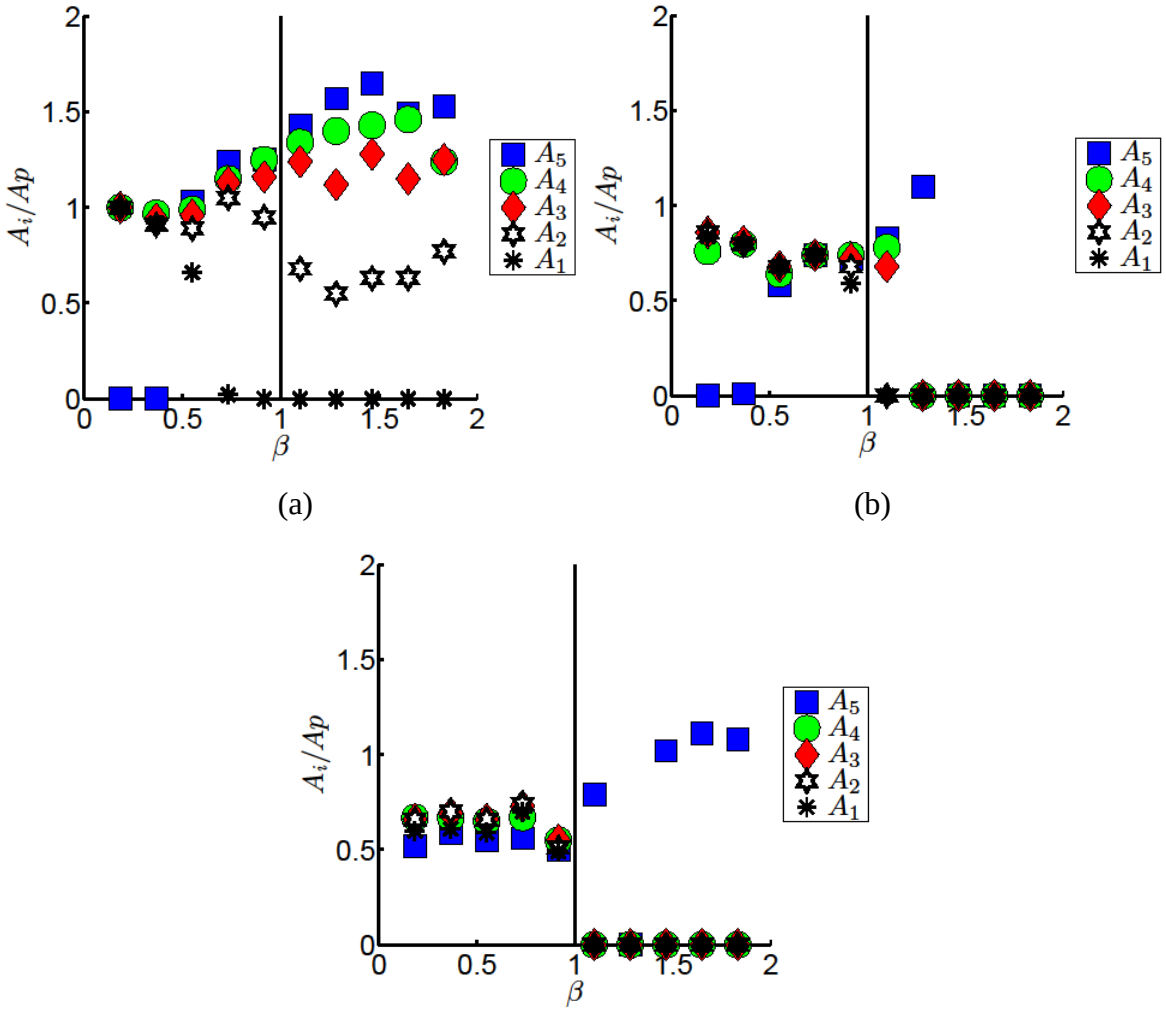

Figure 4.18. Plots of the equilibrium values of the average horizontal cross-section modified cell area over the last 100 iterations of a single CPM simulation of 2000 iterations against different cell regimes, β at five pixel layers. a) Plots the cases with a modified cell ratio of $S^*/S = 1$ and no additional lateral contraction, $\Gamma^*/\Gamma = 0$. b) Plots the cases with no additional lateral modified cell contraction ratio, $\Gamma^*/\Gamma = 0$, and a low modified cell ratio to $S^*/S = 0.2$. c) Plots the cases with a larger additional modified cell contraction ratio to $\Gamma^*/\Gamma = 6$ and a low modified cell adhesion ratio of $S^*/S = 1$. Other parameters are $k = 100$, $\Gamma = 50$, $\alpha = 2S$, $V_p = 500$ with $N = 25$ cells on a $50 \times 50 \times 10$ hexagonal layered pixel grid.

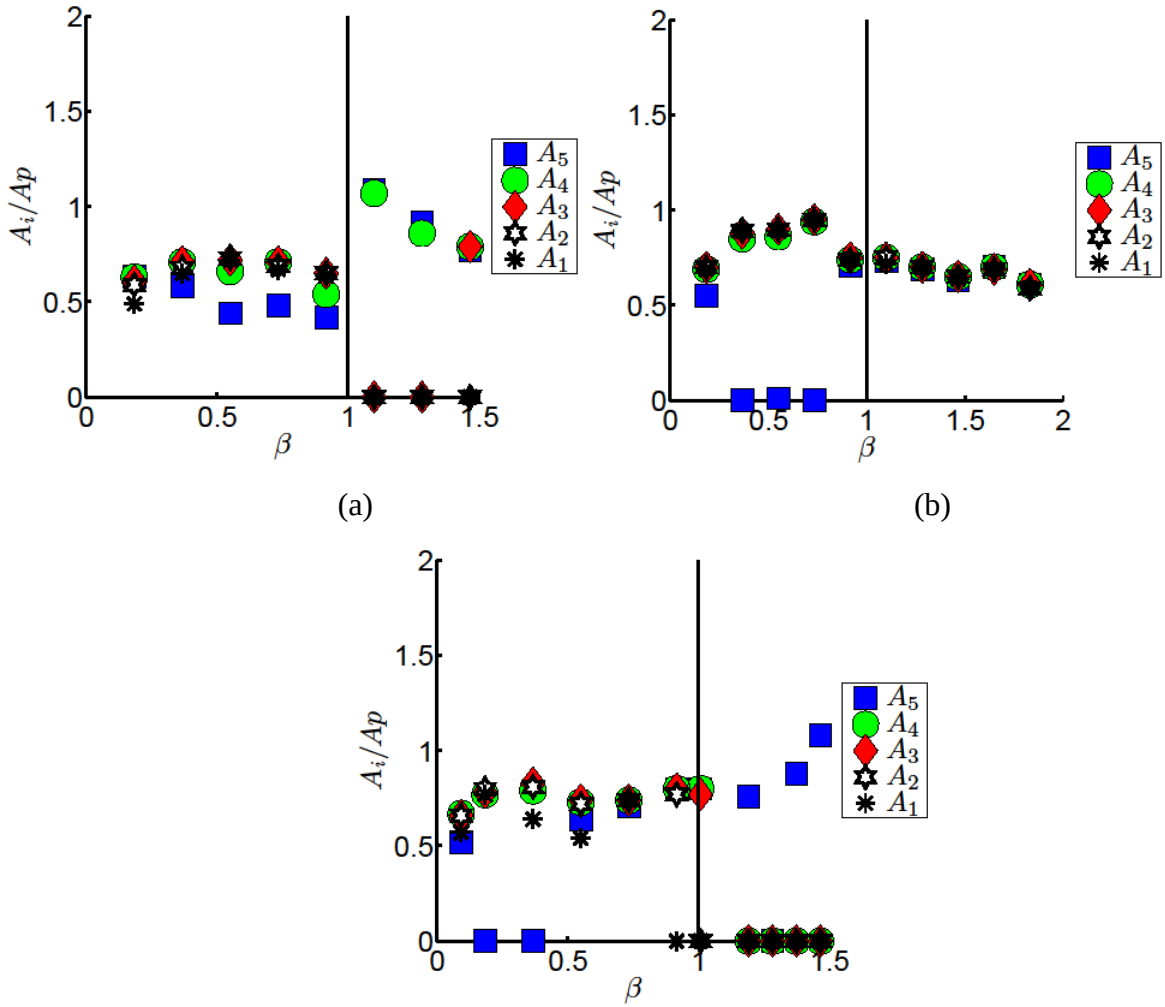

Figure 4.19. Plots of the equilibrium values of the average horizontal cross-section modified cell area over the last 100 iterations of a single CPM simulation of 2000 iterations against different cell regimes, β at five pixel layers. The plots represents cases with a larger additional modified cell contraction ratio to $\Gamma^*/\Gamma = 6$ and a low modified cell ratio to $S^*/S = 0.2$, with a) the inclusion of an apical perimeter contraction of $\Gamma_t = 300$ and substrate adhesion of $\alpha = 2S$, on the cells; b) a reduction in the substrate adhesion to $\alpha = S$; and c) the inclusion of a basal perimeter contraction of $\Gamma_b = 300$ and a substrate adhesion of $\alpha = 2S$, on the modified cell to the case with a modified cell ratio, $S^*/S = 1$. Other parameters are $k = 100$, $\Gamma = 50$, $V_p = 500$ with $N = 25$ cells on a $50 \times 50 \times 10$ hexagonal layered pixel grid.

4.6.2 Spherical representation of an extruded modified cell for theoretical analysis

The geometric representation of the modified cell system draws on the concepts of the geometric representation of the system with an empty wound; however, instead of a wound there is a modified cell that is allowed to leave the monolayer. All non-modified cells are represented as truncated cones with the apical and basal layers of the cells represented by radii R_t and R_b, respectively. The modified cell on the other hand is represented by two shape components: a truncated cone, with the apical and basal radii represented by R_t^* and R_b^* in the monolayer; and a sphere, with the radius R_{ot}^* , representing the extruded component of the modified cell, see Figure 4.20. As the geometric representation is considered to be a simplified representation of the extrusion of the modified cell, we consider these two shape components to be separate from each other. While other shapes can be used to represent the extruded component of the modified cell, the sphere is selected as it can be defined by a single variable, the radius. The radius of the sphere can be expressed as

$$R_{ot}^* = \sqrt[3]{\frac{3}{4\pi}V_p - \frac{1}{4}(R_t^{*2} + R_t^* R_b^* + R_b^{*2})h},$$

with two additional assumptions. Firstly, the height of the monolayer is fixed. Secondly, the volume of the modified cell, V^*, will always have a place to occupy, i.e. the volume of the sphere is fixed at V_p.

The energy function of this geometric model is derived from Function (4.16) and is expressed with the modified and non-modified cell terms with the geometry represented above, where the modified components are represented with "*",

$$\mathrm{E} = \frac{k(N-1)}{2}\left(V - V_p\right)^2 + \frac{\Gamma(N-1)}{2}A^2 \ + \frac{\Gamma^*}{2}A^{*2} - \frac{\mathrm{S}}{2}A_s - \frac{S^*}{2}A_s^* - \frac{\alpha}{2}A_b - \frac{\alpha^*}{2}A_b^* + \frac{\Gamma_t}{2}\mathrm{L}_t^2 + \frac{\Gamma_t^*}{2}\mathrm{L}_t^{*2} + \frac{\Gamma_b}{2}L_b^{*2}. \quad (4.17)$$

The non-modified cell's apical, basal and lateral surface areas are represented with A_t, A_b and A_s, respectively, and the total surface area, A, as a summation of all three surface area components. The modified cell's apical, basal and lateral surface areas of the truncated cone are represented by A_t^*, A_b^* and A_s^*, respectively, and the sphere surface area is represented by A_o^*. Unlike the non-modified cells, the modified cell's total surface area is a combination of the truncated cone and the sphere.

The sphere radius must always be non-negative, $R_{ot}^* \geq 0$. A heavy-side step function, η, is used to remove the sphere if $R_{ot}^* < 0$. The total surface area of the modified cell is given by

$$\mathrm{A}^* = A_s^* + A_t^* + A_b^* + A_o^*\big(\eta(R_{ot}^*)\big).$$

As with the geometric representation of the wounds in two and three dimensions, we assume the pixel layers of the epithelium have a conserved area. This means that the apical and basal radii of the non-modified cells, (R_t, R_b), and modified cell, (R_t^*, R_b^*), are related by Equation (4.6), where R_t^* and R_b^* represent the modified cell instead of the wound. This means the energy function can be expressed with the modified cell pair of variables,

$$\begin{aligned} E(R_t^*, R_b^*) = {} & \frac{k(N-1)}{2}\big(V(R_t^*, R_b^*) - V_p\big)^2 + \frac{\Gamma(N-1)}{2}\big(A(R_t^*, R_b^*)\big)^2 \\ & + \frac{\Gamma}{2}\big(A^*(R_t^*, R_b^*)\big)^2 + \frac{\Gamma^*}{2}(A_s^*(R_t^*, R_b^*) +)^2 - \frac{S(N-1)}{2}A_s(R_t^*, R_b^*) \\ & + \frac{S-2S^*}{2}A_s^*(R_t^*, R_b^*) - \frac{\alpha(N-1)}{2}A_b(R_t^*, R_b^*) - \frac{\alpha^*}{2}A_b^*(R_t^*, R_b^*) \\ & + \frac{\Gamma_t(N-1)}{2}L_t(R_t^*)^2 + \frac{\Gamma_t^*}{2}L_t^*(R_t^*)^2 + \frac{\Gamma_b}{2}L_b^*(R_b^*)^2. \end{aligned} \quad (4.18)$$

The non-modified cell volume is expressed with Function (4.9), surface areas with Functions (4.10), (4.11) and (4.13), and perimeter with Function (4.15). The modified cell volume is expressed with function

$$V(R_t^*, R_b^*) = \frac{1}{3}\pi h\big({R_t^*}^2 + {R_b^*}^2 + R_t^* R_b^*\big) + \frac{4}{3}\pi {R_o^*}^3,$$

basal perimeter with Function (4.14), and surface areas with Functions (4.12) and

$$A_b^*(R_b^*) = 2\pi {R_b^*}^2,$$

and the total surface area of the modified cell is represented as

$$A^*(R_t^*, R_b^*) = \pi(R_t^* + R_b^*)\sqrt{(R_t^* - R_b^*)^2 + h^2} + \pi {R_t^*}^2 + \pi {R_b^*}^2 + 4\pi\eta(R_{ot}^*)^2.$$

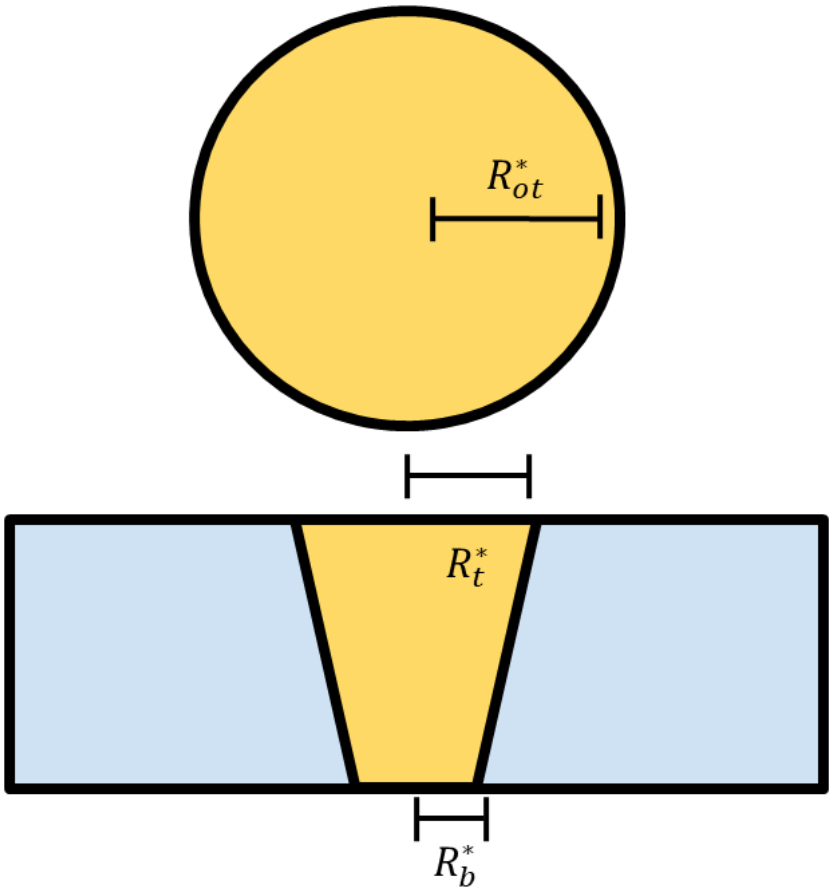

Figure 4.20. Geometric representation of the modified cell as a truncated cone inside the monolayer, with radii of R_t^* and R_b^* , and a sphere representing the extruded component, with radius R_{ot}^*.

Results of the modified cell geometric model

Energy Function (4.16) is expressed with the apical and basal radii of the modified cell and is plotted in Figure 4.21 as a contour plot. The figure highlights three states of the modified cell, namely, a non-extruded modified cell ($R_t^* > 0, R_b^* > 0$) in Figure 4.21a, a partially extruded modified cell or inverted cone ($R_t^* > 0, R_b^* = 0$) in Figure 4.21b, and an extruded modified cell ($R_t^* = 0, R_b^* = 0$) in Figure 4.21c.

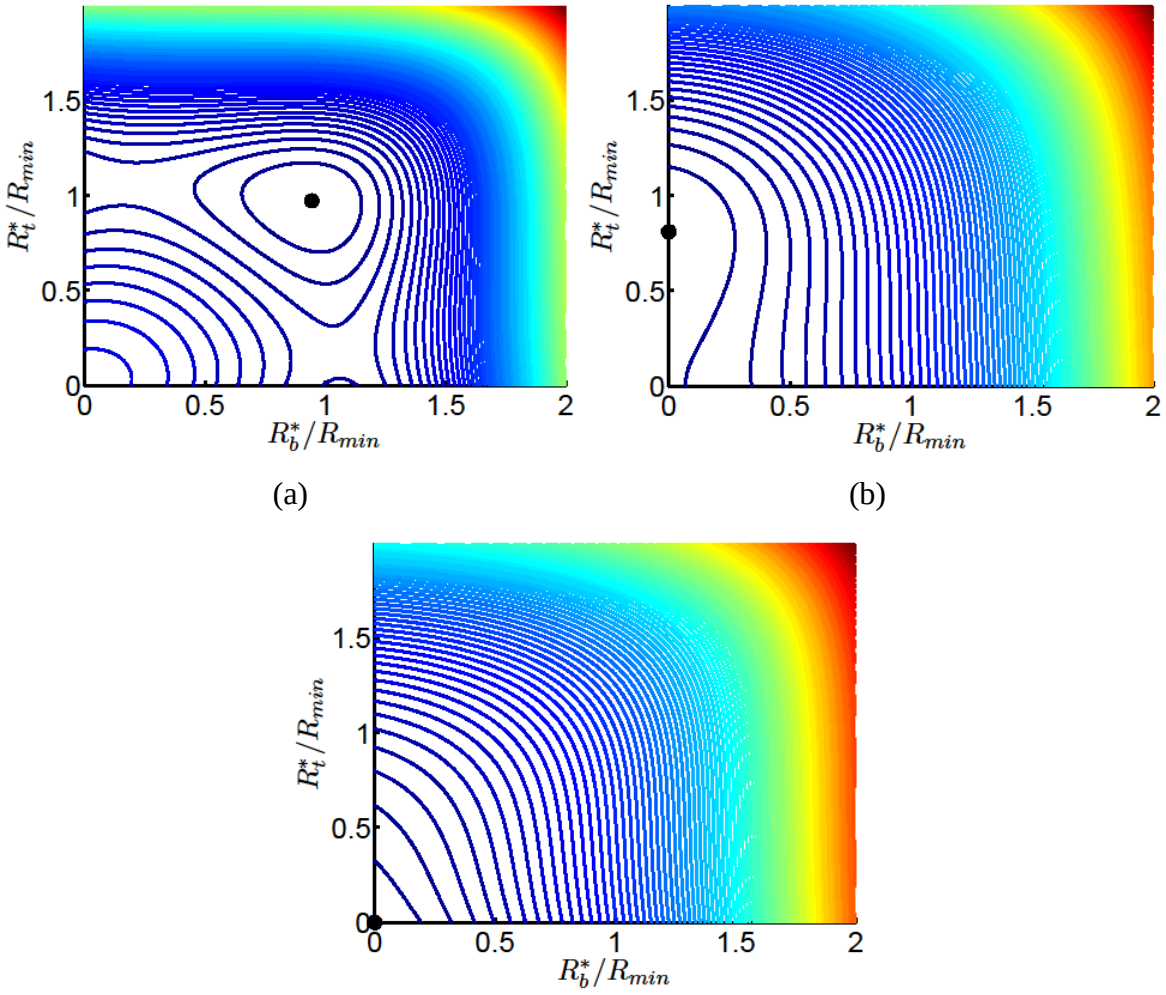

(a) (b)

(c)

Figure 4.21. Contour plots for the energy Function (4.17) of the spherical geometric representation of the modified cell. A black point represents the local minimum energy function. a) An non-extruded modified cell, with $S^*/S = 0.5$ and $= 1000$ ($\beta = 0.0265$), b) a partially extruded modified cell, with $S^*/S = 0.5$ and $S = 60000$ ($\beta = 1.5905$), and c) an extruded modified cell, with $S^*/S = 0.1$ and $S = 60000$ ($\beta = 1.5905$). Other parameters include $\Gamma = 50$, $k = 100$, $\alpha = 2S$, $V_p = 500$ and $h = 5$ with $N = 25$ cells.

Changing the relative strengths of the modified cell adhesion changes how the modified cell interacts with the neighbouring cells. If the modified cell adhesion is the same as the other cells in the system, the modified cell itself should have little or no change. However, given that the adhesion to the substrate is absent the basal radius would reduce to zero. Decreasing the relative value of the modified cell's adhesion means that the cell itself would become "harder" than the neighbouring cells, but the lower adhesion would reduce the surface area in contact with other cells and can extrude the modified cell. Figure 4.22a shows these different cases of the modified cell's extrusion by plotting the apical (solid line) and basal (dashed line) radii of the modified cell, where R_{min} (or R_p) is the radius of a cylindrical cell with a volume V_p and height h. The black line in the plot represents a system with an adhesion ratio $S^*/S = 1$, the green $S^*/S = 0.5$, and red $S^*/S = 0.1$. The figure shows a similar result to the simulations, namely, that decreasing the modified cell adhesion will facilitate extruding the modified cell for "soft" cell regimes. As the modified cell adhesion gets closer to zero the plots and system become similar to the wound system. However, unlike the wound case, the radii of the modified cell does not increase much above the ratio $R/R_{min} = 1$. This is due to the assumption of the fixed volume of the modified cell. If the modified cell is not extruded, then the largest volume the cell can have is V_p, from which R_p is derived. The wound does not have this restriction and the wound can be larger as is evident in the hard regime in Figure 4.14.

The addition of the extra cortical contraction around the modified cell would create a harder cell and the surface area of the cell would decrease. We expected that this change would be similar to the change in the relative modified cell adhesion; however, this is not the case. Figure 4.22b shows plots of the relative radii of the modified cell against the regime, β, with changing values of additional contraction on the modified cell. The black line represents the contraction ratio $\Gamma^*/\Gamma = 0$, green line $\Gamma^*/\Gamma = 4$ and red line $\Gamma^*/\Gamma = 8$. The plot shows that the increase in the modified cell's additional lateral contraction can assist with the modified cell extrusion; this reduction is shown by the reduction in the modified cell's apical radius. There is a difference between the simulations and the geometric model related to the connection between the modified cell and its neighbouring cells. The geometric model assumes that the cells are connected to each other, whereas in the CPM the cells can detach from each other so long as there are empty spaces connected to the junctions. So, in the geometric model the contraction of the modified cell can not only "shrink" the modified cell, but the "shrinking" of the modified cell "pulls" other neighbouring cells with it. However, in the simulations, large contraction parameters can separate the cells from one another, see Figure 4.4. In particular, with the additional lateral contraction of the modified cell, the modified cell can separate from its neighbours.

The behaviour of the modified cell in the geometric model when both the modified cell adhesion and additional lateral contraction are changed is observed in the phase diagrams in Figures 4.23 and 4.24. These phase diagrams include the three cases of the modified cell extrusion: the non-extrusion case represented by the blue points, the partial extrusion represented by the green points, and the extrusion of the modified cell represented by the red points. While the geometric model phase diagrams have clear differences compared to the simulation phase diagrams in Figures 4.16 and 4.17, the main behaviour of the modified cell in the geometric model is similar to the simulations of changes in the modified cell adhesion and additional lateral contraction.

When the modified cell adhesion decreases the modified cell is able to extrude. The system with a cell regime of $\beta = 1.7230$ and a substrate adhesion of $\alpha = 2S$ in Figure 4.23a shows there is a divide represented by as a gradient between the three modified cell extrusion cases when $\Gamma^*/\Gamma \leq 2$. However, when $\Gamma^*/\Gamma > 2$ there is a distinct threshold, at $S^*/S = 0.8$, between only the partial extrusion and extrusion of the modified cell. This threshold is a clear difference between the geometric model and the simulation data shown in Figure 4.16a where no such threshold is observed.

Changing the substrate adhesion of the system in Figure 4.23a from $\alpha = 2S$ to $\alpha = 0$ shown in Figure 4.23b does "hinder" the extrusion of the modified cell. Some of the modified cell partial extrusion and extrusion cases change to non-extrusion cases when $\Gamma^*/\Gamma \leq 2$. Therefore, systems with $\Gamma^*/\Gamma \leq 2$ require the modified cell adhesion ratio to be smaller for the modified cell to extrude. When $\Gamma^*/\Gamma > 2$ there is still a threshold at $S^*/S = 0.8$, but this threshold is between non-extrusion and extrusion instead of partial-extrusion and extrusion of the modified cell.

Reducing the cell substrate adhesion to zero makes the apical and basal layers appear similar. This similarity can be seen in Figure 4.25a, which plots the apical (solid line) and basal (dashed line) radii of the modified cell against the cell regime, where the system with no substrate adhesion (red) has the same value for the apical and basal radii.

Different cell regimes in the simulations change the behaviour of the modified cell in the phase diagram. Although, in simulations there was little change in softer regimes, in the hard regimes hindering the modified cell extrusion. The geometric model does not follow the behaviour of the modified cell simulations, except when $\Gamma^*/\Gamma = 0$.

The cell regime of the systems in Figure 4.23 is $\beta = 1.7230$ and Figure 4.24a shows a harder cell regime system than Figure 4.23a with $\beta = 0.7952$. Unlike the simulations, the modified cell extrusion in the geometric model is not hindered, except when $\Gamma^*/\Gamma = 0$. When $\Gamma^*/\Gamma = 0$ the

plot in Figure 4.24a shows that the adhesion ratio of the modified cell must be decreased further to extrude the modified cell. For the systems where $\Gamma^*/\Gamma > 0$ we find that there is a divided by a gradient similar to Figure 4.23a but there is no distinct threshold of S^*/S between two modified cell extrusion cases. Although the geometric model behaviour is different than the simulation in this case, reducing the substrate adhesion to zero in Figure 4.24b does confirm that a reduction in the substrate adhesion hinders the extrusion of the modified cell.

The cell regime of the system in Figure 4.23a is $\beta = 1.7230$ and Figure 4.24c shows a softer cell regime system with $\beta = 2.3857$. Unlike the simulations there is an observable difference in the behaviour of modified cell extrusion in the geometric model. A distinct threshold exists between the two cases of the extruded modified cell and the partially extruded cell, although it is shifted from $\Gamma^*/\Gamma \approx 0.8$ to $\Gamma^*/\Gamma \approx 0.7$. There is also a gradient observed between the non-extruded cell and partially extruded cases. Again, reducing the substrate adhesion to zero in this regime in Figure 4.24d shows the extrusion of the modified cell is hindered in a similar way to Figure 4.23b.

Adding the apical perimeter contraction of the non-modified cells, $\Gamma_t = 500$, and the basal perimeter contraction of the modified cell, $\Gamma_b = 300$, to the systems shown in the phase diagram in Figure 4.23a are shown in the phase diagrams in Figures 4.23c and 4.23d, respectively. These phase diagrams show no significant quantitative change to the modified cell extrusion behaviour with the addition of either mechanism. In simulations, the adding of the apical perimeter contraction of the non-modified cells showed a clear change of behaviour of the modified cell. Systems where the modified cell extruded, in Figure 4.16a, would only partially extrude when the apical perimeter was added to the non-modified cells, in Figure 4.16c. Figure 4.25b, which plots the apical (solid line) and basal (dashed line) radii of the modified cell against the cell regime, does show that no apical perimeter contraction and an apical perimeter contraction of $\Gamma_t = 500$ have the same radii. However, for a much larger apical perimeter contraction of $\Gamma_t = 5000$ there is a difference. The plot is similar to the plot of the lateral contraction of $\Gamma^*/\Gamma = 8$ (red) in Figure 4.22b.

The addition of the basal perimeter contraction to the modified cell shows very little change in Figure 4.23d. This is different to the results of the CPM simulations where there was some change to the basal pixel layer of the modified cell between Figures 4.18a and 4.19c. While there are no observed changes in phase diagram in Figure 4.23d, there is an observable change in plot of the modified cell radii in Figure 4.25c, which plots the apical (solid line) and basal (dashed line) radii of the modified cell against β. The change in Figure 4.25c shows that adding the basal perimeter contraction to the modified cell can "close" the basal layer. Increasing the strength of the

basal perimeter contraction does not affect the system a lot because once the basal layer of the modified cell is “closed” the cell is no longer affected by the basal perimeter contraction.

One possible reason for the difference between the geometric model and simulations is the classification of the lateral contraction of the modified cell. The geometric model assumes that all the cells are connected to one another and, as such, a stronger lateral contraction on the modified cell would pull the cells in to “close” the gap that would be left behind after extrusion. However, softer cells in the lateral contraction case have difficulty reaching their preferred cell surface area leading to the results seen in the figures discussed above.

The geometric model produces some results that differ compared to the CPM simulation. While changes in adhesion give similar results, the results with changing lateral contraction have greater differences partially due to the connectivity assumptions between the cells. The assumption of connectivity for the geometric model affects the modified cell’s extrusion more significantly than for the wound system; however, this assumption of connectivity is needed to model the modified cell in the geometric model.

Comparing the geometric modified cell case to the geometric representation of the wound shows that some of the plots in Figures 4.22 and 4.25 have similarities to the wound plots in Figure 4.14. In particular when the basal radii drop to zero, the discontinuity seen in the apical radii in Figure 4.14 is also observed in Figures 4.22 and 4.25. While most plots in Figures 4.22 and 4.25 also show the apical radii decreasing then dropping to zero, seen in Figure 4.14, some plots in Figure 4.22 show the apical radii increasing when the adhesion increases. This is caused by the presence of the modified cell in the monolayer and the modified cell having a similar cell-cell adhesion as its neighbours. When increasing the adhesion the cells rearrange to cover a larger surface area between each other. For the modified cell this is achieved by forming a cone $(R_t^* > 0, R_b^* = 0)$, due to the lack of substrate adhesion.

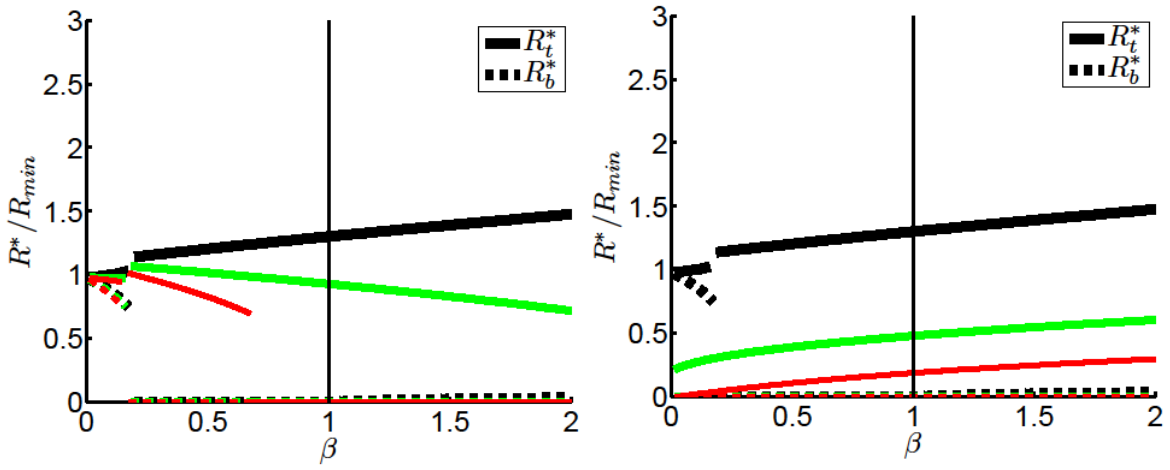

Figure 4.22. Plots of the apical (solid line) and basal (dashed line) modified cell radii at the local minima of the energy function with a spherical geometric representation of the extruded modified cell, against the regime of the system, β. a) Represents changes to the modified cell adhesion with the ratios of $S^*/S = 1$ (black), $S^*/S = 0.5$ (green) and $S^*/S = 0.1$ (red). b) Represents changes to the modified cell's additional contraction, $\Gamma^*/\Gamma = 0$ (black), $\Gamma^*/\Gamma = 4$ (green) and $\Gamma^*/\Gamma = 8$ (red). Other parameters are $k = 100$, $\Gamma = 50$, $\alpha = 2S$, $V_p = 500$ and $h = 5$ with $N = 25$ cells.

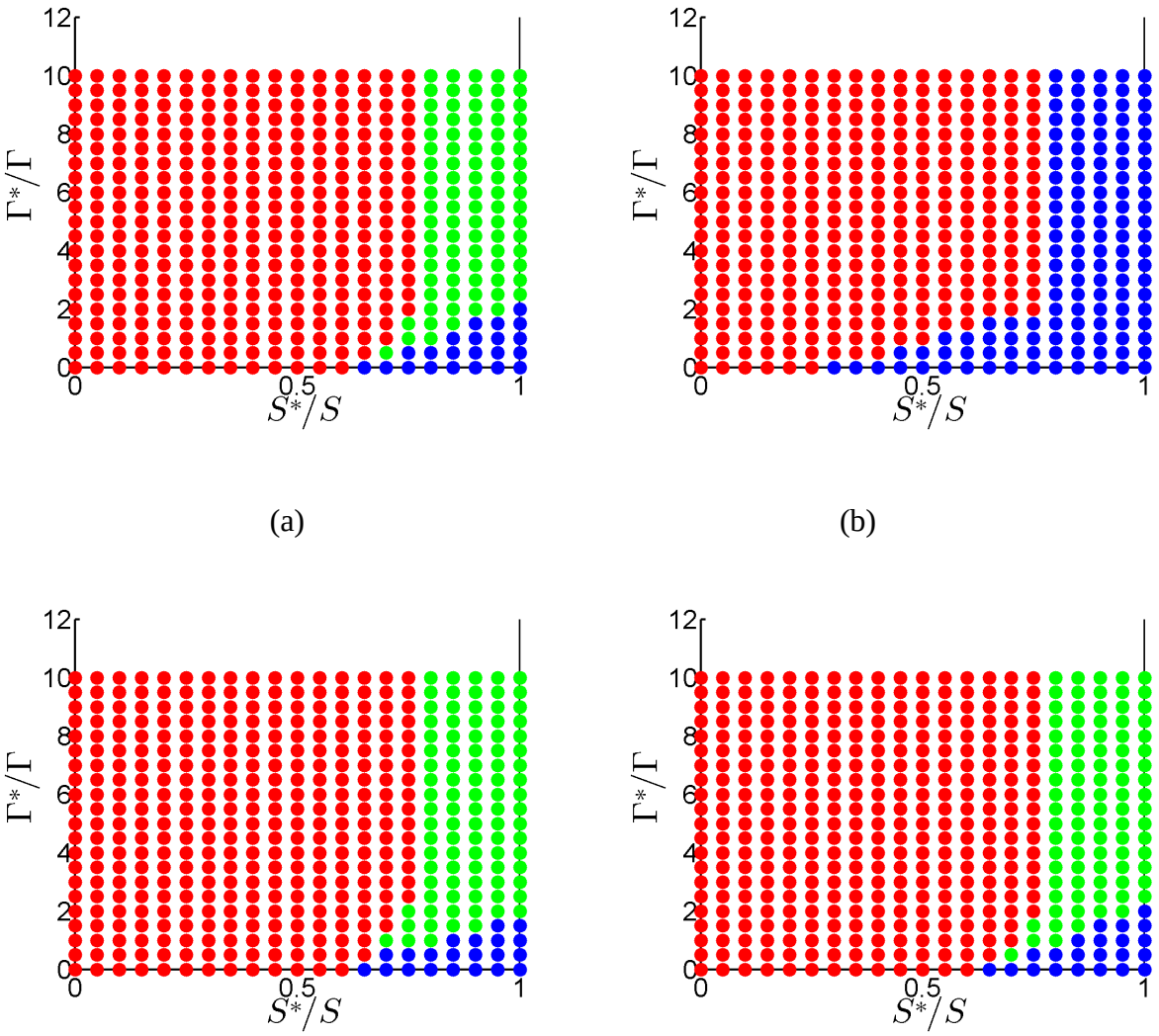

Figure 4.23. Phase diagrams comparing the modified cell adhesion ratio, S^*/S, and additional modified cell contraction ratio, Γ^*/Γ, for the spherical representation of the modified cell. An extruded cell in the diagram is identified with the red marker, partially extruded with a green marker, and not extruded with a blue marker. a) Represents a the systems with a substrate adhesion of $\alpha = 2S$, b) represents a reduction in the substrate adhesion, $\alpha = 0$, c) has a substrate adhesion of $\alpha = 2S$ and includes an apical perimeter contraction, $\Gamma_t = 500$, for all the cells, and d) has a substrate adhesion of $\alpha = 2S$ and includes the basal perimeter contraction, $\Gamma_b = 300$, for the modified cell. Other parameters include parameters include $k = 100$, $S = 65000$, $\Gamma = 50$ ($\beta = 1.7230$), $V_p = 500$ and $h = 5$ with $N = 25$ cells.

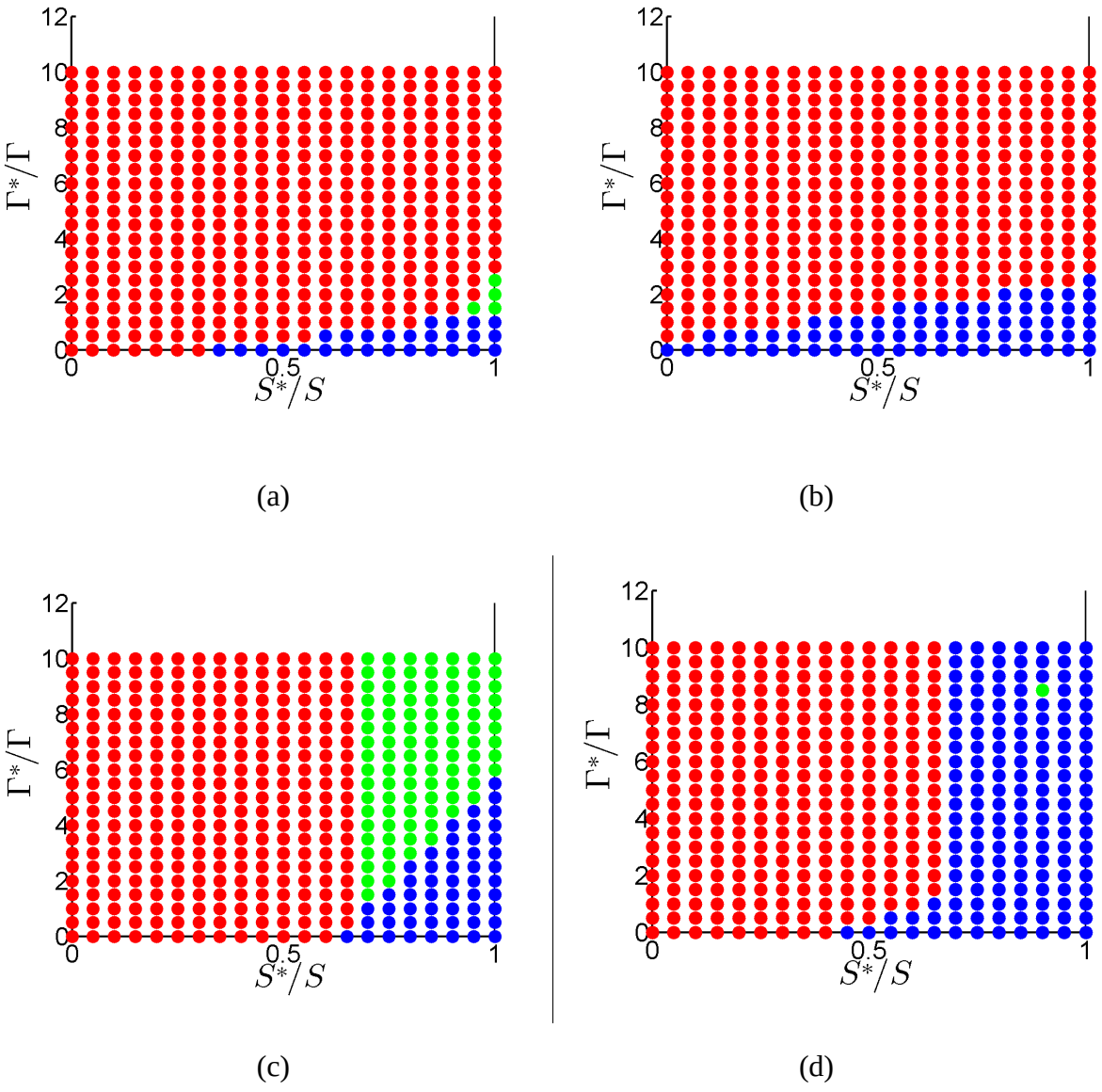

Figure 4.24. Phase diagrams comparing the modified cell adhesion ratio, S^*/S, and additional modified cell contraction ratio, Γ^*/Γ , for the spherical representation of the modified cell. An extruded cell in the diagram is identified with the red marker, partially extruded with a green marker, and not extruded with a blue marker. a) Represents a harder system with cell-cell adhesion, $= 30000$ ($\beta = 0.7952$), and substrate adhesion, $\alpha = 2S$. b) Represents the harder system with cell-cell adhesion, $= 30000$ ($\beta = 0.7952$), and a substrate adhesion, $\alpha = 0$. c) Represents a softer system with cell-cell adhesion, $= 90000$ ($\beta = 2.3857$), and substrate adhesion, $\alpha = 2S$. d) Represents the softer system with cell-cell adhesion, $= 90000$ ($\beta = 2.3857$), and substrate adhesion, $\alpha = 0$. Other parameters include $k = 100$, $\Gamma = 50$, $V_p = 500$ and $h = 5$ with $N = 25$ cells.

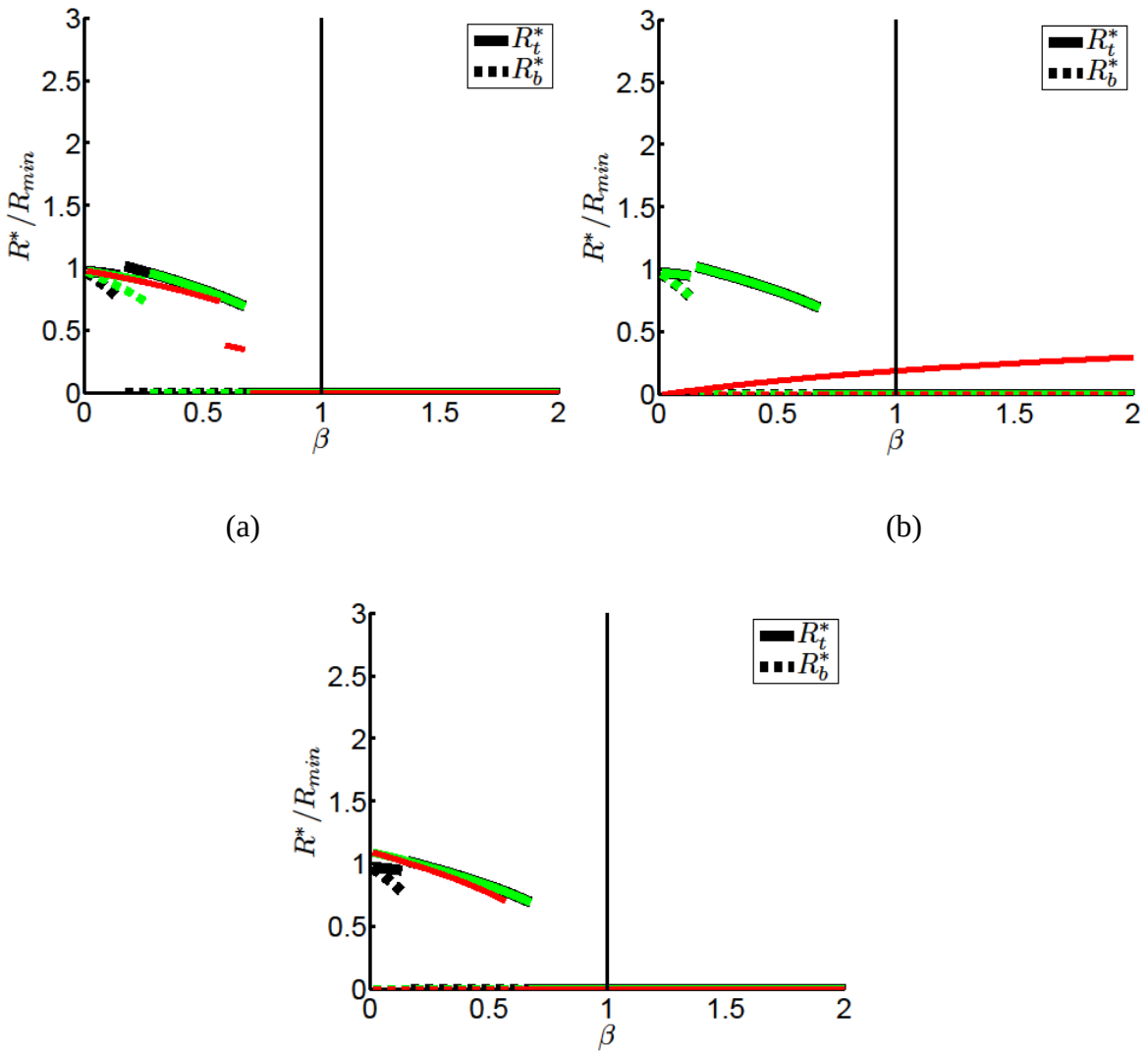

Figure 4.25. Plots of the apical (solid line) and basal (dashed line) modified cell radii at the local minima of the energy function with a spherical geometric representation of the extruded modified cell, against the regime of the system, β. a) Represents systems with changes to the substrate adhesion $\alpha = 2S$ (black), $\alpha = S$ (green) and $\alpha = 0$ (red). b) Represents systems with $\alpha = 2S$ and changes to the additional apical perimeter contraction with $\Gamma_t = 0$ (black), $\Gamma_t = 500$ (green) and $\Gamma_t = 5000$ (red). c) Represents systems with $\alpha = 2S$ and changes to the additional cell basal perimeter contraction with $\Gamma_b = 0$ (black) and $\Gamma_b = 500$ (green) and $\Gamma_b = 5000$ (red). Other parameters are $k = 100$, $\Gamma = 50$, $V_p = 500$ and $h = 5$ with $N = 25$ cells.

4.6.3 Hemispherical representation of an extruded modified cell for theoretical analysis

Rather than representing the extruded component of the modified cell as a sphere we can instead represent it with a hemisphere, with a radius of R_{ot}^*. The hemisphere is connected to the truncated cone component of the modified cell inside the monolayer, see Figure 4.26. The change of the geometry and position of the extruded component of the modified cell in the geometric model does influence the results. As with the spherical model, all non-modified cells are represented as truncated cones with the same height, h, and radii (R_t and R_b). Also, all cells in the model are assumed to be connected by their lateral surfaces. By assuming the height, h, and volume of the modified cell, V^*, are fixed, the radius R_{ot}^* can be expressed as a function of the modified cell's radii, R_t^* and R_b^*. Assuming the modified cell's volume will always find a space to fill, it is fixed at V_p, and the radius of the hemisphere is expressed as

$$R_{ot}^* = \sqrt[3]{\frac{V_p}{\pi} - \frac{1}{3}(R_t^{*2} + R_t^* R_b^* + R_b^{*2})}.$$

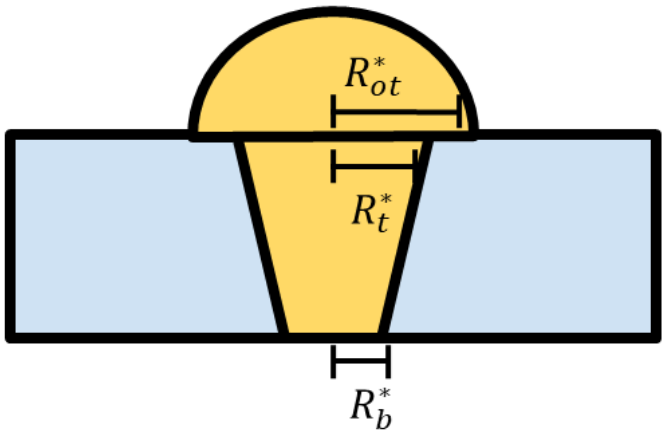

Figure 4.26. Geometric representation of the modified cell. A truncated cone represents the modified cell inside the monolayer, and a connected hemisphere represents the extruded component of the modified cell.

By attaching the hemisphere to the truncated cone the modified cell can take four shapes. The first is where the modified cell is only represented as a truncated cone in the monolayer and the cell has not extruded at all. The second is where there is a hemisphere, but its radius is smaller than the apical surface of the truncated cone. The third is the hemisphere with a larger radius than the apical surface of the truncated cone. Finally, only the hemisphere is present representing an extruded modified cell.

The total surface area of the modified cell is a combination between the two shape components,

$$\mathrm{A}^* = A_b^* + A_s^* + |A_t^* - A_{ot}^*| + A_{ht}^*.$$

Where A_{ot}^* represents the area of the hemisphere in contact with the monolayer and A_{ht}^* represents the remaining surface area of the hemisphere. In order to account for the common surface area between the hemisphere and the truncated cone only the absolute value of the difference between the apical surface of the modified cell truncated cone and the surface of the hemisphere in contact with the monolayer contributes to the total surface area of the modified cell.

To account for the common surface area between the hemisphere and the truncated cone of the modified cell we introduce a Heaviside step function,

$$\eta(x) = \begin{cases} x & x > 0 \\ 0 & x \leq 0 \end{cases}.$$

Following these additions, the energy function becomes Function (4.17) where the expressions describing the modified and unmodified cell terms are separated, and where the surface area of the modified cell is included in the total surface area contraction and the cell-cell adhesion. The surface area of the hemisphere in contact with the apical surface of the neighbouring cells contributes to the modified cell-cell adhesion.

The energy function is expressed with either the radii of the unmodified cells, R_t and R_b, or the modified cell, R_t^* and R_b^*, given the assumption of a conservation of the total area in a cross-section of the monolayer. This is the same function, Function (4.18), as the spherical geometric model except with the changes to the total surface area of the modified cell,

$$A^*(R_t^*, R_b^*) = \pi(R_t^* + R_b^*)\sqrt{(R_t^* - R_b^*)^2 + h^2} + \pi {R_b^*}^2 + \pi\eta\left({R_t^*}^2 - {R_{ot}^*}^2\right) + 2\pi\eta(R_{ot}^*)^2,$$

and the addition of adhesion from the hemisphere, $S^*\,\eta(A_t^* - A_{ot}^*)/2$. All other measurements are the same as expressed in the spherical geometric model.

Results of the modified cell geometric model

Much like the other energy functions above expressed with the apical and basal radii of the modified cell the energy function of the hemispherical geometry is shown as contour plots in Figure 4.27. These contour plots show the three states of the modified cell: non-extruded in Figure 4.27a with the radii $R_t^* > 0$ and $R_b^* > 0$, an inverted cone in Figure 4.27b with the radii $R_t^* > 0$ and $R_b^* = 0$, and an extruded cell in Figure 4.27c, with radii $R_t^* = 0$ and $R_b^* = 0$.

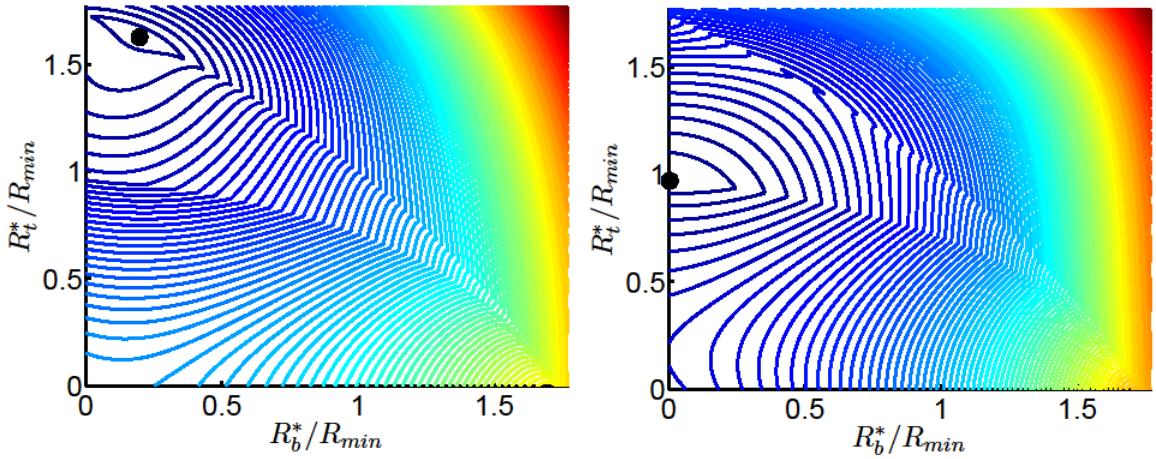

(a) (b)

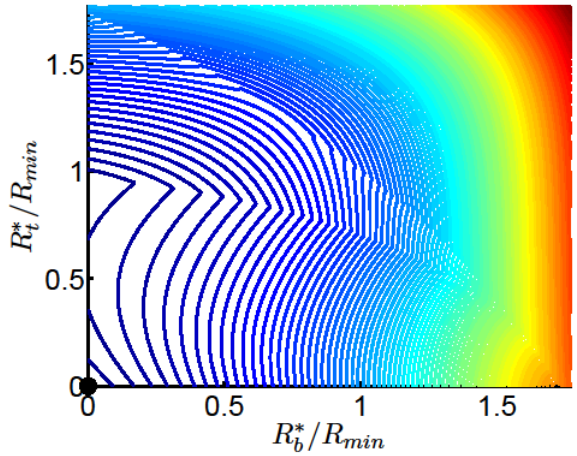

(c)

Figure 4.27. Contour plots for the energy of the hemispherical geometric representation of the modified cell. A black point represents the local minimum energy for the hemispherical model energy function. a) A non-extruded modified cell, $S^*/S = 1$, b) a partially extruded modified cell, $S^*/S = 0.5$, and c) an extruded modified cell, $S^*/S = 0.1$. Other parameters include $\Gamma = 50$, $S = 60000$ ($\beta = 1.5905$), $k = 100$, $\alpha = 2S$, $V_p = 500$ and $h = 5$ with $N = 25$ cells.

Much like the simulations and the spherical geometric model, the reduction of the modified cell adhesion and the additional lateral contraction can assist in extruding the modified cell. Figure 4.28 plots phase diagrams similar to the ones seen in the simulations and the spherical representation of the modified cell. The red represents the extrusion of the modified cell, the green represents the partial extrusion of the modified cell and the blue is no extrusion of the modified cell. Initially we compare Figure 4.28a, at a cell regime of $\beta = 1.7230$, with the plot of the spherical representation of the modified cell, Figure 4.23a, and the simulations, Figure 4.16a. The hemispherical model follows a similar behaviour as seen in the spherical model and the CPM simulations, specifically, lowering the modified cell adhesion or increasing the additional lateral modified cell contraction can extrude the modified cell. However, the thresholds between the states of the modified cell of the hemispherical model are different to the spherical model and the CPM simulations. In the hemispherical model the threshold shows a non-linear relationship between the modified cell adhesion and additional lateral contraction separating the partial extrusion and extrusion of the modified cell, and the threshold separating the partially extruded and the non-extruded modified cell appears "linear". However, these are different to the CPM simulations and the spherical model. The threshold in the CPM simulations shows a linear relationship between the modified cell adhesion and additional lateral contraction separating the partial extrusion and extrusion of the modified cell. In the spherical model there is a distinct threshold at a specific modified cell adhesion value separating the two modified cell states.

The changes and addition of other parameters in the hemispherical model have a similar effect on the behaviour of the modified cell as shown in the spherical model. From the CPM simulations we know that reducing the substrate adhesion hinders the extrusion of the cells. Figure 4.28b plots the phase diagram of different states of the modified cell where there is no substrate adhesion. Comparing the phase diagram in Figure 4.28b with the phase diagram that contains a substrate adhesion of $\alpha = 2S$ in Figure 4.28a, shows that mainly the partial extruded modified cells are hindered, i.e. the modified cell is in a non-extrusion state, and only the modified cell at $(0.15,0)$ in the extruded state in Figure 4.28a is hindered in Figure 4.28b. However, there was a larger effect on the modified cell in the CPM simulations, in Figure 4.16b, and the spherical model, in Figure 4.23b.

Apical contraction, $\Gamma_t = 500$, is added to the hemispherical model in the phase diagram in Figure 4.28c. Comparing this phase diagram to the phase diagram with no apical contraction in Figure 4.28a shows there is little to no change in the system. However, we do see at $(0.15,0)$ the modified cell changes from an extruded state to a partial extruded state and within the non-extruded cell states there are some partially extruded cells.

The addition of the basal perimeter contraction to the modified cell in the hemispherical model has similar modified cell behaviour as the spherical model where there is no change to the modified cell behaviour. Comparing simulations with a basal perimeter contraction of $\Gamma_b = 500$ in Figure 4.28d to systems without basal perimeter contraction in Figure 4.28a shows there is no change in the phase diagram.

Changing the cell regime will change the how the modified cell behaves in the hemispherical model. A softer cell regime can either extrude or hinder the extrusion of the modified cell depending on the modified cell's cell-cell adhesion and additional lateral contraction. The cells in the phase diagram in Figure 4.30a have a softer regime than those in the phase diagram in Figure 4.28a. Systems with low modified cell adhesion, for example a ratio less than 0.35, and low additional lateral contraction, for example less than 4, would have a partially extruded modified cell in Figure 4.28a; however, in Figure 4.30a the modified cell is extruded. In comparison the systems with higher modified cell adhesion ratio, such as 0.7 and 0.75, that were able to extrude in Figure 4.28a are only partially extruded in the softer system in Figure 4.30a. This change also occurs between the partial extruded cell and the non-extruded cell systems.

A harder system has the opposite effect of the softer cell regimes. Some of the low modified cell adhesion, for example a ratio less than 0.35, and low additional lateral contraction, for example less than 2, that extrude in the phase diagram in Figure 4.28a only partially extrude in the harder regime in the phase diagram in Figure 4.30b. Also, for the systems that have a partially extruded modified cell in Figure 4.28a with a large additional lateral contraction, larger than 6, and adhesion ratio close to one, larger than 0.6, can extrude in the harder regime system in Figure 4.30b.

The effect of the change of the cell regime on the modified cell for different points in the phase diagrams can be seen in Figure 4.29 that plots the radius of the apical (solid line) and basal (dashed line) layers of the modified cell. Figure 4.29a plots the radii of the modified cell for the minimum energy from the energy function of hemispherical model against different cell regimes when the $S^*/S = 1$ and $\Gamma^*/\Gamma = 0$. As the cell regime becomes softer, β increases, the apical radius of the modified cell increases and the basal radii decreases; however, the cell never extrudes or partially extrudes when $\beta < 2$.

Reducing the adhesion ratio of the systems in Figure 4.29a to $S^*/S = 0.2$ in Figure 4.29b shows softer cell regimes are able to partially extrude ($R_t^* > 0$ and $R_b^* = 0$) and completely extrude ($R_t^* = 0$ and $R_b^* = 0$) a modified cell. However, the radii of the modified cell are in the partial modified state which is unexpected.

Increasing the additional modified cell lateral contraction ratio of the systems in Figure 4.29a to $\Gamma^*/\Gamma = 6$ in Figure 4.29c shows harder cell regimes are able to extrude ($R_t^* = 0$ and $R_b^* = 0$) rather than the softer cell regime. The softer the cell regime is the larger modified cell radii become, and both the apical and basal radii are equivalent in Figure 4.29c. This is the opposite result from the expectation based on the simulations and the spherical geometric model.

We can also show that changing other parameters does have an effect on the modified cell at different regimes. Comparing Figure 4.29b with a substrate adhesion of 0.2 with the system in Figure 4.31a which has no substrate adhesion, "hinders" the extrusion of the cell and other than decreasing the modified cell adhesion a softer cell regime would be needed to extrude the cell. The addition of apical perimeter contraction to the system in Figure 4.31b shows little to no difference to the systems without any apical perimeter contraction in Figure 4.29b. Adding a basal perimeter contraction to the modified cell in the systems in Figure 4.31c shows little difference to the systems with no basal perimeter contraction on the modified cell in Figure 4.29b. Except there is a difference between the non-extruded cell and the extruded cell state in the harder regime, i.e. the basal radius of the modified cell disappears in harder regimes, and the curve of the non-extruded cell state does not change as it does in Figure 4.29b.

We also observe that while the plots in Figures 4.29 and 4.31 are largely different to the plots of the geometric wound case in Figure 4.14 and spherical representation for the modified cell in Figures 4.22 and 4.25, there are still discontinuities occurring when the basal radii drop to zero. Figure 4.31a shows that there is also an additional discontinuity which is different to the one above. This discontinuity occurs when the system shifts into a soft regime. The values before the discontinuity are constant representing a cylinder with volume $V_p = 500$ and the discontinuity suddenly occurs, in the soft regime, when the cell partially extrudes.

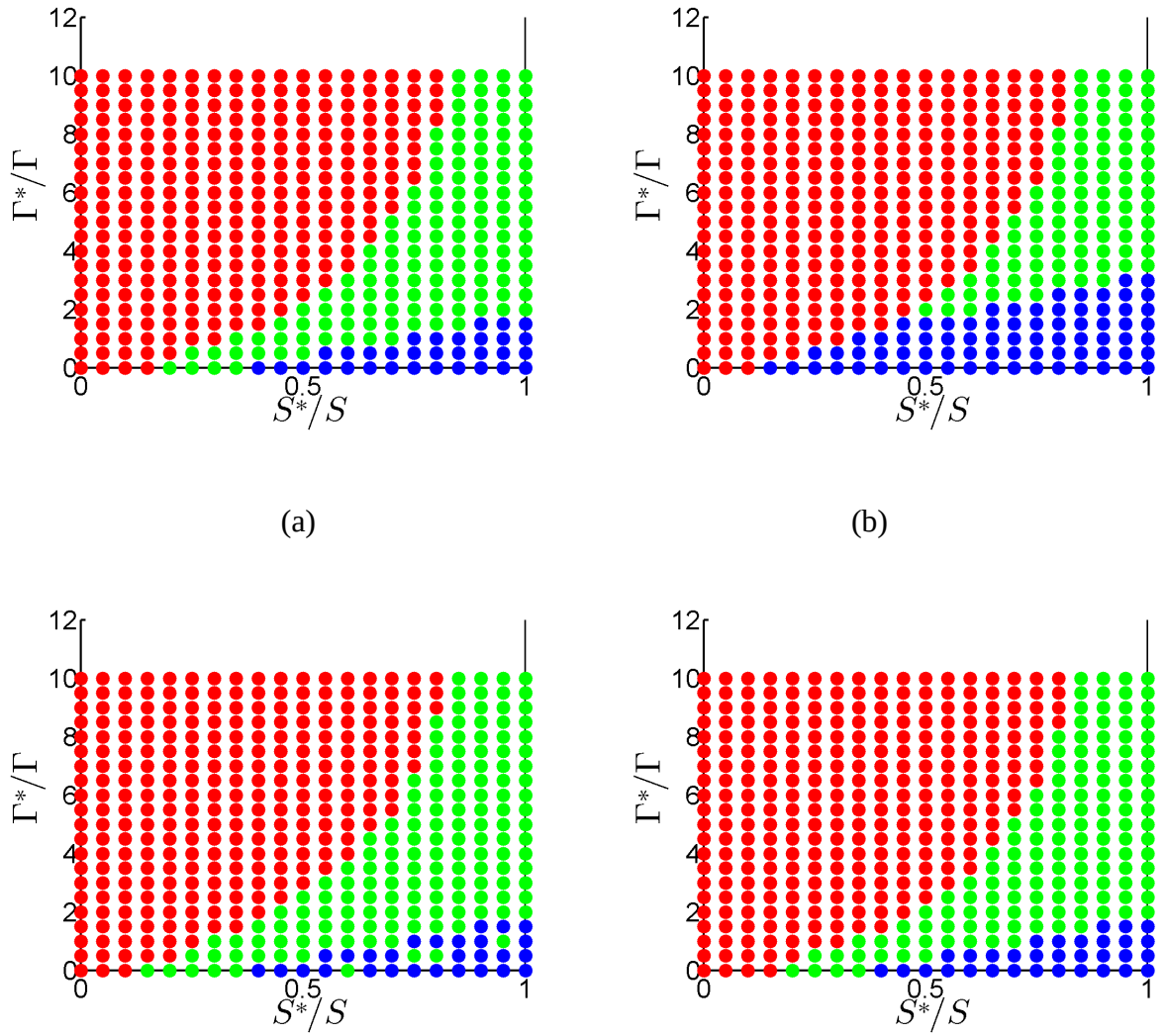

Figure 4.28. Phase diagrams comparing the modified cell adhesion ratio, S^*/S, and additional modified cell contraction ratio, Γ^*/Γ, for the hemispherical representation of the modified cell. An extruded cell in the diagram is identified with the red marker, partially extruded with a green marker, and not extruded with a blue marker. a) Represents a phase diagram with a substrate adhesion of $\alpha = 2S$, no apical perimeter contraction, $\Gamma_t = 0$, and no basal modified cell perimeter contraction, $\Gamma_b = 0$; b) represents a phase diagram with no substrate adhesion, $\alpha = 0$, no apical perimeter contraction, $\Gamma_t = 0$, and no basal modified cell perimeter contraction, $\Gamma_b = 0$; c) represents a phase diagram with a apical perimeter contraction of $\Gamma_t = 500$, no substrate adhesion, $\alpha = 0$, and no basal modified cell perimeter contraction, $\Gamma_b = 0$; and d) represents a phase diagram with a basal modified cell perimeter contraction of $\Gamma_b = 500$, noapical perimeter contraction, $\Gamma_t = 0$, and no substrate adhesion, $\alpha = 0$. Other parameters include $k = 100$, $S = 65000$, $\Gamma = 50$, $\beta = 1.7230$, $V_p = 500$ and $h = 5$ with $N = 25$ cells.

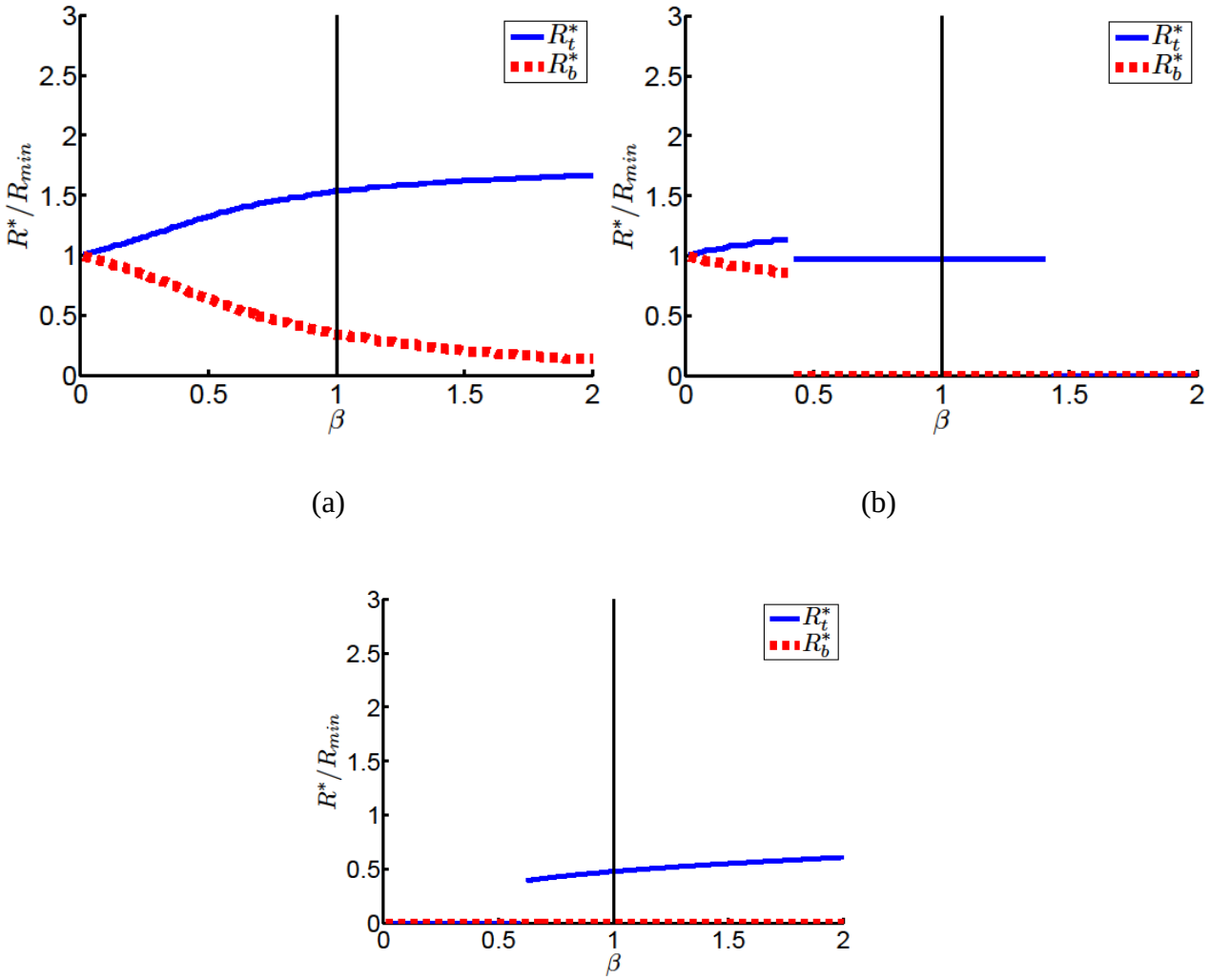

Figure 4.29. Plots of the apical (solid line) and basal (dashed line) modified cell radii at the local minima of the energy function with a spherical geometric representation of the extruded modified cell, against the regime of the system, β. a) Represents systems of the modified cell with an adhesion ratio of $S^*/S = 1$ and modified cell's additional contraction of $\Gamma^*/\Gamma = 0$. b) Represents the modified cell systems of the modified cell with an adhesion ratio of $S^*/S = 0.2$ and modified cell's additional contraction of $\Gamma^*/\Gamma = 0$. c) Represents systems of the modified cell with an adhesion ratio of $S^*/S = 1$ and modified cell's additional contraction of $\Gamma^*/\Gamma = 6$. Other parameters include $k = 100$, $\Gamma = 50$, $\alpha = 2S$, $V_p = 500$ and $h = 5$ with $N = 25$ cells.

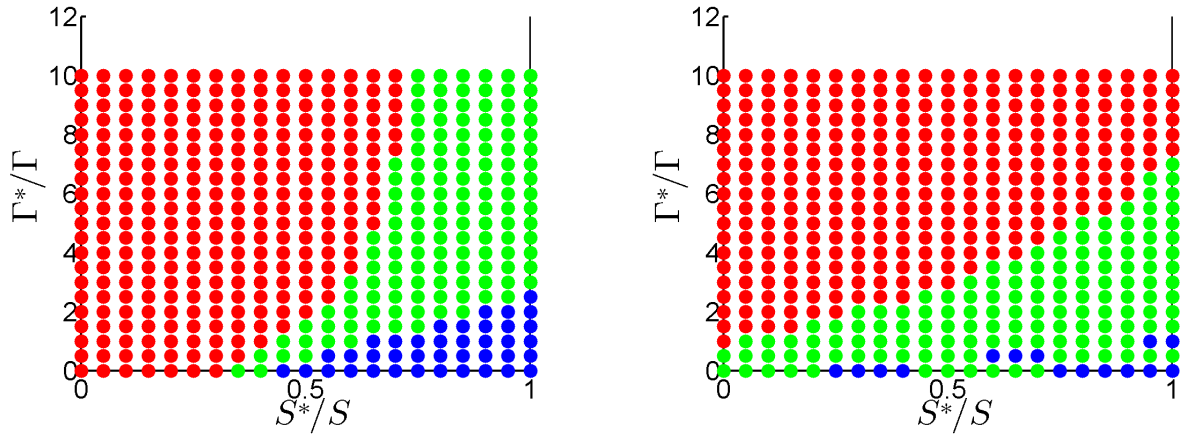

(a) (b)

Figure 4.30. Phase diagrams comparing the modified cell adhesion ratio, S^*/S, and additional modified cell contraction ratio, Γ^*/Γ, for the spherical representation of the modified cell. An extruded cell in the diagram is identified with the red marker, partially extruded with a green marker, and not extruded with a blue marker. a) Represents a softer system with cell-cell adhesion, $= 90000$ ($\beta = 2.3857$), and substrate adhesion, $\alpha = 2S$. b) Represents a hard system with cell-cell adhesion, $= 30000$ ($\beta = 0.7952$), and substrate adhesion, $\alpha = 2S$. Other parameters include $k = 100$, $\Gamma = 50$, $\alpha = 2S$, $V_p = 500$ and $h = 5$ with $N = 25$ cells.

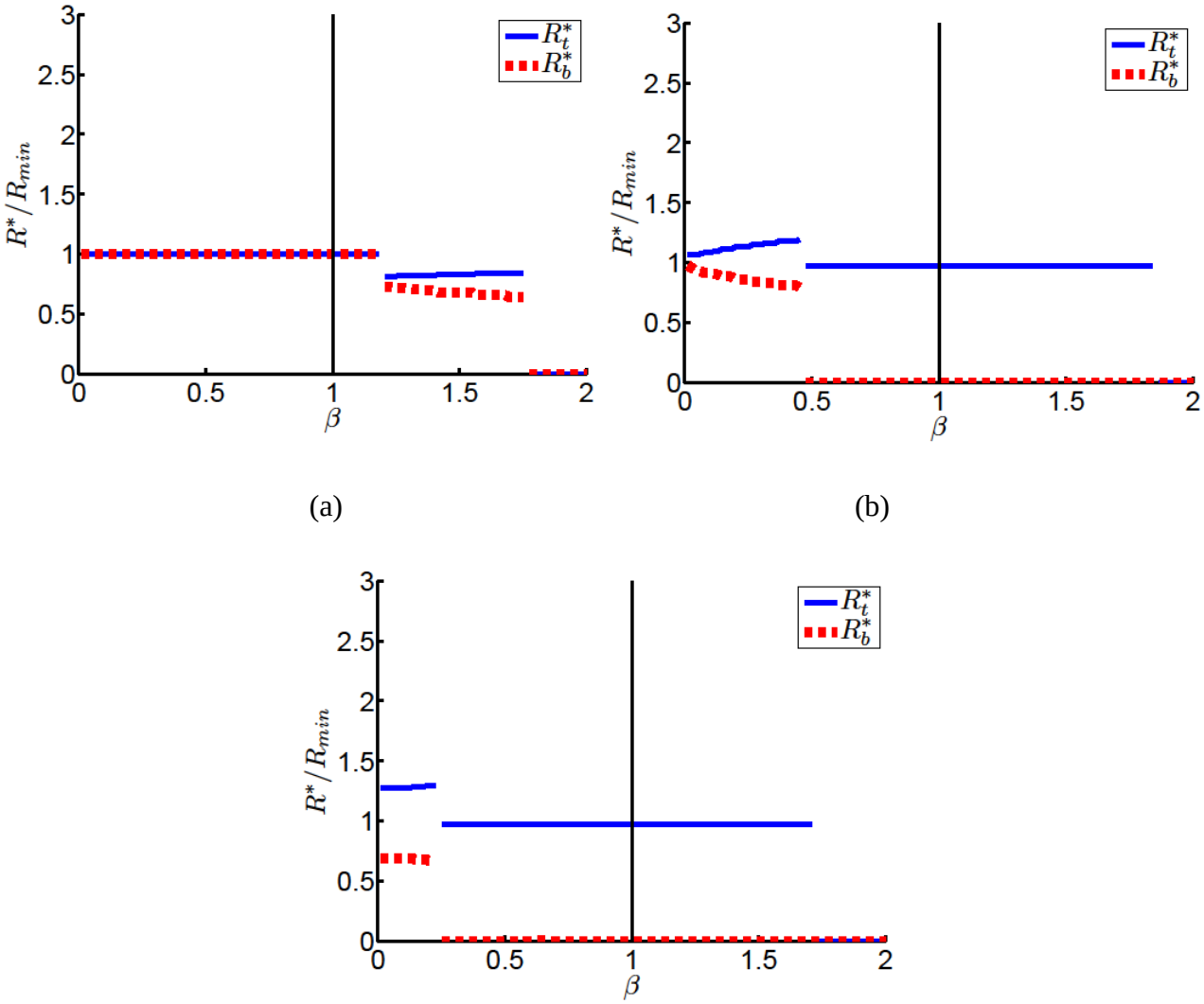

Figure 4.31. Plots of the apical (solid line) and basal (dashed line) modified cell radii at the local minima of the energy function with a spherical geometric representation of extruded modified cell, against the regime of the system, β. a) Represents systems with a reduced modified cell adhesion with the ratio of $S^*/S = 0.2$, and a reduced substrate adhesion, $\alpha = 0$. b) Represents systems with a reduced modified cell adhesion with the ratio of $S^*/S = 0.2$, substrate adhesion $\alpha = 2S$, and an added apical perimeter contraction of $\Gamma_t = 500$. c) Represents systems with a reduced modified cell adhesion with the ratio of $S^*/S = 0.2$, substrate adhesion $\alpha = 2S$, and an added basal contraction perimeter contraction to the modified cell of $\Gamma_b = 500$. Other parameters include $k = 100$, $\Gamma = 50$, $V_p = 500$ and $h = 5$ with $N = 25$ cells.

4.7 DISCUSSION

The three-dimensional CPM has been used to describe a monolayer of epithelial cells, including mechanical representations of adhesion, contraction and a volume constraint of the cells (Glazier & Graner, 1993; Graner & Glazier, 1992; Kabla, 2012). The combination of cell-cell adhesion and surface area contraction results in the cells in the three-dimensional CPM existing in two different regimes, namely, the hard and soft regime. This is similar to the regimes that exist in the two-dimensional vertex model (Farhadifar et al., 2007) and two-dimensional CPM (Noppe et al., 2015), with the combination of surface area contraction and cell-cell adhesion. In a hard regime the cell shape is governed by contraction and in a soft regime the cell shape is determined by cell-cell adhesion. Unlike the two-dimensional CPM, the three-dimensional CPM can include localised mechanisms which can affect the regimes between the apical and basal pixel layers of the cells in the monolayer. One of these mechanisms includes the apical perimeter contraction which causes the apical pixel layer of the cells to occur in a harder cell regime than the basal pixel layer of the cells. As with the two-dimensional case, if apical perimeter contraction is too large it can also cause the cells to separate from one another in the simulations. However, the substrate adhesion does not affect the cell pixel layer cell regimes.

Representing a wound with a void in the three-dimensional CPM and geometric models reaffirms the results of the two-dimensional CPM in Chapter 2. The size of a wound can increase (open) or decrease (close) depending on the relative balance between cell-cell adhesion and surface area contraction. Other mechanisms, such as the substrate adhesion, apical contraction and basal perimeter contraction of the wound, can influence the degree to which the wound closes. Decreasing the substrate adhesion shifts the transition value, β_c, to a softer regime, and with no substrate adhesion both the apical and basal layers of the cells behave similarly. Adding apical perimeter contraction to the cells can “harden” the apical cell regime; however, increasing the apical perimeter contraction will hinder the wound closure process. Increased contraction around the wound will help to close the wound (Noppe et al., 2015). While a contraction around the wound’s lateral surface area would be a suitable mechanism to add to the system, it is difficult to apply the contraction on only the surface of the wound in the CPM. Instead the contraction is added to the basal perimeter of the wound facilitating the closure of the wound. The contraction of the basal perimeter of the wound works in the opposite way to the apical perimeter contraction of the cells. The basal adhesion shifts the transition value further into the hard regime for the lower levels of the cell and the other pixel layers above follow suit, meaning that the lower pixel layers of the wound are easier to close. However, the apical layer of the wound behaves differently and has a larger transition value, β, than the lower pixel layers of the simulated monolayer.

Comparing the wound to a modified cell extruding from a monolayer, an extruded cell is related to a closed wound and a non-extruded cell is related to an open wound. Unlike the wound case, changes in the monolayer regime, β, do not extrude the modified cell as the wound is able to be either open or closed. Instead, the changes to the mechanisms of the modified cell, such as the modified cell adhesion and the additional lateral contraction, are able to extrude the modified cell in different cell regimes comparable to the closure of the wound. Hard cell regimes still hinder the extrusion of the modified cell but softer cells regimes are able to extrude the modified cell from the monolayer. The modified cell is able to be extruded by either decreasing the modified cell's adhesion or adding and increasing the contraction on the modified cell's lateral surface area connected to the neighbouring cells. Both mechanisms can work together as shown in the phase diagrams. There is a difference in the way the mechanisms behave between the simulations and the geometric models.

Changes in substrate adhesion affect the extrusion of the modified cell. Decreasing the substrate adhesion hinders the extrusion of the modified cell, similar to the hindering of wound closure. Adding apical contraction does not change the extrusion of the modified cell. Finally, applying contraction on the basal layer of the modified cell affects only the basal pixel layer of the modified cell. Once the basal pixel layer has been "closed", then the basal pixel layer no longer contributes to the energy.

The modified cell geometric models and CPM simulations have similarities between them, such as the increase of the apical radius (horizontal cross-section area) and decrease of the basal radius (horizontal cross-section area) of the modified cell as β increases seen in Figures 4.18a, 4.22a and 4.29a. However, there are different behaviours, in particular at some of the regime extremes, indicating how differently the mechanisms affect the extrusion in these cases. The true biological cell behaviour would most likely be somewhere within the results achieved from these models. Moreover, the use of other models, such as the vertex model, may assist in further testing these mechanisms and behaviours.

Chapter 5: Discussion

This thesis uses our own code of a two and three-dimensional CPM to simulate epithelial cells and their collective behaviour in three aggregate cases: the introduction of a micro-wound in a monolayer of cells, the equilibrium state of a cluster of cells, and the extrusion of a single modified cell from a monolayer.

Wound healing and cell extrusion are essential behaviours of the epithelium in order to form and maintain protective layers around the body's internal organs. The malfunction of these epithelial cells can lead to a number of biological complications, such as intestinal diseases (Iizuka & Konno, 2011), embryo development problems (P. Martin & Lewis, 1992; Osterfield et al., 2013), and even cancer-related growths (Arwert et al., 2012; Gu et al., 2015; Hogan et al., 2009; Kajita et al., 2014). While biological experiments on epithelial cells provide important results, mathematics can generate insights into the behaviour of cells through the use of models such as the CPM, vertex model and other discrete and continuous models.

The adhesion and the tensions of the junctions between cells in the epithelium are important components for the behaviour of epithelial cells relating to their geometry and their response to wounding and the extrusion of cells. The adhesion and tensions in the cells are associated with the changes in the molecules and proteins of the epithelial cells, such as concentration of acto-myosin. The CPM applies mechanisms, such as the adhesion and contraction, in the energy functions in order to mimic the biological cell behaviours within the epithelium.

We determined that the interaction between the adhesion and cell perimeter contraction in the two-dimensional CPM affect the cell morphology. This is replicated in the three-dimensional CPM with the mechanisms of cell adhesion and cell surface area contraction. Using the parameters of adhesion, S, and contraction, Γ, the cells can be classified into two cell regimes based on parameter β, which is a normalised ratio of adhesion and contraction. A hard cell regime occurs when $\beta < 1$ and a soft cell regime occurs when $\beta > 1$. In the hard cell regime the cells are dominated by the contraction terms creating rigid polygonal cell structures. In two dimensions the cell perimeter is approximately fixed at a constant value based on the preferred area and in three dimensions the surface area of the cells is also approximated by an almost constant value based on the preferred volume. Cells in the soft cell regime are dominated by the adhesion interaction between neighbouring cells, creating flexible and malleable cell boundaries. In two dimensions the cell perimeter achieves a preferred perimeter and in three dimensions the cell surface area achieves

a preferred surface area. These preferred perimeters and surface areas are both ratios between the adhesion and contraction of the cells, $S/2\Gamma$.

The addition of a mechanism, such as the apical perimeter contraction in the three-dimensional CPM, can change the behaviour of the pixel layers within the monolayer of cells. Adding the apical perimeter contraction can make the soft cells mimic hard cell structures on the apical pixel layer while retaining the behaviour of the soft cells on the basal pixel layer. However, other mechanisms, such as the substrate adhesion, do not affect the cell regime of the basal or apical pixel layer in the monolayer of cells.

We observed that the interaction between the adhesion and contraction of the cells can also affect the closure of a micro-wound. Cells in a very hard regime cannot close the wound; however, cells in a softer regime are able to close the wound by "zipping" the junctions between neighbouring cells together and expanding the cells into the void represented by the empty wound. The transition between an open and closed wound occurs at a transition value of the cell regime, β_c.

The transition value, β_c, can vary with changes to and the addition of other mechanisms. In two dimensions the transition value is seen to decrease with the addition of a contractile perimeter ring around the wound in the geometric model, meaning that cells in harder regimes are able to close the wound. In three dimensions (Chapter 4) the removal of substrate adhesion hinders wound closure, such that a softer cell regime is required for the wound to close. The addition of an apical contraction mechanism creates a much greater difference between the transition values of the apical and basal pixel layers of the wound. We noted that additional mechanisms would assist the closure of the micro-wound, such as the inclusion of a contractile ring around the wound. This was demonstrated with the geometric representation results of the two-dimensional CPM and the results of the three-dimensional CPM for the simulations, as well as the three-dimensional geometric approximations.

The simulated wound in the CPM opens or closes monotonically depending on the cell regime. Biological experimental data and information show there is an initial increase in the wound size and then a gradual closure of the wound. This could suggest the monolayer in a system with a micro-wound has a gradual change in the value of cell regime parameter, β, (or other mechanisms such as substrate adhesion) to eventually shift the transition value to allow closure of the wound. Nagai and Honda (2009) investigated a similar micro-wound situation with a vertex model; however, the wound closure was driven by a positive linear term of the wound area rather than the interaction between the adhesion and contraction of the cells.

The extrusion of a modified cell using the three-dimensional CPM uses similar adhesive and contraction mechanisms to the micro-wound case. The modified cell will not extrude if it has the same adhesion and contraction parameters as its neighbouring cells. However, the cell will extrude as the adhesion value trends to zero if the system is in a regime with the mechanism which enables it to close a wound in the micro-wound case and the modified cell adhesion is decreased. When the modified cell adhesion is zero, the cell is no longer connected to the monolayer and the system is similar to the micro-wound case, except with an object occupying the void of the wound that can leave on its own or be pushed out by the neighbouring cells. The other mechanism to consider is an additional contraction added to the modified cell on the surface areas that are in contact with its neighbouring cells. The modified cell can extrude with a large enough contraction, providing the neighbouring cells can close the void that would be left behind (reminiscent of the wound case). If the neighbouring cells do not close the void created by the contracted modified cell, the modified cell will detach from the monolayer and sit within the void.

The mechanisms for extrusion of the modified cell are similar to those for the closure of a wound. Decreasing the substrate adhesion of neighbouring cells hinders the extrusion of the modified cell. Adding the apical perimeter contraction term can alter the “closure” of the neighbouring cells when extruding the modified cell. This can create a “bowl” effect where the cells neighbouring the modified cell create a “bowl” where the basal pixel layer is “closed” but the top pixel layer is open and the modified cell sits inside this “bowl”. These results from the three-dimensional CPM simulation suggest that the modified cell will only extrude if the system can close a void. However, we noted there is a difference between this finding with the CPM and the results from the geometric model.

The geometric model is an approximation of the results of the CPM. Rather than running multiple CPM simulations, the aim of the geometric model is to generate results more rapidly so as to provide an understanding of the system more quickly. In the two-dimensional case the geometric model shows a quantitative similarity between the CPM and geometric model for the closure of a micro-wound for all the behaviours of the cells and wound. However, there are differences between the measurements of the cell island perimeter in the geometric model and the CPM in the two-dimensional case of a cell island. The difference occurs in the hard cell regime and is a result of the assumption of fixed cell island geometry in the geometric model. This difference can be amplified because, while we can tile the system to the optimal configuration in the geometric model, the cells in the CPM within a hard cell regime may not be able to move into the optimal configurations and are fixed in position.

We find three-dimensional geometric models result in further differences with the outcomes of the CPM from the addition of more components and assumptions than the two-dimensional geometric models. The geometric representation of the horizontal cross-section of the cells in three dimensions is simpler when compared to the two-dimensional geometric model; however, the geometric representation contains the additional complexities of a third spatial dimension. The three-dimensional geometric model for a wound case provides reasonable qualitative information on the behaviour of the cells and the wound using a cylindrical geometry or more complicated segmented cone geometry.

Different cell geometries can produce different patterns of cell behaviour. This is seen in the geometric representation of the extruded component of the modified cell. While some of the behaviours from the three-dimensional CPM are replicated in the geometric model, there are some clear differences. These similarities and differences are represented in the phase diagrams of the CPM, spherical geometric model and the hemispherical geometric model. Both the spherical and hemispherical geometric models show that decreasing the modified cell adhesion or increasing the modified cell additional lateral contraction can extrude the modified cell from the monolayer, similar to the CPM. However, a key difference in how the modified cell behaves is noted when the cell regime of the system changes; while the hardening of the cell regime should hinder the extrusion of the modified cell, in the hemispherical model representation this only occurs with a low value of additional modified cell lateral contraction.

The connection of the cells is another mechanism that affects the behaviour of CPM and the geometric models of the modified cell differently. In the three-dimensional CPM cells are able to detach from one another, whether occurring randomly in the simulation or due to strong contraction mechanisms. However, in the geometric models it is assumed that the cells are always connected to each other and therefore do not detach. This assumption partially explains the different behaviours between the CPM and geometric models at large contraction values. The assumption of a connection between the cells in the geometric models means that the contraction mechanisms of a cell will pull the junctions of neighbouring cells, whereas in the CPM the adhesion is the only mechanism connecting the cells and therefore the cells can detach from one another at certain contraction strengths if there is empty space adjacent to the cells.

While there are differences between the behaviour of cells from the geometric models and the CPM, the geometric models provide insight into the energy functions and mechanisms of the CPM without the need to run the simulations, especially those with a larger system sizes.

The CPM provides one example of a discrete model to investigate biological mechanisms. To date, the CPM has largely been applied to simulate the behaviour of the epithelium as a whole. In terms of the epithelial response to a wound the CPM has been used to simulate large wounds, such as in the scratch assay experiments. In this thesis we have examined the closure of micro-wounds and the extrusion of a single cell. While the CPM provides an insight into the possible involvement of different cell mechanisms, the application of the CPM is restricted by the simplicity in which the parameters are applied. For example, the actual values of the parameter strengths, such as adhesion and contraction, are not measurable values in biological cells. This does not mean the mathematical model cannot connect with biological experiments, since cell shape, tension and motility are a few cell properties that can be measured biologically and be compared with the CPM. Investigating the properties of cells with a range of mathematical models helps to build an understanding of cell behaviour and allows biologists to better design and focus experiments. As insufficient biological data was found to allow direct comparisons, the models in this thesis are intended to motivate and allow further investigation into the mechanisms involved in cell behaviour. Future investigations of cell micro-wound healing and cell extrusion requires a combination of multiple mathematical models to more quantitatively reflect the biological measurements determined from both physical and chemical cell property changes observed in experiments.

References

Abate, A., Vincent, S., Dobbe, R., Silletti, A., Master, N., Axelrod, J. D., & Tomlin, C. J. (2012). A mathematical model to study the dynamics of epithelial cellular networks. *IEEE/ACM Transactions on Computational Biology and Bioinformatics, 9*(6), 1607-1620. doi:10.1109/tcbb.2012.126

Abreu-Blanco, M. T., Verboon, J. M., Liu, R., Watts, J. J., & Parkhurst, S. M. (2012). Drosophila embryos close epithelial wounds using a combination of cellular protrusions and an actomyosin purse string. *Journal of Cell Science, 125*(24), 5984-5997. doi:10.1242/jcs.109066

Aceto, N., Bardia, A., Miyamoto, D. T., Donaldson, M. C., Wittner, B. S., Spencer, J. A., . . . Maheswaran, S. (2014). Circulating tumor cell clusters are oligoclonal precursors of breast cancer metastasis. *Cell, 158*(5), 1110-1122. doi:10.1016/j.cell.2014.07.013

Alber, F., Dokudovskaya, S., Veenhoff, L. M., Zhang, W., Kipper, J., Devos, D., . . . Rout, M. P. (2007). The molecular architecture of the nuclear pore complex. *Nature, 450*(7170), 695-701. doi:10.1038/nature06405

Anderson, A., Chaplain, M., L. Newman, E., Steele, R., & Thompson, A. (2000). Mathematical modelling of tumour invasion and metastasis. *Journal of Theoretical Medicine, 2*(2), 129-154. doi:10.1080/10273660008833042

Andrade, D., & Rosenblatt, J. (2011). Apoptotic regulation of epithelial cellular extrusion. *Apoptosis, 16*(5), 491-501. doi:10.1007/s10495-011-0587-z

Anon, E., Serra-Picamal, X., Hersen, P., Gauthier, N. C., Sheetz, M. P., Trepat, X., & Ladoux, B. (2012). Cell crawling mediates collective cell migration to close undamaged epithelial gaps. *Proceedings of the National Academy of Sciences, 109*(27), 10891-10896. doi:10.1073/pnas.1117814109

Antunes, M., Pereira, T., Cordeiro, J. V., Almeida, L., & Jacinto, A. (2013). Coordinated waves of actomyosin flow and apical cell constriction immediately after wounding. *The Journal of Cell Biology, 202*(2), 365-379. doi:10.1083/jcb.201211039

Armstrong, N. J., Painter, K. J., & Sherratt, J. A. (2006). A continuum approach to modelling cell-cell adhesion. *Journal of Theoretical Biology, 243*(1), 98-113. doi:10.1016/j.jtbi.2006.05.030

Arwert, E. N., Hoste, E., & Watt, F. M. (2012). Epithelial stem cells, wound healing and cancer. *Nature Reviews Cancer, 12*(3), 170-180. doi:10.1038/nrc3217

Bement, W. M., Forscher, P., & Mooseker, M. S. (1993). A novel cytoskeletal structure involved in purse string wound closure and cell polarity maintenance. *Journal of Cell Biology, 121*(3), 565-578.

Blanpain, C., Horsley, V., & Fuchs, E. (2007). Epithelial stem cells: Turning over new leaves. *Cell, 128*(3), 445-458. doi:10.1016/j.cell.2007.01.014

Brock, J., Midwinter, K., Lewis, J., & Martin, P. (1996). Healing of incisional wounds in the embryonic chick wing bud: characterization of the actin purse-string and demonstration of a requirement for Rho activation. *Journal of Cell Biology, 135*(4), 1097-1107.

Brugues, A., Anon, E., Conte, V., Veldhuis, J. H., Gupta, M., Colombelli, J., . . . Trepat, X. (2014). Forces driving epithelial wound healing. *Nature Physics, 10*(9), 683-690. doi:10.1038/nphys3040

Cai, A. Q., Landman, K. A., & Hughes, B. D. (2007). Multi-scale modeling of a wound-healing cell migration assay. *Journal of Theoretical Biology, 245*(3), 576-594. doi:10.1016/j.jtbi.2006.10.024

Caldwell, B. J., Lucas, C., Kee, A. J., Gaus, K., Gunning, P. W., Hardeman, E. C., . . . Gomez, G. A. (2014). Tropomyosin isoforms support actomyosin biogenesis to generate contractile tension at the epithelial zonula adherens. *Cytoskeleton (Hoboken), 71*(12), 663-676. doi:10.1002/cm.21202

Chanez, P. (2005). Severe asthma is an epithelial disease. *European Respiratory Journal, 25*(6), 945-946. doi:10.1183/09031936.05.00038605

Chen, N., Glazier, J. A., Izaguirre, J. A., & Alber, M. S. (2007). A parallel implementation of the Cellular Potts Model for simulation of cell-based morphogenesis. *Computer Physics Communications, 176*(11-12), 670-681. doi:10.1016/j.cpc.2007.03.007

Chien, S., & Wilhelmi, B. J. (2012). A simplified technique for producing an ischemic wound model. *Journal of Visualized Experiments*(63), 1-12. doi:10.3791/3341

Chowdhury, D., Schadschneider, A., & Nishinari, K. (2005). Physics of transport and traffic phenomena in biology: from molecular motors and cells to organisms. *Physics of Life Reviews, 2*(4), 318-352. doi:10.1016/j.plrev.2005.09.001

Coburn, L., Lopez, H., Caldwell, B. J., Moussa, E., Yap, C., Priya, R., . . . Gomez, G. A. (2016). Contact inhibition of locomotion and mechanical cross-talk between cell-cell and cell-substrate adhesion determine the pattern of junctional tension in epithelial cell aggregates. *Molecular Biology of the Cell, 27*(22), 3436-3448. doi:10.1091/mbc.E16-04-0226

Coulombe, P. A., & Wong, P. (2004). Cytoplasmic intermediate filaments revealed as dynamic and multipurpose scaffolds. *Nature Cell Biology, 6*(8), 699-706. doi:10.1038/ncb0804-699

Cumming, B. D., McElwain, D. L., & Upton, Z. (2010). A mathematical model of wound healing and subsequent scarring. *Journal of The Royal Society Interface, 7*(42), 19-34. doi:10.1098/rsif.2008.0536

Dallon, J. C., Sherratt, J., Maini, P., & Ferguson, M. (2000). Biological implications of a discrete mathematical model for collagen deposition and alignment in dermal wound repair. *IMA Journal of Mathematics Applied in Medicine and Biology, 17*(4), 379-393. doi:10.1093/imammb/17.4.379

Dallon, J. C., Sherratt, J. A., & Maini, P. K. (1999). Mathematical modelling of extracellular matrix dynamics using discrete cells: fiber orientation and tissue regeneration. *Journal of Theoretical Biology, 199*(4), 449-471. doi:10.1006/jtbi.1999.0971

Dallon, J. C., Sherratt, J. A., & Maini, P. K. (2001). Modeling the effects of transforming growth factor-beta on extracellular matrix alignment in dermal wound repair. *Wound Repair and Regeneration, 9*(4), 278-286. doi:10.1046/j.1524-475X.2001.00278.x

Denning, D. P., Hatch, V., & Horvitz, H. R. (2012). Programmed elimination of cells by caspase-independent cell extrusion in C. elegans. *Nature, 488*(7410), 226-230. doi:10.1038/nature11240

Deroulers, C., Aubert, M., Badoual, M., & Grammaticos, B. (2009). Modeling tumor cell migration: From microscopic to macroscopic models. *Physical Review E, 79*(3), 031917. doi:10.1103/PhysRevE.79.031917

Domb, C., & Potts, R. B. (1951). Order-disorder statistics IV. A two-dimensional model with first and second interactions. *Proceedings of the Royal Society of London. Series A. Mathematical and Physical Sciences, 210*(1100), 125.

Du, X. X., Osterfield, M., & Shvartsman, S. Y. (2014). Computational analysis of three-dimensional epithelial morphogenesis using vertex models. *Physical Biology, 11*(6), 066007. doi:10.1088/1478-3975/11/6/066007

Edelblum, K. L., & Turner, J. R. (2015). Chapter 12 - Epithelial Cells: Structure, Transport, and Barrier Function. In J. Mestecky, W. Strober, M. W. Russell, B. L. Kelsall, H. Cheroutre, & B. N. Lambrecht (Eds.), *Mucosal Immunology (4th Edition)* (pp. 187-210). Boston: Academic Press.

Eisenhoffer, G. T., Loftus, P. D., Yoshigi, M., Otsuna, H., Chien, C. B., Morcos, P. A., & Rosenblatt, J. (2012). Crowding induces live cell extrusion to maintain homeostatic cell numbers in epithelia. *Nature, 484*(7395), 546-549. doi:10.1038/nature10999

Eisenhoffer, G. T., & Rosenblatt, J. (2013). Bringing balance by force: Live cell extrusion controls epithelial cell numbers. *Trends in Cell Biology, 23*(4), 185-192. doi:10.1016/j.tcb.2012.11.006

Farhadifar, R., Roper, J. C., Aigouy, B., Eaton, S., & Julicher, F. (2007). The influence of cell mechanics, cell-cell interactions, and proliferation on epithelial packing. *Current Biology, 17*(24), 2095-2104. doi:10.1016/j.cub.2007.11.049

Fernandez-Gonzalez, R., Simoes Sde, M., Roper, J. C., Eaton, S., & Zallen, J. A. (2009). Myosin II dynamics are regulated by tension in intercalating cells. *Developmental Cell, 17*(5), 736-743. doi:10.1016/j.devcel.2009.09.003

Fernandez-Gonzalez, R., & Zallen, J. A. (2013). Wounded cells drive rapid epidermal repair in the early Drosophila embryo. *Molecular Biology of the Cell, 24*(20), 3227-3237. doi:10.1091/mbc.E13-05-0228

Fernando, A. E., Landman, K. A., & Simpson, M. J. (2010). Nonlinear diffusion and exclusion processes with contact interactions. *Physical Review E, 81*(1), 011903. doi:10.1103/PhysRevE.81.011903

Fisher, R. A. (1937). The wave of advance of advantageous genes. *Annals of Eugenics, 7*(4), 355-369. doi:10.1111/j.1469-1809.1937.tb02153.x

Fletcher, A. G., Osborne, J. M., Maini, P. K., & Gavaghan, D. J. (2013). Implementing vertex dynamics models of cell populations in biology within a consistent computational framework. *Progress in Biophysics & Molecular Biology, 113*(2), 299-326. doi:10.1016/j.pbiomolbio.2013.09.003

Fletcher, A. G., Osterfield, M., Baker, R. E., & Shvartsman, S. Y. (2014). Vertex models of epithelial morphogenesis. *Biophysical Journal, 106*(11), 2291-2304. doi:10.1016/j.bpj.2013.11.4498

Frisch, S. M., & Francis, H. (1994). Disruption of epithelial cell-matrix interactions induces apoptosis. *Journal of Cell Biology, 124*(4), 619-626. doi:10.1083/jcb.124.4.619

Gennes, P. G. d. (1979). *Scaling concepts in polymer physics / Pierre-Gilles de Gennes*. Ithaca, N.Y: Cornell University Press.

Gerisch, A., & Chaplain, M. A. (2008). Mathematical modelling of cancer cell invasion of tissue: local and non-local models and the effect of adhesion. *Journal of Theoretical Biology, 250*(4), 684-704. doi:10.1016/j.jtbi.2007.10.026

Glazier, J. A., & Graner, F. (1993). Simulation of the differential adhesion driven rearrangement of biological cells. *Phys Rev E Stat Phys Plasmas Fluids Relat Interdiscip Topics, 47*(3), 2128-2154. doi:10.1103/PhysRevE.47.2128

Gomez, G. A., McLachlan, R. W., Wu, S. K., Caldwell, B. J., Moussa, E., Verma, S., . . . Yap, A. S. (2015). An RPTPalpha/Src family kinase/Rap1 signaling module recruits myosin IIB to support contractile tension at apical E-cadherin junctions. *Molecular Biology of the Cell, 26*(7), 1249-1262. doi:10.1091/mbc.E14-07-1223

Gomez, G. A., McLachlan, R. W., & Yap, A. S. (2011). Productive tension: force-sensing and homeostasis of cell-cell junctions. *Trends in Cell Biology, 21*(9), 499-505. doi:10.1016/j.tcb.2011.05.006

Graner, F., & Glazier, J. A. (1992). Simulation of biological cell sorting using a two-dimensional extended Potts model. *Physical Review Letters, 69*(13), 2013-2016. doi:10.1103/PhysRevLett.69.2013

Grieve, A. G., & Rabouille, C. (2014). Extracellular cleavage of E-cadherin promotes epithelial cell extrusion. *Journal of Cell Science, 127*(Pt 15), 3331-3346. doi:10.1242/jcs.147926

Gu, Y., Forostyan, T., Sabbadini, R., & Rosenblatt, J. (2011). Epithelial cell extrusion requires the sphingosine-1-phosphate receptor 2 pathway. *Journal of Cell Biology, 193*(4), 667-676. doi:10.1083/jcb.201010075

Gu, Y., & Rosenblatt, J. (2012). New emerging roles for epithelial cell extrusion. *Current Opinion in Cell Biology, 24*(6), 865-870. doi:10.1016/j.ceb.2012.09.003

Gu, Y., Shea, J., Slattum, G., Firpo, M. A., Alexander, M., Mulvihill, S. J., . . . Rosenblatt, J. (2015). Defective apical extrusion signaling contributes to aggressive tumor hallmarks. *eLife, 4*, e04069. doi:10.7554/eLife.04069

Hales, T. C. (2001). The Honeycomb Conjecture. *Discrete & Computational Geometry, 25*(1), 1-22. doi:10.1007/s004540010071

Hannezo, E., Prost, J., & Joanny, J.-F. (2014). Theory of epithelial sheet morphology in three dimensions. *Proceedings of the National Academy of Sciences U S A, 111*(1), 27-32. doi:10.1073/pnas.1312076111

Hogan, C., Dupre-Crochet, S., Norman, M., Kajita, M., Zimmermann, C., Pelling, A. E., . . . Fujita, Y. (2009). Characterization of the interface between normal and transformed epithelial cells. *Nature Cell Biology, 11*(4), 460-467. doi:10.1038/ncb1853

Honda, H., & Eguchi, G. (1980). How much does the cell boundary contract in a monolayered cell sheet? *Journal of Theoretical Biology, 84*(3), 575-588. doi:10.1016/S0022-5193(80)80021-X

Hooper, C. E. (1956). Cell turnover in epithelial populations. *Journal of Histochemistry & Cytochemistry, 4*(6), 531-540. doi:10.1177/4.6.531

Hutson, M. S., Tokutake, Y., Chang, M. S., Bloor, J. W., Venakides, S., Kiehart, D. P., & Edwards, G. S. (2003). Forces for morphogenesis investigated with laser microsurgery and quantitative modeling. *Science, 300*(5616), 145-149. doi:10.1126/science.1079552

Iizuka, M., & Konno, S. (2011). Wound healing of intestinal epithelial cells. *World Journal of Gastroenterology, 17*(17), 2161-2171. doi:10.3748/wjg.v17.i17.2161

Ishimoto, Y., & Morishita, Y. (2014). Bubbly vertex dynamics: A dynamical and geometrical model for epithelial tissues with curved cell shapes. *Physical Review. E, Statistical, Nonlinear, and Soft Matter Physics, 90*(5-1), 052711. doi:10.1103/PhysRevE.90.052711

Ising, E. (1925). Beitrag zur Theorie des Ferromagnetismus. *Zeitschrift für Physik, 31*(1), 253-258. doi:10.1007/BF02980577

Kabla, A. J. (2012). Collective cell migration: leadership, invasion and segregation. *Journal of The Royal Society Interface, 9*(77), 3268-3278. doi:10.1098/rsif.2012.0448

Kajita, M., Sugimura, K., Ohoka, A., Burden, J., Suganuma, H., Ikegawa, M., . . . Fujita, Y. (2014). Filamin acts as a key regulator in epithelial defence against transformed cells. *Nature Communications, 5*, 4428. doi:10.1038/ncomms5428

Kovacs, E. M., Verma, S., Ali, R. G., Ratheesh, A., Hamilton, N. A., Akhmanova, A., & Yap, A. S. (2011). N-WASP regulates the epithelial junctional actin cytoskeleton through a non-canonical post-nucleation pathway. *Nature Cell Biology, 13*(8), 934-943. doi:10.1038/ncb2290

Kuipers, D., Mehonic, A., Kajita, M., Peter, L., Fujita, Y., Duke, T., . . . Gale, J. E. (2014). Epithelial repair is a two-stage process driven first by dying cells and then by their neighbours. *Journal of Cell Science, 127*(Pt 6), 1229-1241. doi:10.1242/jcs.138289

Landman, K. A., & Fernando, A. E. (2011). Myopic random walkers and exclusion processes: Single and multispecies. *Physica A: Statistical Mechanics and its Applications, 390*(21), 3742-3753. doi:10.1016/j.physa.2011.06.034

Lange K. (2004) Karush-Kuhn-Tucker Theory. In: *Optimization*. Springer Texts in Statistics. Springer, New York, NY doi:10.1007/978-1-4757-4182-7_4

Laukoetter, M. G., Bruewer, M., & Nusrat, A. (2006). Regulation of the intestinal epithelial barrier by the apical junctional complex. *Curr Opin Gastroenterol, 22*(2), 85-89. doi:10.1097/01.mog.0000203864.48255.4f

Li, J. F., & Lowengrub, J. (2014). The effects of cell compressibility, motility and contact inhibition on the growth of tumor cell clusters using the Cellular Potts Model. *Journal of Theoretical Biology, 343*, 79-91. doi:10.1016/j.jtbi.2013.10.008

Li, Y., Naveed, H., Kachalo, S., Xu, L. X., & Liang, J. (2011). Mechanical forces mediate localized topological change in epithelia. *Conference proceedings : Annual International Conference of the IEEE Engineering in Medicine and Biology Society, 2011*, 178-181. doi:10.1109/iembs.2011.6089923

Liang, C. C., Park, A. Y., & Guan, J. L. (2007). In vitro scratch assay: a convenient and inexpensive method for analysis of cell migration in vitro. *Nature Protocols, 2*(2), 329-333. doi:10.1038/nprot.2007.30

Liang, X., Gomez, G. A., & Yap, A. S. (2015). Current perspectives on cadherin-cytoskeleton interactions and dynamics. *Cell Health and Cytoskeleton, 7*, 11-24. doi:10.2147/CHC.S76107

Liggett, T. M. (1999). *Stochastic Interacting Systems: Contact, Voter and Exclusion Processes*. Berlin, Germany: Springer.

Lowe, J. S., & Anderson, P. G. (2015). Chapter 3 - Epithelial Cells. In J. S. Lowe & P. G. Anderson (Eds.), *Stevens & Lowe's Human Histology* (4th ed., pp. 37-54). Philadelphia: Mosby.

Lubkov, V., & Bar-Sagi, D. (2014). E-cadherin-mediated cell coupling is required for apoptotic cell extrusion. *Current Biology, 24*(8), 868-874. doi:10.1016/j.cub.2014.02.057

Maini, P. K., McElwain, D. L., & Leavesley, D. I. (2004). Traveling wave model to interpret a wound-healing cell migration assay for human peritoneal mesothelial cells. *Tissue Engineering, 10*(3-4), 475-482. doi:10.1089/107632704323061834

Maître, J. L., & Heisenberg, C. P. (2013). Three functions of cadherins in cell adhesion. *Current Biology, 23*(14), R626-R633. doi:10.1016/j.cub.2013.06.019

Manning, M. L., Foty, R. A., Steinberg, M. S., & Schoetz, E. M. (2010). Coaction of intercellular adhesion and cortical tension specifies tissue surface tension. *Proceedings of the National Academy of Sciences U S A, 107*(28), 12517-12522. doi:10.1073/pnas.1003743107

Marée, A. F. M., Grieneisen, V. A., & Hogeweg, P. (2007). The Cellular Potts Model and biophysical properties of cells, tissues and morphogenesis. In A. R. A. Anderson, M. A. J. Chaplain, & K. A. Rejniak (Eds.), *Single-Cell-Based Models in Biology and Medicine* (pp. 107-136). Basel, Switzerland: Birkhäuser Basel.

Marinari, E., Mehonic, A., Curran, S., Gale, J., Duke, T., & Baum, B. (2012). Live-cell delamination counterbalances epithelial growth to limit tissue overcrowding. *Nature, 484*(7395), 542-545. doi:10.1038/nature10984

Marshall, T. W., Lloyd, I. E., Delalande, J. M., Nathke, I., & Rosenblatt, J. (2011). The tumor suppressor adenomatous polyposis coli controls the direction in which a cell extrudes from an epithelium. *Molecular Biology of the Cell, 22*(21), 3962-3970. doi:10.1091/mbc.E11-05-0469

Martin, A. C., Gelbart, M., Fernandez-Gonzalez, R., Kaschube, M., & Wieschaus, E. F. (2010). Integration of contractile forces during tissue invagination. *The Journal of Cell Biology, 188*(5), 735. doi:10.1083/jcb.200910099

Martin, P., & Lewis, J. (1992). Actin cables and epidermal movement in embryonic wound healing. *Nature, 360*(6400), 179-183. doi:10.1038/360179a0

McDougall, S., Dallon, J., Sherratt, J., & Maini, P. (2006). Fibroblast migration and collagen deposition during dermal wound healing: mathematical modelling and clinical implications. *Philosophical Transactions. Series A, Mathematical, Physical, and Engineering Sciences, 364*(1843), 1385-1405. doi:10.1098/rsta.2006.1773

Meghana, C., Ramdas, N., Hameed, F. M., Rao, M., Shivashankar, G. V., & Narasimha, M. (2011). Integrin adhesion drives the emergent polarization of active cytoskeletal stresses to pattern cell delamination. *Proceedings of the National Academy of Sciences U S A, 108*(22), 9107-9112. doi:10.1073/pnas.1018652108

Merks, R., & Glazier, J. (2005). A cell-centered approach to developmental biology. *Physica A, 352*(1), 113-130. doi:10.1016/j.physa.2004.12.028

Mertz, A. F., Che, Y., Banerjee, S., Goldstein, J. M., Rosowski, K. A., Revilla, S. F., . . . Horsley, V. (2013). Cadherin-based intercellular adhesions organize epithelial cell-matrix traction forces. *Proceedings of the National Academy of Sciences U S A, 110*(3), 842-847. doi:10.1073/pnas.1217279110

Metropolis, N., Rosenbluth, A. W., Rosenbluth, M. N., Teller, A. H., & Teller, E. (1953). Equation of State Calculations by Fast Computing Machines. *The Journal of Chemical Physics, 21*(6), 1087-1092. doi:10.1063/1.1699114

Mirams, G. R., Arthurs, C. J., Bernabeu, M. O., Bordas, R., Cooper, J., Corrias, A., . . . Gavaghan, D. J. (2013). Chaste: an open source C++ library for computational physiology and biology. *PLoS Computational Biology, 9*(3), e1002970. doi:10.1371/journal.pcbi.1002970

Mombach, J. C., & Glazier, J. A. (1996). Single cell motion in aggregates of embryonic cells. *Physical Review Letters, 76*(16), 3032-3035. doi:10.1103/PhysRevLett.76.3032

Monier, B., Gettings, M., Gay, G., Mangeat, T., Schott, S., Guarner, A., & Suzanne, M. (2015). Apico-basal forces exerted by apoptotic cells drive epithelium folding. *Nature, 518*, 245. doi:10.1038/nature14152

Moore, T., Wu, Selwin K., Michael, M., Yap, Alpha S., Gomez, Guillermo A., & Neufeld, Z. (2014). Self-organizing actomyosin patterns on the cell cortex at epithelial cell-cell junctions. *Biophysical Journal, 107*(11), 2652-2661. doi:10.1016/j.bpj.2014.10.045

Motegi, S., Okazawa, H., Ohnishi, H., Sato, R., Kaneko, Y., Kobayashi, H., . . . Matozaki, T. (2003). Role of the CD47–SHPS-1 system in regulation of cell migration. *Embo j, 22*(11), 2634-2644. doi:10.1093/emboj/cdg278

Muliyil, S., Krishnakumar, P., & Narasimha, M. (2011). Spatial, temporal and molecular hierarchies in the link between death, delamination and dorsal closure. *Development, 138*(14), 3043-3054. doi:10.1242/dev.060731

Murray, J. D. (2002). *Mathematical Biology I. An Introduction* (3rd ed.). New York, NY: Springer New York.

Nagai, T., & Honda, H. (2001). A dynamic cell model for the formation of epithelial tissues. *Philosophical Magazine B, 81*(7), 699-719. doi:10.1080/13642810108205772

Nagai, T., & Honda, H. (2009). Computer simulation of wound closure in epithelial tissues: cell-basal-lamina adhesion. *Physical Review. E, Statistical, Nonlinear, and Soft Matter Physics, 80*(6), 061903. doi:10.1103/PhysRevE.80.061903

Naszai, M., Carroll, L. R., & Cordero, J. B. (2015). Intestinal stem cell proliferation and epithelial homeostasis in the adult Drosophila midgut. *Insect Biochemistry and Molecular Biology, 67*, 9-14. doi:10.1016/j.ibmb.2015.05.016

Niessen, C. M., Leckband, D., & Yap, A. S. (2011). Tissue organization by cadherin adhesion molecules: dynamic molecular and cellular mechanisms of morphogenetic regulation. *Physiological Reviews, 91*(2), 691-731. doi:10.1152/physrev.00004.2010

Noppe, A. R., Roberts, A. P., Yap, A. S., Gomez, G. A., & Neufeld, Z. (2015). Modelling wound closure in an epithelial cell sheet using the cellular Potts model. *Integrative Biology (Camb), 7*(10), 1253-1264. doi:10.1039/c5ib00053j

Osterfield, M., Du, X., Schupbach, T., Wieschaus, E., & Shvartsman, S. Y. (2013). Three-dimensional epithelial morphogenesis in the developing Drosophila egg. *Developmental Cell, 24*(4), 400-410. doi:10.1016/j.devcel.2013.01.017

Otani, T., Ichii, T., Aono, S., & Takeichi, M. (2006). Cdc42 GEF Tuba regulates the junctional configuration of simple epithelial cells. *Journal of Cell Biology, 175*(1), 135-146. doi:10.1083/jcb.200605012

Painter, K. J., Armstrong, N. J., & Sherratt, J. A. (2010). The impact of adhesion on cellular invasion processes in cancer and development. *Journal of Theoretical Biology, 264*(3), 1057-1067. doi:10.1016/j.jtbi.2010.03.033

Pang, S. C., Daniels, W. H., & Buck, R. C. (1978). Epidermal migration during the healing of suction blisters in rat skin: a scanning and transmission electron microscopic study. *American Journal of Anatomy, 153*(2), 177-191. doi:10.1002/aja.1001530202

Pellettieri, J., & Sanchez Alvarado, A. (2007). Cell turnover and adult tissue homeostasis: from humans to planarians. *Annual Review of Genetics, 41*, 83-105. doi:10.1146/annurev.genet.41.110306.130244

Pitt-Francis, J., Pathmanathan, P., Bernabeu, M. O., Bordas, R., Cooper, J., Fletcher, A. G., . . . Gavaghan, D. J. (2009). Chaste: A test-driven approach to software development for biological modelling. *Computer Physics Communications, 180*(12), 2452-2471. doi:10.1016/j.cpc.2009.07.019

Posta, F., & Chou, T. (2010). A mathematical model of intercellular signaling during epithelial wound healing. *Journal of Theoretical Biology, 266*(1), 70-78. doi:10.1016/j.jtbi.2010.05.029

Radice, G. P. (1980). The spreading of epithelial cells during wound closure in Xenopus larvae. *Developmental Biology, 76*(1), 26-46. doi:10.1016/0012-1606(80)90360-7

Ratheesh, A., Gomez, G. A., Priya, R., Verma, S., Kovacs, E. M., Jiang, K., . . . Yap, A. S. (2012). Centralspindlin and alpha-catenin regulate Rho signalling at the epithelial zonula adherens. *Nature Cell Biology, 14*(8), 818-828. doi:10.1038/ncb2532

Reddig, P. J., & Juliano, R. L. (2005). Clinging to life: cell to matrix adhesion and cell survival. *Cancer and Metastasis Reviews, 24*(3), 425-439. doi:10.1007/s10555-005-5134-3

Rosenblatt, J., Raff, M. C., & Cramer, L. P. (2001). An epithelial cell destined for apoptosis signals its neighbors to extrude it by an actin- and myosin-dependent mechanism. *Current Biology, 11*(23), 1847-1857.

Rudnick, J., & Gaspari, G. (2010). *Elements of the Random Walk: An introduction for Advanced Students and Researchers*: Cambridge University Press.

Schleich, J. M., Abdulla, T., Summers, R., & Houyel, L. (2013). An overview of cardiac morphogenesis. *Archives of Cardiovascular Disease, 106*(11), 612-623. doi:10.1016/j.acvd.2013.07.001

Scianna, M. (2015). An extended Cellular Potts Model analyzing a wound healing assay. *Computers in Biology and Medicine, 62*, 33-54. doi:10.1016/j.compbiomed.2015.04.009

Seung, H. S., & Nelson, D. R. (1988). Defects in flexible membranes with crystalline order. *Physical review. A, General physics, 38*(2), 1005-1018. doi:10.1103/PhysRevA.38.1005

Sherratt, J. A., Martin, P., Murray, J. D., & Lewis, J. (1992). Mathematical models of wound healing in embryonic and adult epidermis. *Mathematical Medicine and Biology: A Journal of the IMA, 9*(3), 177-196. doi:10.1093/imammb/9.3.177

Sherratt, J. A., & Murray, J. D. (1990). Models of epidermal wound healing. *Proceedings of the Royal Society B: Biological Sciences, 241*(1300), 29-36. doi:10.1098/rspb.1990.0061

Sherratt, J. A., & Murray, J. D. (1992). Epidermal wound healing: the clinical implications of a simple mathematical model. *Cell Transplant, 1*(5), 365-371. doi:10.1177/096368979200100505

Shewan, A. M., Maddugoda, M., Kraemer, A., Stehbens, S. J., Verma, S., Kovacs, E. M., & Yap, A. S. (2005). Myosin 2 is a key Rho kinase target necessary for the local concentration of E-cadherin at cell-cell contacts. *Molecular Cell Biology, 16*(10), 4531-4542. doi:10.1091/mbc.E05-04-0330

Shirinifard, A., Gens, J. S., Zaitlen, B. L., Poplawski, N. J., Swat, M., & Glazier, J. A. (2009). 3D multi-cell simulation of tumor growth and angiogenesis. *PLoS One, 4*(10), e7190. doi:10.1371/journal.pone.0007190

Shraiman, B. I. (2005). Mechanical feedback as a possible regulator of tissue growth. *Proceedings of the National Academy of Sciences U S A, 102*(9), 3318-3323. doi:10.1073/pnas.0404782102

Simpson, M. J., Landman, K. A., & Hughes, B. D. (2009). Multi-species simple exclusion processes. *Physica A: Statistical Mechanics and its Applications, 388*(4), 399-406. doi:10.1016/j.physa.2008.10.038

Simpson, M. J., Landman, K. A., Hughes, B. D., & Fernando, A. E. (2010). A model for mesoscale patterns in motile populations. *Physica A: Statistical Mechanics and its Applications, 389*(7), 1412-1424. doi:10.1016/j.physa.2009.12.010

Slattum, G., McGee, K. M., & Rosenblatt, J. (2009). P115 RhoGEF and microtubules decide the direction apoptotic cells extrude from an epithelium. *The Journal of Cell Biology, 186*(5), 693. doi:10.1083/jcb.200903079

Smutny, M., Cox, H. L., Leerberg, J. M., Kovacs, E. M., Conti, M. A., Ferguson, C., . . . Yap, A. S. (2010). Myosin II isoforms identify distinct functional modules that support integrity of the epithelial zonula adherens. *Nature Cell Biology, 12*(7), 696-702. doi:10.1038/ncb2072

Sonnemann, K. J., & Bement, W. M. (2011). Wound repair: toward understanding and integration of single-cell and multicellular wound responses. *Annual Review of Cell and Developmental Biology, 27*, 237-263. doi:10.1146/annurev-cellbio-092910-154251

Sturm, A., & Dignass, A. U. (2008). Epithelial restitution and wound healing in inflammatory bowel disease. *World Journal of Gastroenterology, 14*(3), 348-353. doi:10.3748/wjg.14.348

Summers, R., Abdulla, T., & Schleich, J. M. (2014). *Advances in Modelling of Epithelial to Mesenchymal Transition.* Paper presented at the XIII Mediterranean Conference on Medical and Biological Engineering and Computing 2013, Cham, Switzerland.

Swat, M. H., Thomas, G. L., Belmonte, J. M., Shirinifard, A., Hmeljak, D., & Glazier, J. A. (2012). Multi-scale modeling of tissues using CompuCell3D. *Methods in Cell Biology, 110*, 325-366. doi:10.1016/b978-0-12-388403-9.00013-8

Szabo, A., Unnep, R., Mehes, E., Twal, W. O., Argraves, W. S., Cao, Y., & Czirok, A. (2010). Collective cell motion in endothelial monolayers. *Physical Biology, 7*(4), 046007. doi:10.1088/1478-3975/7/4/046007

Tabatabai, M. A., Eby, W. M., & Singh, K. P. (2011). Hyperbolastic modeling of wound healing. *Mathematical and Computer Modelling, 53*(5), 755-768. doi:10.1016/j.mcm.2010.10.013

Taddei, M. L., Giannoni, E., Fiaschi, T., & Chiarugi, P. (2012). Anoikis: an emerging hallmark in health and diseases. *The Journal of Pathology*, *226*(2), 380-393. doi:10.1002/path.3000

Tamada, M., Perez, T. D., Nelson, W. J., & Sheetz, M. P. (2007). Two distinct modes of myosin assembly and dynamics during epithelial wound closure. *The Journal of Cell Biology, 176*(1), 27-33. doi:10.1083/jcb.200609116

Tapia, J. J., & D'Souza, R. M. (2011). Parallelizing the Cellular Potts Model on graphics processing units. *Computer Physics Communications, 182*(4), 857-865. doi:10.1016/j.cpc.2010.12.011

Van Den Brenk, H. A. (1956). Studies in restorative growth processes in mammalian wound healing. *The British Journal of Surgery, 43*(181), 525-550. doi:10.1002/bjs.18004318115

van Roy, F., & Berx, G. (2008). The cell-cell adhesion molecule E-cadherin. *Cellular and Molecular Life Sciences, 65*(23), 3756-3788. doi:10.1007/s00018-008-8281-1

Vedula, S. R., Leong, M. C., Lai, T. L., Hersen, P., Kabla, A. J., Lim, C. T., & Ladoux, B. (2012). Emerging modes of collective cell migration induced by geometrical constraints. *Proceedings of the National Academy of Sciences U S A, 109*(32), 12974-12979. doi:10.1073/pnas.1119313109

Vedula, S. R., Peyret, G., Cheddadi, I., Chen, T., Brugues, A., Hirata, H., . . . Ladoux, B. (2015). Mechanics of epithelial closure over non-adherent environments. *Nature Communications, 6*, 6111. doi:10.1038/ncomms7111

Versaevel, M., Grevesse, T., & Gabriele, S. (2012). Spatial coordination between cell and nuclear shape within micropatterned endothelial cells. *Nature Communications, 3*, 671. doi:10.1038/ncomms1668

Wang, F., Wang, F., Zou, Z., Liu, D., Wang, J., & Su, Y. (2011). Active deformation of apoptotic intestinal epithelial cells with adhesion-restricted polarity contributes to apoptotic clearance. *Laboratory Investigation, 91*(3), 462-471. doi:10.1038/labinvest.2010.182

Weber, G. F., Bjerke, M. A., & DeSimone, D. W. (2012). A mechanoresponsive cadherin-keratin complex directs polarized protrusive behavior and collective cell migration. *Developmental Cell, 22*(1), 104-115. doi:10.1016/j.devcel.2011.10.013

Weliky, M., & Oster, G. (1990). The mechanical basis of cell rearrangement. I. Epithelial morphogenesis during Fundulus epiboly. *Development, 109*(2), 373-386.

Wu, S. K., Budnar, S., Yap, A. S., & Gomez, G. A. (2014). Pulsatile contractility of actomyosin networks organizes the cellular cortex at lateral cadherin junctions. *European Journal of Cell Biology, 93*(10-12), 396-404. doi:10.1016/j.ejcb.2014.09.001

Wu, S. K., Gomez, G. A., Michael, M., Verma, S., Cox, H. L., Lefevre, J. G., . . . Yap, A. S. (2014). Cortical F-actin stabilization generates apical–lateral patterns of junctional contractility that integrate cells into epithelia. *Nature Cell Biology, 16*, 167. doi:10.1038/ncb2900

Wu, Y., Kanchanawong, P., & Zaidel-Bar, R. (2015). Actin-delimited adhesion-independent clustering of E-cadherin forms the nanoscale building blocks of adherens junctions. *Developmental Cell, 32*(2), 139-154. doi:10.1016/j.devcel.2014.12.003

Wyczalkowski, M. A., Chen, Z., Filas, B. A., Varner, V. D., & Taber, L. A. (2012). Computational Models for Mechanics of Morphogenesis. *Birth Defects Research, 96*(2), 132-152. doi:10.1002/bdrc.21013

Zajac, M., Jones, G. L., & Glazier, J. A. (2003). Simulating convergent extension by way of anisotropic differential adhesion. *Journal of Theoretical Biology, 222*(2), 247-259. doi:10.1016/S0022-5193(03)00033-X

Appendix A

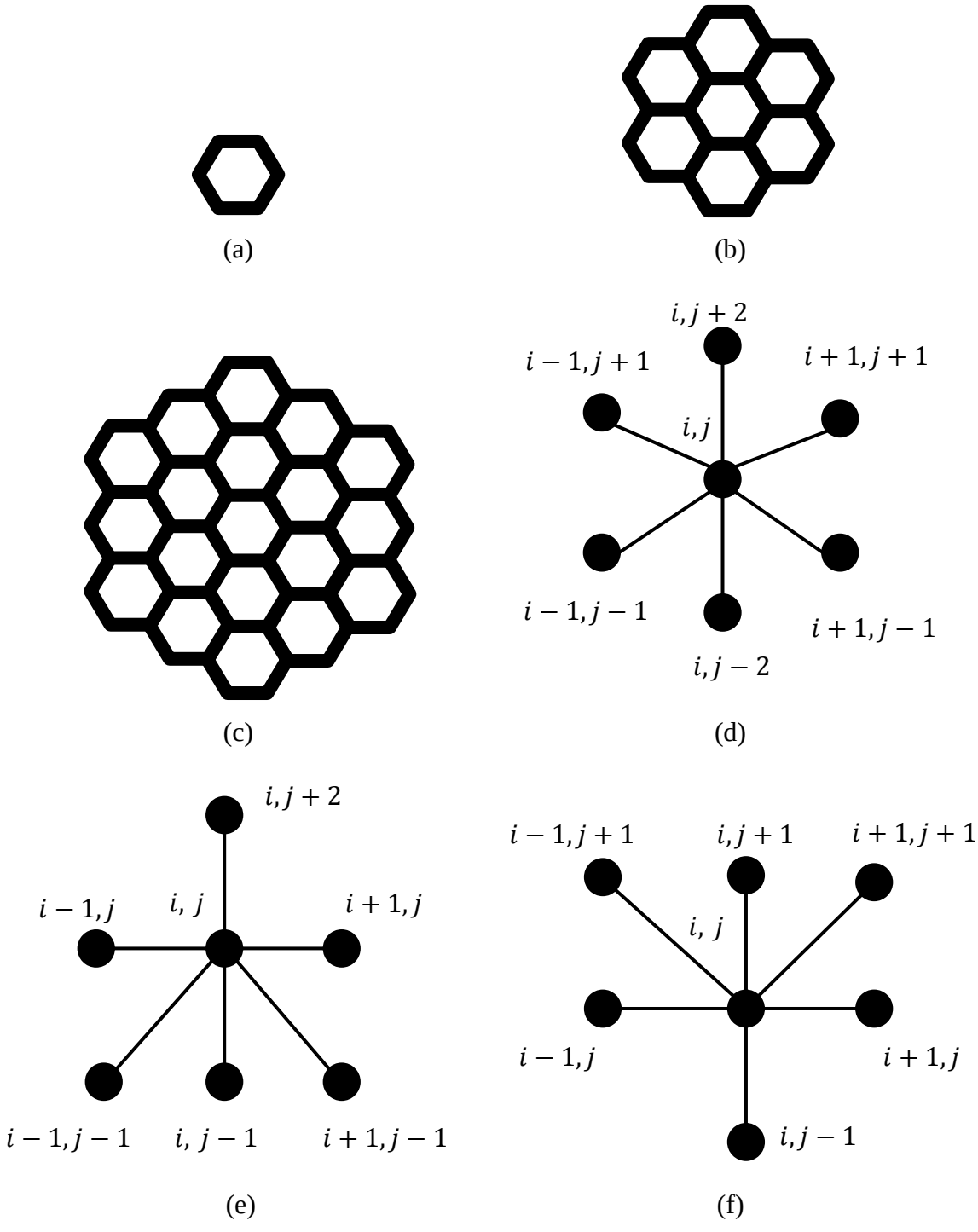

Figure A.1. a) An example of hexagonal pixels. b-c) Shows cells with a number of pixel "layers" $n = 2$ and $n = 3$ respectively surrounding the centre. This can be used to find the minimum perimeter and area perimeter ratio, g, for the geometric approximations. d) A two-dimensional lattice representation for the organisation of the hexagonal pixel organisation. e-f) The two-dimensional lattice representation for the organisation of the hexagonal pixels for coding.

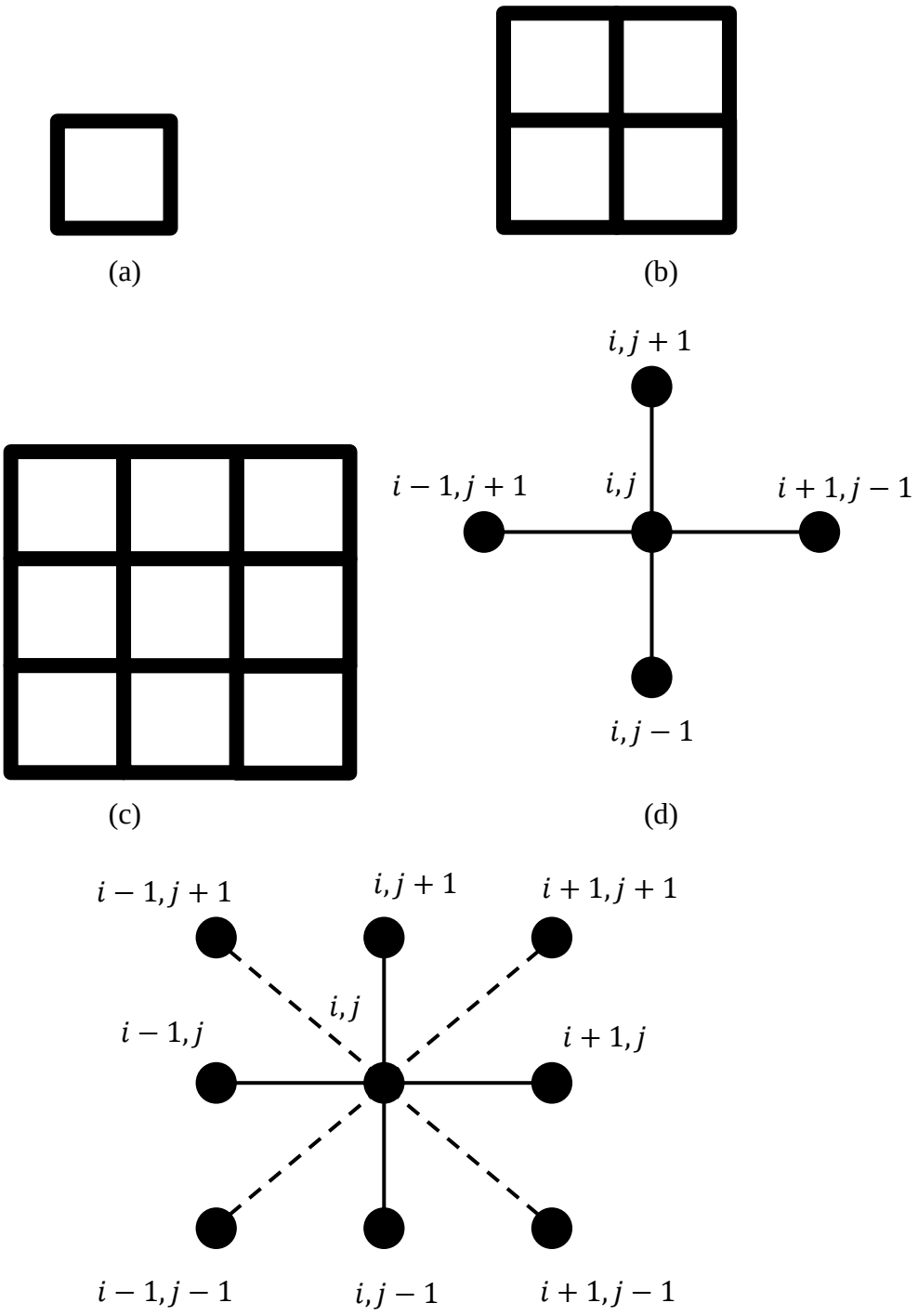

Figure A.2. a) An example of square pixels. b-c) Shows larger rectangular cells with the number of pixels on the side $n = 2$ and $n = 3$, respectively. This can be used to find the minimum perimeter and area perimeter ratio, g, for the geometric approximations. d) A two-dimensional lattice representation for the organisation of the square pixel organisation. e) A two-dimensional lattice representation for the organisation of the square pixel organisation with a connecting the corner pixels to the central (i, j) pixel site.

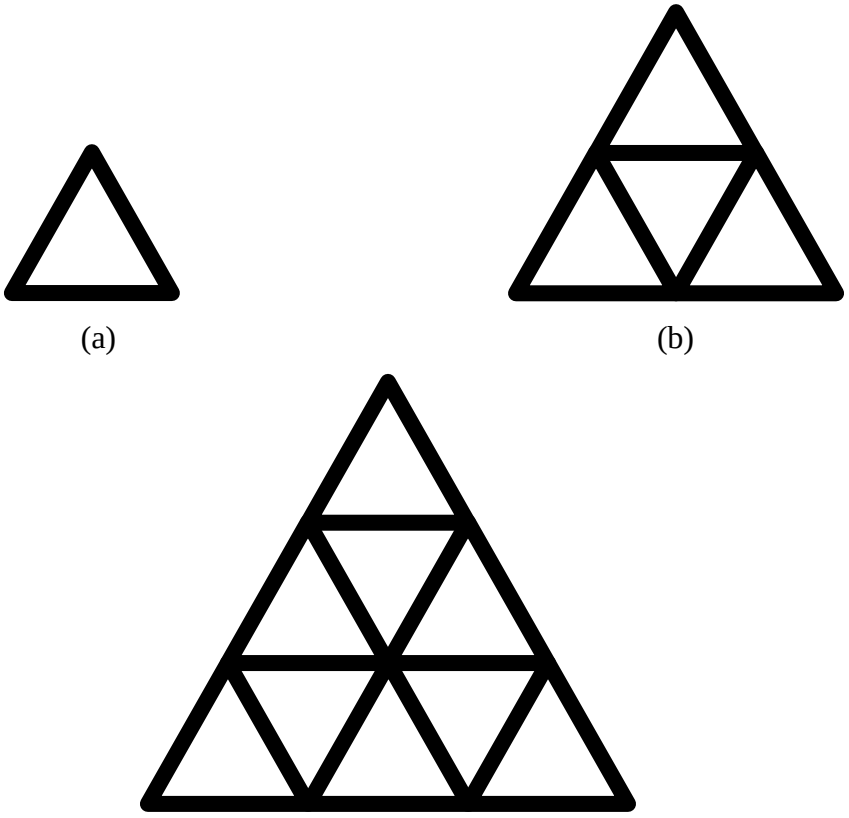

(a) (b)

(c)

Figure A.3. a) An example of square pixels. b-c) Shows larger triangular cells with the number of pixels on the side $n = 2$ and $n = 3$, respectively. This can be used to find the minimum perimeter and area perimeter ratio, g, for the geometric approximations. Compared to other pixel representations there is a difference between the other pixel representations because the pixels have a different orientation. This will give two representations of the lattice system.

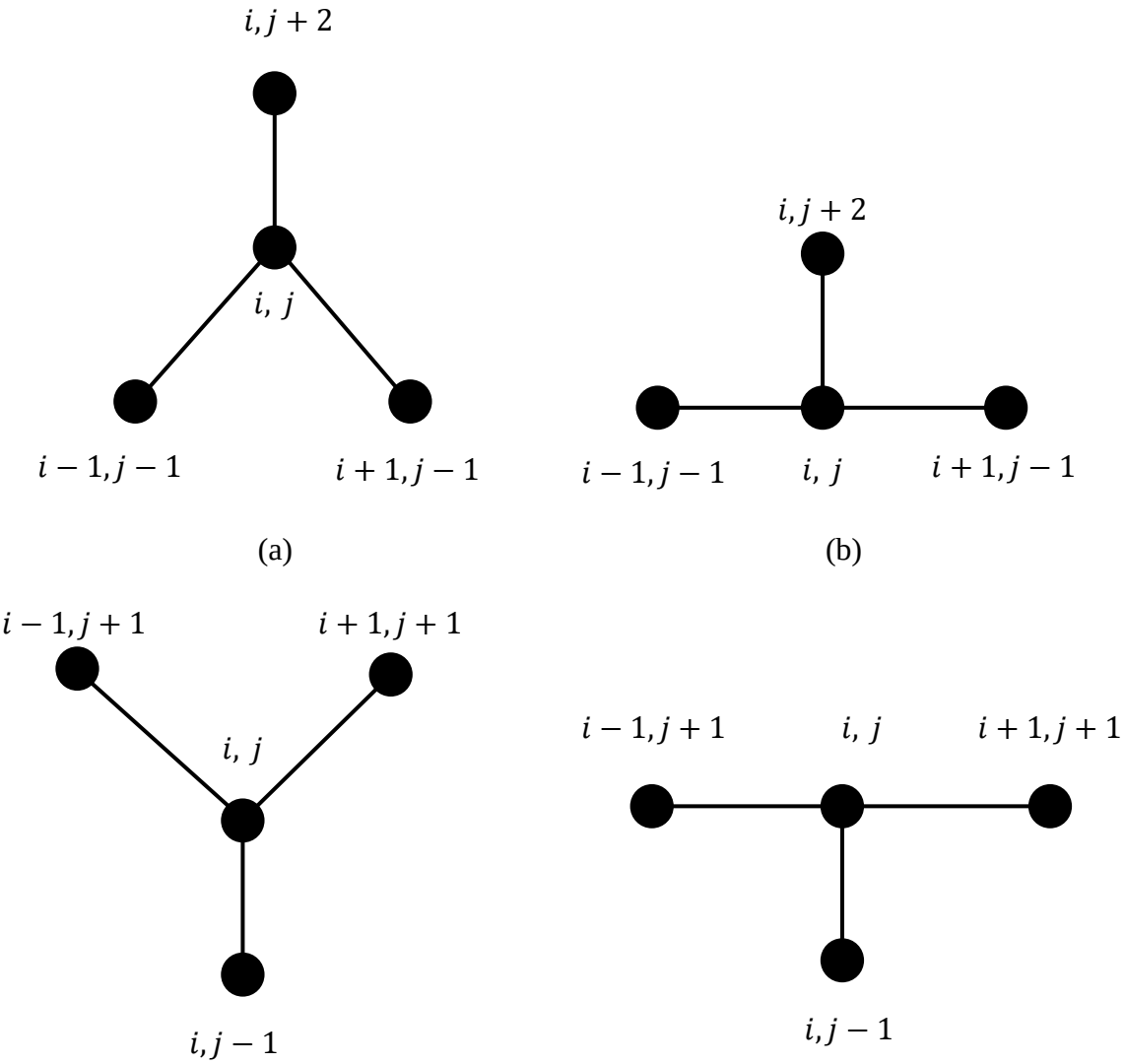

Figure A.4. a-b) Two different representations of the two-dimensional lattice representation of the triangular pixels. c-d) The two different representations of the two-dimensional lattice representation of the triangular pixels for coding.

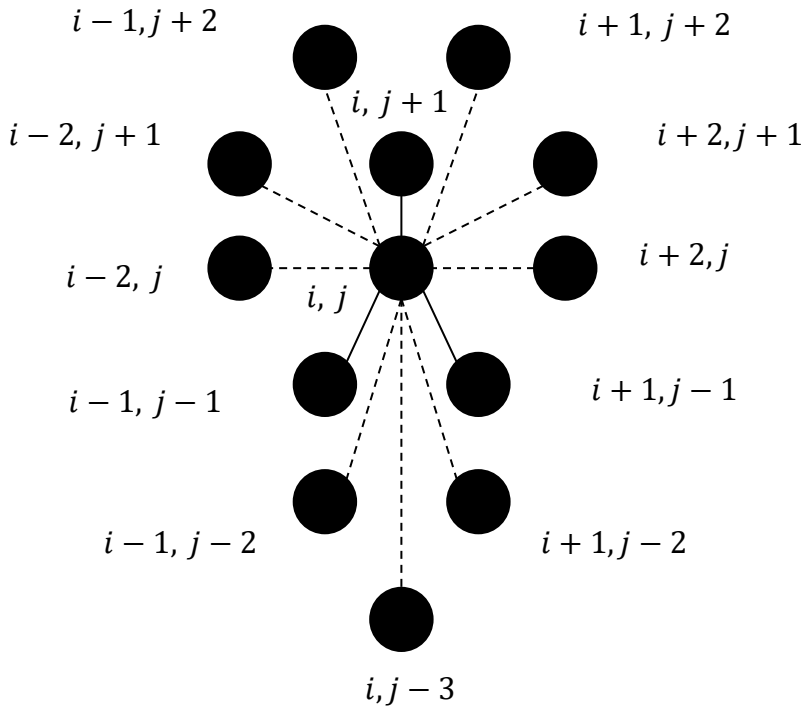

(a)

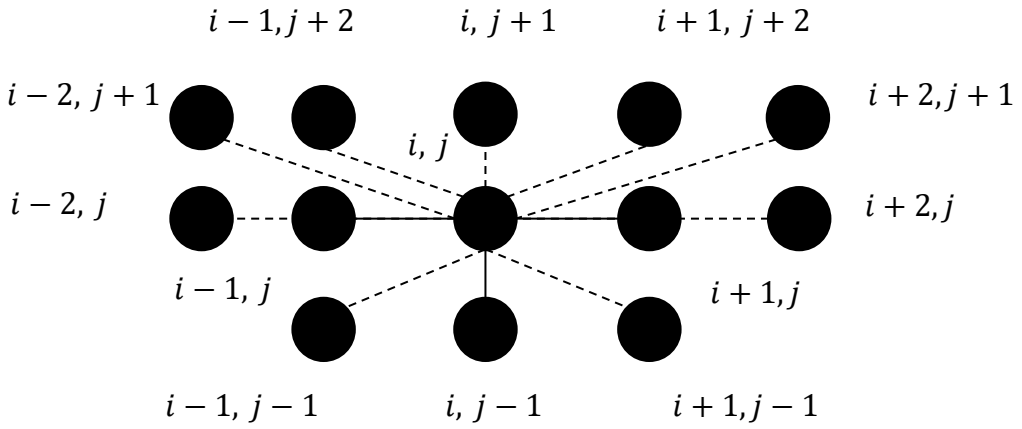

(b)

Figure A.5. a-b) Representations of the two-dimensional lattice representation of the triangular pixels including connections with the corners for preferred coding.

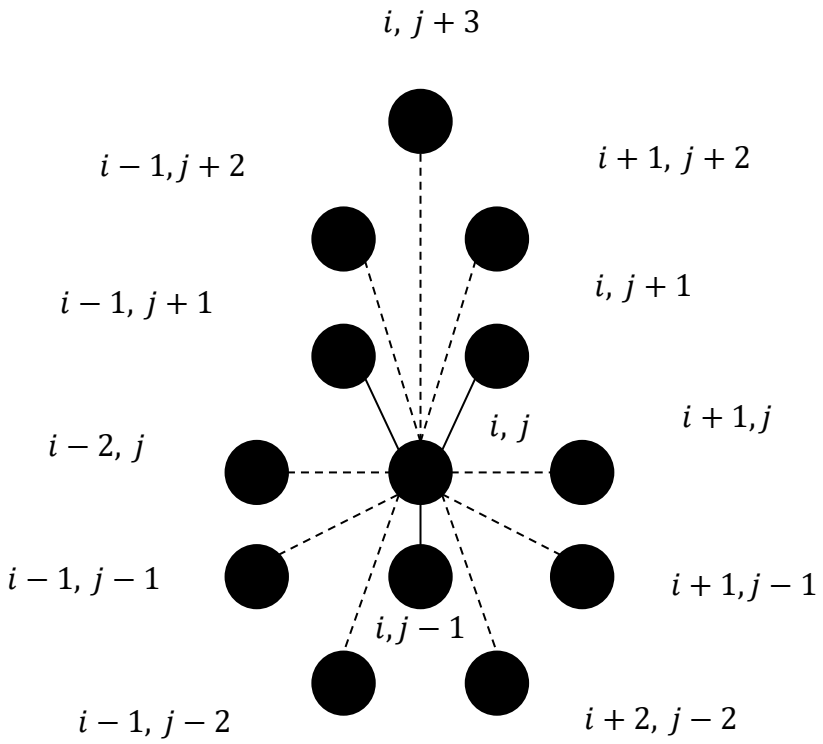

(a)

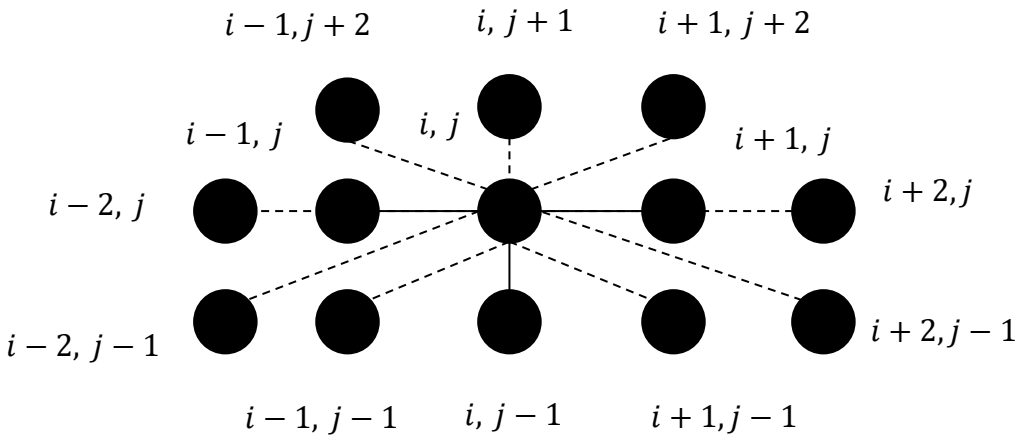

(b)

Figure A.6. a-b) Representations of the two-dimensional lattice representation of the triangular pixels including connections with the corners for preferred coding.

Appendix B

Algorithm 1: Pseudo-code of the 2D Cellular Potts Model algorithm used in Chapter 2

k, the area constraint parameter

Γ, the perimeter contraction parameter

S, the adhesion parameter

E_1, E_2, the energy values for the system without or without the pixel label change.

n, the number of columns of hexagonal pixels

m, the number of hexagonal pixels inside the columns

N, the number of cells in the system

$tend$, the number of iterations of the CPM

C_{save}, a variable to save the changed pixel label

C, a $n \times 2m$ array of the pixel labels. The empty space is labeled, 0, and cells, $1, 2, \dots, N$

P, a $1 \times (N + 1)$ array of the perimeter of the empty space, 0, and cells, $1, 2, \dots, N$

A, a $1 \times (N + 1)$ array of the area of the empty space, 0, and cells, $1, 2, \dots, N$

$Sites$, a $2 \times nm$ array of the position of all the sites in the system, (i, j)

$Neig$, a 1×6 array to collect the different labeled neighbours of the selected site

TP, a $1 \times (N + 1)$ array of the temporary perimeter change of the empty space, 0, and cells $1, 2, \dots, N$

INPUT the initial configuration of the cells in the system in C

CALCULATE the perimeter, P, of the empty space and the cells in the initial configuration

CALCULATE the area, A, of the empty space and the cells in the initial configuration

CALCULATE energy of the system, E_1

FOR $t = 1$ to $tend$

Randomise the list of the cell sites, $Sites$, to a new array, $RSites$, keeping the pairs (i, j) together

FOR $k = 1$ to nm

$i \leftarrow RSites_{1,k}$

$j \leftarrow RSites_{2,k}$

$C_{save} \leftarrow C_{i,j}$

IF $C_{i,j} \neq C_{i,j+2}$ **OR** $C_{i,j} \neq C_{i+1,j+1}$ **OR** $C_{i,j} \neq C_{i+1,j-1}$ **OR** $C_{i,j} \neq C_{i,j-2}$ **OR** $C_{i,j} \neq C_{i-1,j-1}$ **OR** $C_{i,j} \neq C_{i-1,j+1}$ **THEN**

Select a new site

ENDIF

FOR $c = 0$ to N

$TP_c \leftarrow 0$

ENDFOR

$i_{neig} \leftarrow 0$

IF $C_{i,j} \neq C_{i,j+2}$ **THEN**

$TP_{C_{i,j}} \leftarrow TP_{C_{i,j}} + 1$

$TP_{C_{i,j+2}} \leftarrow TP_{C_{i,j+2}} + 1$

$i_{neig} \leftarrow i_{neig} + 1$

$Neig_{i_{neig}} \leftarrow C_{i,j+2}$

ENDIF

IF $C_{i,j} \neq C_{i+1,j+1}$ **THEN**

$TP_{C_{i,j}} \leftarrow TP_{C_{i,j}} + 1$

$TP_{C_{i+1,j+1}} \leftarrow TP_{C_{i+1,j+1}} + 1$

$i_{neig} \leftarrow i_{neig} + 1$

$Neig_{i_{neig}} \leftarrow C_{i+1,j+1}$

ENDIF

IF $C_{i,j} \neq C_{i+1,j-1}$ **THEN**

$TP_{C_{i,j}} \leftarrow TP_{C_{i,j}} + 1$

$TP_{C_{i+1,j-1}} \leftarrow TP_{C_{i+1,j-1}} + 1$

$i_{neig} \leftarrow i_{neig} + 1$

$Neig_{i_{neig}} \leftarrow C_{i+1,j-1}$

ENDIF

IF $C_{i,j} \neq C_{i,j-2}$ **THEN**

$TP_{C_{i,j}} \leftarrow TP_{C_{i,j}} + 1$

$TP_{C_{i,j-2}} \leftarrow TP_{C_{i,j-2}} + 1$

$i_{neig} \leftarrow i_{neig} + 1$

$Neig_{i_{neig}} \leftarrow C_{i,j-2}$

ENDIF

IF $C_{i,j} \neq C_{i-1,j-1}$ **THEN**

$TP_{C_{i,j}} \leftarrow TP_{C_{i,j}} + 1$

$TP_{C_{i-1,j-1}} \leftarrow TP_{C_{i-1,j-1}} + 1$

$i_{neig} \leftarrow i_{neig} + 1$

$Neig_{i_{neig}} \leftarrow C_{i-1,j-1}$

ENDIF

IF $C_{i,j} \neq C_{i-1,j+1}$ **THEN**

$TP_{C_{i,j}} \leftarrow TP_{C_{i,j}} + 1$

$TP_{C_{i-1,j+1}} \leftarrow TP_{C_{i-1,j+1}} + 1$

$i_{neig} \leftarrow i_{neig} + 1$

$Neig_{i_{neig}} \leftarrow C_{i-1,j+1}$

ENDIF

SET the $C_{i,j}$ to one of the elements in $Neig$

IF $C_{i,j} \neq C_{i,j+2}$

IF $C_{i,j+2} = C_{i+1,j-1}$

IF $\left[C_{i,j+2} \neq C_{i+1,j+1}\right]$ **AND** $\left[C_{i,j+2} \neq C_{i-1,j+1}\right.$ **OR** $C_{i,j+2} \neq$ $\left.C_{i-1,j-1}\right.$ **OR** $\left.C_{i,j+2} \neq C_{i,j-2}\right]$ **THEN**

Do not keep the change pixel label $C_{i,j} \leftarrow C_{save}$

ENDIF

ENDIF

IF $C_{i,j+2} = C_{i,j-2}$

IF $\left[C_{i,j+2} \neq C_{i+1,j+1}\right.$ **OR** $\left.C_{i,j+2} \neq C_{i+1,j-1}\right]$ **AND** $\left[C_{i,j+2} \neq\right.$ $\left.C_{i-1,j+1}\right.$ **OR** $\left.C_{i,j+2} \neq C_{i-1,j-1}\right]$ **THEN**

Do not keep the change pixel label $C_{i,j} \leftarrow C_{save}$

ENDIF

ENDIF

IF $C_{i+1,j+1} = C_{i-1,j-1}$

IF $\left[C_{i+1,j+1} \neq C_{i+1,j+1}\right.$ **OR** $C_{i+1,j+1} \neq C_{i+1,j-1}$ **OR** $\left.C_{i+1,j+1} \neq\right.$ $\left.C_{i,j-2}\right]$ **AND** $\left[C_{i+1,j+1} \neq C_{i-1,j+1}\right]$ **THEN**

Do not keep the change pixel label $C_{i,j} \leftarrow C_{save}$

ENDIF

ENDIF

ENDIF

IF $C_{i,j} \neq C_{i+1,j+1}$

IF $C_{i+1,j+1} = C_{i,j-2}$

IF $\left[C_{i+1,j+1} \neq C_{i+1,j-1}\right]$ **AND** $\left[C_{i+1,j+1} \neq C_{i,j+2}\right.$ **OR** $C_{i+1,j+1} \neq C_{i-1,j+1}$ **OR** $\left.C_{i+1,j+1} \neq C_{i-1,j-1}\right]$ **THEN**

Do not keep the change pixel label $C_{i,j} \leftarrow C_{save}$

ENDIF

ENDIF

IF $C_{i+1,j+1} = C_{i-1,j-1}$

IF $\left[C_{i+1,j+1} \neq C_{i,j-2}\right.$ **OR** $\left.C_{i+1,j+1} \neq C(4)\right]$ **AND** $\left[C_{i+1,j+1} \neq C_{i,j+2}\right.$ **OR** $\left.C_{i+1,j+1} \neq C_{i-1,j+1}\right]$ **THEN**

Do not keep the change pixel label $C_{i,j} \leftarrow C_{save}$

ENDIF

ENDIF

IF $C_{i+1,j+1} = C_{i-1,j+1}$

IF $\left[C_{i+1,j+1} \neq C_{i+1,j-1}\right.$ OR $C_{i+1,j+1} \neq C_{i,j-2}$ OR$\left.C_{i+1,j+1} \neq C_{i-1,j-1}\right]$ **AND** $\left[C_{i+1,j+1} \neq C_{i,j+2}\right]$ **THEN**

Do not keep the change pixel label $C_{i,j} \leftarrow C_{save}$

ENDIF

ENDIF

ENDIF

IF $C_{i,j} \neq C_{i+1,j-1}$

IF $C_{i+1,j-1} = C_{i-1,j-1}$

IF $\left[C_{i+1,j-1} \neq C_{i,j-2}\right]$ **AND** $\left[C_{i+1,j-1} \neq C_{i+1,j+1}\right.$ **OR** $C_{i+1,j-1} \neq$ $\left.C_{i,j+2}\right.$ **OR** $\left.C_{i+1,j-1} \neq C_{i-1,j+1}\right]$ **THEN**

Do not keep the change pixel label $C_{i,j} \leftarrow C_{save}$

ENDIF

ENDIF

IF $C_{i+1,j-1} = C_{i-1,j+1}$

IF $\left[C_{i+1,j-1} \neq C_{i,j-2}\right.$ **OR** $\left.C_{i+1,j-1} \neq C_{i-1,j-1}\right]$ **AND** $\left[C_{i+1,j-1} \neq\right.$ $\left.C_{i+1,j+1}\right.$ **OR** $\left.C_{i+1,j-1} \neq C_{i,j+2}\right]$ **THEN**

Do not keep the change pixel label $C_{i,j} \leftarrow C_{save}$

ENDIF

ENDIF

ENDIF

IF $C_{i,j} \neq C_{i,j-2}$

IF $C_{i,j-2} = C_{i-1,j+1}$

IF $\left[C_{i,j-2} \neq C_{i-1,j-1}\right]$ **AND** $\left[C_{i,j-2} \neq C_{i+1,j-1}\right.$ **OR** $C_{i,j-2} \neq$ $\left.C_{i+1,j+1}\right.$ **OR** $\left.C_{i,j-2} \neq C_{i-1,j-1}\right]$ **THEN**

Do not keep the change pixel label $C_{i,j} \leftarrow C_{save}$

ENDIF

ENDIF

ENDIF

IF $C_{i,j} \neq C_{i,j+2}$ **THEN**

$TP_{C_{i,j}} \leftarrow TP_{C_{i,j}} - 1$

$TP_{C_{i,j+2}} \leftarrow TP_{C_{i,j+2}} - 1$

ENDIF

IF $C_{i,j} \neq C_{i+1,j+1}$ **THEN**

$TP_{C_{i,j}} \leftarrow TP_{C_{i,j}} - 1$

$TP_{C_{i+1,j+1}} \leftarrow TP_{C_{i+1,j+1}} - 1$

ENDIF

IF $C_{i,j} \neq C_{i+1,j-1}$ **THEN**

$TP_{C_{i,j}} \leftarrow TP_{C_{i,j}} - 1$

$TP_{C_{i+1,j-1}} \leftarrow TP_{C_{i+1,j-1}} - 1$

ENDIF

IF $C_{i,j} \neq C_{i,j-2}$ **THEN**

$TP_{C_{i,j}} \leftarrow TP_{C_{i,j}} - 1$

$TP_{C_{i,j-2}} \leftarrow TP_{C_{i,j-2}} - 1$

ENDIF

IF $C_{i,j} \neq C_{i-1,j-1}$ **THEN**

$TP_{C_{i,j}} \leftarrow TP_{C_{i,j}} - 1$

$TP_{C_{i-1,j-1}} \leftarrow TP_{C_{i-1,j-1}} - 1$

ENDIF

IF $C_{i,j} \neq C_{i-1,j+1}$ **THEN**

$TP_{C_{i,j}} \leftarrow TP_{C_{i,j}} - 1$

$TP_{C_{i-1,j+1}} \leftarrow TP_{C_{i-1,j+1}} - 1$

ENDIF

CALCULATE the new perimeter, P, of the empty space and the cells in the initial configuration using the local change array TP

CALCULATE the new area, A, of the empty space and the cells in the initial configuration

CALCULATE energy of the system, E_2 with the new values of perimeter, P,and area, A

GET a random number, $rand$, from a uniform distribution between 0 and 1

IF $rand > exp((E_1 - E_2)/T)$

Do not keep the pixel label change $C_{i,j} \leftarrow C_{save}$

CALCULATE the previous perimeter of the empty space and the cells using TP

CALCULATE the previous area of the empty space and the cells

ELSE

$E_1 \leftarrow E_2$

ENDIF

ENDFOR

ENDFOR
